Universidad Autónoma de Madrid

Facultad de Ciencias
Departamento de Física Teórica

Tesis Doctoral

A spatially resolved study of ionized regions in galaxies at different scales

Rubén García Benito

Directores:

Ángeles I. Díaz Beltrán
&
Enrique Pérez Jiménez

Universidad Autónoma de Madrid
Facultad de Ciencias
Departamento de Física Teórica
Grupo de Astrofísica

A spatially resolved study of ionized regions in galaxies at different resolutions

Rubén García Benito

Supervisors:

Ángeles I. Díaz Beltrán
&
Enrique Pérez Jiménez

A thesis submitted for the admission to the degree of
Doctor en Ciencias Físicas

A Abigaíl, mi *ut*

A mi familia, por su apoyo

AGRADECIMIENTOS

La trayectoria de una persona es la suma de las influencias de muchas otras en su vida. La mayoría de las veces son más los que no son recordados que los que una persona puede enumerar. Intetaré reflejar todas esas influencias en estas breves líneas.

En primer lugar, tengo que agradecer mucho a mi directora de tesis, Ángeles. Lo primero es por dame la oportunidad de trabajar en el Observatorio Astronómico de la Universidad Autónoma de Madrid, donde tuve mi primer contacto con el mundo de la astronomía observacional y pude disfrutar de "cacharrear" con telescopios, CCDs, filtros y demás cachivaches del observatorio. Esta, sin duda, fue una etapa importante en mi formación inicial y gracias a ella pude aprender muchas cosas que de otro modo sólo hubieran formado parte de la experiencia a través del papel. En segundo lugar, y no por ello menos importante, por acogerme en su grupo de trabajo y por su confianza, tiempo, dedicación, y guía incluso cuando me encontraba a 10000 kilómetros de distancia. Sin ella, este trabajo no hubiera sido escrito.

Otra persona que merece mi más sincera gratitud es mi codirector ES. Enrique. Gracias por confiar en mí y presentarme a NGC 5471. Gracias por acogerme repetidas veces en su despacho, por "pythonizarme", por infinidad de consejos, charlas sobre ciencia, divulgación, filosofía, meditación y un sinfín de experiencias que han llenado la parte más humana del trabajo científico, el contacto con las personas. Muchas gracias, Enrique, he aprendido y disfrutado mucho contigo, y espero seguir haciéndolo.

Otra persona que también es parte relevante en la creación de este trabajo y en mi formación es Enrique P. Montero. Un buen amigo que siempre ha estado ahí cuando lo necesitaba, me ha enseñado los secretos del cálculo de abundancias y de CLOUDY, me ha dado siempre su sincera opinión y ha compartido sin rechistar las habitaciones dobles cuando íbamos de congreso. Gracias por llevarme a observar al WHT, mi primera experiencia observacional. Espero que sigamos compartiendo trabajos científicos (y habitación).

Tampoco quisiera olvidar a otras muchas personas que han aportado su granito de arena a estas páginas, como Guillermo Hägele, Jesús Maíz, Miguel Cerviño, Pepe Vílchez (por su carta a Liu), Rosa González, Fabián Rosales, Elena y Roberto Terlevich, Jesús López, Sebastián Sánchez, Víctor Muñoz y tantos otros.

La gente del grupo de Astrofísica ha compartido muchos momentos y, de una u otra manera, ha compartido conmigo sus conocimientos: Raúl, Alcione, Mónica (y Vale, por sus sonrisitas), Marta (que sigue sin perdonarme que me fuera del observatorio), Jesús, Mariluz, Yago, Manuel, Carlos y Alfredo.

Mi estancia en Beijing no hubiera sido la misma sin la fantástica acogida en el KIAA por Liu Xiaowei, Zhang Ning, Fang Xuan, Yuan Haibo, Bob Rubin, Herbert Lau, Huo Zhiying, Li Shulin, Pei Yu, Clement Baruteau, Douglas Lin, Xiaoyin y muchos otros.

De los amigos que han pasado por mi vida, sin lugar a dudas parte de mí no sería lo que es hoy sin la amistad de Alberto y Jorge, amigos con mayúsculas. A pesar de la distancia, siempre están presentes en mi corazón. También a Raúl, amigo de la infancia, a Roberto y Ernesto, por su avidez por la ciencia, a Jaime, por sus aventuras, y a David y Francisco, por su amor por la música (¡aupa el "Trío Castilla"!).

Mi familia ha sido la fuerza inicial y origen de todo este trabajo. Gracias a mis padres, Begoña y Lorenzo, por darme la libertad de elegir mi camino, por la multitud oportunidades que me han ofrecido, por su más que infatigable apoyo, sacrificio y amor incondicional, por enseñarnos a mi hermana y a mí "la osa y el osito pequeño" en la terraza junto a una lámpara de queroseno, y por llevarnos a infinidad de lugares. A mi hermana Nagore, por su confianza, su compañia (mi único "compañero" de universidad cuando estudiaba en la UNED) y porque siempre vela por mi salud, física o mental. Muchas gracias, familia.

Y por último, a la persona que me ha acompañado realmente en este viaje de principio a fin, a la que he quitado más tiempo del que me hubiera gustado, la que me ha apoyado en todo momento, la que ha llenado de instrumentos y música mi vida. Gracias por acompañarme a lugares muy muy lejanos, por la paciencia que ha mostrado en todo momento (sobre todo con la maquetación del trabajo ...), y por un sinfín de cosas de las que sólo ella es capaz. Gracias por su valor (¡ese día al volver de Tabarca!), pues ella es la que ha apostado verdaderamente por mí. Gracias por todo, Abi.

ABSTRACT

In this thesis we have studied star formation processes in galaxies at different scales: giant HII regions in spiral discs and individual starburst knots in HII galaxies.

The first has revealed that star formation in these regions is complex and, at lest in NGC 5471, has proceeded in a general spatio-temporal sequence from the halo inwards to the core. A remarkable abundance uniformity is found confirming previous results from classical works and validating the use of integrated spectroscopy to obtain abundances in distants objects.

The second has allowed a detailed abundance analysis of several star forming knots in two HII galaxies which shows no conclusive spatial variations of the total abundances. Since there are stellar populations old enough as to have produced supernovae, this implies either a very fast and effective mixing with the surroundings or that the metals whose abundances are inferred proceed from from previous star formation events.

RESUMEN

En esta tesis presentamos un estudio de los procesos de formación estelar en galaxias a dos escalas diferentes: regiones HII gigantes en discos de espirales y brotes individuales en galaxias HII .

La primera parte ha mostrado que la formación estelar en ese tipo de regiones es compleja y, al menos en NGC 5471, ha procedido en una secuencia general espacio-temporal desde el halo hacia el núcleo. También se ha hallado una abundancia uniforme confirmando resultados anteriores de trabajos clásicos, validando el uso de la espectroscopía integrada para obtener abundancias en objetos más distantes.

En la segunda parte se ha llevado a cabo un análisis detallado de varios nodos de formación estelar en dos galaxias HII . De los resultados no se concluye que haya variaciones espaciales de las abundancias totales. Ya que se encuentran poblaciones lo suficientemente viejas como para producir supernovas, esto implica que, o se produce un mezclado rápido y efectivo con el entorno, o los metales de los que se derivan las abundancias proceden de episodios anteriores de formación estelar.

Contents

List of Figures v

List of Tables ix

1 • Introduction 1
- 1.1 Overview . . . 1
  - 1.1.1 Giant Extragalactic HII regions . . . 2
  - 1.1.2 HII Galaxies . . . 5
- 1.2 Aims and structure of this work . . . 8

2 • The star formation history of NGC 5471 11
- 2.1 Introduction . . . 11
- 2.2 Observations and Data Reduction . . . 13
  - 2.2.1 GALEX data . . . 13
  - 2.2.2 HST/WFPC2 Imaging . . . 14
  - 2.2.3 Near-infrared photometry . . . 17
- 2.3 Results . . . 19
  - 2.3.1 Cluster Photometry . . . 19
  - 2.3.2 Resolved Stellar Photometry . . . 24
- 2.4 Discussion . . . 29
  - 2.4.1 Cluster Analysis . . . 29
  - 2.4.2 CMD . . . 33

3 • IFS of a GEHR in NGC 6946 39
- 3.1 Introduction . . . 39
- 3.2 Observations . . . 42
- 3.3 Data Reduction . . . 45
  - 3.3.1 Pre-reduction . . . 46
  - 3.3.2 Identification of the position of the spectra . . . 47
  - 3.3.3 Spectra extraction . . . 48

3.3.4 Wavelength solution (dispersion correction) . . . 50
3.3.5 Fiber-to-fiber response correction . . . 51
3.3.6 Flux-calibration . . . 52
3.3.7 Sky-subtraction . . . 57
3.3.8 Mosaics . . . 58
3.3.9 Correction for atmospheric absorption . . . 59
3.3.10 Correction for differential atmospheric refration . . . 61
3.4 Results . . . 63
3.4.1 Subtraction of the underlying population . . . 63
3.4.2 Line intensities . . . 66
3.4.3 Hα maps and morphology . . . 68
3.4.4 Reddening correction and c(Hβ) map . . . 72
3.4.5 Electron density . . . 74
3.4.6 Ionization structure and excitation . . . 75
3.4.7 Wolf-Rayet stellar population . . . 78
3.4.8 Physical properties and chemical abundances from the integrated spectra . . . 81
3.5 Discussion . . . 92
3.5.1 Mass of the ionized gas . . . 92
3.5.2 Derived properties of the WR population . . . 94
3.5.3 Metal content . . . 96
3.5.4 Ionization structure . . . 99

4 • Long-slit spectrophotometry of multiple knots of H II galaxies 105
4.1 Introduction . . . 105
4.2 Observations and reduction . . . 107
4.2.1 CAHA observations . . . 107
4.2.2 WHT observations . . . 108
4.2.3 Data reduction . . . 109
4.3 Results . . . 112
4.3.1 Line intensities and reddening correction . . . 112
4.3.2 Physical conditions of the gas . . . 121
4.3.3 Chemical abundance derivation . . . 127
4.4 Discussion . . . 131
4.4.1 Gaseous physical conditions and element abundances . . . 131
4.4.2 Chemical abundances from empirical calibrators for Knots A and D of IIZw71 . . . 136
4.4.3 The stellar population . . . 142
4.4.4 Ionising stellar populations . . . 146
4.4.5 Kinematics and dynamics of the polar ring . . . 147

5 • Conclusions and future work 149

A • Interstellar Reddening Corrections 159

B • Physical conditions of the gas and abundances 161
B.1 Physical conditions of the gas . . . 161
B.1.1 Density . . . 161
B.1.2 Temperature . . . 163
B.2 Ionic abundances . . . 164

C • Empirical calibrators 169

D • Stellar photometry results of NGC 5471 173

References 189

List of Figures

1.1 Sample of different scale and morphology HII regions . . . 3
1.2 Comparison of morphology of a GEHR and a BCD . . . 6
1.3 Color-magnitude diagram of IZw18 . . . 7

2.1 Large scale image of M101 . . . 12
2.2 HST WFPC2 images of NGC 5471 . . . 15
2.3 Color composite of HST WFPC2 images of NGC 5471 . . . 16
2.4 JHK$_s$ grayscale images and contour plots of NGC 5471 . . . 18
2.5 Plot of the defined eleven polygons . . . 20
2.6 Circular aperture of 15″ overplotted on the Hα image . . . 22
2.7 Decontamination of the NGC 5471 observed CMD . . . 27
2.8 Final CMD of NGC 5471 with isochrones . . . 29
2.9 Hα and J-V versus J-H plot . . . 31
2.10 Final CMD with isochrones divided in bins and luminosity function . . . 34
2.11 Spatial distribution of the star formation with time . . . 37

3.1 Color composition image of NGC 6946 . . . 41
3.2 Layout and dimensions of the PPak IFU . . . 43
3.3 Hα image of NGC 6946 showing the position of the PPak field . . . 44
3.4 Section of a PPak raw data . . . 47
3.5 Comparison of methods for the aperture extraction reduction step . . . 48
3.6 Left panel: Example of distortion along the cross-dispersion axis. Right panel: Example of shifts produces by a bad second order correction . . . 49
3.7 Example of sky lines used in the red spectra to find the wavelength solution . . . 51
3.8 Examples of extraction 1D spectrum of a standard star in a one-pointing frame and in a mosaic of three exposures . . . 54
3.9 Comparison of flux ratios for a one-pointing frame and a mosaic of three exposures . . . 55
3.10 Atmospheric absorption features in the spectrum of the standard star . . . 56
3.11 Correction for atmospheric water-vapour absorption bands . . . 60

3.12 Example of the DAR correction . . . 63
3.13 Two regions of the blue spectrum together with the spectral fits and maps of residuals in the continuum fit for two sets of metallicity templates . . . 65
3.14 Upper panel: Hα flux map obtained from the IFU data. Lower panel: Hα image taken at the KPNO 2.1-meter telescope. . . . 69
3.15 Maps in the continuum near Hα and Hβ with isocontours of the corresponding emission line fluxes . . . 70
3.16 Map in the continuum near 8500 Å with isocontours of Hα . . . 71
3.17 c(Hβ) map . . . 73
3.18 Electron density map . . . 74
3.19 Diagnostic diagrams derived from different line ratios . . . 76
3.20 Hα and excitation maps . . . 77
3.21 Wolf-Rayet bumps of the integrated spectrum of knot A . . . 78
3.22 Wolf-Rayet spatial distribution . . . 80
3.23 Blue and red spectra for the knots A and B. . . . 83
3.24 Blue and red spectra for the knots C and D. . . . 84
3.25 Blue and red spectra for the whole PPak-field. . . . 85
3.26 Relation between intensity and equivalent width of the WR blue bump as a function of the age of the cluster for solar metallicity according to Starburst 99 predictions . . . 95
3.27 BPT diagrams including the values of the integrated spectra . . . 101
3.28 S_{23} map . . . 102
3.29 Point-to-point variations of [NII]/[SII] and S_{23} versus the excitation . . . 103

4.1 False colour image of J1657 . . . 108
4.2 Spatial profile of J1657 along the slit for Hα and the adjacent continuum . . . 110
4.3 Left Panel: Spatial profile of IIZw71 along the slit for Hα and the adjacent continuum. Right Panel: Hα image with the identification of the knots, R-band contours and the position of the slit . . . 111
4.4 Blue and red spectra up to 7200 Å for the knots A and B of IIZw71. . . . 113
4.5 Blue and red spectra up to 7200 Å for the knots C and D of IIZw71. . . . 114
4.6 Blue and red spectra up to 9600 Å for the knots A and B of J1657. . . . 115
4.7 Blue and red spectra up to 9600 Å for the knot C of J1657. . . . 116
4.8 Deblending of the [OII] $\lambda\lambda$ 3727, 3729 Å lines for IIZw71 . . . 117
4.9 Results of the STARLIGHT fit for knot C . . . 118
4.10 Constant of reddening for the knots of IIZw71 . . . 120
4.11 Detail of the rest-frame spectra of the knots B and C of IIZw71 around the [OIII] 4363 Å emission line. . . . 121
4.12 Relation between t_e([OII]) and t_e([OIII]) for the knots of J1657 and HII galaxies from the literature . . . 132
4.13 Relation between t_e([SII]) and t_e([OII]) for the knots of J1657 and HII galaxies from the literature . . . 133
4.14 Relation between t_e([SIII]) and t_e([OIII]) for the knots of J1657 and HII galaxies from the literature . . . 134
4.15 N/O and S/O ratio as a function of 12+log(O/H) . . . 137
4.16 Ne/O and Ar/O ratio as a function of 12+log(O/H) . . . 138

4.17 Oxygen abundances for each observed knot of IIZw71 derived using empirical calibrators 140
4.18 Oxygen abundances for each observed knot of J1657 derived using empirical calibrators 141
4.19 Mass fraction and visual light histograms derived by STARLIGHT for IIZw71 . 143
4.20 Mass fraction and visual light histograms derived by STARLIGHT for J1657 . 144
4.21 Rotation curve of IIZw71 148

5.1 Multiwavelength 30 Doradus nebula image 153

List of Tables

1.1 Integrated properties of some HII regions 4

2.1 Journal of HST/WFPC2 observations of NGC 5471 14
2.2 Journal of TNG/ARNICA observations of NGC 5471. 17
2.3 Integrated magnitudes and Hα flux for the eleven regions of NGC 5471 . . . 21
2.4 Integrated Hα flux and derived parameters for the eleven regions of NGC 5471 23
2.5 Stellar photometry of the first 20 stars of the final CMD of NGC 5471 28

3.1 NGC 6946 general properties 40
3.2 Journal of observations and instrumental configuration. 43
3.3 Luminosities, relative intensities and equivalent widths of the Wolf-Rayet features 81
3.4 Relative observed and reddening corrected line intensities for the integrated spectrum of the PPak-field 86
3.5 Relative observed and reddening corrected line intensities for the integrated spectrum of the knots A and B 87
3.6 Relative observed and reddening corrected line intensities for the integrated spectrum of the knots C and D 88
3.7 Electron densities and temperatures for the integrated spectra 90
3.8 Ionic and total chemical abundances for helium 91
3.9 Ionic chemical abundances derived from forbidden emission lines, ICFs and total chemical abundances for elements heavier than helium. 93
3.10 Hα flux and derived parameters for the integrated spectra of the four knots . 94
3.11 Derived number of WR stars and ratios between WR and O stars. 96
3.12 Abundances derived using empirical calibrators 100

4.1 WHT and CAHA instrumental configuration 109
4.2 Equivalent widths of the hydrogen recombination lines Hβ, Hγ and Hδ of IIZw71 once the underlying populations have been removed 119

4.3 Relative observed and reddening corrected line intensities for the different observed knots of IIZw71 . . . 122
4.4 Relative reddening corrected line intensities for the three knots of J1657 . . . 123
4.5 Electron densities and temperatures for the knots of J1657 and IIZw71 . . . 126
4.6 Ionic and total chemical abundances for helium for the knots of J1657 . . . 128
4.7 ICFs, ionic and total chemical abundances for the knots of J1657 . . . 130
4.8 ICFs, ionic and total chemical abundances for knots B and C of IIZw71 . . . 131
4.9 Values of the extinction, total stellar mass, and mass fraction predicted by STARLIGHT . . . 145
4.10 Derived properties of the observed knots from the Hα fluxes . . . 146

D.1 Stellar photometry results of NGC 5471. . . . 187

Chapter 1

Introduction

1.1 Overview

On the large scale, stars are the basic building blocks of galaxies. They are responsible for the generation of metal elements. The birth of new stars has a significant impact on the surrounding interstellar medium (ISM), the main material within galaxies. This medium is made up of several components. The more complex constituents are dust and gas. This gas is a mix of complex elements formed both during a star's life (via nuclear processes) and during its death (supernovae). By far, the most ubiquitous components are the three forms of hydrogen. The simplest form is atomic hydrogen (H) (T $\approx$ 100K and $n_p \approx 10^6$ - 10^9 particles m^{-3}), followed by molecular hydrogen (H2) (T $\approx$ 5 - 30K and $n_p > 10^9$ particles m^{-3}) and finally ionized hydrogen (H^+). The molecular hydrogen is the component of the ISM from which stars form. Massive young stars emit most of their radiation in the ultraviolet part of the spectrum. Some of these photons will dissociate and ionize the molecular hydrogen and will be absorbed by the surrounding gas out to considerable distance. These ionized regions are called HII regions, very easily detectable in the sky and cradles of active star formation.

Star formation is an ongoing process in the local universe, with observed rates of the order of 10^{-2} $M_\odot$ yr^{-1} Mpc^{-3} (Madau et al., 1996). Most of the light and metals are produced in the most massive among the newly formed stars. The most extreme regions forming massive stars are often referred to as starbursts. In the local universe they account for about a quarter of all star formation (Heckman, 1997), and this fraction may be larger in the younger universe.

The origin of the term "starburst" dates back to the early observations of dust-obscured star-forming regions in the centers of nearby galaxies at the end of the seventies and beginning of the eighties, but the basic concept extends back much further (*e.g.*, Hodge, 1969a; Searle et al., 1973).

The level of intensity of a starburst is highly variable. According to Terlevich (1997), in a starburst galaxy the energy output of the starburst (L_{SB}) is much bigger than the one coming from the rest of the galaxy (L_G), a galaxy with $L_{SB} \sim L_G$ is a galaxy with starbursts, and in a normal galaxy $L_{SB} \ll L_G$. This classification shows the variety of environments of the bursts. It is clear that the visibility of the burst depends not only on its intensity but also on its environment.

Terlevich (1997) also proposed a division in phases of the starburst. The first one, the nebular phase, is characterized by the presence of strong emission lines form gas photoionized by young massive stars, with an age of less than 10 Myr. The early continuum phase, from 10 to 100 Myr, with some Balmer lines in absorption and others in emission. Finally, the late continuum phase, with only some weak emission lines. In this work we will pay special attention to the first phase, of which HII galaxies are typical examples.

Spectroscopically, HII galaxies are essentially identical to the giant HII regions found in nearby irregular and late-type galaxies. The correlation among structural parameters (Hβ luminosity, velocity dispersion, line widths) and between these parameters and chemical composition (Terlevich and Melnick, 1981) favours the interpretation of HII galaxies as giant HII regions in distant dwarf irregular galaxies similar to the ones found nearby (Melnick et al., 1985). However, there are also HII galaxies with masses and luminosities in the range typical for elliptical galaxies, suggesting that they may be young galaxies.

Therefore, studies of HII galaxies and giant HII regions are of relevance to understand HII regions and processes of formation and evolution of massive stars, as well as the evolution of galaxies.

1.1.1 Giant Extragalactic HII regions

Giant Extragalactic HII regions (GEHRs) are the most spectacular star-forming regions in normal galaxies. The class of giant HII regions consists of a very heterogeneous group of objects in terms of size, brightness and metallicity. For example, it is intriguing that the spiral galaxy M101, which is quite similar to the Milky Way, has HII regions that are so much larger and brighter than the largest one in our Galaxy (Giannakopoulou-Creighton et al., 1999).

GEHRs are large, very bright HII regions that can be observed in the discs of both late-type spiral (Sc) and irregular galaxies. The large amount of ionized gas (10^4 - 10^6 $M_\odot$) is surrounded by massive molecular clouds. Clusters of OB stars, generating ionizing photons at a rate of 10^{51} - 10^{52} s^{-1}, ionize the surrounding low density gas ($N_e \approx 10$ - 100 cm^{-3}), creating

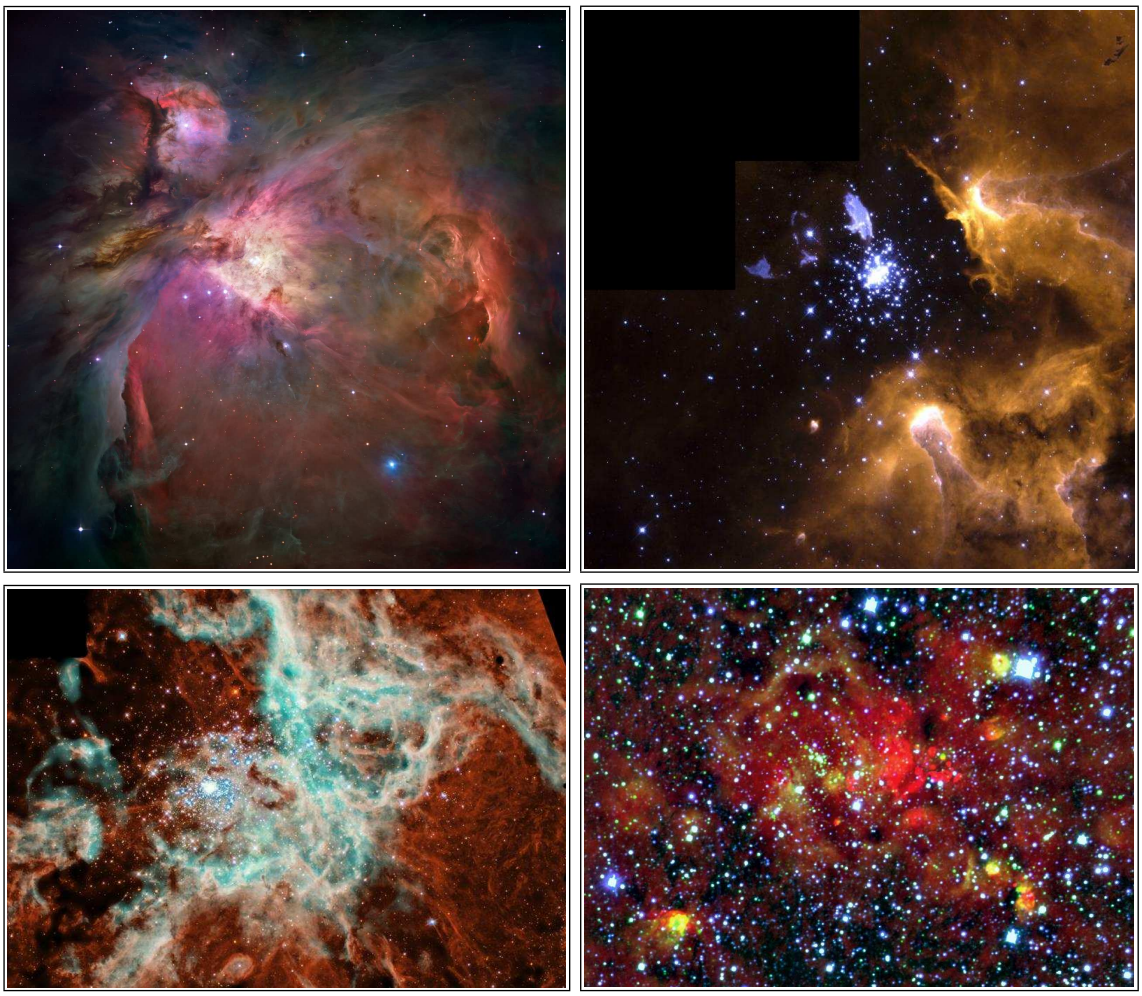

Figure 1.1: Sample of different scale and morphology HII regions: Orion Nebula obtained with the HST/ACS (*upper left*; credits: NASA, ESA, M. Robberto and HST Orion Treasury Project Team); giant HII region NGC 3603 observed with HST/WFPC2 (*upper right*; credits: W. Brandner, E.K. Grebel, Y.-H. Chu and NASA); 30 Doradus in the Large Magellanic Cloud (LMC) taken with HST/WFPC2 (*lower left*; credits: NASA, N. Walborn, J. Maíz-Apellániz and R. Barbá); radio and near-infrared composite of W49A (*lower right*; credits: ESO).

giant complexes with linear dimensions of the order of 10^2 - 10^3 pc, varied morphology, and an inhomogeneous distribution of gas (Shields, 1990). The luminosities and densities of the largest HII regions in different galaxies vary widely and independently, although the objects in any one galaxy are often similar. Figure 1.1 shows a sample of HII regions of different scale and morphology and Table 1.1 some general integrated properties of well known HII regions.

The reasons for studying giant HII regions in the Local Universe are numerous. Because they are sites of intense star formation, they are used to study large groups of massive young stars, such as OB associations and star clusters. Due to their proximity, it is possible to perform detailed studies of their individual stars, but also their relative larger distance as compared to the regions in our Galaxy, allows to obtain integrated properties. Very im-

Object	Galaxy	Diameter (pc)	L(Hα) (erg s^{-1})	M(HII) ($M_\odot$)	N (O5V)
Orion	MWG	5	1.0×10^{37}	50	0.2
NGC 3603	MWG	100	1.5×10^{39}	3.9×10^{4}	20
W49	MWG	150	1.8×10^{39}	4.5×10^{4}	27
NGC 604	M33	400	4.5×10^{39}	7.0×10^{5}	65
30 Doradus	LMC	370	1.5×10^{40}	6.0×10^{5}	230
NGC 5455	M101	750	2.5×10^{40}	...	380

Table 1.1: Integrated properties of some HII regions. M(HII) is the mass of ionized hydrogen and N (O5V) the equivalent number of O5 V stars needed to match the ionizing luminosity of the region. The abbreviations MWG and LMC stand for the Milky Way Galaxy and Large Magellanic Cloud, respectively. Based on Kennicutt (1984).

portantly, they are used to measure abundances of various elements through their emission lines. These emission lines can be used to determine some of the physical properties of the ionized gas and how the metallicity changes within a galaxy and among galaxies (McCall et al., 1985). Theses studies give clues for models of the chemical evolution of galaxies. Furthermore, these emission lines yield kinematic information about the gas in the galaxy, and therefore, allows us to study the dynamics of galaxies.

GEHRs have a wide range of metallicities. In principle, the effective temperature of ionizing stars should be lower in regions of higher metallicity due to the increasing opacity of the stellar material (McGaugh, 1991). However, highly evolved massive O stars, Wolf-Rayet (WR) stars, would increase their surface temperature to very high values because of loss of the outer envelope due to the strength of stellar winds (which increases with metallicity). As the limiting mass for a star to enter the WR phase decreases with increasing metallicity, it is expected to find a higher fraction of WR stars in high metallicity environments. Thus, the finding of WR stars in this type of HII regions would indicate a relatively high excitation.

Since the models predict larger equivalent widths and luminosities of the WR "bump" at higher metallicities, the detection of these WR features combined with a detailed analysis of the emission line spectra can be a powerful tandem for the determination of both metallicity and age in these regions.

GEHRs are an excellent environment to study large groups of massive young stars such as star clusters. Massive stars play an important role in the structure and evolution of galaxies due to their ionizing radiation, mechanical energy in the form of winds, and chemical enrichment of the ISM. Most of them are born in stellar clusters ranging from those with one or a few massive stars to massive young clusters with hundreds or thousands of massive stars, which can change the global appearance of their host galaxy, even ejecting a good fraction of the ISM in a superwind (Tenorio-Tagle et al., 2006).

These massive star clusters can have diverse morphologies (Maíz-Apellániz, 2007). Some consist of a single core, others contain double cores, and others are coreless. Also, some are surrounded by a strong halo that contains more stars than the core and some have few stars outside the core. Those without a core are likely to be not real, bound clusters, but simply unbound Scaled OB Associations. Those with a core are also called Super Star Clusters and may last long enough to become globular clusters in the distant future, but their survival depends on whether they can retain their halos. The (partial) halo retention in turn depends on the detailed star-formation history, since mass loss through winds and supernovae in the first 5 Myr of a cluster can make it expand significantly (Bastian and Goodwin, 2006).

It has been commonly assumed that massive star clusters are formed instantaneously. However, studies of 30 Doradus have revealed that these objects can have complex star-formation histories. In this region it is observed that not all stars were formed simultaneously (Walborn et al., 2002), an assumption that often underlies studies of massive star clusters and that is likely true only for the cluster core but not for the halo. Such multiple populations have been recently revealed in the long-term descendants of SSCs, globular clusters (Mackey et al., 2008).

1.1.2 HII Galaxies

Dwarf galaxies, the most numerous type in the Universe, can be classified into dwarf spheroidal/dwarf elliptical systems, dwarf irregulars (Magellanic systems), and active star-forming dwarf galaxies, also known as blue compact dwarf galaxies (BCDs). This last group was first identified as a new class of galaxy by Haro (1956) and Zwicky (1966). Several years later, Sargent and Searle (1970) found that some of these objects have spectra similar to those of HII regions in spiral galaxies. They called these new objects "*isolated extragalactic H II regions*". In the bluest galaxies known before this discovery, as the early type spirals or irregulars, the stellar light was not dominated by the massive stars but by the oldish underlying population. However, the new type of galaxies did not show evidence of old population stars, indicating a high star formation rate. They have radius of less than 2 kpc, surface brightness $\mu_v \geq 19$ mag arcsec^{-2} and total masses of less than 10^{11} $M_\odot$.

Nowadays, they are referred to by different names, the most common being BCDs and HII galaxies. Although these two terms are commonly used interchangeably, the term HII galaxy is used when the objects have been selected for their strong, narrow emission lines in objective prism plates (Terlevich et al., 1991). On the other hand, BCDs have been defined according to different observational criteria: they are selected mainly for their blue colors and compactness. At any rate, both terms are used to design the same objects, since their observed properties in the optical are dominated by their HII region spectrum. Nevertheless, in general the optical properties of HII galaxies are dominated by one or a few HII regions and their starbursts tend to be younger (Telles and Terlevich, 1995). Strictly speaking, not

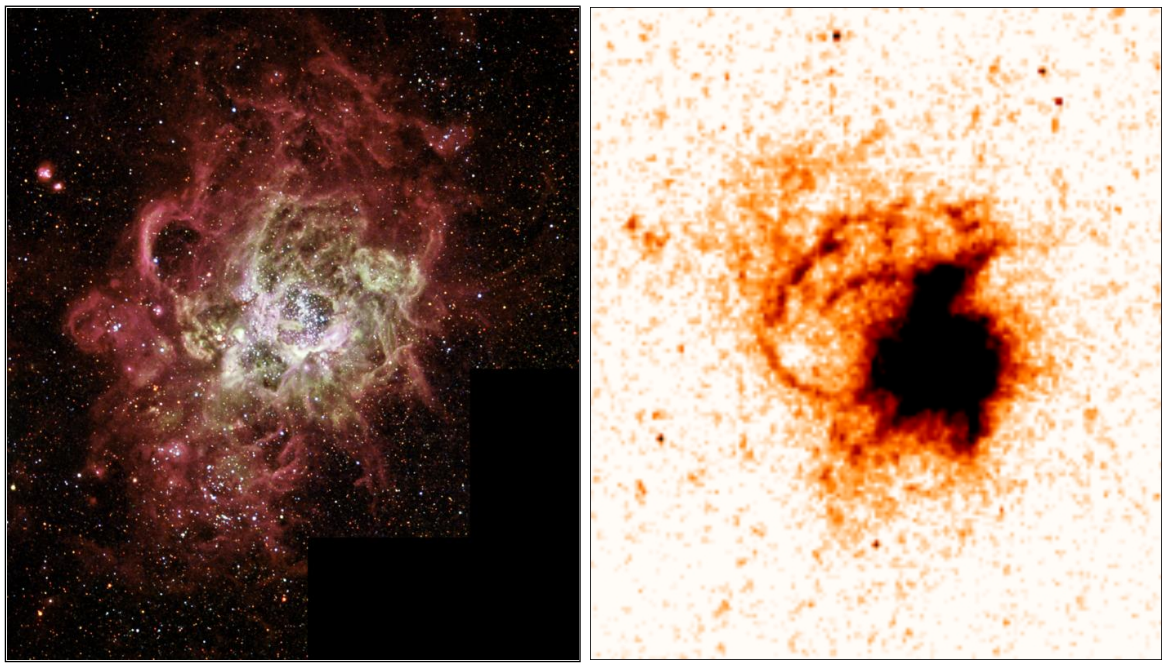

Figure 1.2: Comparison of morphology of a giant HII region and a BCD: giant HII region NGC 604 (in MÂ·3) obtained with the HST/ACS (*left*; credits: NASA, AURA/STScI, D. Garnett, J. Hester, and J. Westphal) and Hα image of the BCD SBS-0335-052E observed with HST/ACS (*right*; program 10575.

all BCDs are HII galaxies, as only in a fraction of BCDs are the HII regions dominant (Cairós et al., 2001).

From the point of view of the emission line classification, Star Forming Galaxies are a subset of Emission Line Galaxies, identified as having strong and narrow nebular emission lines and low chemical abundances (contrary to active galaxies, which have higher metallicities and broadlines), some of them being the least evolved galaxies known and candidates for young galaxies just beginning to form stars.

Several taxonomies have been suggested for this group. Melnick et al. (1985) proposed a subclassification in Starburst Nuclei, Clumpy Irregulars, and HII Galaxies. This classification is by increasing order of the luminosity ratio of the Star Formation to that of the host galaxy. According to this taxonomy, HII galaxies are gas-rich dwarf galaxies experiencing a violent star formation period which dominates the optical spectrum of the host galaxy. They have one of the highest intensity levels of star forming activity.

In general, HII galaxies have a central region which contains one or more star forming knots, with a diameter of several hundred parsecs with high surface brightness, and a low luminosity underlying galaxy ($M_V \geq$ -17). The activity of the star formation episodes cannot be sustained continuously for long periods of time, since the central region cannot have enough gas to fuel that processes for longer than 10^9 years and to match the gas content and metallicity with theoretical considerations (Thuan et al., 2004).

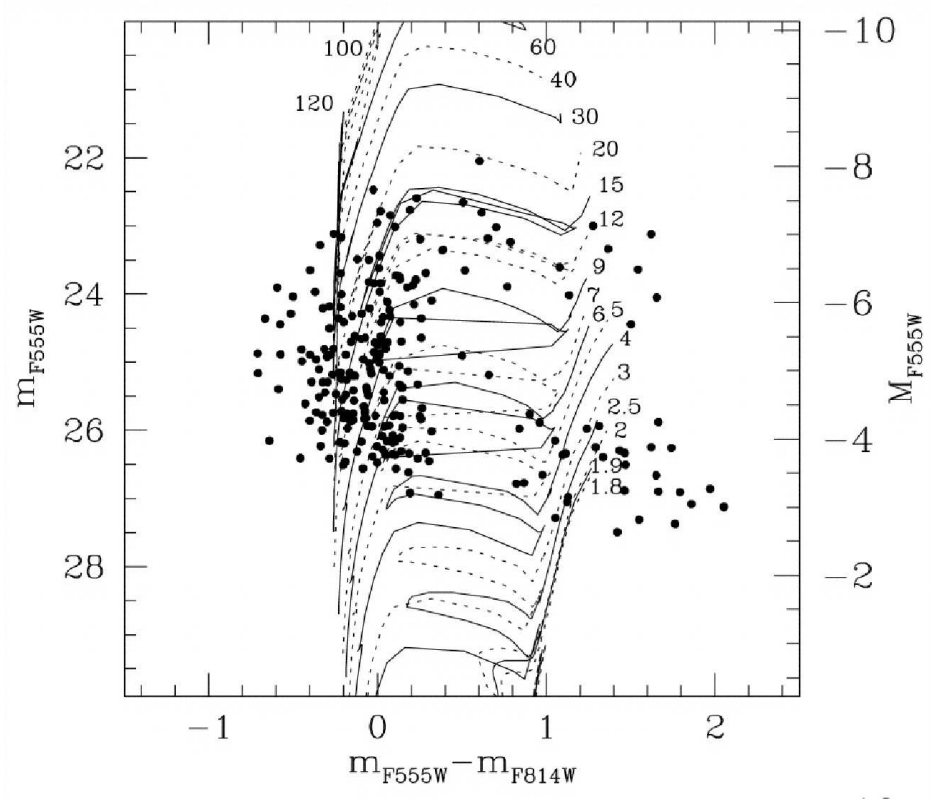

Figure 1.3: Color-magnitude (CMD) diagram V vs. V-I of IZw18 compared with Padova tracks with Z = 0.0004 from Aloisi et al. (1999), Figure 9 of that work. The stellar mass of each track is given in M⊙. The faintest clump of red objects in the CMD can be populated by old stars, extending the look-back time of the galaxy up to several Gyr.

Regarding morphology, these galaxies form a heterogeneous class. Figure 1.2 shows the color composition of NGC 604 (*left panel*, Hα in red color), a prototypical giant HII region in M33 and an Hα image of the BCD SBS-0335-052E. As it is clearly seen, both present a remarkable similar morphology, with filamentary structure and multiple well structured shells. See also Figure 10 of Tenorio-Tagle et al. (2006).

Other important characteristic of HII galaxies is their low metallicity ($Z_\odot/50 \leq Z \leq Z_\odot/3$; Kunth and Sargent, 1983). The galaxy with the lowest metallicity in the Local Universe is IZw18, with $Z \approx Z_\odot/50$, first reported by Searle and Sargent (1972) together with IIZw40. The fact that HII galaxies are metal-poor objects and very blue seems to point that they are young objects. Nevertheless, there are evidences which indicate the presence of populations older than the ones in the starburst. This is seen in the behaviour of the surface brightness profile which is exponential in the external zones, or in the the color index, which turns redder in the V-R and V-I. In the particular case of IZw18, it was considered as the best candidate for a truly young galaxy. Early studies of the stellar population of IZw18 did not reveal any old population (Hunter and Thronson, 1995). This contradicted some models which predict that during a starburst, the heavy elements produced by the massive stars are ejected with high

velocities into a hot phase, leaving the starburst region without immediate contribution to the enrichment of the interstellar medium (Tenorio-Tagle, 1996). In this scenario, the metals observed now would have their origin in a previous star formation event, and an underlying old stellar population would be expected. In fact, a reanalysis of HST archive data (Aloisi et al., 1999) showed that stars older than 1Gyr must be present (see Figure 1.3). Moreover, studies of the resolved stellar population in the near infrared with NICMOS (Östlin, 2000) found also that while the Near Infrared colour-magnitude diagram was dominated by stars 10-20 Myr old, the presence of numerous AGB stars require an age of at least 10^8 years.

1.2 Aims and structure of this work

HII galaxies have knots of star formation that can be identified with GEHRs in terms of sizes, number of ionizing photons (ionizing power), etc. The study of the physical properties of these separate knots can provide important information about the evolution of these dwarf galaxies and how star formation at large scales takes place in these otherwise small and structureless systems.

However, the reliability of these findings relies ultimately on the correct interpretation of observations, the main assumption being that the results obtained from the analysis of integrated spectra of a given knot is representative of the whole region. The properties usually derived include: elemental abundances and ages which are subsequently used to characterize the evolutionary state and star formation history at a given galaxy.

There are several reasons to probe the adequacy of the main underlying assumptions that, *i*) the abundances are uniform troughout the whole region and representative of it, and *ii*) there is a unique age of the stellar population of a given region. Firstly, the derivation of abundances requires the previous knowledge of the physical conditions of the gas, including excitation, density and geometrical effects, and these conditions are known to vary from site to site in a given nebula (*e.g.* Diaz et al., 1987). Integrated spectra are weighted by luminosity and/or surface brightness, therefore the assertion that the abundances of the brightest part of a nebula are representative of the whole needs to be substantiated. Secondly, young star clusters take a finite time to form and therefore the term "age of the cluster" probably needs a clearer definition. Can a given giant HII region (or a star-forming knot in an HII galaxy) be characterised by a single stellar population? What do we mean when we refer to "cluster age"?

The questions above can only be addressed with the use of spatial information. Until the final decade of the XX century, very little two-dimensional information existed of individual giant extragalactic HII regions that was generally obtained from long slit spectroscopy, mainly for three bright regions in nearby galaxies: NGC 5471 in M101 (Skillman, 1985), NGC 604 in M 33 (Diaz et al., 1987), and 30 Doradus in the LMC (Rosa and Mathis, 1987).

However, with the advent of the HST, high spatial resolution photometry has allowed

the study of the high mass stellar content of some regions in nearby galaxies. The results are rather complex showing that, in general, the stellar populations found in giant HII regions include evolved intermediate mass stars (Walborn and Blades, 1997). More recently, Integral Field Spectroscopy is revealing itself as a powerful tool to obtain two-dimensional spectrophotometric data which can provide simultaneously information about the physical conditions and abundances of the ionized gas and the stellar content of star forming regions.

This technique is also being applied to the study of HII galaxies, but in this case, the spatial resolution applies to the whole galaxy and the resolved units are individual GEHR (*e.g.* Kehrig et al., 2008; Lagos et al., 2009).

In the present work we have studied in detail the stellar populations of the giant HII region in the outskirts of M 101, NGC 5471, for which previous abundance information exists. It is one of the brightest relatively compact Hα sources in the local universe and considered a "cluster of superclusters" with five bright clusters, each one of them comparable in Hα luminosity to 30 Doradus. It is unclear whether we are seeing a series of two-stage starbursts (Walborn, 2002). Our study is based on the analysis of IR photometry obtained with the TNG in the Observatory of the Roque de los Muchachos in La Palma and archival optical data obtained with HST and the WFPC2 camera. The first allows a photometric study of subclusters inside the region while the second provides a CMD for the brightest stars.

Integral Field Spectroscopy obtained with PPAK and the 3.5m telescope at the Calar Alto Observatory has been used, as a pilot project, to study an outer HII region in the well studied galaxy NGC 6946 for which integrated spectroscopy dos not exist. This technique provides detailed maps of the region in different emission lines yielding precise information about the physical properties of the gas. Also, it allows to identify the location of WR stars which provides information about the age of the clusters.

In the second part of this work we have used long slit spectroscopy of two BCD galaxies, one of them classified as a "polar-ring", to study the properties of the gas and ionizing population properties of some of their ionized starforming regions.

Chapter §2 deals with the giant extragalactic HII region NGC 5471 and its integrated and stellar photometric properties.

In Chapter §3, a detailed analysis of a high metallicity GEHR by means of Integral Field Spectroscopy is performed. Maps of some relevant emission lines, excitation ratios, physical properties and parameters are presented. Wolf-Rayet population and chemical abundances of the main knots of the regions are also analyzed.

Chapter §4 is devoted to the detailed study of the physical properties of the emitting gas of each particular knot of a sample of two HII galaxies.

Finally, in the last Chapter of this work, §5, we present the general conclusions of this thesis and we list some of the future projects.

Chapter 2

The star formation history of NGC 5471 from cluster and resolved stellar photometry

2.1 Introduction

Giant Extragalactic H II Regions (GEHRs) are important star formation tracers in the chemical evolution of galaxies and can be used as standard candles to estimate cosmological distances, thus they have been intensively studied. Equally important, they are the best indicators of the conditions that lead to massive star formation. These objects are very luminous Hα emitters. Their Hα luminosities, in the range $10^{39}-10^{41}$ erg s^{-1}, imply large numbers of ionizing photons, $10^{51}-10^{53}$ s^{-1}, an ionizing power equivalent to up to several thousand of O5V stars. Such a massive stellar concentration provides an excellent laboratory to study the modes of massive star formation.

The energy deposited in the interstellar medium in the form of stellar winds, supernova explosions and ultraviolet light produce complex stellar and gaseous spatial distributions which change rapidly during the few Myr following the onset of the first massive star generation. Although the massive young clusters that power the GEHRs are expected to form on a timescale shorter than 10 Myr, some studies in regions such as 30 Doradus in the LMC reveal that their stars may not be coeval (Walborn et al., 1999). The first population formed in the central regions may have induced star formation in the periphery through the action of UV radiation and stellar winds that compress the surrounding molecular clouds. Therefore,

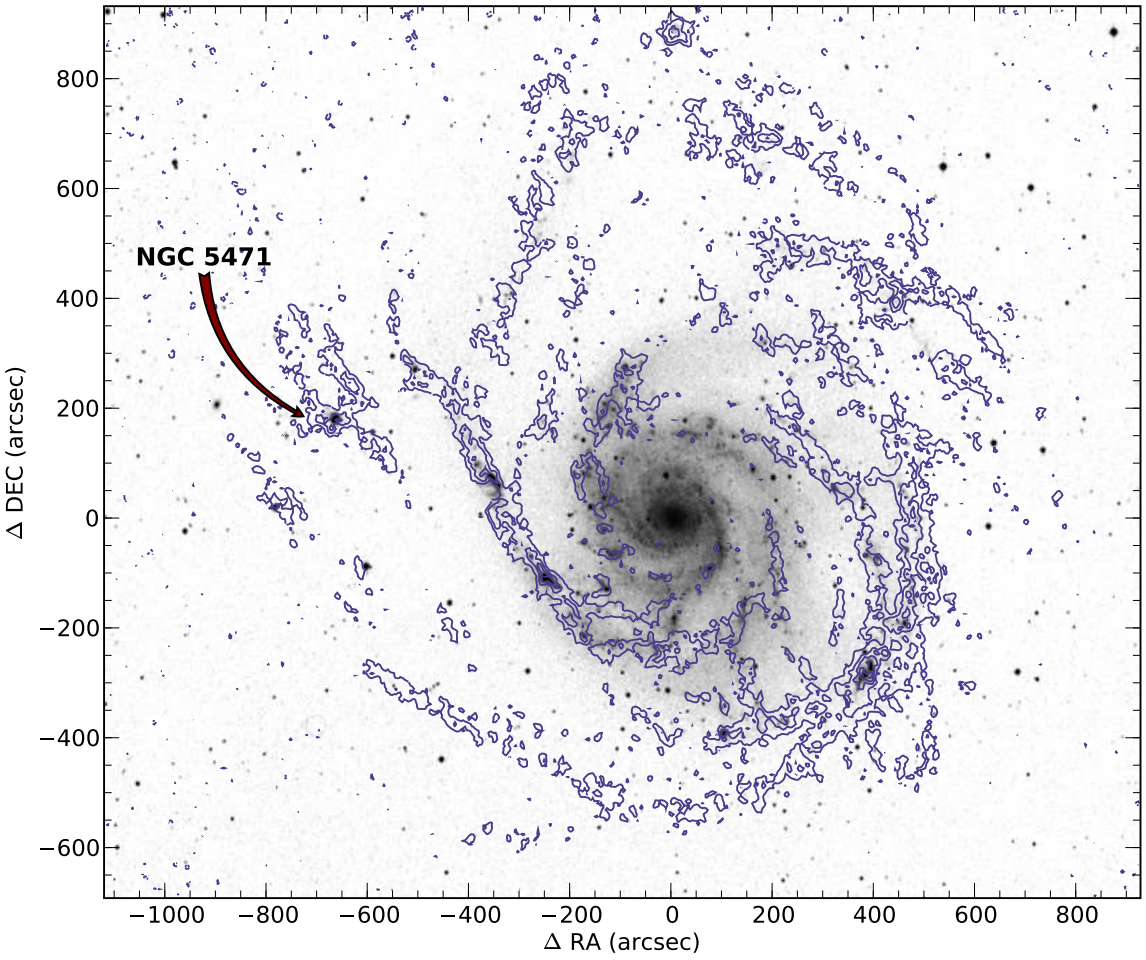

Figure 2.1: Large scale image of M101. The grayscale is the Digital Sky Survey image and the contour image is the H I from the VLA (Braun, 1995). NGC 5471 is located in the outskirts of the galaxy, in an arm concentration of H I.

the study of the interrelation between stars, gas and dust components is highly relevant to understand the nature of these regions.

30 Doradus in the Large Magellanic Cloud (LMC) and NGC 604 in M33 are the two largest GEHRs in the Local Group and they have been the subject of very detailed analyses. Both are dominated by very young (2-4 Myr) ionizing stellar populations, but they present two rather different stellar distributions. While NGC 604 is an extended *Scaled OB Association* (SOBA) with $\sim$ 200 O+WR massive stars surrounded by nebular filamentary structures, 30 Doradus is powered by a Super Star Cluster (SSC) – a much more compact core (Maíz-Apellániz, 2001) – and a halo, with different stellar populations ranging from 2 to 20 Myr (Walborn and Blades, 1997). Both GEHRs include an ongoing star formation with young stars still embedded in their parent molecular cloud. The structural similarities and differences between these well studied and spatially well resolved Local Group GEHRs have made them obvious ideal laboratories in which to study massive star formation, but in

order to extrapolate our knowledge to distant luminous unresolved starbursts it is critically necessary to go a step further and to analyze in detail the somewhat more distant GEHRs just outside the neighbourhood of the Local Group.

M101 (NGC 5457) is a giant spiral galaxy located at a distance of 7.2 Mpc (Stetson et al., 1998), yielding a linear scale of 34.9 pc/″.This galaxy contains a large number of very luminous GEHRs, of which NGC 5471 ($\alpha_{2000} = 14^h04^m29^s$, $\delta_{2000} = +54°23'48''$; l = 101.°78, b = +59.°63) is one of the outermost, at a galactocentric radius of about 25 kpc (see Figure 2.1). The Hα morphology of NGC 5471 shows multiple cores with surrounding nebular filaments, extending over a diameter of $\sim 17''$, or ~ 600 pc. Ground-based photometry shows five bright knots, designated by Skillman (1985) as components A, B, C, D and E. Component A is as luminous as 30 Doradus, while components B, C and E are comparable to NGC 604, the two prototypical spatially resolved mini-starbursts in the Local Group. Thus NGC 5471 is truly a giant star forming region.

All these features make of NGC 5471 an excellent candidate for the study of complex star formation, being close to the limit distance between the spatially well resolved Local Group GEHRs and the more distant unresolved starbursts, thus providing an intermediate step in our understanding of very massive star forming regions.

This chapter is organized as follows. Section 2.2 describes the observations and data reduction. Section 2.3 presents the integrated analysis of both the individual large clusters and the whole of NGC 5471, and the photometry of the resolved stars. The results found in section 2.3 are elaborated and discussed in section 2.4.

2.2 Observations and Data Reduction

For NGC 5471 we have obtained near infrared JHK images and have retrieved the broad and narrow band optical images available in the HST archive. Ultraviolet NUV and FUV images of M101 have also been retrieved from the GALEX archive.

2.2.1 GALEX data

The *Galaxy Evolution Explorer* (GALEX) far-ultraviolet (FUV; $\lambda_{ref} = 1530$ Å, $\Delta\lambda = 400$ Å) and near-ultraviolet (NUV; $\lambda_{ref} = 2310$ Å, $\Delta\lambda = 1000$ Å) images of M101 were retrieved from the Nearby Galaxies Survey (NGS).

The GALEX instrument is described by Martin et al. (2005) and its on-orbit performance by Morrissey et al. (2005). GALEX FUV and NUV imaging was obtained with total exposure times of 1041 s in each band. The 1σ NUV (FUV) sensitivity limit of the GALEX images is 27.6 (27.5) AB mag arcsec^{-2} for these data (Bianchi et al., 2005). At the distance of M101, the linear scale of 34.9 pc/″ implies that the GALEX point spread function (PSF) of 4.6 arcsec translates to 160 pc; this is barely sufficient to resolve some of the structure in NGC 5471,

Filter	Band	Exposure (s)	Observation ID
F547M	Strömgren y	2 × 600	U4DN030DR, U4DN030ER
		2 × 100	U4DN030FR, U4DN030GR
		20	U4DN030HM
F675W	WFPC2 R	2 × 400	U4DN0308R, U4DN0309R
		2 × 50	U4DN030AR, U4DN030BR
		10	U4DN030CR
F656N	Hα	180	U4DN0305R
		2 × 600	U4DN0306R, U4DN0307R
F673N	[S II]	3 × 700	U4DN0301R, U4DN0302R, U4DN0303R
		300	U4DN0304R

Table 2.1: Journal of HST/WFPC2 observations of NGC 5471. All images were obtained on 1997 November 1 for the cycle 6 program GO-6928, with You-Hua Chu as PI. The object of study is centered in the WF3 camera.

and we will only use the GALEX data to study the integrated photometry.

2.2.2 HST/WFPC2 Imaging

Hubble Space Telescope (HST) Wide Field Planetary Camera 2 (WFPC2) images of NGC 5471 were retrieved from the HST archive. The images were taken on 1997 November 1 through two emission-line filters: F656N (Hα) and F673N ([S II]), and two continuum filters: F547M (Strömgren y) and F675W (WFPC2 R) (Heyer, 2004). Each camera images onto a Loral 800×800 CCD which gives a plate scale of $0\farcs046$ pixel^{-1} for the PC camera and $0\farcs10$ pixel^{-1} for the three WF cameras, with a readout noise of ∼5 e$^-$ and a gain of 7 e$^-$/DN for this observations. NGC 5471 is centered in the WF3 camera in all images. The scale of the WF CCDs at NGC 5471, for which we assume a distance modulus of $(m - M) = 29.3$ (Stetson et al., 1998), is 3.5 pc pixel^{-1}. Table 2.1 lists the details concerning the WFPC2 data.

The HST pipeline processed WFPC2 images were subjected to the usual processing using the IRAF[1] and STSDAS[2] software packages, following the procedures outlined in the HST Data Handbook. We used the multiple exposures to correct for the incidence of cosmic rays as well as to eliminate hotpixels and other defects on the CCD. We finally co-added the images to produce deep mosaics.

Given the luminosity of NGC 5471, its Hα and [SII] emission contributes significantly

[1]IRAF is distributed by the National Optical Observatory, which is operated by the Association of Universities for Research in Astronomy, Inc., under cooperative agreement with the National Science Foundation.

[2]Space Telescope Science Data Analysis System (STSDAS) is a product of the Space Telescope Science Institute, operated by AURA for NASA

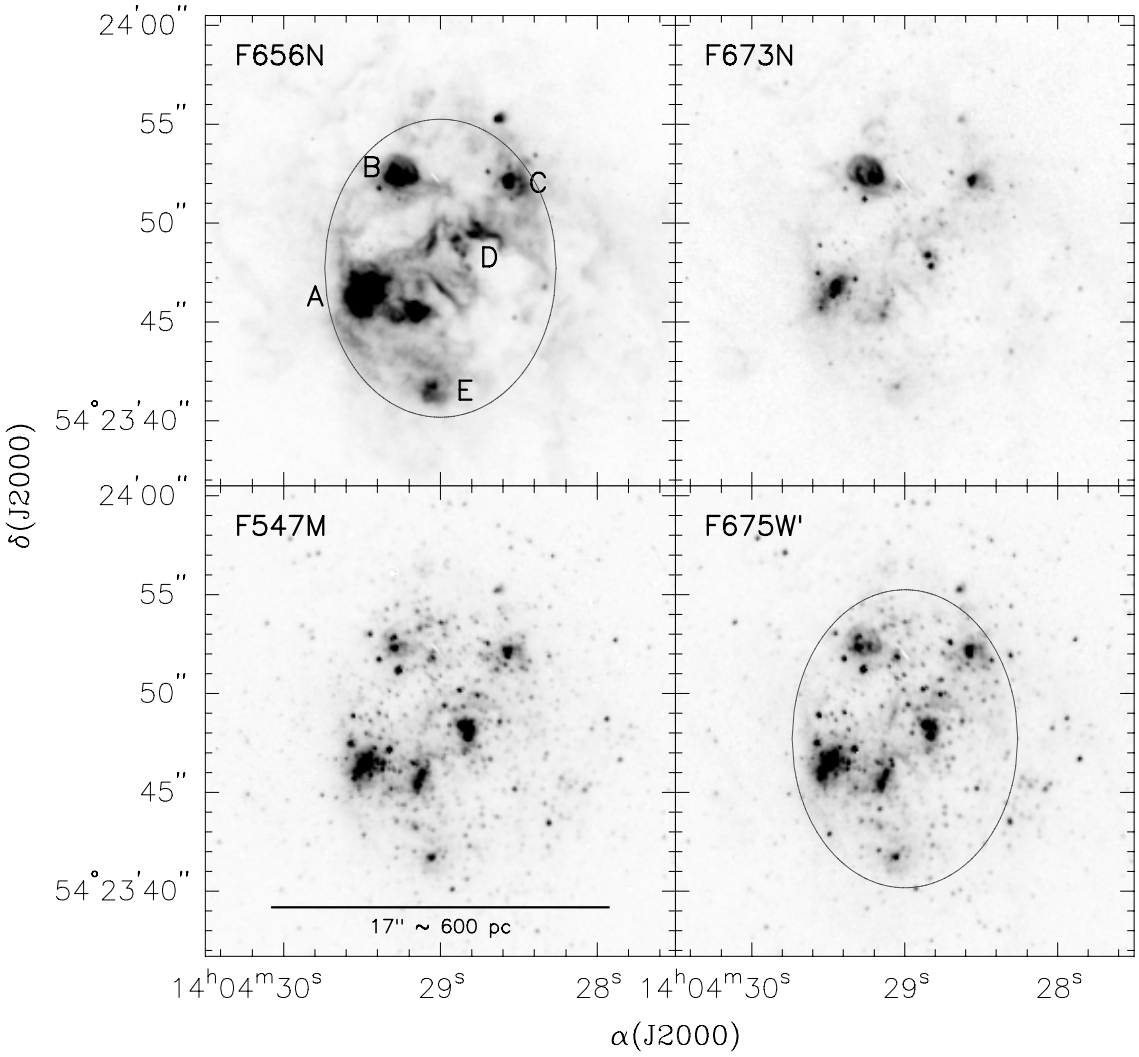

Figure 2.2: HST WFPC2 images of NGC 5471 in continuum corrected nebular filters Hα (F656N), [SII] (F673N), and emission line corrected continuum filters F547M and F675W′. The five knots from Skillman (1985) are marked in the Hα image. An ellipse indicating the core of the region is drawn in the Hα and F675W′ images. North is up and east to the left.

to the broad band (F675W) image. To eliminate the nebular contribution from the broad band and to produce continuum-free Hα and [SII] emission line images, we followed the procedure described below. First we multiplied the images by the PHOTFLAM parameter obtained by *synphot* to convert from count rates to flux densities, and then divided them by its time exposure. From the SYNPHOT task in STSDAS we determined the filter widths, and multiplied the flux densities found by the corresponding filter widths in order to obtain fluxes. The correct filter widths are the filter rectangular width RECTW (Luridiana et al., 2003). RECTW is defined as the width in Ångstroms of a rectangle with the same total area as the total transmission curve and a height given by the peak in the curve. We then scaled the Hα, [S II] and F675W images and performed an iterative subtraction to obtain a new,

Figure 2.3: Color composite of HST WFPC2 images of NGC 5471. Each image has its own filter combination label, in the usual RGB (Red, Green, Blue) color sequence . North is up, and east to the left.

Band	Time (UT)	Duration (s)	Air mass
J	04:09:00	1 × 60	1.38
H	01:03:08	3 × 15	1.11
K_s	21:59:29	10 × 5	1.31

Table 2.2: Journal of TNG/ARNICA observations of NGC 5471.

emission line free, broad band image (F675W′).

Figure 2.2 shows NGC 5471 in the four bands. An ellipse indicating the core of the region is drawn in the Hα and F675W′ images. The five brightest components first noted by Skillman (1985) and designated as A, B, C, D and E, are distinctly observed in the Hα image. The presence of a supernova remnant (NGC 5471B) is clearly seen as an intense [SII] emission source in the B-component in the F673N image. Previous works have associated X-ray sources with supernova remnants (SNRs) in M101. Chen et al. (2002) conclude that the energetic SNR in NGC 5471B (first identified by Skillman, 1985) was very likely produced by a hypernova, an explosion one or two orders of magnitude brighter than the canonical 10^{51} erg energy explosion associated with a normal SN, although this result has been questioned recently (Jenkins et al., 2004).

Several color images of NGC 5471 are shown in Figure 3.1. Each image has its own filter combination label, which indicates the used filters in the composition in the usual RGB (Red, Green, Blue) color sequence.

2.2.3 Near-infrared photometry

JHK_s photometry was performed on 2000 April 29, using the 3.58m TNG (*Telescopio Nazionale Galileo*) at the Observatorio del Roque de los Muchachos in La Palma. The camera used was ARNICA (*ARcetri Near Infrared CAmera*), with a CCD detector NICMOS 256×256 HgCdTe and gain of 19 e^-/ADU. The spatial scale was $0''.35$ pixel^{-1} and the field of view 90×90 arcsec^2. The details of these observations are given in Table 2.2.

The flux calibration of the images has been done using 2MASS images of NGC 5471, retrieved from the 2MASS Extended Source Catalog. We first measured the integrated flux of the 2MASS images in a circle containing the region and then, we used that aperture centered in the same coordinates and covering the same area in the ARNICA images. We obtained the photometric constants comparing the calibrated 2MASS fluxes with those from ARNICA by means of the transformation equations of the two systems.

In order to compare the two sets of optical and NIR data, we aligned the HST and TNG images. We degraded the WFPC2 images to the spatial scale and seeing of the IR ones, then we identified several objects in both data sets and marked them with the IRAF `center` routine. Next, we aligned the images with the `geomap` and `geotran` routines, using the HST

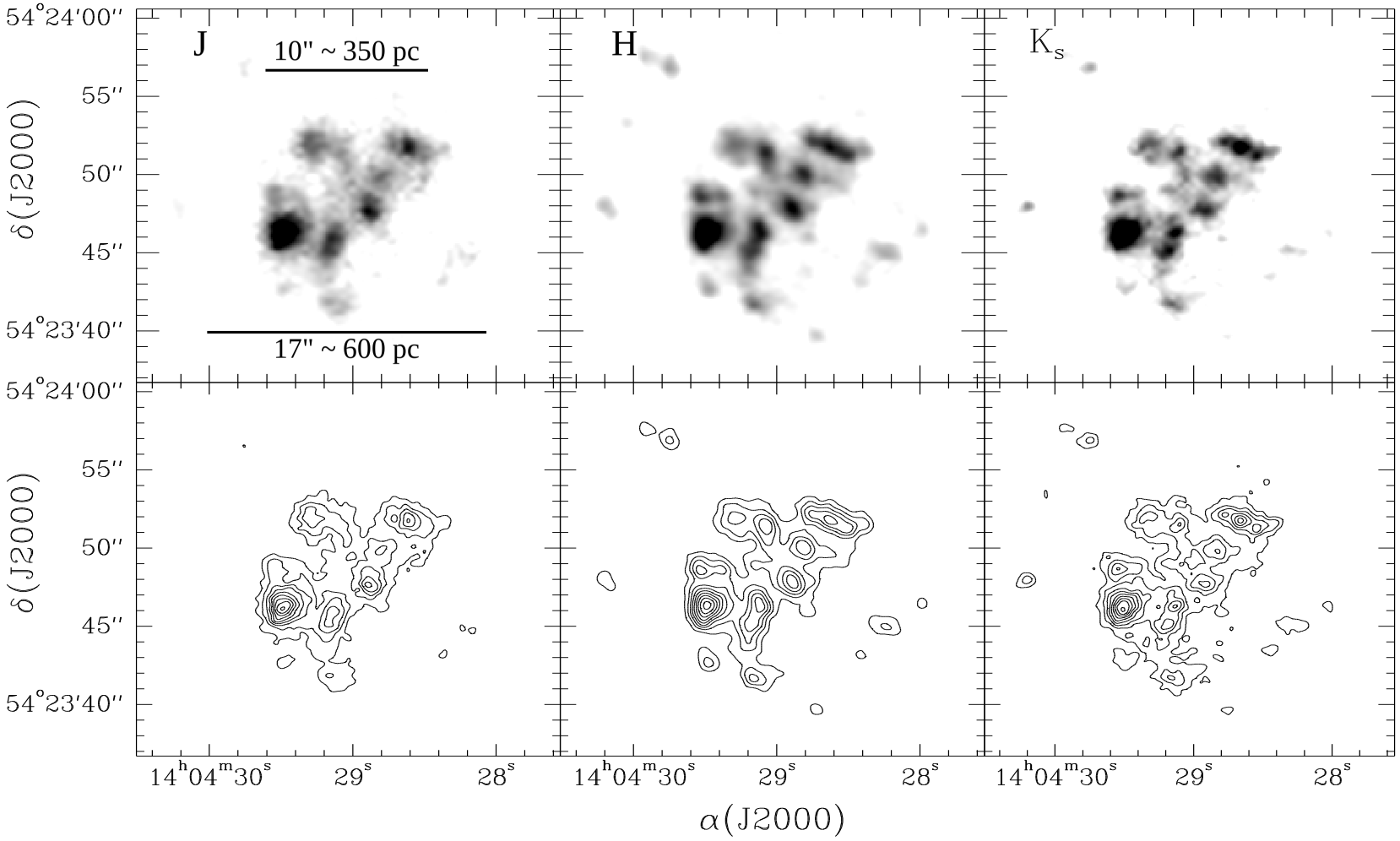

Figure 2.4: JHK$_s$ grayscale images and contour plots. The isophotes range from 20 up to 100 per cent of the peak value of the image.

images as reference.

Figure 2.4 shows the images and contour plots of the infrared bands. The multiple knots present in these images are well identified with those in Figure 2.2 in the F547M and F673W′ filters.

2.3 Results

2.3.1 Cluster Photometry

We have derived the integrated magnitudes and colors in eleven different apertures covering the main components in the core of NGC 5471. The apertures were chosen and defined in the H-band image, maximizing the area in order to include the features of all images, since there were some small offsets in the position and intensity of the knots in the optical and infrared images respectively. Then, the same polygons were used for the J, K_s and HST images. Polygons were marked by using the IRAF task `polymark` and the integrated magnitudes were computed using the IRAF task `polyphot`. The integrated magnitudes of the HST images are given in the VEGAMAG system. The polygons defined are shown in Figure 2.5.

The integrated magnitudes and colors derived in each area were corrected for the Galactic foreground extinction toward M101 using the color excess E(B-V) = 0.01 (Schlegel et al., 1998), although its effect is negligible. The absorption coefficients for the 5 bands were derived assuming $R_V = A_V/E(B-V) = 3.1$, and using the A_λ curve from Cardelli et al. (1989). The uncertainty of the individual fluxes have been computed including the Poisson photon count error, the uncertainty on the background setting and the photometric calibration uncertainty. Results of the integrated photometry in the five bands are given in Table 2.3.

We also have measured the Hα flux for each polygon. To measure the integrated Hα flux of the whole region, we have decontaminated the F656N image from the broad band F675W contribution. Then, we have then plotted the contour at 3σ from the sky (with isophotal flux 6.3×10^{-15} erg cm^{-2} s^{-1} arcsec^{-1}) and found the circular aperture centered in the region that best fits that isophotal contour. The radius of this aperture is 15 arcsec from the center (see Figure 2.6). The flux measured inside this circular aperture is $(3.65 \pm 0.17) \times 10^{-12}$ erg cm^{-2} s^{-1}. We have used the PHOTFLAM value given by *synphot* and a value of RECTW of 28.3 Å. Measured Hα fluxes for each of the polygonal selections and the parameter derived from them are given in Table 2.4. The effective radii (R_{eff}) of a polygon is defined as the radii of a circular aperture of the same area.

Since GALEX images do not have enough resolution, we were not able to get the fluxes for each polygon. As in the case of the nebular flux, we measured the FUV and NUV fluxes inside 15″ radii apertures centered in NGC 5471. We obtain a FUV flux of $(9.9 \pm 0.1) \times 10^{-14}$ erg cm^{-2} s^{-1} Å^{-1} (14.19 ± 0.05 AB magnitudes) and a NUV flux of $(4.5 \pm 0.1) \times 10^{-14}$ erg

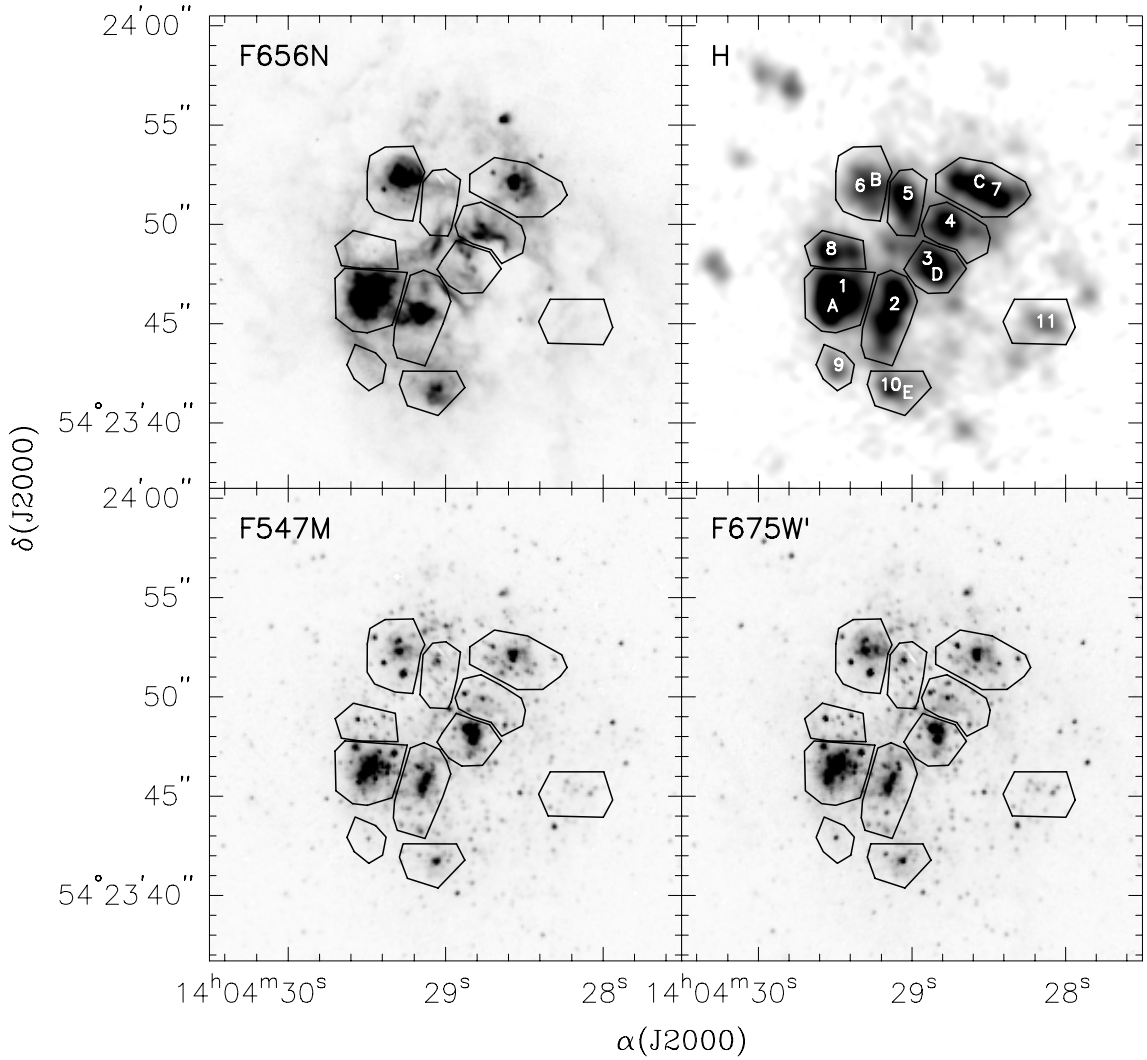

Figure 2.5: Plot of the eleven polygons, limiting the different areas where the integrated magnitudes are computed. The numbers belong to our own definition while the A, B, C, D and E letters are the knots identified by Skillman (1985). The hypernova is located in knot 6.

$\mathrm{cm}^{-2}\ \mathrm{s}^{-1}\ \text{Å}^{-1}$ (14.24 ± 0.05 AB magnitudes).

In order to use these values in the analysis, we need to transform AB magnitudes to the VEGAMAG system. The transformation formula is (Maíz-Apellániz, 2007):

$$AB_p = (m_p - ZP_p) + AB_p(Vega) \tag{2.1}$$

where AB_p is the magnitude of the object in the AB system and filter passband p, m_p the magnitude of the object in filter p using Vega as reference spectral energy distribution (SED), ZP_p is the zero point of the p filter in the Vega system and AB_p(Vega) is the AB magnitude of Vega in filter p. This magnitude is given by:

Aperture	J	H	K_s	m_{547M}	m_{675W}	$m_{675W'}$
N5471-1	16.43 ± 0.11	16.26 ± 0.12	16.03 ± 0.14	16.66 ± 0.06	15.56 ± 0.06	16.30 ± 0.06
N5471-2	16.90 ± 0.11	16.57 ± 0.12	16.48 ± 0.14	17.21 ± 0.06	16.30 ± 0.06	16.94 ± 0.06
N5471-3	17.35 ± 0.11	17.09 ± 0.12	17.12 ± 0.14	17.22 ± 0.06	16.84 ± 0.06	17.11 ± 0.06
N5471-4	17.52 ± 0.11	17.08 ± 0.12	16.99 ± 0.14	18.17 ± 0.06	17.07 ± 0.06	17.77 ± 0.06
N5471-5	17.83 ± 0.11	17.28 ± 0.12	17.27 ± 0.14	18.58 ± 0.06	17.59 ± 0.06	18.16 ± 0.06
N5471-6	17.34 ± 0.11	17.21 ± 0.12	17.00 ± 0.14	17.62 ± 0.06	16.41 ± 0.06	17.12 ± 0.06
N5471-7	16.98 ± 0.11	16.59 ± 0.12	16.47 ± 0.14	17.56 ± 0.06	16.49 ± 0.06	17.10 ± 0.06
N5471-8	17.89 ± 0.11	17.41 ± 0.12	17.39 ± 0.14	18.70 ± 0.06	17.68 ± 0.06	18.22 ± 0.06
N5471-9	19.15 ± 0.13	18.63 ± 0.13	18.63 ± 0.15	20.23 ± 0.06	18.71 ± 0.06	19.54 ± 0.06
N5471-10	18.14 ± 0.11	17.80 ± 0.12	17.57 ± 0.15	18.63 ± 0.06	17.45 ± 0.06	18.22 ± 0.06
N5471-11	18.55 ± 0.12	18.00 ± 0.12	18.11 ± 0.15	19.27 ± 0.06	18.40 ± 0.06	18.84 ± 0.06
NGC 5471	14.14 ± 0.10	13.84 ± 0.12	13.74 ± 0.14	14.67 ± 0.06	13.62 ± 0.06	14.27 ± 0.06

Table 2.3: Integrated magnitudes and Hα flux for the eleven regions of NGC 5471. Magnitudes from HST are given in the VEGAMAG system. Results for $m_{675W'}$ column were measured from the emission line free F675W image. The last row belongs to the integrated magnitude of the whole region.

$$AB_p(Vega) = -2.5\, log_{10}\left(\frac{\int P_p(\lambda) f_{\lambda,Vega}(\lambda)\lambda d\lambda}{\int P_p(\lambda)(c f_{\nu,AB}/\lambda)d\lambda}\right) \tag{2.2}$$

where $P_p(\lambda)$ is the dimensionless filter sensitivity function of filter p, $f_{\lambda,Vega}(\lambda)$ is the Vega spectrum and $f_{\nu,AB} = 3.63079 \times 10^{-20}$ erg s^{-1} cm^{-2} Hz^{-1} is the reference spectral energy distribution of the AB system.

We have used FUV and NUV filter passbands to calculate the AB magnitudes of Vega by means of equation 2.2. As the zero points for GALEX are ZP = 0.000 in both bands, we have

$$m_{FUV} = AB_{FUV} - 2.073 \tag{2.3}$$

$$m_{NUV} = AB_{NUV} - 1.647 \tag{2.4}$$

Finally, the GALEX VEGAMAG magnitudes of NGC 5471 used below are m_{FUV} = 12.12 and m_{NUV} = 12.59.

The integrated photometric measurements have been analyzed with the help of CHORIZOS[3], a code written in IDL by Maíz-Apellániz (2004). This code compares photometric data with model spectral energy distributions (SEDs), calculating the likelihood for the full parameter range specified, allowing for the identification of multiple solutions. In general, models are parameterized in terms of physical quantities: some of them are intrinsic, *i.e.* they might depend on the nature and distance to the objects (*e.g.* age, metallicity, ...), while

[3] *CHi-square cOde for parameteRized modeling and characterIZation of phOtometry and Spectrophotmetry.* The latest version can be obtained from `http://www.iaa.es/~jmaiz`

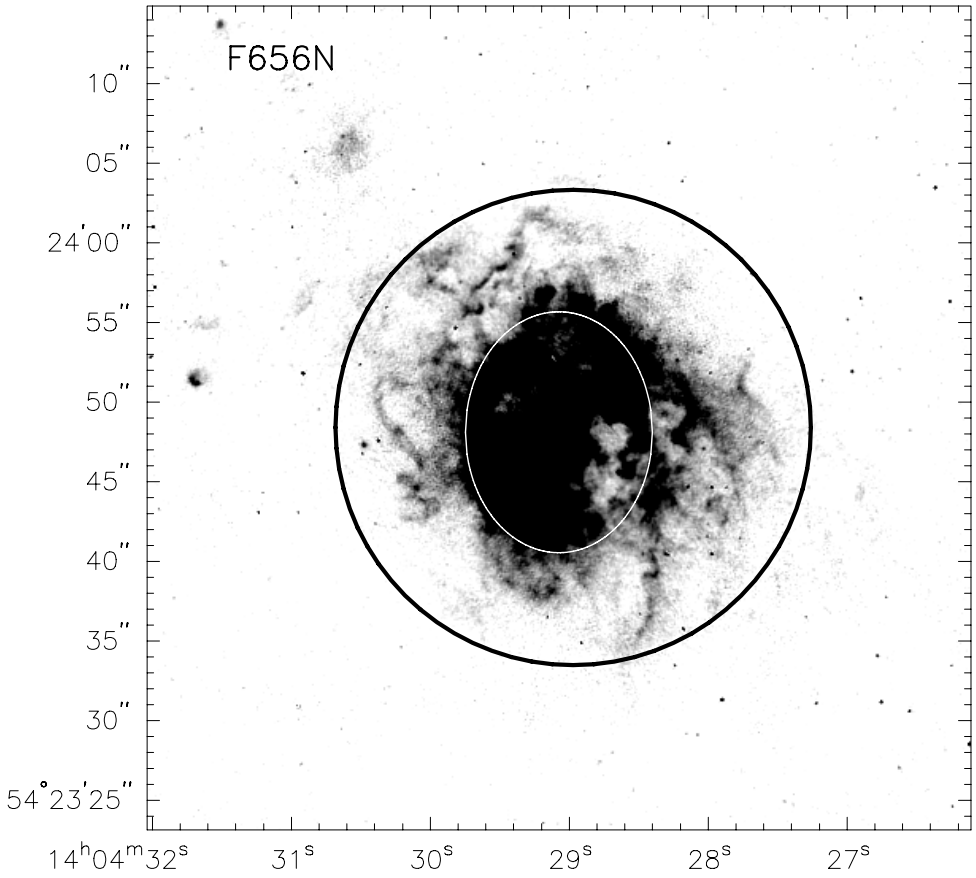

Figure 2.6: Continuum free Hα image of NGC 5471. The circular aperture of 15″ where the integrated photometry was performed to obtain the total flux is overplotted. The ellipse indicating the core of the region is drawn as reference.

others are extrinsic and depend on the properties of the interstellar matter (reddening and extinction law). CHORIZOS can handle SED families for stellar atmospheres and clusters (Starburst99; Leitherer et al., 1999) and uses χ^2 minimization to find all models compatible with the observed data in a (2 intrinsic +2 extrinsic)-dimensional parameter space. It includes a wide list of filters for different systems (Johnson-Cousins, HST/WFPC2, 2MASS, ...) and allows for published magnitudes to be used directly. For a set of objects with measured magnitudes $m_1, m_2, \ldots, m_{M+1}$ (with independent uncertainties $\sigma_1, \sigma_2, \ldots, \sigma_{M+1}$), derived independent colors $c_1, c_2, \ldots, c_M$, and a set of N parameters with $M > N$, no strict solutions, but only approximate ones, can be found since the problem has more equations or sets of model parameters that produce a given color than model parameters. Hence, the code finds the N-volume of approximate solutions by using χ^2 minimization.

The first step of the program is to read the unreddened SED models, extinguish them according to a given extinction law, and obtain the synthetic photometry; the code includes pre-calculated tables for all the models and filters. To run the program, CHORIZOS requires

Aperture	R_{eff} pc	F(Hα) 10^{-13} erg s^{-1} cm^{-2}	L(Hα) 10^{39} erg s^{-1}	Q(H^0) 10^{51} s^{-1}	M II 10^4 $M_\odot$	EW(Hα) Å
NGC5471-1	61.1	6.63 ± 0.31	4.1	4.1	13.0	1187 ± 77
NGC5471-2	60.9	3.07 ± 0.14	1.9	1.9	6.1	993 ± 64
NGC5471-3	47.0	0.93 ± 0.04	0.6	0.6	1.9	354 ± 23
NGC5471-4	51.2	1.59 ± 0.07	1.0	1.0	3.2	1103 ± 71
NGC5471-5	46.0	0.79 ± 0.04	0.5	0.5	1.6	788 ± 51
NGC5471-6	58.9	2.42 ± 0.11	1.5	1.5	4.8	919 ± 59
NGC5471-7	63.1	2.34 ± 0.11	1.5	1.4	4.7	872 ± 57
NGC5471-8	43.5	0.72 ± 0.03	0.5	0.4	1.4	756 ± 49
NGC5471-9	34.0	0.38 ± 0.02	0.2	0.2	0.8	1369 ± 90
NGC5471-10	46.2	1.22 ± 0.06	0.8	0.8	2.4	1282 ± 83
NGC5471-11	53.6	0.31 ± 0.01	0.2	0.2	0.6	585 ± 37
NGC 5471	525	36.5 ± 1.70	23	22	73	783 ± 40

Table 2.4: Integrated Hα flux and derived parameters for the eleven regions of NGC 5471. R_{eff} is the effective radius of the polygon. The last row belongs to the integrated values of the whole region.

a file with the photometry data and a series of input parameters, such as the model family, understood as the collection of SED from stellar atmosphere models or synthetic stellar populations, and the range of the parameters to be used. Then, CHORIZOS reads the model photometry from the tables calculated previously, interpolates, calculates the likelihood for each grid point, and write the results for each of the four parameters (mode, mean, standard deviation, median, ...). The program contains a useful module which reads the results and produces spectra, probability contour plots and additional statistics.

In the case of our study, we have used the STARBURST99 models (Leitherer et al., 1999) with the implementation by Smith et al. (2002) which includes a grid of blanketed stellar atmospheres at different metallicities. We fixed two parameters: the known metallicity of NGC 5471 and the type of dust, leaving unconstrained the amount of extinction and the age.

Regarding extinction, CHORIZOS works with $E(4405-5495)$ and R_{5495}, which are the monochromatic equivalent to $E(B-V)$ and R_V respectively, the values 4405 and 5495 referring to the central wavelength (in Å) of the B and V filters. We used the standard type of dust characterized by a value $R_{5495} = 3.1$. The metallicity of the region was assumed to be traced by the oxygen abundance. Recent derivations from detailed spectrophotometric studies give a mean value of 12+log(O/H) of 8.06 ± 0.03 for components A, C and D; a slightly lower abundance of 7.94 ± 0.03 is found for component B (Kennicutt et al., 2003). These values correspond to about 0.25 the solar oxygen abundance, if the value by Asplund et al. (2005) for the solar oxygen abundance is assumed. Therefore we used the

value $Z = 0.2Z_{\odot}$ in CHORIZOS.

2.3.2 Resolved Stellar Photometry

WFPC2 Photometry

The stellar photometric analysis was performed with the *HSTphot* package (Dolphin, 2000b). This package is specifically designed for use with HST WFPC2 images. It uses a library of Tiny Tim (Krist, 1995) undersampled point-spread functions (PSFs) for different locations of the star on the camera and of the star center within the pixel, to center the star and to find its magnitude, given in the flight system magnitude. It also contains several programs for general reduction procedures. The first step is to run the `mask` task to mask out the bad pixels and other image defects identified in the data quality images. The sky computation is made by `getsky`, which takes all pixels in an annulus around each pixel, determines the sky value and calculates the sky background map. The next step is to run `crmask` for cosmic ray removal, which uses the sky file created by `getsky`. It has the capability of cleaning images that are not perfectly aligned, and it can handle images from different filters. To combine multiple images per filter and to produce a final deep image per filter, the `coadd` procedure was used. The final step requires the `hotpixels` procedure, which uses the result from `getsky` and tries to locate and remove all hot pixels. This is an important step, since hot pixels can create false detections and also, can throw off the PSF solutions.

The `hstphot` routine was run on the images in the F547M and F675W′ bands. This task performs stellar PSF photometry on multiple images from different filters, including alignment and aperture corrections, as well as PSF modifications to correct for errors of geometric distortion via the Holtzman et al. (1995) distorsion correction equations and the 34th row error, noted by Shaklan et al. (1995) (see also Anderson and King, 1999), and correction for charge transfer inefficiency (Dolphin, 2000a). There are several parameters to use during the run of `hstphot`. We enabled the determination of the "local sky" (from now on, *nebular* case), because of the rapidly-varying background of NGC 5471, but we also used, in a different run, the usual (*stellar*) fit done by `getsky`. We made a cross-correlation between the *nebular* and *stellar* lists of stars in order to match them and find the sources detected using both types of sky determination. To have a better estimate of the sky for those matched stars, we took as magnitude the mean of both measurements $m = (m_{nebular} + m_{stellar})/2$ and as error:

$$\sigma_m = max\left(\sigma_{m_n}, \sigma_{m_s}, \frac{|m_n - ms|}{2}\right)$$

The final list of stars is made up of: i) matched stars; ii) objects from the *stellar* list not included in the *matched* star list (best detected in less nebulous regions); and iii) stars from the *nebular* list with no companion in the *stellar* list.

We selected "good stars" from the `hstphot` output. Object types were classified as good star, possible unresolved binary, bad star, single-pixel cosmic ray or hot pixel, and extended object. Less than 10% of the stars were not classified as "good stars". To ensure that we only have point-like sources, we also used the "sharpness" parameter and a measure of the quality of the fit (χ^2) to reject false star detections in regions with structured nebulosity or artifacts. The final number of stars detected in the WF3 chip with these parameters in both filters were 1261.

Selection Effects

Completeness

In order to face the study of the star formation history (SFH) of an object and simulate synthetic diagrams, it is compulsory to undertake a completeness analysis. A complete description of the completeness analysis can be found in Stetson and Harris (1988) and Aparicio and Gallart (1995). We briefly describe below its basis and main steps.

Incompleteness is mainly due to two factors: overlapping of stellar profiles in crowded regions and background noise. These effects are more important for faint stars in dense stellar regions. Consequently, in a crowded cluster incompleteness will depend on apparent magnitude and spatial position. The best way to account for crowding effects is to add artificial stars to the images and to subject them to the same sample selection as for real stars. The number of injected stars must be sufficiently high as to provide acceptable statistical accuracy, but not so high as to change the level of crowding. To avoid overcrowding effects, no more than some 10% of the number of real stars should be added as artificial stars. This new artificial images (*synthetic frames*) are processed in the same way as the real ones, and the magnitudes of all the stars are obtained following the same criteria and using the same parameters. At this point, we will have three different tables: *i*) the first one containing magnitudes, positions and colors of the real stars (*real stars*); *ii*) the second one including all the data for the *injected stars*, which are known beforehand; *iii*) the third list containing the data from the *synthetic frames*.

The *synthetic table* is then cross correlated with the other two (*real* + *injected*), producing a new table (*completeness*) containing the stars matched from the artificial list. Therefore, in this final list we have the initial and recovered magnitudes and colors of the injected stars, as well as their coordinates. The table will also contain stars which have not been paired, and a flag indicating that they have been lost. The ratio between the number of simulated stars recovered and injected provides the estimate of the completeness factor for each magnitude bin.

A grid of artificial stars was generated on a 2-dimensional CMD and distributed according to the flux of the images with an artificial star routine provided by *HSTphot*. The parameters of the routine are the minimum and maximum of the measured color and magnitude. The

magnitude steps used were multiple of 0.5, while color steps are by 0.25. We asked the routine to distribute artificial stars on the CMD in accordance with the number observed. In the WF3 chip 1261 stars were detected, and hence about 250 were added per each 0.5 magnitude bin (at different trials, in order to leave the crowding conditions unaltered) until the limit magnitude of the data is reached. The 50% completeness of the F547M filter luminosity function derived on the basis of the CMD data is reached at 25.2 magnitude, while for the F675W′ filter is 24.7 mag.

Field star subtraction

Statistical decontamination has been widely used to accomplish the field star subtraction of CMDs. The idea is very simple: our region of study, NGC 5471, consists of the sum of the intrinsic population, IP, and the contaminating population, FS, and therefore our CMD shows both populations. The field star contribution can be estimated using the CMD of an adjacent field FS' containing only foreground and background stars, assuming that it is statistically representative of FS. Accordingly, the FS contribution may be removed by comparing the local density of stars in the two diagrams (Bellazzini et al., 1999):

$$CMD(IP+FS) - CMD(FS') \sim CMD(IP)$$

As NGC 5471 is centered in the WF3, we assume that all of the stars in the other chips are field stars. This is not completely true because this GEHR is in the outskirts of an M101 arm, where a few traces of star formation activity can still be found. Nevertheless, they are easily detected and no more than 20 stars in the WF2 (the only chip used to determine the FS population) were found over the chip. The rest of the stars showed a homogeneous distribution and were considered a sample of field stars. A CMD(IP+FS) was constructed for a region inside a circular aperture of 15″ which includes the core+halo structure of the region.

To perform the statistical decontamination, we followed the procedure described by Mighell et al. (1996) and Bellazzini et al. (1999). For a given star in the CMD(IP+FS) with coordinates $[m \pm \sigma_m; c \pm \sigma_c]$, we count how many stars (N_{IP+FS}) can be found within the ellipse of axes $[max(\sigma_m, 0.1); max(\sigma_c, 0.1)]$ in the original diagram. We also counted the number of stars ($N_{FS'}$) found in the field CMD(FS') within the same ellipse centered at the same coordinates.

The probability P that a given star in the $CMD(IP+FS)$ is actually a member of NGC 5471 is defined as follows:

$$P = 1 - min\left(\frac{\alpha N_{FS'}}{N_{IP+FS}}, 1.0\right)$$

where α is the ratio of the area of the IP+FS field (a circular aperture of 15″) to the area of

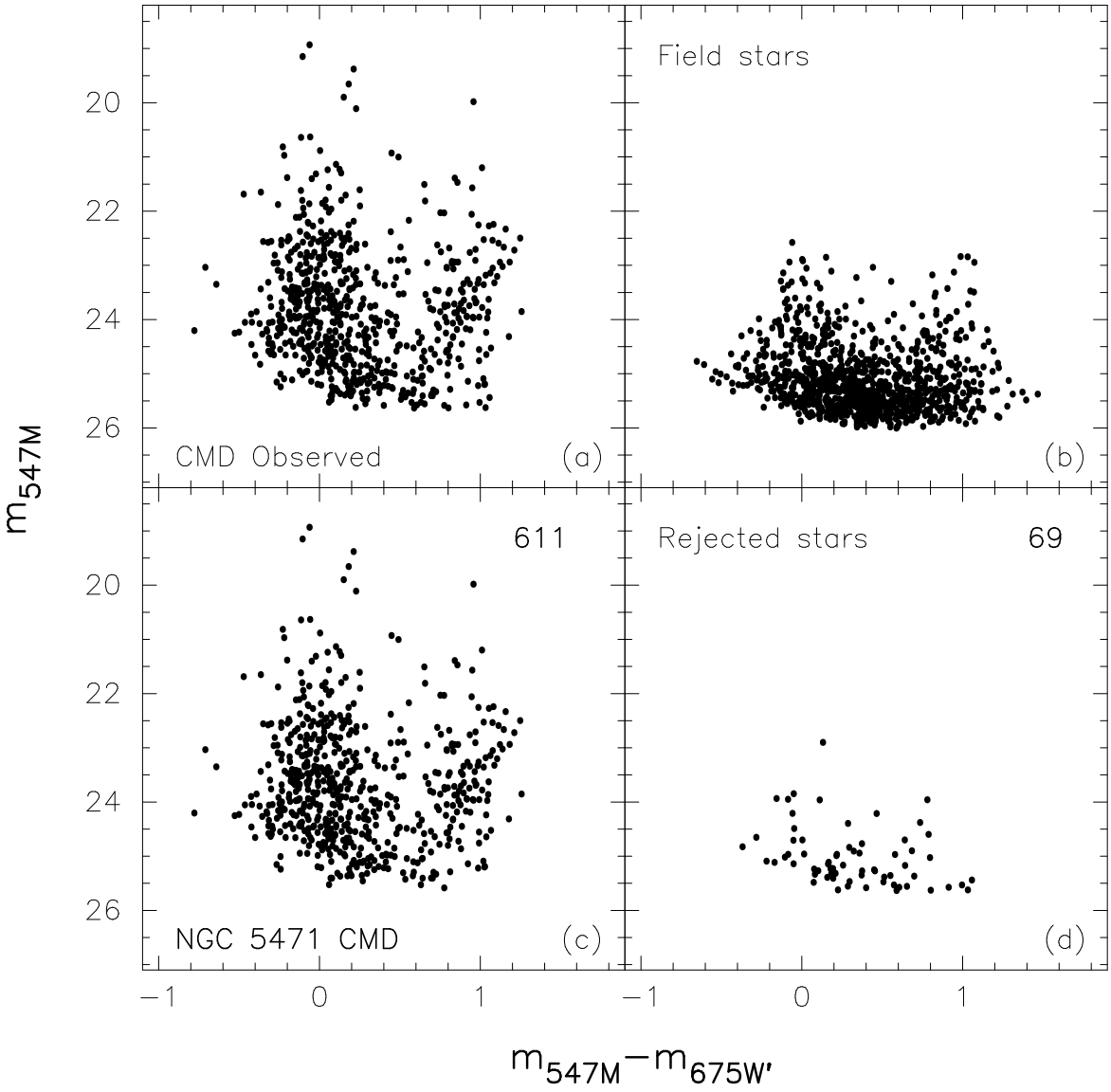

Figure 2.7: Decontamination of the NGC 5471 observed CMD [panel (a)] using the field stars CMD [panel (b)]. The decontaminated NGC 5471 CMD is shown in panel (c) (611 stars) while the CMD of the rejected stars is displayed in the panel (d) (69 stars).

the FS' field (in this case, the whole WF2 chip). We can determine the probable membership of this star by comparing P with an uniform random number $0 < P' < 1$; if $P' \leq P$ then the star is accepted as a member of NGC 5471, otherwise it is rejected and considered as a field star. Since this cleaning method is probabilistic in nature, a decontaminating trial represents only one out of an infinite number of different realizations of the cleaned CMD for NGC 5471.

Figure 2.7 shows the result of this process of decontamination for the CMD of the NGC 5471. Panel (a) displays the CMD observed (with both intrinsic and field stars), panel

ID	X pixel	Y pixel	R.A. (J2000)	Decl. (J2000)	m_{F547M} (mag)	$m_{F675W'}$ (mag)	$m_{F547M} - m_{F675W'}$ (mag)
1	359.56	562.57	14:04:27.50	54:23:41.53	24.24 ± 0.07	23.45 ± 0.05	0.79 ± 0.09
2	324.75	512.37	14:04:27.56	54:23:47.59	24.57 ± 0.10	23.93 ± 0.07	0.65 ± 0.12
3	352.44	544.56	14:04:27.57	54:23:43.36	24.05 ± 0.07	23.95 ± 0.06	0.09 ± 0.09
4	332.62	514.12	14:04:27.61	54:23:46.96	24.59 ± 0.09	24.88 ± 0.19	-0.30 ± 0.21
5	378.56	569.56	14:04:27.62	54:23:39.79	24.04 ± 0.06	23.62 ± 0.06	0.42 ± 0.08
6	323.33	496.44	14:04:27.66	54:23:48.91	24.07 ± 0.06	24.13 ± 0.12	-0.06 ± 0.14
7	373.56	553.15	14:04:27.69	54:23:41.37	24.18 ± 0.07	23.24 ± 0.05	0.94 ± 0.09
8	293.29	455.69	14:04:27.69	54:23:53.94	23.62 ± 0.05	22.57 ± 0.03	1.05 ± 0.06
9	351.67	523.45	14:04:27.71	54:23:45.04	23.85 ± 0.07	23.87 ± 0.11	-0.02 ± 0.13
10	290.75	449.59	14:04:27.71	54:23:54.57	23.86 ± 0.06	23.02 ± 0.04	0.84 ± 0.07
11	368.80	540.45	14:04:27.74	54:23:42.65	23.14 ± 0.03	23.24 ± 0.04	-0.10 ± 0.05
12	346.68	513.49	14:04:27.74	54:23:46.12	25.26 ± 0.15	24.89 ± 0.17	0.38 ± 0.23
13	381.63	555.86	14:04:27.75	54:23:40.66	24.08 ± 0.07	24.18 ± 0.11	-0.10 ± 0.13
14	360.90	530.61	14:04:27.75	54:23:43.91	23.96 ± 0.06	24.09 ± 0.09	-0.14 ± 0.10
15	318.82	469.76	14:04:27.81	54:23:51.25	25.22 ± 0.15	25.04 ± 0.20	0.18 ± 0.26
16	312.47	461.48	14:04:27.81	54:23:52.29	23.20 ± 0.04	23.22 ± 0.04	-0.02 ± 0.05
17	291.51	435.95	14:04:27.81	54:23:55.57	25.38 ± 0.21	25.23 ± 0.19	0.16 ± 0.28
18	359.87	517.56	14:04:27.83	54:23:44.98	24.20 ± 0.09	24.26 ± 0.10	-0.06 ± 0.13
19	354.84	509.85	14:04:27.84	54:23:45.89	24.02 ± 0.06	23.67 ± 0.05	0.34 ± 0.08
20	319.56	460.53	14:04:27.88	54:23:51.91	24.45 ± 0.08	24.87 ± 0.20	-0.42 ± 0.22

Table 2.5: Stellar photometry of the first 20 stars of the resulting clean CMD of NGC 5471.

(b) the field stars, panel (c) the decontaminated CMD of NGC 5471 and panel (d) the CMD of the stars rejected. Table 2.5 shows the magnitudes of the first 20 stars of the resulting clean CMD of NGC 5471 of panel (c).

Isochrones

To study the CMD we use the isochrone set that corresponds to the grid by Girardi et al. (2002)[4], covering the age range $6.60 < \log t < 10.25$ and mass range 0.15 to 100 $M_\odot$, based on the Z=0.004 (1/5 $Z_\odot$) models from Girardi et al. (2000) and Bertelli et al. (1994) that include overshooting and a simple synthetic evolution of TP-AGB (Girardi and Bertelli, 1998). Atmosphere models are from BaSeL 3.1 WLBC 99 corrected library (Westera et al., 2002) at the same metallicity as the isochrone set.

The procedure is as follows: (1) we obtained the magnitudes in the HST filters for all stellar models in the atmosphere grid. (2) For each point in the isochrone we obtained the stellar flux in each of the bands by a linear interpolation in the $\log g - \log T\mathrm{eff}$ grid. (3) The final luminosity was obtained by multiplying the square radius of the star. For $\log g - \log T\mathrm{eff}$ values not covered by the atmosphere grid, the boundary values have been used with a caution

[4]Available at `http://pleiadi.pd.astro.it/`

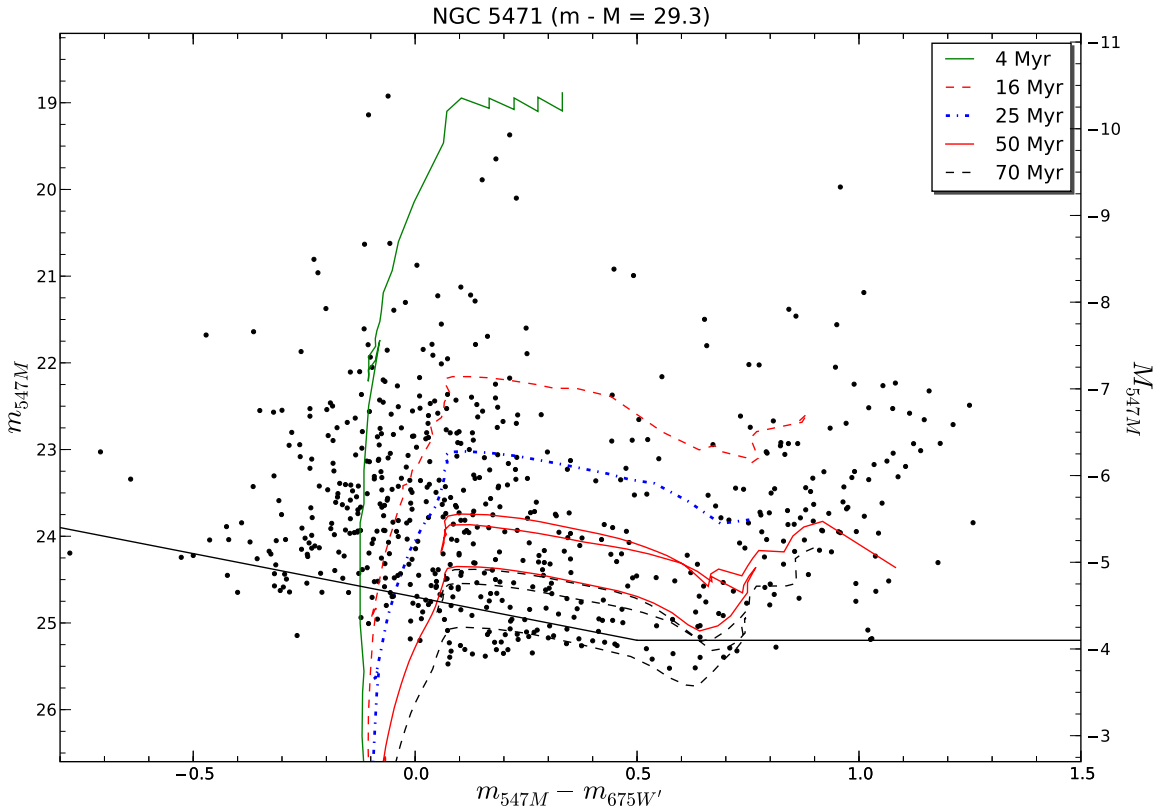

Figure 2.8: Final CMD corrected for field star contamination, together with five isochrones from 4 to 70 Myr. The line across the bottom shows the completeness limit at the 50% level as derived from false star tests. The right-hand side scale gives the absolute magnitudes corresponding to a distance of 7.2 Mpc.

flag. In terms of the present work, these stars do not modify the results obtained.

In Figure 2.8 we show the final CMD (corrected for field star contamination). The 50% completeness limit is also plotted, and five isochones from 4 to 70 Myr are shown in colour. The right hand side scale gives the absolute magnitude corresponding to a distance of 7.2 Mpc.

2.4 Discussion

In this section we discuss the results of the photometry in terms of the integrated properties, both of the individual clusters defined in section 2.3.1 and of the whole star forming complex, and in terms of the resolved stellar photometry in the CMD. We attempt to bring all the results into a coherent picture of the past and present star formation processes in NGC 5471.

2.4.1 Cluster Analysis

Analysing the integrated properties of a complex region like NGC 5471 is an exercise that one has to undertake with care, because the integrated photometry includes a wide range of regions with different ages and extinction values. Thus the result of synthesizing the integrated ultraviolet-to-NIR photometry with CHORIZOS, which finds the most likely single stellar population (SSP), is only of general interest as a guiding signpost. If we use only the optical-to-NIR photometry, CHORIZOS finds a most likely SSP with relatively high extinction and a young age ~ 4 Myr. If we include the FUV and NUV GALEX photometry then CHORIZOS finds two loci of maximum likelyhood for a single SSP, one that corresponds to an age of ~ 8 Myr with moderate extinction and a second maximum at an age around 50 Myr and very low extinction. This result suggests that a significant fraction of the GALEX flux integrated within the 15 arcsec radius aperture from NGC 5471 is produced by a post-nebular stellar population of B stars (see also Waller et al., 1997).

Three previous studies have modelled the age of NGC 5471 using ultraviolet-to-optical spectra. Rosa and Benvenuti (1994) use an HST/FOS spectrum through an aperture of 4.3 arcsec around knot A. Mas-Hesse and Kunth (1999) use an IUE spectrum through an aperture of 10×20 arcsec and the FOS optical spectrum of Rosa and Benvenuti (1994). Pellerin (2006) uses a FUSE spectrum through an aperture of 4×20 arcsec. All three works find that the ultraviolet spectrum of NGC 5471 can be explained with a young burst of less than about 5 Myr and a relatively low extinction. That these previous works are not sensitive to an older blue population may be due to the fact that they are based on data acquired at relative shallow flux levels (as indeed is stated in the three papers), and would thus be biased towards the brightest ultraviolet knots; while the integrated GALEX photometry through a large aperture is more sensitive to the extended, fainter, more evolved stellar population[5].

The photometric analysis of the clusters identified in section 2.3.1 has some advantages and some disadvantages with respect the integrated photometry of the whole NGC 5471 region. On one hand, it is performed on smaller regions, which can be more readily identified with local star forming events, including a spatially well defined stellar cluster with its surrounding emission line nebula. Thus their photometric properties pertain to a more coherent whole, for example, in terms of age and extinction. On the other hand, a smaller cluster means that the stochastic biases may play a more important role. However, we should not forget that even so, each of these knots can be regarded as a giant HII region; for example, knot A is somewhat more luminous in ionizing power than the giant HII region 30 Doradus in the local group.

Figure 2.9 shows a color-color-Hα plot of the individual clusters. The hypernova knot is not shown, and knots 3 and 4 have been summed into a single knot 34. There is a clear correlation in the sense that redder knots have less Hα flux. The flux of Hα can decrease

[5]Recall that the 1σ detection for the GALEX data is $\mathrm{AB_{FUV}} = 27.6$ mag arcsec^{-2}

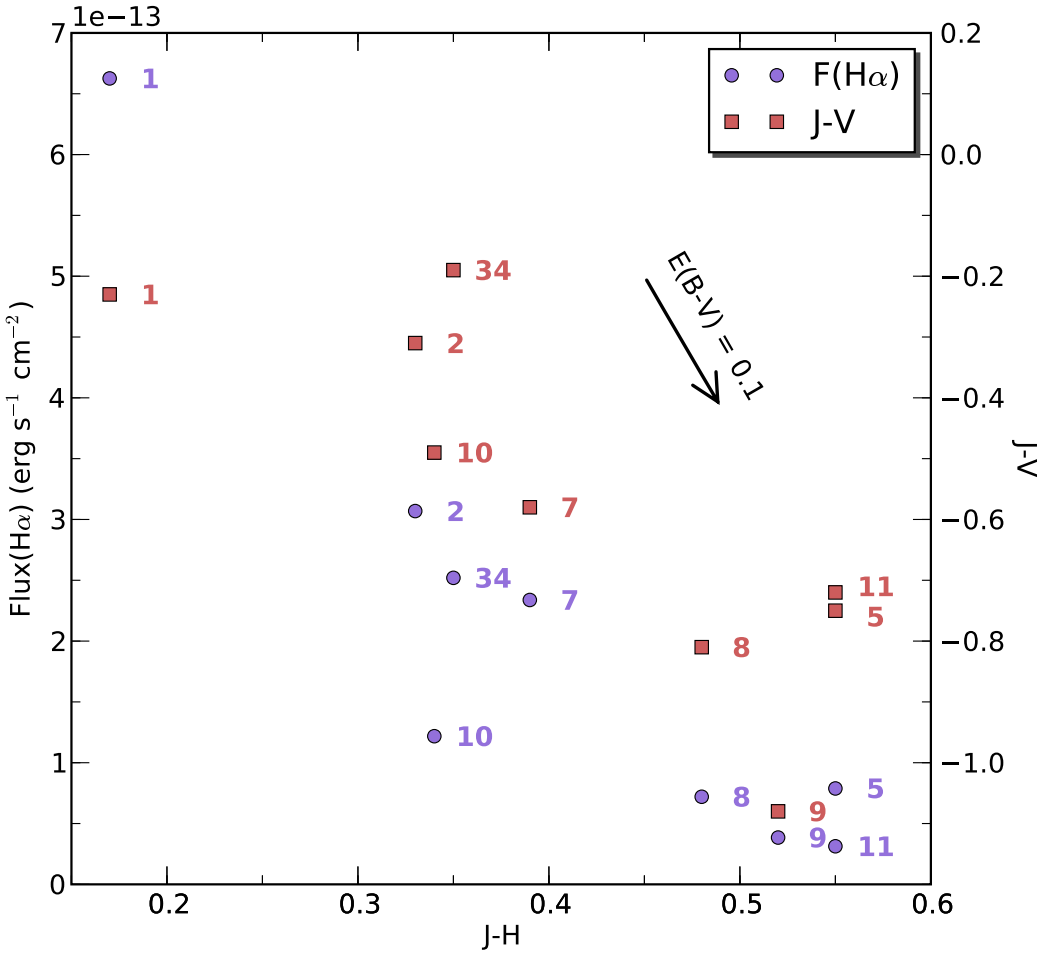

Figure 2.9: Hα and J-V versus J-H plot for the clusters identified in section 2.3.1. A clear correlation of decreasing Hα with redder colors points to an aging effect within the ongoing starburst phase.

due to aging of the burst or to different clusters having different masses, less massive bursts producing fewer ionizing photons[6]. However, if this latter were case there is no clear reason why there should be a relationship with color, which is expected in the scenario of the clusters aging. We conclude that most of the trend seen in this figure may be due to aging, with some component due to different initial masses.

Knot 1 is the brightest in Hα and the results of the photometric analysis using CHORIZOS give the youngest age, ~ 3 Myr, with lowest extinction. Knots 2, 34, 7, 8, 9, 10 have intermediate age, $\sim 4-7$ Myr, with an intermediate extinction, except may be knot 9 which has some indications for a somewhat higher extinction. Knots 5 and 11 are older, ~ 10 Myr.

In summary, from the cluster analysis of individual bright knots and from the integrated photometry of the whole complex there are clear indications that there is a complex history of star formation in NGC 5471, with indications of an older population of B stars and the

[6]Extinction may also play a small role, but it would require extinction values significantly larger than reported in the literature, which are lower than E(B-V)=0.14

luminous young ionizing cluster. This will be well established with the analysis of the CMD in the next section.

Mass of the ionized gas

The H^+ mass and the mass of the ionizing cluster may be derived from the Hα flux. The published values of internal extinction for NGC 5471 differ from different authors, but they are lower than about E(B-V) = 0.14 on average (Skillman, 1985; Torres-Peimbert et al., 1989; Kennicutt and Garnett, 1996; Luridiana et al., 2002; Esteban et al., 2002). Therefore, we have not attempted to correct the measured Hα flux to estimate other magnitudes from this value. The electron density assumed is $n_e = 100$ cm^{-3} (Luridiana et al., 2002).

The Hα flux in a 15″ radius circular aperture (uncorrected for internal extinction) yields a lower limit to the luminosity $L_{H\alpha} \sim 2.3 \times 10^{40}$ erg s^{-1}. The total number of H-ionizing photons, $Q(H^0)$, estimated from Osterbrock (1989) is:

$$Q(H^0) = \frac{\alpha_B}{\alpha_{H\alpha}^{eff}} \times \frac{L_{H\alpha}}{h\nu_{H\alpha}} \sim 2.2 \times 10^{52} s^{-1}$$

where $\alpha_B/\alpha_{H\alpha}^{eff} \sim 2.99$, assuming case B recombination, $\alpha_B \sim 2.59 \times 10^{-13}$ cm^{-3} s^{-1}, and an effective recombination coefficient for Hα of 8.63×10^{-14} cm^{-3} s^{-1} for 10^4 K and $n_e = 100$ cm^{-3} (Osterbrock, 1989). Thus the total (lower limit) ionized mass of the gas cloud is

$$M_{H^+} = Q(H^0)\frac{m_p}{n_e \alpha_B} \sim 7.3 \times 10^5 M_\odot$$

From evolutionary models of single stellar population ionizing clusters and radiation-bounded H II regions, a relation between $Q(H^0)$ per solar mass and the Hβ equivalent width can be found (Díaz, 1998), which allows to estimate the stellar cluster mass by taking into account the cluster evolution:

$$log[Q(H^0)/M_\odot] = 0.86\, log[EW(H\beta)] + 44.48 \quad (2.5)$$

Hence, a lower limit for the mass of the cluster can be estimated by means of the Hβ equivalent width and the Hα luminosity of the region. Using the range of values EW(Hβ)=134-296 Å published by different authors (Luridiana et al., 2002; Esteban et al., 2002; Rosa and Benvenuti, 1994; Rosa, 1981), and the value of Q(H^0) calculated above, equation 2.5 yields a mass of the ionizing cluster in the range $0.6 - 1.1 \times 10^6$ M$_\odot$. Using the calibration of Kennicutt (1998) and the luminosity that we measure, $L_{H\alpha} \sim 2.3 \times 10^{40}$ erg s^{-1}, we obtain a star formation rate of 0.18 M$_\odot$ yr^{-1}, that translates into a cluster mass of 10^6 M$_\odot$ for a burst duration of 10 Myr, which is the duration of the current burst implied by the analysis in the previous section.

Thus we find that the masses of ionized gas and of the stellar cluster in the current star

formation event are both of the same order of magnitude, close to 10^6 $M_\odot$. This similarity may be understood in terms of a very high efficiency in star formation. Given that this is not the first event of star formation in NGC 5471 in the last 100 Myr, this high star formation efficiency takes an important meaning that implies that there has to be a large reservoir of gas to maintain this SFR.

Although optical images show NGC 5471 apparently isolated in the outskirts of M101, the H I distribution of M101 shows that NGC 5471 is, in fact, one of the brightest regions in H I, located in a spiral arm (cf. Figure 2.1). The thermal radio continuum emission from NGC 5471 has the highest observed central emission measure of all the M101 complexes. Closely coincident with this H II radio continuum peak, there is an H I concentration of nearly 10^8 $M_\odot$ (Viallefond et al., 1981). The general distribution of the H I gas in M101 follows that of the diffuse FUV emission, with enhancements in the 21 cm line emission seen near FUV peaks. Smith et al. (2000) include NGC 5471 as one of their 35 PDR candidates. Their UIT FUV flux measurement is in good agreement with our GALEX measurement of 9.8×10^{-14} erg cm^{-2} s^{-1} Å^{-1}, and NGC 5471 is clearly the brightest FUV peak in the whole M101 galaxy. This is reflected in a decreased molecular content surrounding NGC 5471 which has been dissociated by the high star formation efficiency, the highest in M101 as calculated by Giannakopoulou-Creighton et al. (1999).

2.4.2 CMD

The photometry of the individual stars presented in the color-magnitude diagram, m_{547M}-$m_{675'}$ (V-R) vs. m_{547M} (V), of Figure 2.10 is a powerful tool to further understand the star formation history in NGC 5471. The isochrones represented in the figure have been divided into five age bins, (4-10, 10-25, 25-50, 50-75, 75-100) Myr, and drawn by their concave hull, shown with different colours. The right hand side of the figure shows the luminosity function, which peaks at $M_{547M} \approx 24$, and becomes incomplete for fainter stars, as indicated by the 50% completeness limit shown. We recall that this CMD is the result of a careful process of calibration, measurement and cleaning, as detailed in section 2.3.2 above. We have not included in the CMD those point-like sources with a partially resolved PSF, that are likely to be compact clusters. At the distance of M101 some of the point sources are unresolved multiple systems, some of which may have been included in the CMD, but these will not really affect any of the arguments that we present here.

A glance at the CMD tell us at once that star formation has been proceeding more or less continuously for the last 100 Myr. The diagram is populated by stars of $\sim 4 - 50$ $M_\odot$. We can readily identify clear structures in the diagram. A well-defined main-sequence at V-R $\sim$ -0.1, which begins with the brightest star at 19 mag, that corresponds to an age of $\sim$ 4 Myr, and goes all the way down to 25 mag. Red stars span a range of $3 - 4$ magnitudes in brightness, indicating that star formation has occurred during the last $\sim 15 - 70$ Myr. There

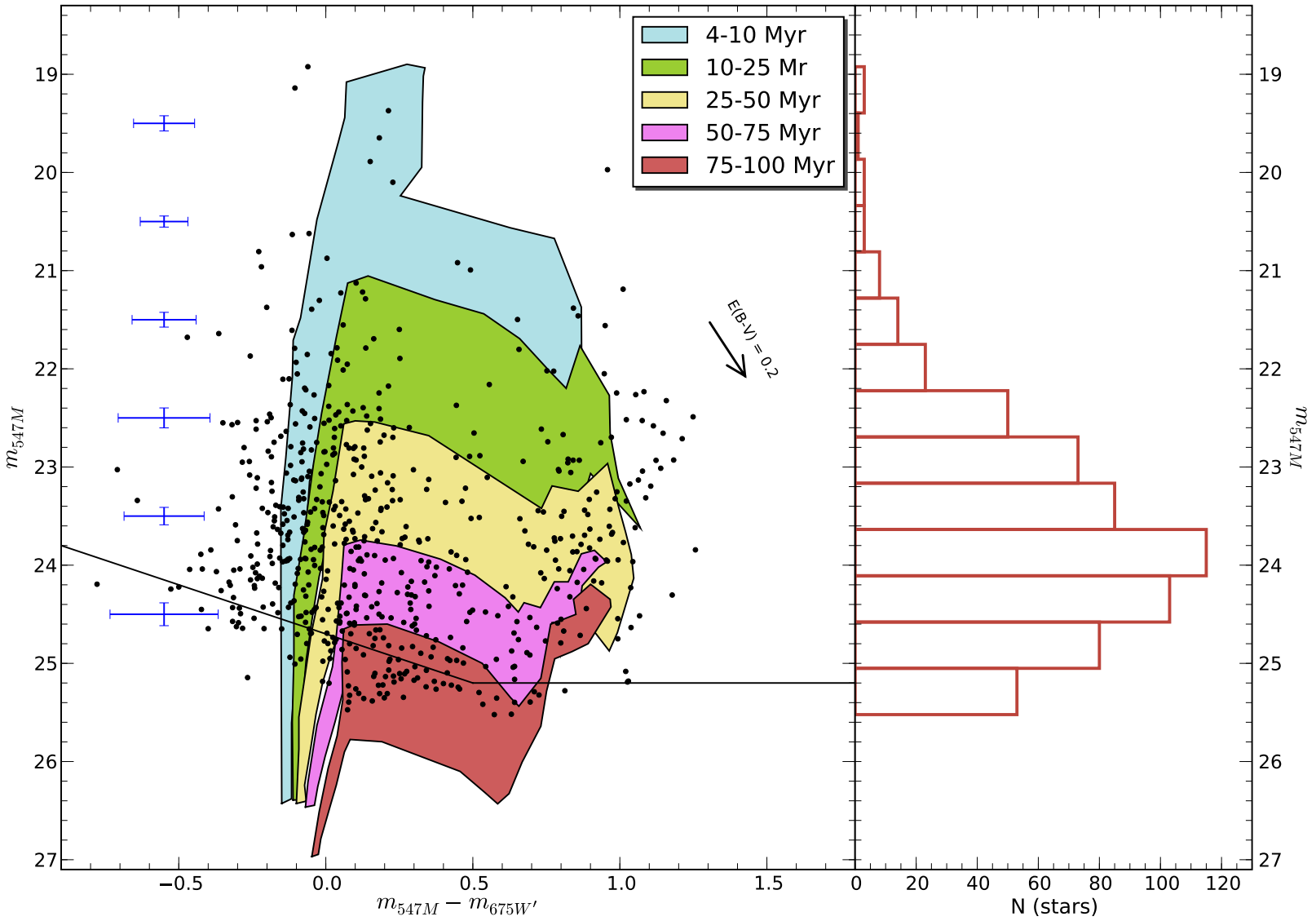

Figure 2.10: Final CMD with isochrones divided into five age bins, drawn by their concave hull, and shown with different colours. The right hand side of the figure shows the luminosity function. The line across the bottom shows the completeness limit at the 50% level.

are some traces of the blue-plume at $M_V = -9$, indicating ongoing star formation. A strip of stars following a patch from [0.6,25] to [1.1,22.5] form the red giant branch.

Mass in stars

In order to quantify the relative importance of the present burst to the star formation history during the previous 100 Myr in NGC 5471, we make a rough estimate of the stellar mass from the CMD. We follow three different approaches. One method consists in assigning a mass to each of the stars in the CMD, corresponding to the closest isochrone, thus counting the stars in the mass range 6-55 $M_\odot$ and integrating a Salpeter IMF in the mass range 1-100 $M_\odot$. The result of this calculation gives $\sim 2 \times 10^5$ $M_\odot$. The second method is as follows: first we assign a mean stellar mass of 6 $M_\odot$ to the stars in the most populated bin of the luminosity function, $m_{547M} = 23.5$. This mass is then scaled up by the ratio of the total m_{547M} of NGC 5471 to the magnitude of the bin $m_{547M} = 23.5$. The resulting mass is used to normalize the IMF at the bin corresponding to 6 $M_\odot$. The result of integrating a Salpeter IMF in the range 1-100 $M_\odot$ thus normalized gives a value of $\sim 5 \times 10^5$ $M_\odot$.

A third independent method to estimate the mass is based on the fit of the CMD by means of Hess diagrams. We have used the code STARFISH (Harris and Zaritsky, 2001, 2002) to find a best fit to the CMD by a linear combination of Hess diagrams at different ages. The solution found by the code is only sensitive to stars in two age bins in the range 50-100 Myr, giving an average SFR ~ 0.01 $M_\odot$ yr^{-1}. Integrating this SFR for 50 Myr gives a total mass of $\sim 5 \times 10^5$ $M_\odot$, in the same range of values found by the previous two methods.

Although these methods give only an order of magnitude estimate, we can conclude that the integrated mass of stars formed in the past 10-100 Myr is of the order of magnitude or less than the current star formation event, that we have calculated above as $\sim 10^6$ $M_\odot$. If the star formation proceeds in an isolated gas cloud, we would expect that the rate at which stars form would decrease with time, as less gas is left available to form new stars. This is what is observed in many giant H II regions with two or more generations of star formation, where the latest event is less massive than the previous. In the case of NGC 5471 the results from the integrated photometry and from the CMD indicate that the current star forming event is more massive than the rate at which stars have formed during the previous 10-100 Myr. This we can understand in the context of the large H I spiral arm in which the region is immersed, as mentioned above. In this respect, Waller et al. (1997) conclude from a morphological study of M101 that NGC 5471 may be the result of tidal interactions of M101 with the nearby galaxies NGC 5477 and NGC 5474 in the time interval 100-1000 Myr ago.

Spatial distribution of the star formation history

Given the long duration of the star formation in NGC 5471, $\sim$ 100 Myr, it is natural to question the spatial location of the star formation through time along the extent of the

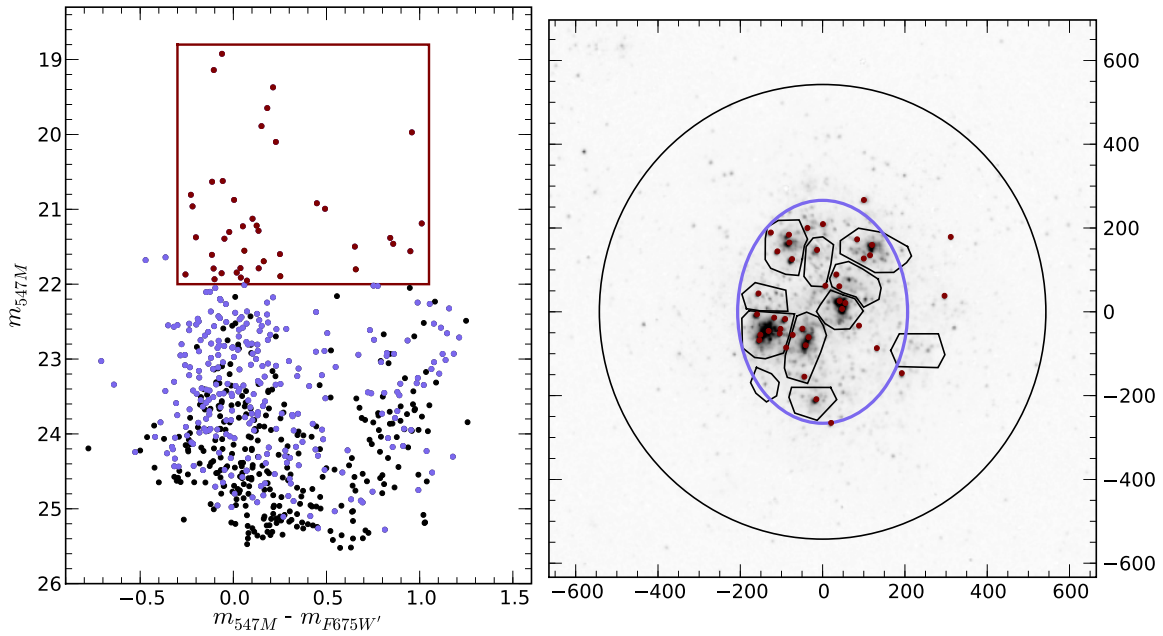
19
20
21
22
23
24
25
26
m_{547M}
−0.5
0.0
0.5
1.0
1.5
m_{547M} - $m_{F675W'}$
600
400
200
0
−200
−400
−600
−600
−400
−200
0
200
400
600

(a)

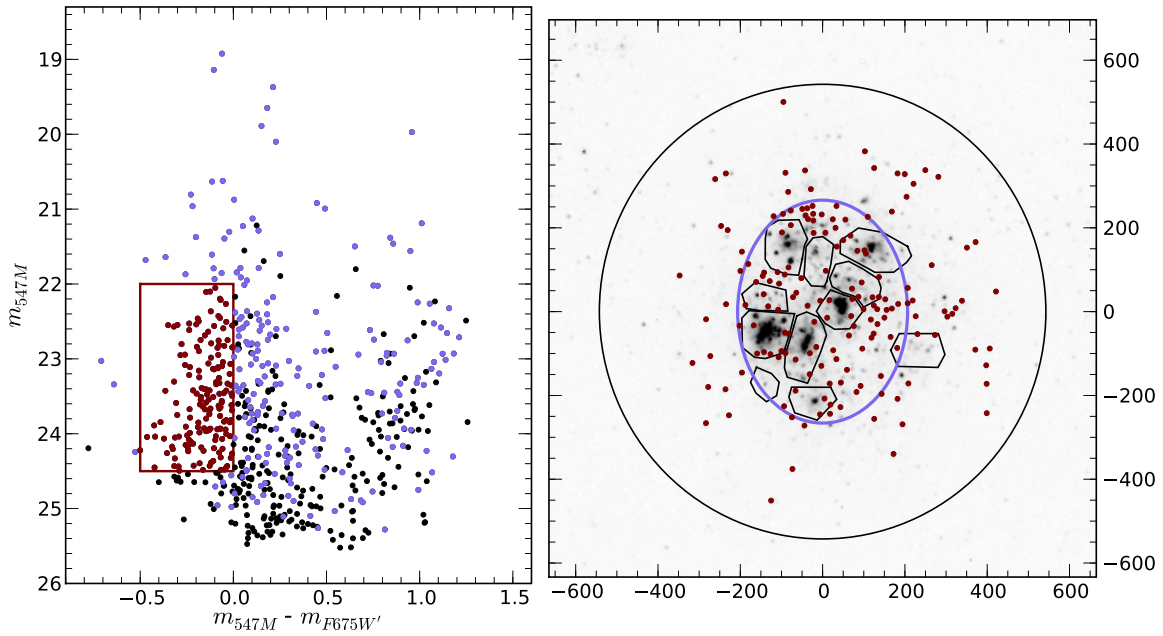
19
20
21
22
23
24
25
26
m_{547M}
−0.5
0.0
0.5
1.0
1.5
m_{547M} - $m_{F675W'}$
600
400
200
0
−200
−400
−600
−600
−400
−200
0
200
400
600

(b)

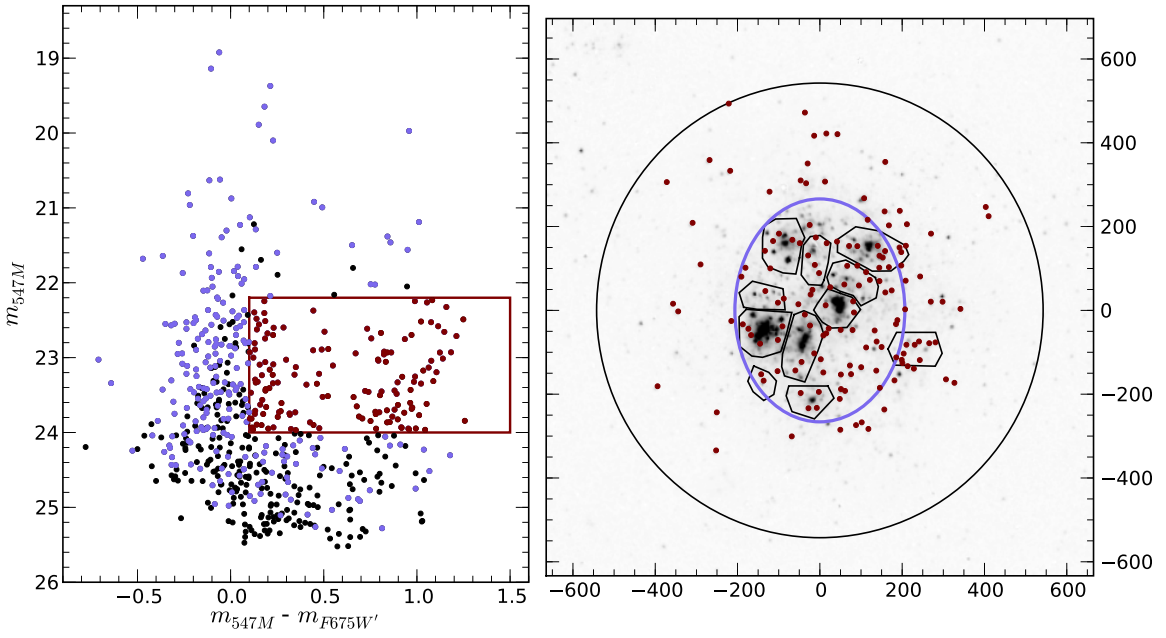

(c)

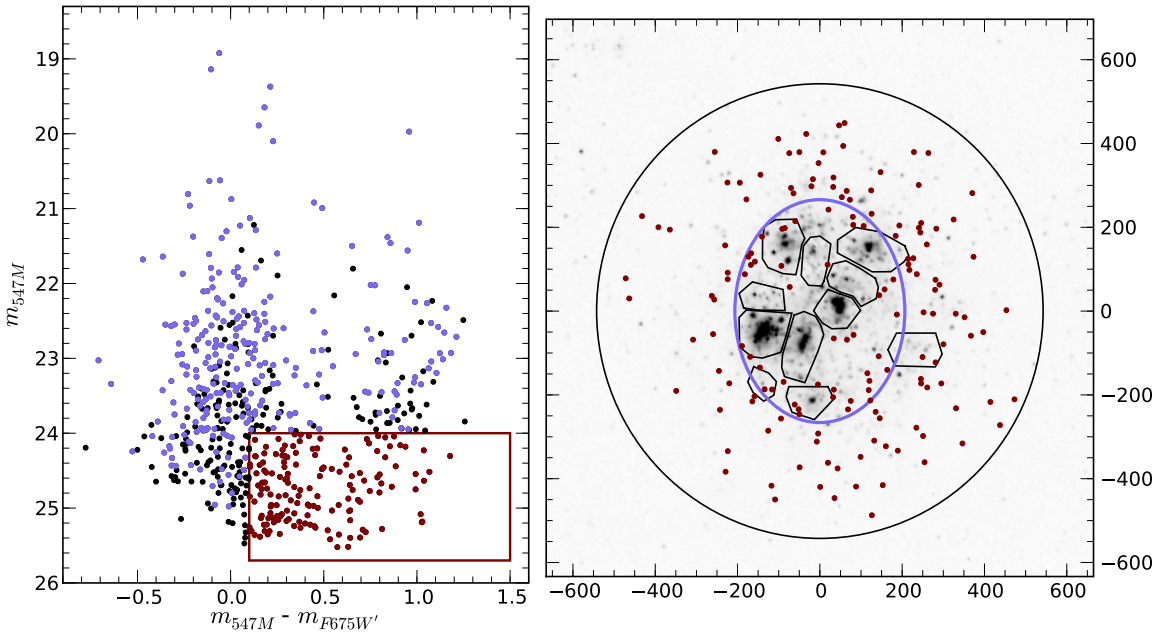

(d)

Figure 2.11: Spatial distribution of the star formation with time. The spatial distribution of the stars within four boxes selected in the CMD are shown in the right hand side images. The images are also drawn with a circle of 15 arcsec radius, indicating the area of the integrated photometry, an ellipse delineating the core region where the present star forming event occurs, and the polygons selected for the cluster analysis. Notice how the younger stars are concentrated in the inner clusters (a) and the older stars are preferentially located in the halo (d), while intermediate age stars populate uniformly the core with some presence in the halo.

region. In order to visualize this, we have selected four different areas in the CMD and proceeded to locate spatially the stars in these four boxes. Figure 2.11 displays the resulting distributions. The youngest and more massive stars (a) are clearly concentrated in the main star forming emission line knots, implying that massive stars form mainly in clusters. Only two stars are not directly associated with these knots, one of which belongs to an isochrone of 20 Myr. Panel (d) displays the distribution of intermediate mass stars ($\sim 5-10$ $M_\odot$) older than about 50 Myr; these stars are distributed mainly towards the halo, with only a few in the core of the region. Panels (b) and (c) show the distribution of intermediate mass stars ($\sim 10-15$ $M_\odot$), both those which are in the main sequence and those which have already evolved out of it. The distributions of stars in these two CMD boxes are clearly fairly uniform throughout the core of NGC 5471, with some of them distributed in the halo, a somewhat complementary spatial distribution to the older lower mass stars in the bottom-right panel. Because the stars in these two intermediate boxes are of the same mass but they are found in a range of evolutionary stages, this implies that star formation has proceeded more or less uniformly in the core for the last $\sim 20-50$ Myr.

From this analysis of the spatial distribution of the CMD, a clear picture emerges in which the star formation in the NGC 5471 complex has proceeded in a general spatio-temporal sequence from the halo inwards to the core. During the first epoch, $\sim 50-100$ Myr ago, the star formation occurred mainly in the halo, then it moved inwards and occurred more or less uniformly in the core $\sim 20-50$ Myr ago, although some of the star formation was also important in the halo, and finally the current ionizing star forming event is mostly concentrated in the singular bright clusters well located within the core. At the same time, we have seen that, both from the integrated photometric analysis and from the CMD, as the events moved inwards from the halo to the core the amount of mass of gas formed into stars seems to have increased.

We note that the current event of ionizing clusters is apparently contained within a large bubble which defines the core of NGC 5471. This bubble, of projected size 400×550 pc, is clearly defined geometrically (cf. Figure 2.2) and kinematically (Munoz-Tunon et al., 1995), and is likely to have been produced by the stars that formed ~ 20 Myr ago.

There are other examples that seem to follow the general process of star formation that we have outlined here for NGC 5471. Walborn and Blades (1997) find a similar spatio-temporal distribution of stars in 30 Doradus, and Úbeda et al. (2007) also find an inwards sequence of star formation and a bubble for cluster I-A in NGC 4214.

Chapter 3

Integral Field Spectroscopy of H II region complexes. The outer disk of NGC 6946

3.1 Introduction

NGC 6946 is a relatively nearby, nearly face–on spiral galaxy with an exceptionally gas–rich disk which shows evidence for a high star formation rate (SFR) throughout (Degioia-Eastwood et al., 1984) and has been classified as having strong nuclear starburst activity (Elmegreen et al., 1998). The six historical supernova remnants recorded during the past century attest to this high star formation and justify the popular name "Fireworks Galaxy". NGC 6946's orientation and large angular size ($D_{25,B} = 11\farcm2$) offers the prospect of studying the structure and star forming properties of the disk.

NGC 6946 and its many supernova remnants have been the subject of numerous X–ray, optical and radio papers. At mm wavelengths the CO molecule, used as a tracer of the dominant molecular species, H_2, has been observed by several authors (Ball et al., 1985; Casoli et al., 1990), showing that the CO distribution has a central density peak and barlike gas structure.

Morphologically, NGC 6946 is a late-type SAB(rs)cd spiral galaxy (de Vaucouleurs et al., 1991), with several spiral arms and star-forming regions scattered throughout the disk, considerable extinction and a small nucleus. Its general properties are summarized in Table 3.1. K-band images reveal four prominent, not very symmetric arms (Regan and Vogel, 1995).

Property	Value
Type	SAB(rs)cd[a]
R.A. (J2000)	20 34 52.3[a]
Dec. (J2000)	60 09 14.2[a]
Distance	5.9 Mpc[b]
$D_{25} \times d_{25}$	11′.2 (16.6 kpc) ×10.0 (14.8 kpc)[a]
V_{sys}	47 ± 4 km s^{-1}[c]
m_0^T(B)	7.78[a]
M_0^T(B)	-20.92
L_0^T(B)	5.3×10^{10} $L_{B\odot}$
$B-V$	0.4[a]
M/L (B) disk	1.2 ± 0.2[c]
M_*	6.4×10^{10} $M_\odot$[c]
M_{HI}	$2.0 \pm 0.1 \times 10^{10}$ $M_\odot$[d]
M_{H_2}	$1.2 \pm 0.1 \times 10^{10}$ $M_\odot$[e]
Inclination	38 ± 5[c]
Position angle	240 ± 3[c]
Central metallicity	12 + log O/H = 9.36[f]
Metal. Gradient	-0.089 dex kpc^{-1}[f]
SFR	2 $M_\odot$ yr^{-1}[g]

[a] RC3 (de Vaucouleurs et al., 1991)
[b] Karachentsev et al. (2000)
[c] Carignan et al. (1990)
[d] Rogstad et al. (1973)
[e] Tacconi and Young (1986)
[f] Belley and Roy (1992)
[g] Ferguson et al. (1998)

Table 3.1: NGC 6946 general properties. Table adapted from Walsh et al. (2002)

NGC 6946 appears in the ARP's atlas, due to the "thick" optical arm in the NE, also seen in the deep Hα map presented by Ferguson et al. (1998).

CO observations have identified NGC 6946 as having one of the most massive and extended molecular gas components observed in a nearby galaxy (Young et al., 1995). Atomic gas is also found throughout the disk, although it is found in highest concentrations in the spiral arms and appears less massive than the molecular component (Tacconi and Young, 1986).

There is a nuclear starburst in the central 11″ of NGC 6946 (Degioia-Eastwood, 1985). Several studies of the HII regions have been made (Hodge, 1969b; Hodge and Kennicutt, 1983). The bright nucleus is characterized as an HII region nucleus on the basis of the strength of [OI]/Hα and [SII]/Hα line ratios (Ho et al., 1997).

The distance to NGC 6946 has been variously quoted to lie within the range 3.2-11 Mpc.

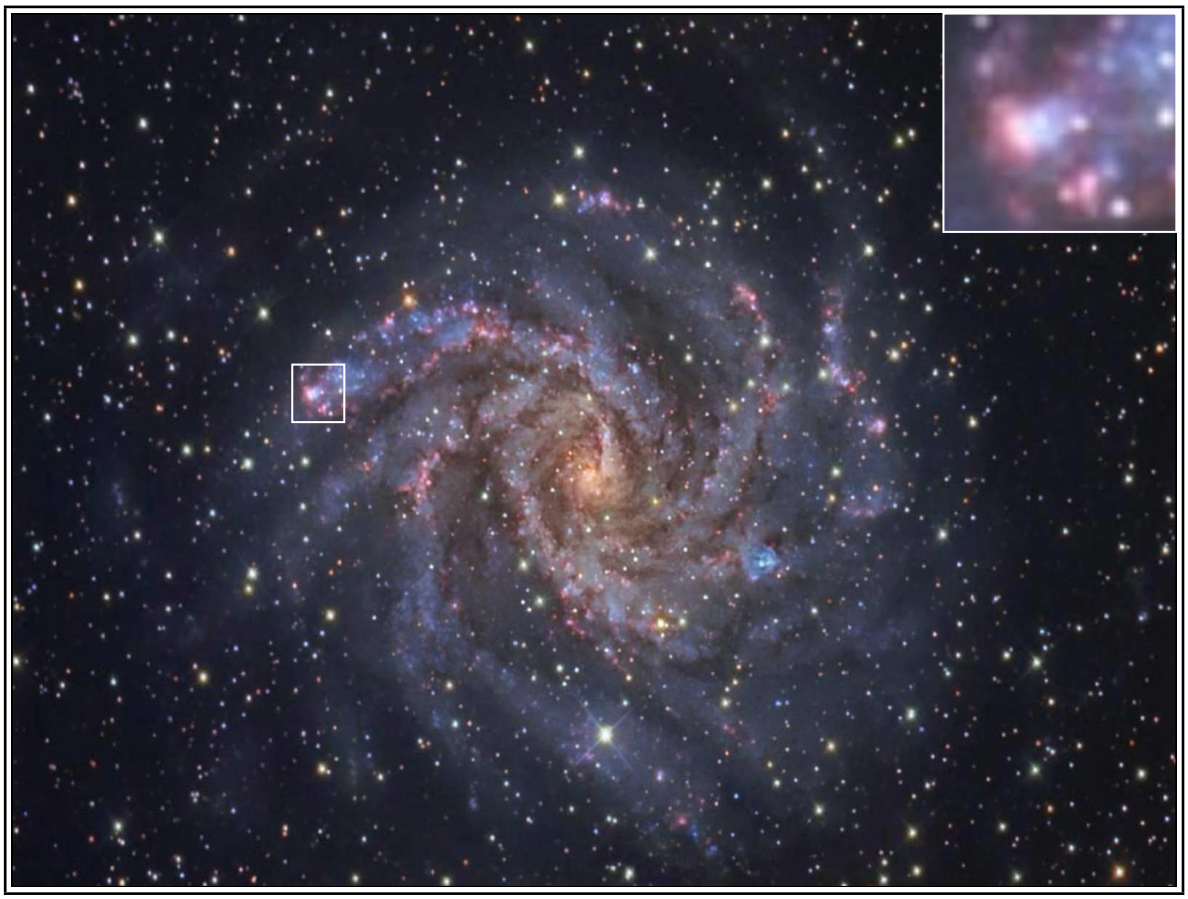

Figure 3.1: Color composition image of NGC 6946 (credits: Volker Wendel). The box indicates the location of the GEHR, at about 4′ from the center of the galaxy. At the upper right corner it is shown a close-up of the region. North is up and East is towards the left-hand side.

This uncertainty is partly because the galaxy is localted at a relatively low Galactic latitude (b = 12°) and is subject to significant foreground extinction from our Galaxy, varying from $A_B = 1.48$ (Schlegel et al., 1998) up to $A_B = 1.62$ (Burstein and Heiles, 1984). The distance to NGC 6946 is listed as 5.5 Mpc in the Nearby Galaxies Catalogue (Tully, 1988), but a more recent value is 5.9 ± 0.4 Mpc (Karachentsev et al., 2000), based on blue supergiants. Here we use a distance of 5.9 Mpc to NGC 6946. Assuming this value, 1″ in the sky corresponds to 28.6 pc.

As mentioned before, NGC 6946 has a particularly extended disk of neutral hydrogen and is among our best examples of galaxies with extreme outer disk star formation. Figure 3.1 shows a color composition image of NGC 6946. From the core outward, the galaxy's colors change from the yellowish light of old stars in the center to young blue star clusters and reddish star forming regions along the loose, fragmented spiral arms. The box indicates the location of a Giant Extragalactic HII Region (GEHR) complex studied in this work, placed in the "thick" optical arm in the NE, at about 4′ from the center of the galaxy. This

northeastern arm is the brightest arm at all wavelengths, indicating a site of vigorous star formation.

As we have seen in Chapter §2, GEHRs observed in many external late-type galaxies, spirals or irregulars, are prominent sites of massive star formation. The large Balmer luminosities of these gigantic volumes of ionized gas attest to the fact that they harbor 10^3 to 10^5 $M_\odot$ in OB stars with total ionizing power equivalent to tens or even several hundreds O5 V stars. The presence of GEHRs in nearby galaxies offer a unique opportunity to study their ionization structure. High spatial resolution imaging has revealed that in many of these objects the ionized material presents a complex structure. Thus, a two-dimensional analysis of the ionized material yields spatially resolved information on properties of the ionized gas. This is important to see whether there are local abundance variations within the region and to check if different degrees of ionization give consistent abundances for locations in different parts of the nebula. To investigate these issues, we obtained integral field spectroscopy of the large GEHR complex showed in figure 3.1. We have produced maps of emission lines, continuum emission and properties of the ionized gas. We have measured the number of Wolf-Rayet stars and traced their location. In the light of all these results, we discuss the issues mentioned before.

In the following section the observations are described. In section 3.3 the reduction process is described in considerable detail. In section 3.4 the results are presented. We discuss these results in section 3.5.

3.2 Observations

The group of HII regions of NGC 6946 were observed with the Postdam Multi-Aperture Spectrophotometer (PMAS; Roth et al., 2005), which is attached to the 3.5 m telescope at Calar Alto. The PPak (PMAS fiber Package) fiber bundle IFU (Kelz et al., 2006) was used. PPak is based on earlier developments, such as INTEGRAL or SparsePak. Like these instruments, PPak uses larger fibers that cannot sample finely the image, but instead collect more flux and allow for wide fields. PPak spans $74'' \times 64''$ on the sky and provides one of the largest fields of view (FOV) of IFU available worldwide. Therefore, PPak is ideally suited for spectroscopic studies of extended astronomical objects with low surface brightness, such as the outskirts of spiral galaxies.

The PPak IFU holds 331 fibers in a densely packed hexagonal grid with a maximum diameter of $74''$ (which correspond to approximately 2.1 kpc at the distance of NGC 6946), while each fiber projects to $2\farcs68$ in diameter on the sky. Figure 3.2 shows the layout and dimensions of the PPak IFU. The fiber-to-fiber pitch is $3\farcs6$ which yields a total filling factor of $0\farcs60$. An additional 36 fibers are distributed among six bundles of 6 fibers each, located following a circular distribution and placed $72''$ from the center to sample the surrounding sky. Finally, there are 15 extra fibers connected to the calibration unit which are not part of

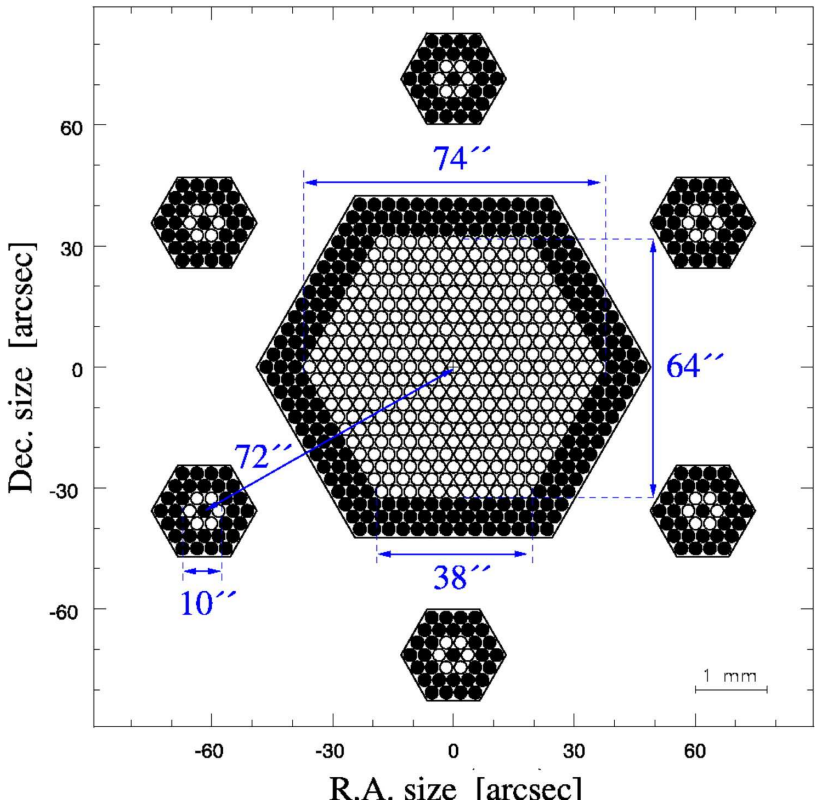

Figure 3.2: Layout and dimensions of the PPak IFU. White circles represent active fibers, while the blacks ones are protective buffers. The physical size of the central IFU is 4 mm, but its coverage on the sky is more than 1′.

Object	Offset (α, δ) (arcsec)	Exptime (s)	Grating	GROT	Spec. Range (Å)	Dispersion (Å pix^{-1})	Date
NGC 6946	0,0	3×500	V300	-75	3700-7000	3.2	09/07/2008
NGC 6946	1.56,0.78	3×500	V300	-75	3700-7000	3.2	09/07/2008
NGC 6946	1.56,-0.78	3×500	V300	-75	3700-7000	3.2	09/07/2008
NGC 6946	0,0	3×500	V300	-72	7000-10100	3.2	09/08/2008
NGC 6946	1.56,0.78	3×500	V300	-72	7000-10100	3.2	09/08/2008
NGC 6946	1.56,-0.78	3×500	V300	-72	7000-10100	3.2	09/08/2008

Table 3.2: Journal of observations and instrumental configuration.

the IFU, and that can be illuminated with light from spectral-line lamps during the science exposures. Therefore, the total number of fibers is 382, distributed in 331 science-fibers, 36 sky-fibers and 15 calibration-fibers.

The observations were acquired on 2007 September 7th and 8th during three nights observing run and under photometric conditions, with a seeing ranging between 0.″8 and 1.″0. The airmass of the science images was always less than 1.1 to avoid large DAR effects (see section 3.3.10). The V300 grating was used with two different Grating Rotator angles (GROT). The value GROT=-75 covers a wavelength range between 3700-7000 Å, while the

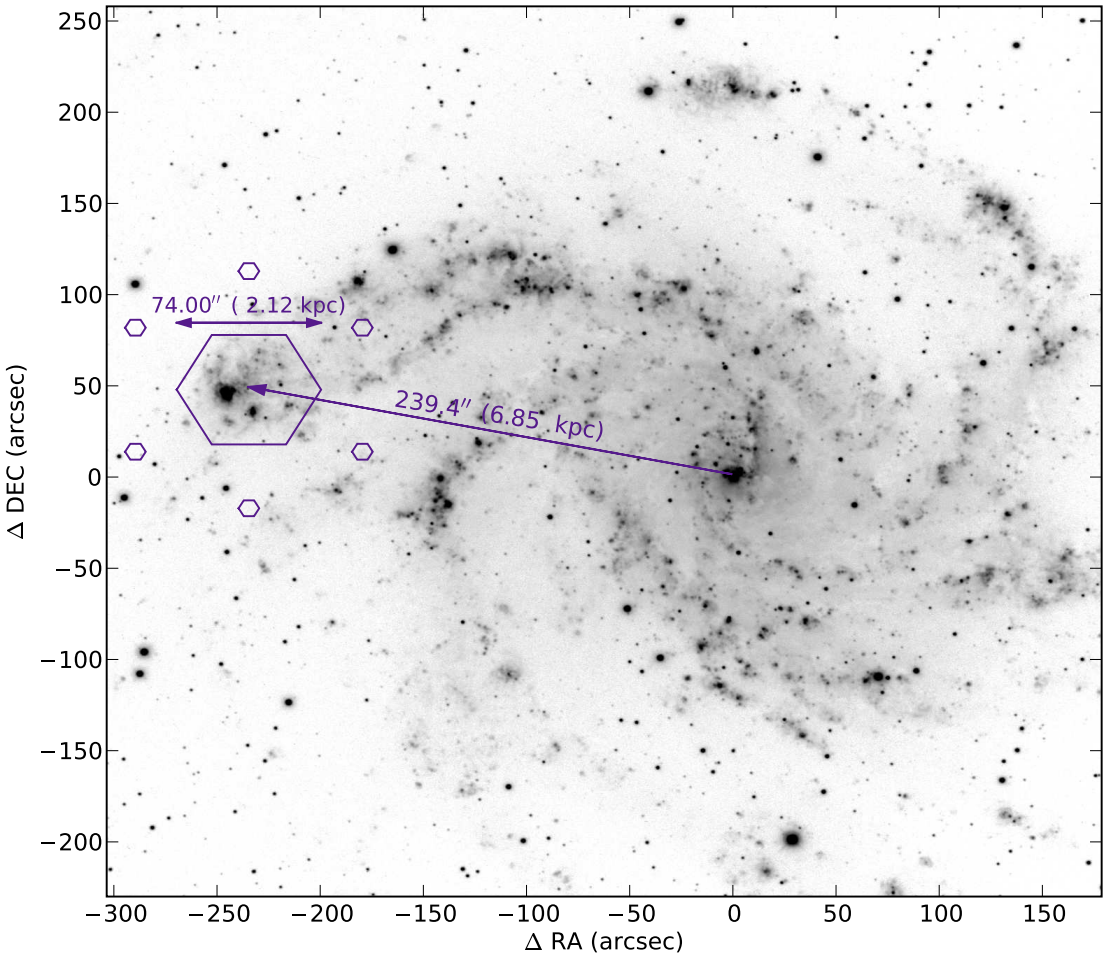

Figure 3.3: Hα image of NGC 6946 taken at the Kitt Peak National Observatory (KPNO) 2.1-meter telescope. The image has not been continuum-subtracted. The big hexagon shows the position of the PPak field and little ones the position of the six bundles of sky-fibers. North is up and East is towards the left-hand side.

value GROT=-72 spans from 7000 up to 10100 Å. Both configurations have a dispersion of 1.6 Å/pixel and a resolution of ∼10 Å FWHM. Nevertheless, the images where taken in the 2×2 pixel binning mode, giving a final dispersion of 3.2 Å/pixel. Instrumental configuration and details on the exposures taken are given in the observational journal in Table 3.2. This configuration was chosen in order to cover the hole spectrum from about 3600 to 10000 Å guarantying the measurement of the [OII] $\lambda\lambda$ 3727,3729 Å and [SIII] $\lambda\lambda$ 9069,9532 Å at both ends of the spectrum and other emission lines crucial when making a plasma diagnostic.

The coordinates of the IFU field centre were $\alpha = 20^h36^m02\overset{s}{.}1$; $\delta = +60°17'12\overset{''}{.}9$ (J2000) and a total of 9 single exposures per object and Grating Rotator Angle of 500 s each were taken. These nine exposures were divided in 3 groups corresponding to different pointings. Each of these three pointings have a small offset in position from the other ones in order to perform a dithering mosaic. This allows to have a final mosaic with a filling factor of 1, so

that there is no flux loss. This procedure was also followed in the case of the standard stars (see section 3.3.6). The observed spectrophotometric standard stars were BD +28°4241 for the blue part of the spectrum (GROT=-75) and BD +17°4708 for the red one (GROT=-72). They were used to obtain the characteristic sensitivity function of the telescope and spectrograph for the spectral flux calibration. Calibration images were obtained following the science exposures and consisted of emission line lamps spectra (HgCdHe) or ARC exposures, and spectra of a continuum lamp needed for the wavelength calibration and to locate the spectra on the CCD, respectively.

Figure 3.3 shows an Hα (not continuum-subtracted) of NGC 6946 showing the position of the PPak field at the NE arm of the galaxy. The center of the pointing is located at 4′ (6.85 kpc) from the center of the galaxy.

3.3 Data Reduction

Integral Field Spectroscopy (IFS) is a technique for obtaining spectroscopic data of astronomical objects, in particular objects in crowded fields and extended objects like galaxies, planetary nebulae, star-forming regions, etc, collecting the spectra of many different regions of the object under identical instrumental and atmospheric conditions.

In contrast to long-slit spectroscopy, IFS offers the opportunity to obtain three-dimensional (two spatial and one spectral dimension) information of an object from a single observation. To store three-dimensional information of a two-dimensional plane of a detector like a Charge-Coupled Device (CCD), it is necessary to discretize at least one dimension, done by the discretization of the focal surface in spatial elements. In most cases, the object is wider than the width of the slit of the long-slit spectrograph, loosing a significant amount of light. This is not the case of an Integral Field Unit (IFU) with lenslet arrays or fiber re-formatters combined with dithering methods in order to have a filling factor of one.[1]

Another problem related with long-slit spectroscopy is the Differential Atmospheric Refraction (DAR), which is usually avoided observing near the Parallactic angle. IFS allows to correct this effect after the main reducing steps and before the data analysis.

As mentioned before, the IFS method allows a determination of physical properties in two dimensions, but studies presenting two-dimensional maps of HII regions (Maiz-Apellaniz et al., 1998) or Planetary Nebulae (PNe) (Rubin et al., 2002; Wesson and Liu, 2004) using different methods are not new. Nevertheless, due to the reasons mentioned before, IFS is a specific and powerful tool to perform maps analysis of physical properties.

A considerable amount of time was invested in learning and developing reduction and analysis tools due to the complexity of the data from IFU instruments and the still in

[1] The difference among the major techniques of IFS reside, basically, in the fact that they just vary the way how the focal plane is segmented, and how the light is coupled into the spectrograph. A detailed discussion of all the different IFS techniques can be found in Allington-Smith and Content (1998).

development existent tools.

Reducing data of IFUs is slightly different from the reduction of pure imaging or spectroscopic data, because IFS is a combination of both a may also depend on the characteristics of the particular IFU. The steps needed for the PMAS data reduction can be summarized in the following sequential list:

- Pre-reduction
- Identification of the position of the spectra on the detector along the dispersion axis
- Extraction of each individual spectrum
- Distortion correction of the extracted spectra and dispersion correction (wavelength calibration)
- Fiber-to-fiber transmission correction
- Flux-calibration (including cosmic-ray detection and removal in standard stars)
- Sky-substraction
- Mosaic/dither reconstruction
- Other corrections (DAR and/or atmospheric absorption)

Data reduction was performed using R3D (Sánchez, 2006), E3D (Sánchez, 2004), PyRAF (a command language for running IRAF[2] tasks based on the Python scripting language), and a self-made Python module (called `pyR3D`) which contains a Python wrapper for R3D, extra tools (as DAR or atmospheric absorption correction) and other routines. This module helps to diminish the number of steps needed for the reduction, working with a final small script which contains the whole reduction process with all the setting values. Moreover, it automatically adds to the header of each processed image all the parameters needed for other routines. This also helps to have a brief information about the main processes that a image has passed through.

3.3.1 Pre-reduction

The pre-reduction steps consist in all the corrections applied to the CCD data that are shared with the reduction of any other CCD-based data and can be easily done by pyRAF. This comprises the creation of a master bias (created from a combination of several bias frames) and the subtraction of this image from *all* raw images. Then it follows the

[2]The Image Reduction and Analysis Facility is distributed by the National Optical Astronomy Observatories, which is operated by the Association of Universities for Research in Astronomy, In. (AURA) under cooperative agreement with the National Science Foundation (NSF).

FlatFielding correction done by the application of the master CCD flat (usually provided by the Calar Alto Observatory) to all the raw images. Next step consists on the combination of different exposures on the same target *and* same pointing. This also performs the cosmic ray rejection. In the case of the standard stars, we had only one exposure per pointing, so it was necessary to clean for cosmic rays using other method. This is briefly explained when describing the flux calibration procedure.

3.3.2 Identification of the position of the spectra

The raw data from a fiber-feed spectrographs consist in a collection of spectra, stored as a 2D frame, aligned along the dispersion axis. For each wavelength, each spectrum is also spread along the perpendicular ("cross-dispersion" or "spatial") axis. As seen in Figure 3.4, spectra are separated by a certain width, following a characteristic profile which may be considered Gaussian. When the spectra are tightly packed, as in PPak mode, contamination occurs among neighbors. This is the so-called cross-talk. It is important to take into account, not only in raw data but also in final processed formats, that adjacent spectra at the CCD may originate from distant locations in the sky plane. Special care has to be taken to compensate effects of instrument flexure, optical distorsions, etc, which cause that the spectra are not perfectly aligned along the dispersion axis. This effect is corrected by calculating the shifts between the calibration frame and the corresponding object frames. Therefore, it is necessary to find the location of the projection of each spectrum at each wavelength along the CCD in order to extract its corresponding flux.

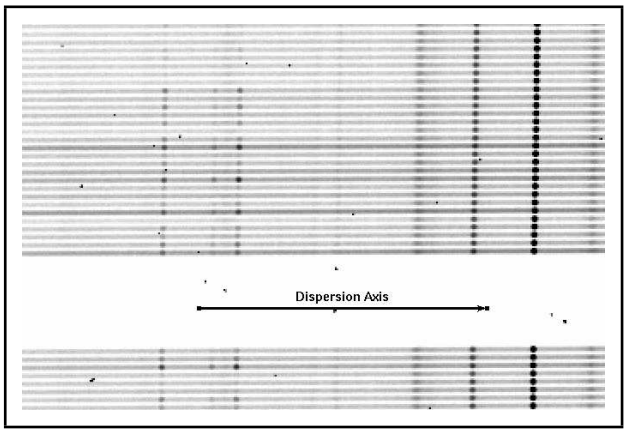

Figure 3.4: Section of a PPak raw data. The arrow indicates the dispersion axis. Spectra are separated 5 $\sim$ pixels across the cross-dispersion axis, following a pseudo-Gaussian of FWHM $\sim$ 3 pixels, contaminating the adjacent spectra.

The very beginning IFS data reduction step is to identify where the spectra lie on the CCD. This is done by using continuum illuminated exposures at every location where the telescope is pointing. An ARC exposure (obtained at the same location) is also needed, since flexures may also affect the wavelength calibration. The location of the spectra (apertures) are identified by extracting a slice perpendicular to the dispersion direction, finding where the peaks are. Each aperture is traced along the dispersion direction usually by fitting a Gaussian function. It is important that the trace is continuous. The aperture mapping is

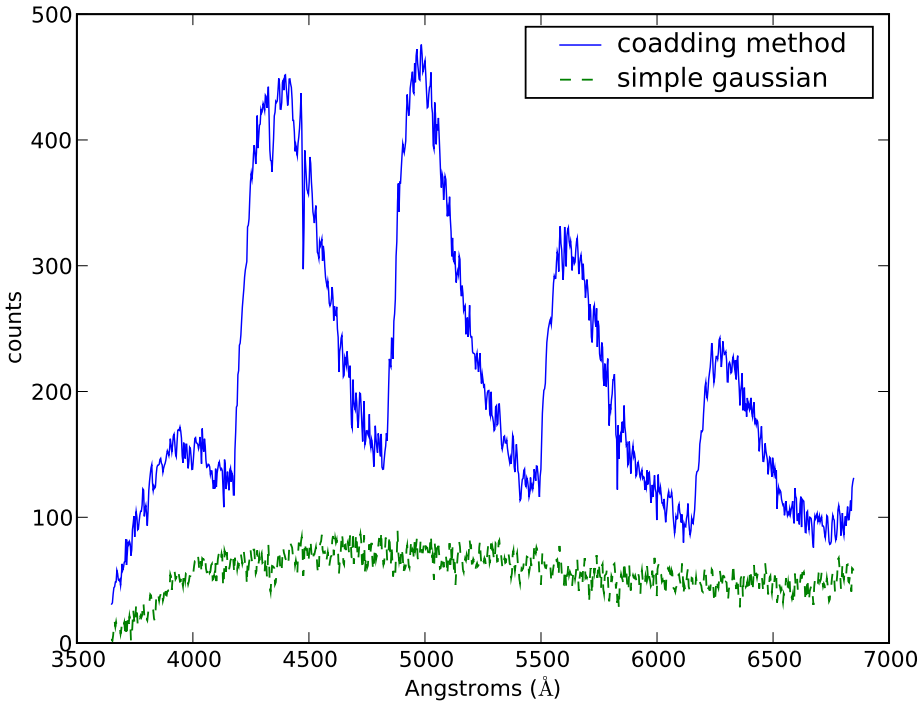

Figure 3.5: Comparison of the coadding (blue continuous line) and simple gaussian (green dot-dashed line) method for the aperture extraction reduction step.

then used as a reference for all other images. In many cases the science frames do not have enough signal-to-noise through all the fibers for an accurate determination of the tracing. Due to this reason, continuum illuminated exposures are used. The final result is stored as a 2D image with the X-axis as the original dispersion axis and the Y-axis the traced spectrum number. In each row is recorded the location of the peak centroid in the original frame. To ensure a continuous behaviour, it is advisable to fit a polynomial function to the traced result (order 4/5 is enough).

3.3.3 Spectra extraction

The next reduction step is to extract the flux corresponding to the different spectra at each pixel along the dispersion axis. This procedure is called aperture extraction. This is usually performed by coadding the flux within a certain aperture around the "trace" of the spectra in the raw data. In PPak data, the aperture extraction normally is done coadding the flux within an aperture of 5 pixels. Nevertheless, sometimes the aperture extraction is not the optimal method to recover the flux corresponding to each spectrum due to the cross-talk problem. Figure 3.5 shows a comparison of the coadding and simple gaussian method for the aperture extraction reduction step in the case of the fiber 167 of one single

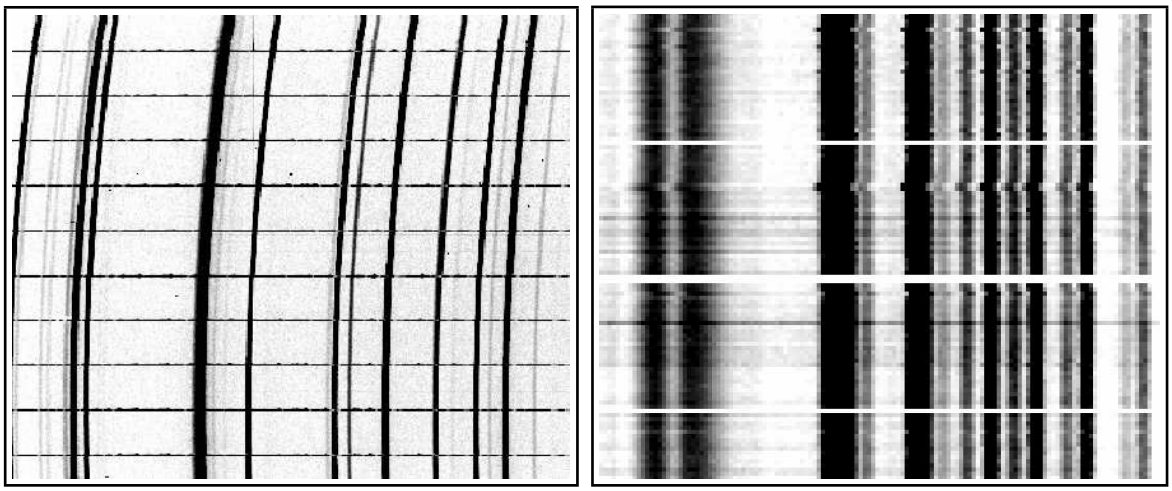

Figure 3.6: *Left panel:* Example of a RSS of a calibration lamp showing the distortion along the cross-dispersion axis. *Right panel:* Example of shifts produced by a bad second order correction for distortion.

pointing of the standard star BD+28°4211. The cross-talk problem can affect fibers with low counts adjacent to intense fibers. This is usually seen as a sinusoidal behaviour in the continuum of the spectra, producing spurious structure which could yield to wrong results in the interpretation of the data[3]. To avoid the cross-talk problem, sometimes it is enough to reduce the coadding width, but this may produce a substantial loss of flux if the aperture is too small. This is strongly dependent on the kind of data, so it is necessary to check if the simple aperture extraction does a good job and, otherwise, use the simple gaussian extraction (which is more time-consuming).

In the 2D image resulting from the aperture extraction, the X-axis corresponds to the original dispersion axis, while the Y-axis corresponds to the ordering of the spectra along the pseudo-slit. This is the so-called row-stacked spectra representation (RSS). Each single spectrum corresponds to a particular fiber and the RSS is just a frame, where all the spectra are sorted in the rows of the frame one after another. This representation is very useful because all the information can be stored in a single image, preserving the two-dimensional structure of the data as detected by the CCD plane. However, an extra file is needed with additional information of the exact location (projected position) of each fiber in the sky (the "position table").

Due to the not homogeneous light dispersion along the cross-dispersion axis, spectrographs present the so-called C distortion, so that the distortion is larger in the edges of the slit than in the center. In IFS, additional distortions are added to the intrinsic curvature for grating spectrographs owing to the placing of the fibers in the pseudo-slit. The left panel in Figure 3.6 shows a RSS where the curvature and distortions are seen. These distortions must

[3] As the case when fitting single stellar populations to the continuum in order to substract the underlying population

be corrected fiber-to-fiber before finding a common wavelength solution, so a 2D modeling of the distortion map with an analytical function cannot be done. Using an ARC exposure, the peak intensity of single emission line is traced along the cross-dispersion axis, an shifted to a common reference, by a linear shift. This is a first order distortion correction. In order to carry out a second order correction, a few emission lines are selected. Their peak intensity is traced and a polynomial distortion correction is performed to recenter all the lines to a common reference. Due to the fact that PMAS is a well behaved instrument in terms of distortion, only a low order polynomial function is needed. In this step it is important to select well separated bright lines and distributed along the dispersion axis (it is not necessary to select a large number; in fact, it is better to have only a few). Otherwise, the algorithm may mistake two lines or the fit may not be correct, producing some anomalous shifts in the trace. This wrong solution is clearly seen in right panel of Figure 3.6, where a detailed portion of a RSS shows shifts along the cross-dispersion axis. Our set of red ARC exposures had only a couple of intense lines, and they were only placed at the very beginning of the left side of the CCD, producing shifts in the second order correction along the last quarter of the frame. To correct for the shifts, it is enough to perform a smoothing operation in the solution. In particular, this can be controlled by the BOX parameter in the `mdist_cor_sp` R3D routine.

Once a satisfactory correction (first and second order) is achieved, the solution is finally applied to the science exposures.

3.3.4 Wavelength solution (dispersion correction)

The wavelength solution is found by identifying the wavelengths of the arc emission lines, using an interactive routine. The solution of the ARC spectra is transformed to a linear wavelength system by a one dimensional spline interpolation. The accuracy of this solution depends on the order of the polynomial selected, the number of lines identified, and the coverage of emission lines along the CCD (the more homogeneously distributed, the better) which, in turn, depends on the instrument. For PMAS in PPAK mode, it is enough with 9 emission lines and a polynomial function of order 4 (accuracy of $\sim$ 0.15 Å). For the blue spectrum, the ARC exposures with a HgCdHe had enough strong emission lines in order to find a good dispersion solution. Unfortunately, the same calibration lamp was used for the red spectra, having only a few intense lines in the left side of the wavelength range, as mentioned in secion 3.3.3. For this reason, sky lines were used in order to perform a dispersion correction. This is achieved by using the science frames themselves, which contains strong emission sky lines. In the red and near-infrared spectral regions, the OH emission bands of the natural night-sky spectrum dominate. Osterbrock and Martel (1992) tabulated accurate wavelengths of the individual lines in these bands. 12 to 15 lines homogeneously distributed along the full wavelength range were selected, achieving an accuracy of 0.5 Å. Figure 3.7

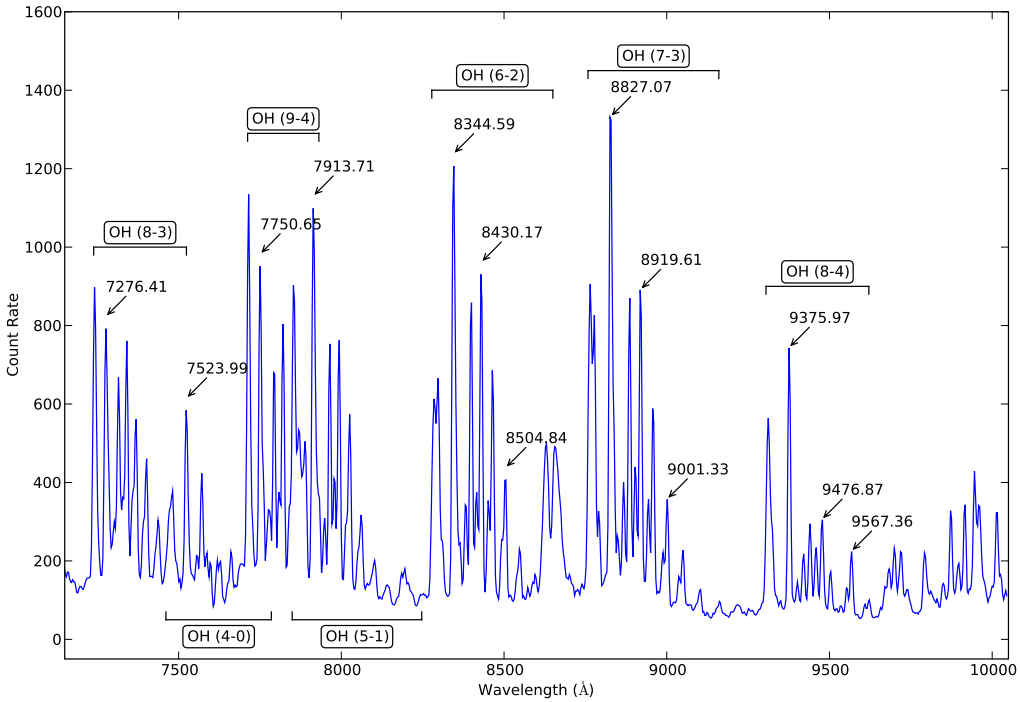

Figure 3.7: Example of sky lines used in the red spectra to find the wavelength solution. The most important transition bands are also labeled.

shows an example of sky spectra; some of the lines used in the wavelength calibration are also labeled.

3.3.5 Fiber-to-fiber response correction

Not all the fibers of the IFU have the same physical properties. In particular, the transmission can vary significantly from fiber to fiber. In addition, the path of the light through the spectrograph optics has an impact on the sensitivity. To correct for this, an exposure of a continuum, well-illuminated, and flat source is required, like a sky flat. The fiber-flat exposures taken during twilight were used to normalize the response of each fiber over the entire wavelength range, assuming that the light input to each fiber is uniform.

The sky flat exposure has to be reduced, tracing the location of each specrum, extracting, correcting the distorsions, and applying a wavelength solution, following the same steps as mentioned above. Then, a median spectrum is obtained using all the spectra in the frame. Finally, each spectrum is divided by this median one, obtaining a fiber-flat file. To correct for the differential transmission fiber-to-fiber, the science files must be divided by the fiber-flat one.

3.3.6 Flux-calibration

Flux calibration converts the count rate measured by the detector into the flux density collected by the telescope. A loss of flux is unavoidable while the light passes trough all the optical elements in the telescope and the instruments, so that an instrumental sensitivity function is needed. The Earths's atmosphere, depending on airmass A and wavelength λ, also absorbs part of the flux emitted from an object. The sensitivity function is obtained by observing a bright star with a well-known flux density[4] and comparing it with the measured count rate I_λ, that is to say, a measure of the ratio between the counts per second and the flux per second:

$$r_\lambda = \frac{I_\lambda}{f_\lambda \cdot t_{exp} \cdot 10^{0.4 \cdot A_V \cdot \kappa_\lambda}}$$

where A_V is the airmass and κ_λ is the extinction. For Calar Alto Observatory, the extinction has three main contributions (Sánchez et al., 2007a): the Rayleigh scattering at the atmospheric atoms and molecules, the extinction due to aerosol particles (mostly dust), and the extinction due to Ozone. Nevertheless, the last one has a marginal effect in the total extinction at any wavelength. Moreover, the Rayleigh scattering is almost constant along the year. Therefore, considering that the extinction in the V-band is due to a fix contribution or Rayleigh scattering and a variable contribution due to Aerosol extinction, the derived total extinction expression is:

$$\kappa_\lambda \sim 0.0935 \left(\frac{\lambda}{5450}\right)^{-4} + (0.8 * \kappa_V - 0.0935) \left(\frac{\lambda}{5450}\right)^{-0.8}$$

Therefore, it is only necessary to know the V-Band extinction for each night. This quantity is measured by the Calar Alto Extinction monitor (CAVEX) each night. The system is fully automatic, opening half an hour after the beginning of the astronomical night and closing an hour before its end, having a record of almost all nights. The extinction for a particular night can be obtained in CAVEX's Historic Page[5].

A star is a point source on the sky, but the image of the star is broadened due to the turbulence in the atmosphere and/or diffraction of the telescope optics. Fiber-fed spectrographs suffer light losses when the fibers are smaller than the seeing-disc and the calibration stars are not completely well centered in a single fiber. IFUs based on pure fiber-bundles like the PPak mode of PMAS (or INTEGRAL), have a filling-factor of 60%, which imposses flux losses, preventing a reliable absolute spectrophotometry. Nevertheless, this can be overcome

[4] Absolute flux calibrated tables of spectrophotometric standard stars can be found in the following web pages:
`ftp://ftp.stsci.edu/cdbs/current_calspec/`
`http://www.caha.es/pedraz/SSS/sss.html`
`http://www.eso.org/sci/observing/tools/standards/spectra/`

[5] `http://www.caha.es/CAVEX/HISTORIC/hcavex.php`

by performing a dithering of the standard star in order to cover the entire field-of-view (see section 3.3.8). The total count rate is measured by summing up all the fibers covering the standard star only.

First of all, it is necessary to have a reduce frame (following all the steps described above) and a final mosaic of a standard observed during the night, and extract a 1D spectrum. This can be done by using the E3D Visualization Tool[6]. This frame has to be free of cosmic ray hits.

In the case of the spectroscopic standard stars, we had only one science frame per pointing, so before performing the flux extraction it was necessary to clean for cosmic rays. We applied the code L.A. COSMIC written by van Dokkum (2001), using a Laplacian edge detection method. Two special versions of the code have been published, one for imaging data and another one for spectroscopic data[7], both written in CL IRAF programming language. Special care has to be taken because the spectroscopic version was designed for long-slit spectroscopic data. The algorithm tends to falsely detect cosmic rays in parts of the science frames with prominent emission lines. Thus, the parameters controlling the detection process are chosen in such a way that the number of false detected cosmic rays is reduced to minimum while the number of correct detected cosmic rays is maximized. The best set of parameters had been found by eye varying the parameters with respect to the default values until an acceptable result was achieved. Another task which we found to work well with this kind of data is the `lineclean` IRAF routine. We applied both methods to the standard star images and chose the best result for each case.

Once the frames are cleaned from cosmic rays, the 1D spectrum can be obtained with E3D. First, the sky must be subtracted. This is accomplished by selecting spaxels in areas clean of source. It is a good procedure to select the most external ring of spaxels of the frame. Then, the median sky spectrum is subtracted to the frame. Normally, in PPak data, only the most intense fiber is extracted, assuming that the star is well centered in a single fiber and that the size of the fiber is bigger than the seeing-disc. Nevertheless, these assumptions may not be right. Moreover, the PPak mode does not cover the entire FOV, having a filling factor of 60%, which imposses flux losses. The most extended approach to solve the problem is to determine a relative spectrophotometry, and recalibrate later using additional information, like broad-band photometry. Another approach is to perform a dithering of the standard star, as in the case of the science frames, covering all the FOV. Once the mosaic is sky-subtracted, spaxels with flux of the star must be selected. If using E3D to extract the flux, it is required to keep the number of selected fibers, n_{fib}, as E3D averages the spectra of them. To recover the total counts of the star, the 1D spectrum should be multiplied by n_{fib}, or include this in a *factor* parameter, which is the number of fibers divided by the exposure time. Finally,

[6]The development of the E3D was a primary goal of the European Commission's Euro3D Research Training Network

[7]`http://www.astro.yale.edu/dokkum/lacosmic/`

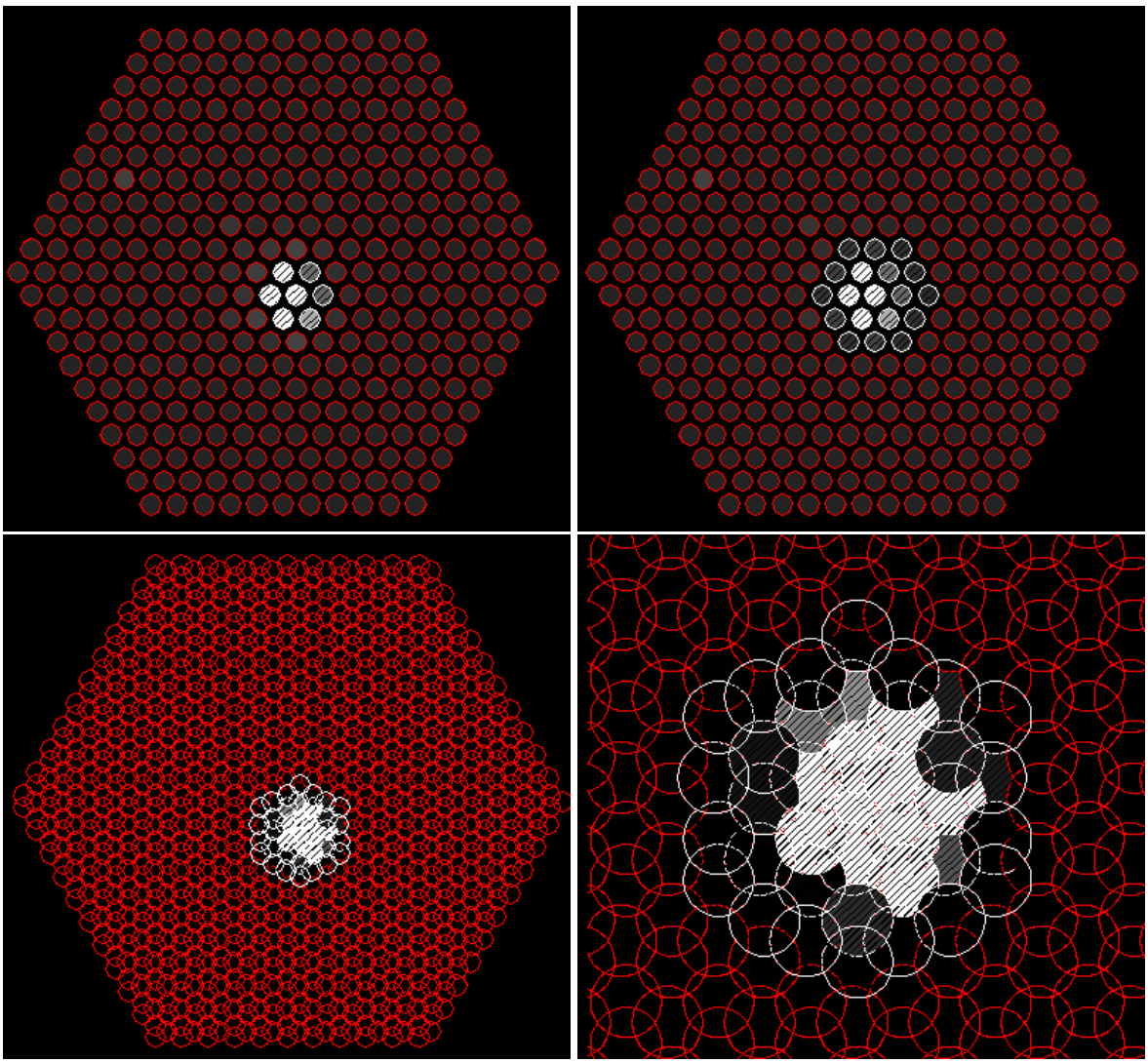

Figure 3.8: Examples of extraction of 1D spectrum of a standard star by selection of fibers in a one-pointing frame (upper figures) and in a mosaic of three exposures (lower figures). Note the space not covered by the fibers in the one-pointing frame. The central fiber is the most intense one in all cases. *Top left:* Selection of 7 fibers (one central + six-fibers ring) in a one pointing frame. *Top right:* Selection of 19 fibers (one central + six-fibers inner ring + twelve-fibers outer ring) in a one pointing frame. *Bottom left:* Selection of 37 fibers (one central + six-fibers inner ring + twelve-fibers middle ring + eighteen-fibers outer ring) in a mosaic of three exposures. *Bottom right:* Zoom of the bottom left image of the extraction of 37 fibers in a mosaic of three exposures.

the mosaic should be multiplied by this factor. If using R3D, this is automatically done if the *factor* is provided.

Figure 3.8 shows a practical example (using E3D) on the extraction of the 1D spectrum of a standard star by selection of fibers in a one-pointing frame (upper figures) and in a mosaic of three exposures (lower figures). Instead of selecting only the most intense fiber, several fibers can be added where the light of the standard star is spread. As seen in Figure 3.8,

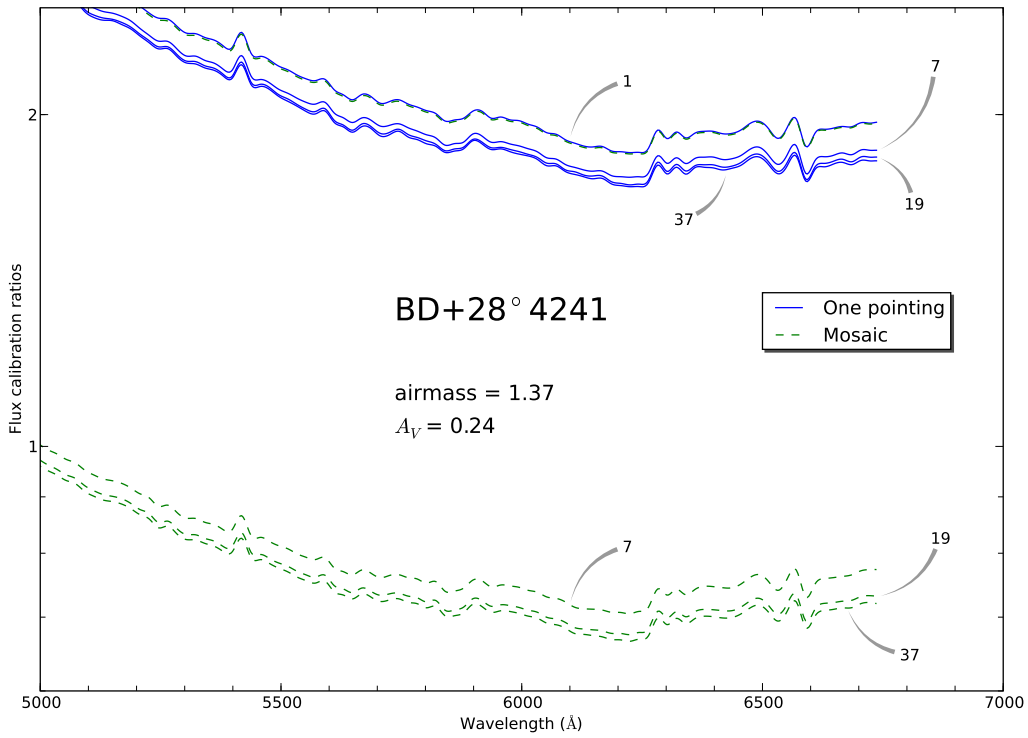

Figure 3.9: Flux ratios of the standard star BD+28°4211 for the flux calibration in the blue range. For the sake of clarity, only a fraction of the full wavelength coverage is shown. Solid (blue) lines represent flux ratios for the extraction of flux around the most intense fiber for 1, 7, 19 and 37 fibers in the case of a one-pointing frame. Dashed (green) lines represents flux ratios for the same number of extracted fibers in the case of a mosaic of three exposures. Numbers in each curve indicate the number of fibers used in the extraction for each curve. The flux ratio for the one-fiber extraction is the same in both cases since it corresponds to the same fiber.

the one-pointing frame of the standard star has space in between the fibers not covered by them. Although several fibers can be extracted, a significant flux could be lost. In the lower figures, selection of 37 fibers along concentric rings around the most intense fiber in a mosaic of three exposures shows how the placement of the fibers covers all the FOV. Adding all these fibers should recover most of the flux from the star.

The effect of flux losses when the IFU does not cover the entire FOV can be see in Figure 3.9. Solid (blue) lines represents flux ratios obtained from the extraction of flux around the most intense fiber for 1, 7, 19 and 37 fibers in the case of a one-pointing frame. The extraction is done in increasing concentric rings around the most intense fiber, as shown in Figure 3.8. Dashed (green) lines stand for the flux ratios for the same number of extracted fibers in the case of a mosaic of three exposures. The flux ratio curve for the one-fiber extraction curve is the same since corresponds to the same fiber. As is clearly seen, there is a big gap between the flux ratios for a one-pointing frame and a mosaic one. The mean difference is by more than a factor of 2.5. This confirms the flux losses and reliability of

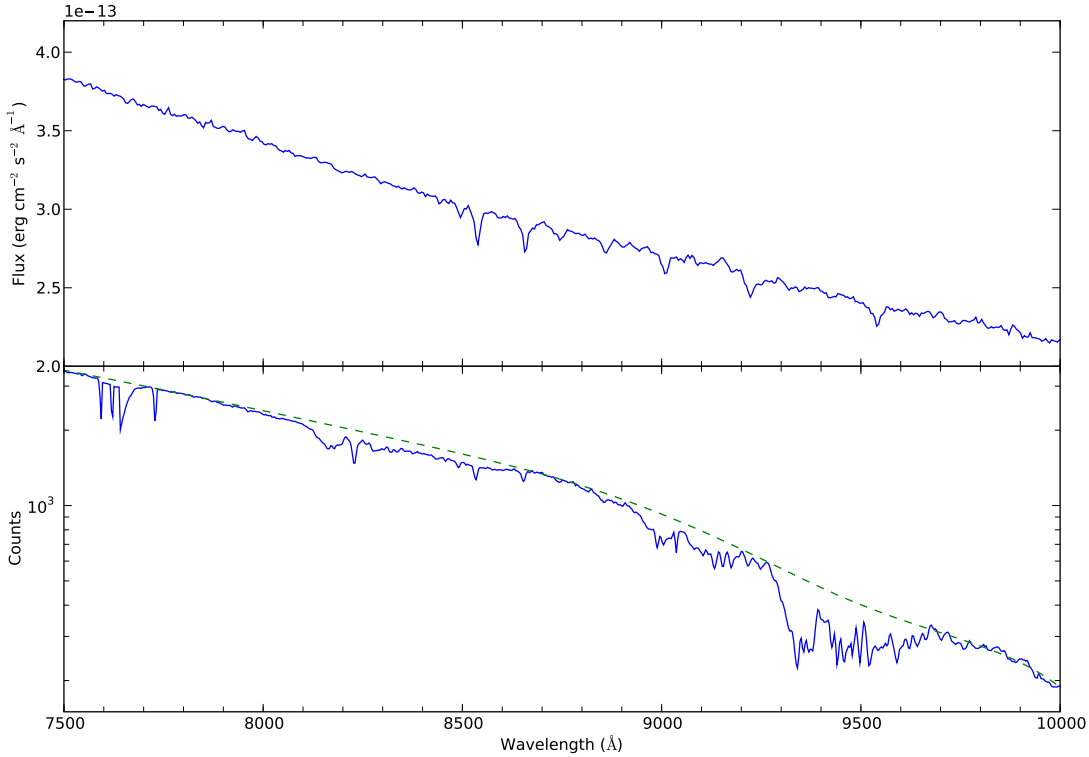

Figure 3.10: *Upper panel:* Spectrophotometric standard star BD+17°4708. *Bottom panel:* Solid (blue) line represents a extrated 1D spectrum of the star BD+17°4708 and dashed (green) line a smooth fit to the continuum. The atmospheric absorption features in the spectrum of the standard star are clearly seen along all the wavelength coverage. Notice the strong absorptions in the 8900 - 9700 Å range. The scale is logarithmic in order to enhance the mean features.

absolute flux calibration in IFUs with filling factors less than 1. Assuming that the point-spread function (PSF) of the star can be represented as a 2-dimensional Gaussian, it can be divided in increasing rings apertures. The maximum is in the center, while the external ring would have a minimum flux. Therefore, most of the flux would be concentrated in the first rings. In the case of the one-pointing frame, the gap between the first ring (the first fiber), and the second one (a ring of 6 fibers, as it can be seen in left upper panel of Figure 3.8), can hold a important fraction of the flux of the star. This effect is clearly seen in the jump of the flux ratio curve derived for a one fiber extraction to the 7 fibers one. Next rings would have less weight in the total flux, as seen in the convergence of curves from 7 up to 37 fibers, taking into account each case independently.

It is important to have a smooth final flux ratio curve. In general, this is accomplished by convolving the spectra with a Gaussian kernel to match solutions between the measured spectrum of the spectrophotometric standard star and its absolute value as obtained from tables, so that the final flux ratio (*i.e.* sensitivity function) is a continuous, smooth curve. Sometimes a smooth spline function of gaussian kernel is not enough, so another approach

is required. Before comparing the 1D count-rate spectrum with the flux table calibration it is advisable to fit a continuum curve to the spectra. This is specially important in the red part of the spectra (8000-11000 Å range), where absorption features from the atmosphere can depress some parts of the spectra, introducing spurious features in the continuum of the standard star, and therefore in the final flux ratio curve.

Figure 3.10 shows an example of the absorption effects in the spectrum of the standard star BD+17°4708. The upper panel shows the absolute flux distribution taken from the standard star table. Notice the almost absence of features in the continuum. The lower panel shows in solid (blue) line the 1D spectrum (in counts) extracted following the steps described above and in dashed (green) a fitted continuum. It can be clearly seen the strong atmospheric water-vapour absorptions bands along the spectrum, specially in the range were the sulphur emission lines [SIII] $\lambda\lambda$ 9069,9532 Å lines are located. The fitted continuum is then used to obtain the flux ratio between the counts and the flux calibrated table.

It is advisable to have several measurements of different standard stars along the night, or several exposures of the same star at different airmasses in order to have a representative sensitivity function. Then, an average sensitivity function is computed from those with the same instrumental setup. If the conditions of the atmosphere changed significantly from one star to another, a gray shift over the the sensitivity function can be performed. This is done by shifting the data so that the mean sensitivity of each star is the same as the star with the greatest mean sensitivity. This compensates for variable grey extinction due to clouds. Sometimes it is necessary to delete one star if its slope/shape is very different from others.

Unfortunately, our set of data had only one observation of a standard star per night, so we had to derive a flux ratio for each wavelength range only from one curve. Despite this fact, after flux calibration, in the overlapping region of the spectra taken for both setups, the agreement in the average continuum level in a fiber-to-fiber comparison was about 5 per cent.

3.3.7 Sky-subtraction

The emission from the Earth's atmosphere contributes to the detected signal. Sky emission lines can be easily identified in the RSS data as vertical lines. Many IFUs provide special fibers placed with an offset from the observed object to obtain a clear sky spectrum. When these fibers are not available or the target is surrounded by contaminating emission from adjacent objects, the usual method consists on taking an additional exposure of the nearby sky after or before the exposure of the target itself, bearing in mind that there should not be any significant contaminating emission from other sources. If the sky is derived form an external sky-frame, the sky subtraction should be performed after the flux calibration. If it is derived from the same dataset, the substraction can be done before. If the target does not fill all the FOV of the IFU, E3D can be used in a similar way as for the sky subtraction of

the spectrophotometric standard star frames.

All the corrections performed to the images, mentioned in precedent sections, do not correct for the differences in the shape of the emission lines along the cross-dispersion axis. This effect is also present in sky-subtracted spectra from long-slit spectroscopy, showing characteristic residuals in the location of the sky emission lines. This effect is more severe in fiber-based spectrographs, since the effective dispersion and shape of the emission lines varies fiber-to-fiber.

As mentioned in Section 3.2, PPak includes additional fibers that probe the sky far enough from the science FOV to avoid contamination by the astronomical object. One simple method to perform the sky subtraction is to extract all the 36 sky fibers, create a median sky spectra and substract it from the science exposures. Nevertheless, this does not take into account the distortion in the wavelength solution along the cross-dispersion. To increase the accuracy of the sky substraction, a second method can be applied. The routine `create_sky_ppak` determines the sky spectra corresponding to any science fiber by an interpolation of the spectra obtained through the sky lines. As the set of HII regions in our images presents an inhomogeneous distribution through the field of view of the IFU, we followed another method to derive a representation of the sky. The routine `create_sky_clip` creates an sky spectra by obtaining the median between a certain number of adjacent spectra, clipping those ones with a flux over a certain threshold of the standard deviation. The results from the last two methods are very close from each other in our case, with differences less than 3%. The use of one or other method depends on the nature of the science observations, so it is advisable to check both solutions. Both results create a better representation of the sky than the simple method, with less deep residuals, but still present. These residuals are specially strong in the red part of the spectrum (8000-11000 Å).

As seen in Section 3.1, the HII complex is located at the extreme of the NE arm of the galaxy. As the sky fibers surround the object, some of them might have some diffuse nebular emission from the end of the arm contaminating the sky spectra. We compared the flux of the Hα line in representative spectra with and without sky subtraction. The difference in the flux was negligible. This reliable, free of nebular emission, sky spectra was subtracted from the science frames.

3.3.8 Mosaics

As explained before, adjacent spectra in a RSS file may not correspond to spatially near positions, so it is important to reorder the spectra to their original position in the sky. A position table is required, relating the spectra to their locations in the sky. Then, is is possible to create a regular gridded data cube by interpolating the data spatially, and reconstruct the original image of the target at any wavelength. This step is needed if DAR correction is compulsory. If it is not the case, this step can be avoided and work with the RSS file and its

corresponding position table.

In the case of PMAS in the PPak mode it is necessary to interpolate at each wavelength the intensity at each spatial location in order to create a data cube in an artificial squared grid pattern. This can be done by using E3D or its complementary routines. Nevertheless, when performing dithering exposures to fill the holes between adjacent fibers to get a filling factor of 1, the procedure is slightly different and interpolation can be avoided. First, all the dithering exposures must be reassembled in a single RSS file. In the case of covering all the FOV, the exposures have to have certain overlap and the offsets between adjacent exposures had to be selected in a way that the overlap is complete between spectra. We used the routine `Mosaic_rss_overlap` of R3D to build a final RSS for each night which covered the entire FOV. As mentioned before, it is possible to construct the datacube without interpolating the data. This is accomplished by means of the *regularization* scheme, in which all the spectra result from the combination of measured values. A grid of a certain pixel scale, smaller than that of the original fibers[8] is constructed over the FOV, and for each pixel the spectrum that enters in it is averaged, obtaining a final datacube.

In the second night, when getting the exposures in the 7000-10100 Å range (GROT = -72), the de-rotator and guiding stopped at the second pointing of the dithering exposures[9], loosing the pointing for the second and the third dithering exposures. This prevents us to perform a mosaic covering all the FOV. We tried to recover the positions of the last dithering, but no good results where achieved in the last mosaic, so we ended with only the first dithering for the red part of the spectrum. Nevertheless, this is not important if only ratios are involved and absolute flux from emission lines are not needed. In section 3.4.8, we will see that this problem will not affect our results when dealing with integrated properties. The mosaic in the blue range was built without any problems. The final RSS blue mosaic contained 993 spectra (3×331), while the red RSS frame 331, since it is only the pointing for the first dithering exposure.

3.3.9 Correction for atmospheric absorption

In some cases, the absorption of the atmosphere is so strong that it can depress some emission lines, altering fluxes and ratios needed to obtain the physical properties of the target. This is specially important in the red range of the spectrum, namely from 8000 Å. We have followed the procedure described by Diaz et al. (1985) to remove the atmospheric water-vapour absorption bands in order to determine the strengths of the sulphur lines [SIII] $\lambda\lambda$ 9069,9532 Å. First, the fitted continuum to the standard star counts-spectrum is

[8] A pixel size of 1/3 of the original spaxel size is recommended. This value should also be used when interpolating to create datacubes when there are no dithering exposures or building maps for emission lines. In this case, a nearest neighbour interpolation is also recommended.

[9] It has to be taken into account that the dithering method in PPak is experimental, so the telescope does not record in the header any information of the offsets. These values have to be kept in the log of observations in order to build the mosaic.

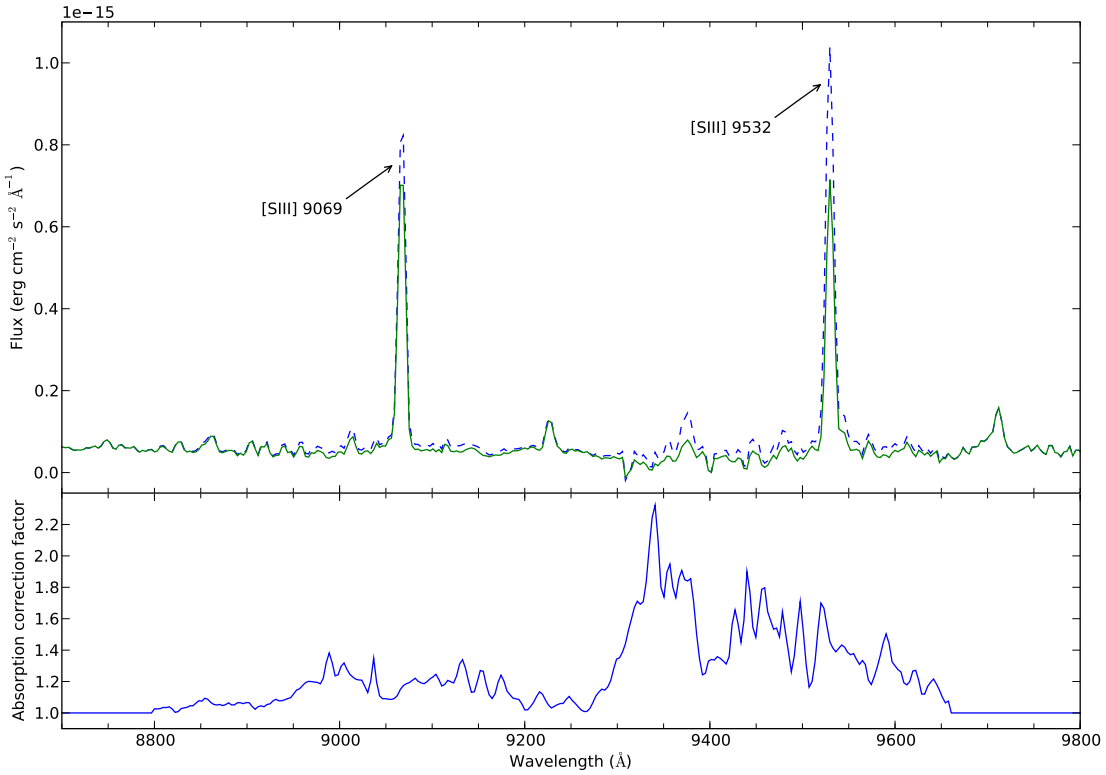

Figure 3.11: Correction for atmospheric water-vapour absorption bands. *Upper panel:* Spectrum from one intense fiber of the red RSS file of the object. Dashed (blue) line represents the corrected final spectrum and solid (green) line the uncorrected one. Sulphur lines [SIII] $\lambda\lambda$ 9069,9532 Å are labeled. *Bottom panel:* Absorption correction factor applied to the RSS file (see text for an explanation on how to obtain the correction factor).

divided by the original 1D spectrum with the absorption features. This creates a normalized correction spectrum, with values equal to unity when both continua are the same, and a value greater that 1 which indicates the absorption factor. The correction spectrum is set to one at all wavelengths except for the range in which the correction is going to be applied. Then, the final flux calibrated mosaic of the science target has to be multiplied by the correction spectrum. This correction should be applied *after* the flux calibration. To build the correction spectrum, the standard star closer in time and position in the sky to the science exposures is chosen, in order to ensure that the conditions of the atmosphere were similar[10].

Figure 3.11 shows an example of atmospheric absorption correction for a particular fiber of the RSS file of the object. In the lower panel, the absorption correction factor applied to all spectra in the red RSS is plotted, obtained as explained above. In the upper level, the solid (green) line represents the uncorrected spectrum for a particular intense fiber, while the dashed (blue) line is the spectrum after multiplying by the correction factor. The strong absorption is clearly seen particularly at 9300 Å with corrections around a factor

[10]The atmospheric absorption features change in shape and intensity along the night.

of 2. Taking into account that the theoretical ratio between the sulphur lines is I(9532Å) $\simeq$ 2.44 · I(9069Å), it is immediately obvious that the intensity of the [SIII] 9532Å line is heavily cut up by atmospheric absorptions bands, since both sulphur lines are of the same intensity before correction. After applying the correction factor both lines are pushed to higher intensities. Nevertheless, the total intensity of the 9532 Å line is not recovered, since the ratio between them is still well below the theoretical one. This ratio is not accomplished at any fiber, meaning that the absorption in the range from 9300 Å is stronger. Thus, we must rely on the 9069Å line when deriving temperatures or using empirical calibrators, applying the theoretical ratio to obtain the intensity of the 9532 Å line. Taking into account the low correction factors obtained near the location of the 9069 Å line, we can assume that the intensity recovered is good to an estimated accuracy of about 7 per cent.

3.3.10 Correction for differential atmospheric refration

The refraction of light by the Earth's atmosphere is wavelength-dependent. This effect is called differential atmospheric refraction (DAR), and results in the image of an object to appear at different positions in the telescope focal plane depending on the wavelength of observation. The amplitude of the shift due to DAR is a function of zenith distance, causing that the red and blue ends of an object spectrum will appear at different spatial positions. The effect is important when *fiber-to-fiber* intensities of different wavelengths are combined, but negligible if spatially integrated intensities are used.

IFUs have the advantage over traditional long-slit spectroscopy of determining and correcting for DAR (Arribas et al., 1999), once the data is totally reduced and converted to datacube format. Any DAR correction requires to resample the data spatially, which produces a loss of the initial spatial configuration of the spaxels, changing from one spectrum (wavelength versus flux) per spaxel (spatial coordinate) to a 2D flux image at each wavelength point.

There are several ways of correcting for DAR. One approach is to apply a theoretical correction based on the Filippenko (1982) formulae, in which an image offset vector for each wavelength bin is used[11]. Each image, at every wavelength, is thereafter shifted with respect to a pre-defined reference wavelength, using a (fractional) bi-linear interpolation procedure. Doing this the intensity in each spaxel becomes a function of four spaxels - introducing an unavoidable smoothing. Nevertheless, in many cases the empirical correction works better than the theoretical one. The reason is that theory assumes that the layers of the atmosphere with equal refration index are flat an perpendicular to the zenith of the telescope. However, it is known that this is only a first order approximation, since these layers depend strongly on the orography of the observatory.

[11] Parallactic angle (orientation of the IFU with respect to the downward direction), and physical conditions at the time of the observations like humidity, pressure, and temperature are needed.

The empirical DAR correction is performed by tracing the intensity peak of a reference object in the FOV, like a star or an unresolved point source (*i.e.* cluster or nucleus of a type I AGN). Thus, the effect of the DAR can be easily measured by fitting a two-dimensional Gaussian function to each narrow-band image of the datacube to the bright point source to determine the centroid position. This can be done by using the `imcntr` task in IRAF. A medium-order polynomial function (3 to 5 is usually enough) is fitted to the distribution of the centroid coordinates as a function of wavelength, giving the relative shifts in right ascension and declination (that is to say, shifts in x and y pixel coordinates) for each slide. When fitting a polynomial function to the centroid coordinates, it is important to introduce some kind of rejection limits below and above the fit according to the residual sigma, in the same way as when fitting a continuum to the 1D spectrum of a standard star in the flux calibration procedure. This avoids bad fits due to errors in the centroid measurement or common artifacts at the edges of the resampled images. The measured offsets are used to shift each spectral image of the datacube to a common centroid position. The shift is estimated from the difference between the polynomial-fit coordinates and the fixed one. The `imshift` task in IRAF can be used to perform the relative shifts to each image. It has to be stressed that using empirical correction for DAR is only possible if a point source in the FOV is available.

There are several factors which determine the extent of effects for DAR. Among the most important ones are the airmass and the geometrical size of the spaxels. In effect, the smaller the spaxels the more of the flux at different wavelengths end up on separate spaxels. As described before, the fibers on the PPak IFU are circular, of $2\farcs68$ diameter, and are separated by $3\farcs6$. On the other hand, DAR effects become important for large airmasses, with values greater than 1.1. The fact that all our observations were obtained at airmasses lower than the nominal value, combined with the large size of the fibers on the PPak IFU, allows us to neglect DAR corrections.

To check the last statement, we transformed the blue RSS file to a datacube format, and we measured the centroid coordinates of a star in the FOV. The results are presented in Figure 3.12. The estimated centroid coordinates are plotted as a function of wavelength. The red line represents a polynomial fit to the distribution. As it can be seen, the position does not change significantly along the whole wavelength range, implying that the DAR effect is negligible. This allows us to work with RSS files, which are more friendly in terms of data analysis, and avoids to transform it to datacube format, which would impose an inevitable interpolation of the data in single ditherings (as in the case of the red data).

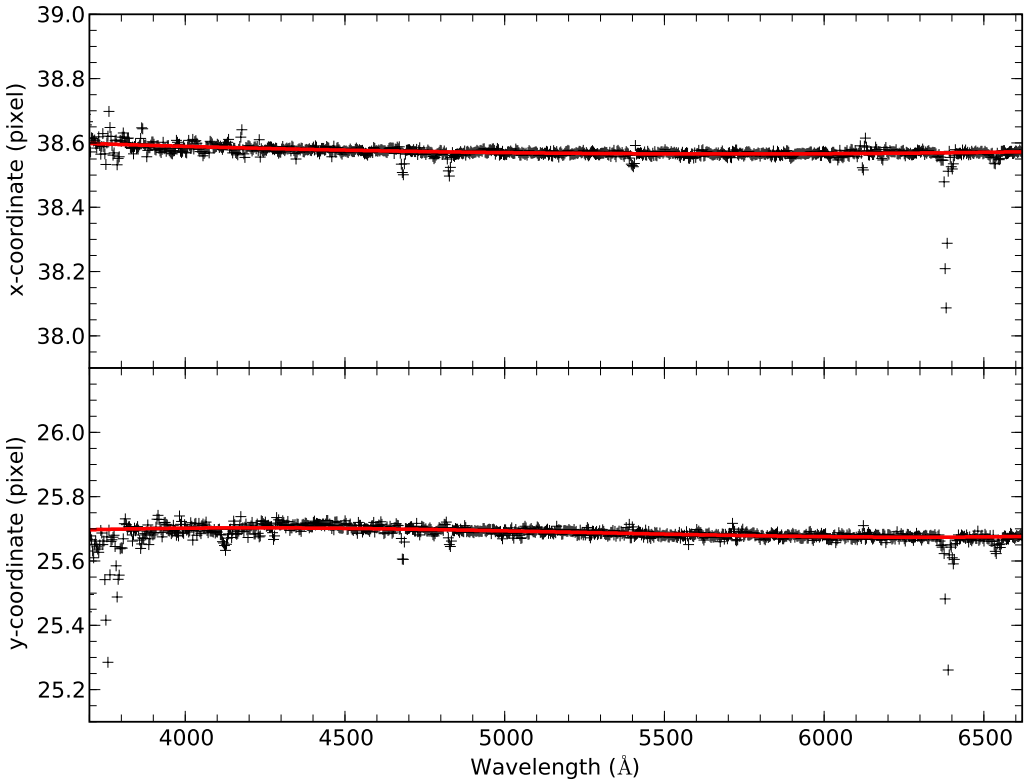

Figure 3.12: Example of the DAR correction for the blue datacube. The estimated centroid coordinates of a point source in the FOV are plotted as a function of wavelength in x direction (upper panel) and y coordinate (lower panel). The crosses correspond to the measurements in the datacube, where the red line denote a polynomial fit to the distribution.

3.4 Results

3.4.1 Subtraction of the underlying population

Underlying stellar populations in starburst galaxies have several effects in the measurement of the emission lines produced by the ionized gas. Firstly, since they contribute to the continuum of the galaxy, the measurement of the equivalent widths of the emission lines is not a trustable estimator of the age of the ionizing stellar population (Terlevich et al., 2004). Secondly, the presence of a conspicuous underlying stellar population depresses the Balmer and Paschen emission lines and do not allow to measure their fluxes with an acceptable accuracy (Diaz, 1988). This can affect all the properties derived from the relative intensities to the flux of these recombination lines, like the reddening or the ionic abundances. In the case of helium recombination lines, this effect is present too, complicating the derivation of the helium abundance (Olive and Skillman, 2001).

FIT3D (Sánchez et al., 2006) is a package to fit and deblend emission lines which can handle both RSS images and datacubes. It includes several spectral synthesis routines to fit

simple stellar populations (SSPs, or instantaneous burst) synthetic spectra to the continuum of the object and subtract the underlying population, giving a final spectra which, in theory, should only contain the gas emission spectra. Each spectrum from the IFU sample is fitted with synthetic SSP models. As explained in Sánchez et al. (2007b), models were created using the GISSEL code (Bruzual and Charlot, 2003), assuming a Salpeter IMF, for different ages and metallicities. FIT3D has 72 models covering a discrete grid of 12 ages (5, 25, 100, 290, 640 Myr, 0.9, 1.4, 2.5, 5, 11, 13 and 17 Gyr), and six metallicities (Z = 0.0001, 0.0004, 0.004, 0.008, 0.02 and 0.05). In order to reduce the number of free parameters, we only used a template of 3 metallicities, namely 0.02, 0.008 and 0.004, with the whole set of ages. The set of metallicities were chosen to have an interval which contained the published metallicity of the region. Each spectrum then was fitted to each of the 36 models. FIT3D re-samples the model to the resolution of the data, convolves it with a certain velocity dispersion, and scales it to match the data set by a χ^2 minimization scheme. In order to fit the continuum, it is necessary to create a mask file giving wavelength intervals of the spectra containing emission lines, features (Wolf-Rayet bumps), and strong residuals from the sky subtraction and other artifacts. We only performed the fitting on the blue mosaic, *i.e.*, only the spectral region at wavelengths bluer than 7000 Å was used. At redder wavelengths the strong nightsky emission lines and the telluric absorptions have strong residuals, so they were masked. Nevertheless, the absorption of the underlying population to the emission lines in the red spectral region is negligible.

To illustrate the fit results, we show in the upper panels of Figure 3.13 the spectrum of the spaxel 635 (green line) with the best fit found by FIT3D (blue line) in the ranges 4200-5100 Å and 6150-6850 Å. The measured intensities of the most prominent Balmer emission lines of the subtracted spectrum (free of underlying population) result within the errors as compared with some test measurements using `splot` from IRAF, adopting a pseudo-continuum as explained in Hägele et al. (2006). In both upper panels of Figure 3.13 we can appreciate that small errors in the fit of the underlying stellar population could become a great unquantifiable error in the emission line fluxes of the fainter emission lines. Nevertheless, for the strongest emission lines, the differences between the measurements done after the subtraction of the FIT3D fit and those using the pseudo-continuum approximation are well below the observational errors, giving almost the same result. It must be highlighted that in this type of objects the absorption lines, used to fit the underlying stellar populations, are mostly affected by the presence of emission lines. There are a few that are not affected, such as some calcium and magnesium absorption lines. To make the FIT3D fit it is necessary to mask the contaminated lines, thus the fit is based on the continuum shape and takes into account only a few absorption lines. Hence, it is not surprising that the FIT3D results are not so good for this kind of objects. This result can be extended to other fitting codes such us STARLIGHT. It must be noted too that this methodology is very advantageous for statistical and comparative studies and when dealing with a large number of spectra, as in

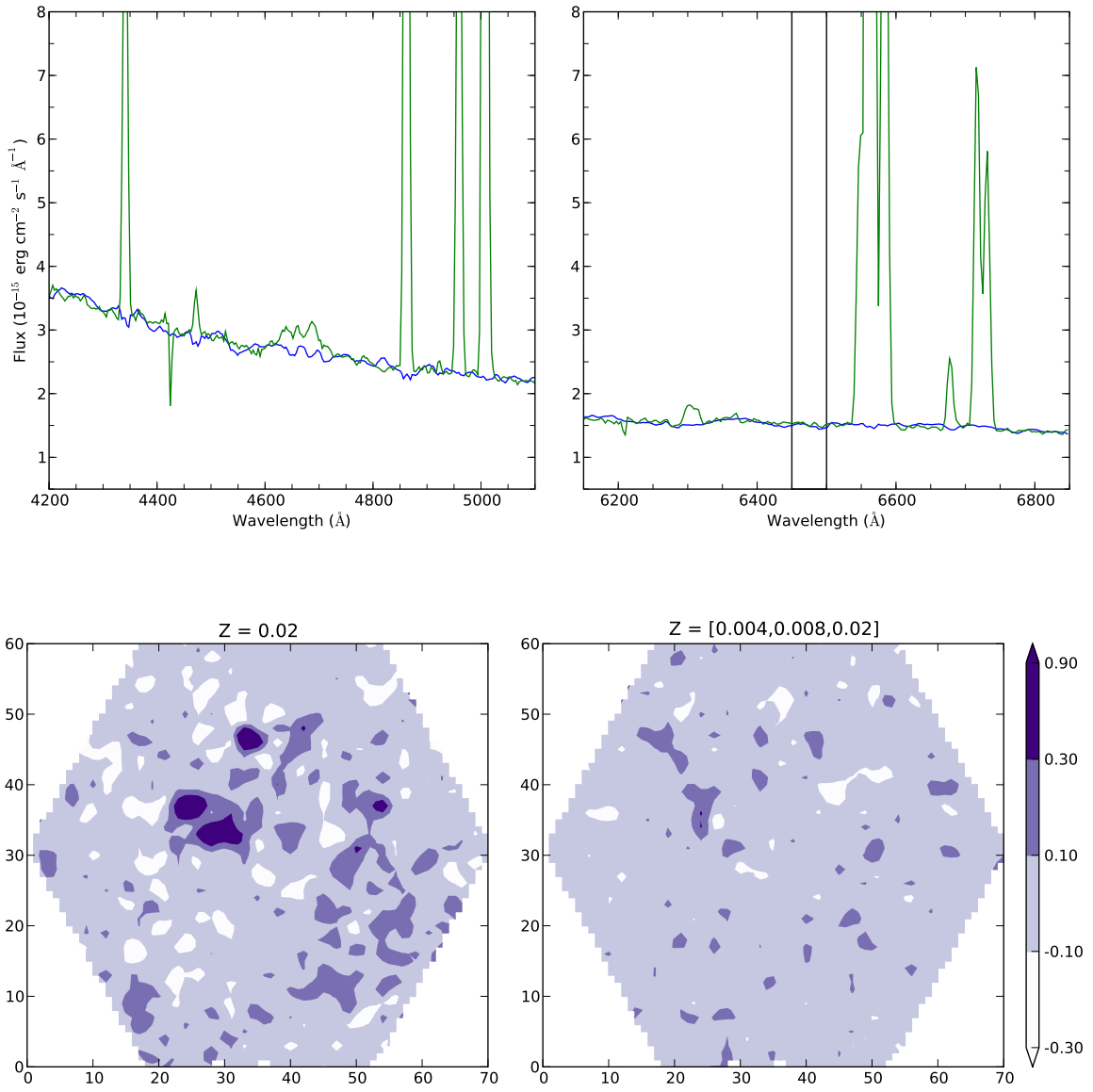

Figure 3.13: Two regions of the blue spectrum together with the best spectral fitting (upper panels) and maps of residuals in the continuum fitting for two sets of metallicity templates (lower panels). Each metallicity covers a discrete grid of 12 ages (see text). *Upper left panel:* Spectra of the spaxel 635 of the blue RSS file (green line) in the spectral range 4200 - 5100 Å, together with the spectral best fit (blue line) of the continuum using FIT3D. *Upper right panel:* Spectra of the same spaxel (green line) in the spectral range 6150 - 6850 Å, together with the spectral fit (blue line). The vertical lines in the range 6450-6500 Å delimit the range used for creating the maps of the residuals. *Lower left panel:* Residual map for the spectral range 6450-6500 Å for a template with solar metallicity. *Lower right panel:* Residual map for a template with metallicities 0.004, 0.008, and 0.02 in the same spectral range. This map has been created using the results from the fits shown in the upper panels.

the case of IFUs. These kind of studies only consider the results derived from the strongest emission lines which have small proportional errors. However, we must be careful when the aim of the work is the detailed and precise study since the errors introduced by the fitting are higher for the weakest lines, including the auroral ones.

We have produced good continuum fits for each of the 993 spectra in the blue mosaic wavelength range. This can be checked by creating maps (see section 3.4.2) of several regions (free of emission lines) of the continuum after model subtraction. In other words, this kind of maps are plots of the fit residuals, since the subtracted spectrum should be around zero in the continuum, except for the emission lines. The fit residuals can be spatially checked creating a map with the values obtained by adding the contribution of a small interval of the continuum near an emission line for each spectrum (spaxel) in the RSS file. Two vertical lines in the upper right panel of Figure 3.13 show the interval used for the maps of the residuals plotted in the lower panels. The lower left panel represents the residual map in the spectral range 6450-6500 Å (near the emission lines of HII and [NII] $\lambda\lambda$ 6548,6584 Å) for a fit to the continuum using a template with only solar metallicity and a grid of 12 ages, as explained before. The lower right panel shows the residual map for a template with metallicities 0.004, 0.008, and 0.02 in the same spectral range and same grid of ages. Two wavelength ranges of the fit used to create the last map can be seen in the upper panels. Whenever the fit is good, the sum over the small wavelength interval should be around zero. As it can be seen, the map for a template with a single (solar) metallicity (lower left panel) gives higher residuals than using the three-metallicities template (lower right panel). In the last one, the colormap shows a very uniform distribution with almost all the values contained between -0.1 and 0.1, and only a few regions with larger deviations. On the contrary, the former map has several regions with strong differences between the continuum and the fit, reaching values as high as 0.9 (notice that top values in the other map are below 0.3). It must be noted that the deviations are related with spatial regions with strong emission, usually correlated with the intense knots. The shape of the continuum near these zones cannot be properly matched with one metallicity template alone, so a combination of them are needed. The best fit using the lowest number of metallicities was using a combination of 0.004, 0.008 and 0.02.

3.4.2 Line intensities

As mentioned in last subsection, FIT3D is a package to fit and deblend emission lines. Using this software, we fitted line profiles on each of the 993 blue spectra and 331 red spectra in order to derive the integrated flux of each emission line. The program fits the data with a given model computing a minimization of the reduced χ^2 and using a modified Levenberg-Marquardt algorithm. The data is provided through a configuration file where the model is described. The functions available to built the model are a one dimensional gaussian, a N-order polynomial function and a spectrum background. A single Gaussian was fitted to each

emission line, using a low order polynomial function to describe the continuum emission. Instead of fitting the entire wavelength range in a row, we used shorter wavelength ranges for each spectrum that sampled one or a few of the analyzed emission lines. For example, an interval of 4800 to 5100 Å was used for measuring Hβ and [OIII] $\lambda\lambda$ 4959,5007 Å. This ensures a characterization of the continuum with the most simple polynomial function, and a way to simplify the fitting procedure. The software also allows definition of emission line systems. This linking method is useful to fit lines that share some properties (*e.g.*, lines that are kinematically coupled with the same width) or include lines whose line ratio is known (*e.g.*, the line ratio between [OIII] λ 5007 Å and [OIII] λ 5007 Å). This was essential for accurate deblending of the lines, when necessary. Following Gonzalez-Delgado et al. (1994), Castellanos et al. (2002) and Pérez-Montero and Díaz (2003), the statistical errors associated with the observed emission fluxes have been calculated using the expression:

$$\sigma_l = \sigma_c \sqrt{N \left(1 + \frac{EW}{N\Delta}\right)}$$

where σ_l is the error in the observed line flux, σ_c represents the standard deviation in a box near the measured emission line and stands for the error in the continuum placement, N is the number of pixels used in the measurement of the line flux, EW is the line equivalent width of the line, and Δ is the wavelength dispersion in Å per pixel. This expression takes into account the error in the continuum and the photon count statistics of the emission line.

The procedure of fitting all desired emission lines has the advantage of creating flux maps of any line with the continuum subtracted. This is not the case of narrow-band imaging, where a careful cleaning method has to be applied to obtain free-continuum images. Moreover, sometimes these narrow-band images include more than one line (*e.g.*, Hα, the [NII] $\lambda\lambda$ 6548,6584 Å doublet or the [SII] $\lambda\lambda$ 6717,6731 Å doublet), reducing its usability to study the basic parameters of the ionized gas. This another advantage of using IFU data.

In order to handle the data obtained from FIT3D and analyze them, we have built two python modules called `pyfit3D` and `pyabund`. The combination of both modules allows to create maps from emission line measurements and clipping the data according to a certain value. This is useful if there are data that needs masking, as in the case when errors in the flux measurement or in the ratios from a combination of several lines are too high. The first module also contains a general routine for automatic measurement of flux emission lines for *fits* files of any dimension, in particular for RSS files. It is based on the `ngaussfit` task from IRAF. We have measured the Hα flux in the blue RSS with the `pyfit3D` task. The comparison of these results with the ones obtained with FIT3D gives the same flux measurement for each spaxel, within the errors. This is not suprising since both codes uses a similar algorithm for fitting lines. The module `pyabund` also contains a routine which performs the abundance analysis and estimates the physical properties from a table which contains the flux line measurements and their corresponding errors.

Creating maps

Maps are data files stored in 2D fits files, reflecting the original arrangement of the spaxels in the sky. In the case of non regularly gridded IFU or RSS files, it is necessary to interpole the data, as mentioned in previous sections. We have used `interpol` routine from E3D with a nearest neighbour interpolation, a grid parameter[12] of 10^{-12} and a pixel size of $1''$, close to the recommended 1/3 of the original spaxel size. All the maps shown in next sections, unless mentioned, have a North *down* and East left orientation, and a $1''$/pixel scale. A distance of 5.9 Mpc to NGC 6946 is assumed, so $1''$ in the sky corresponds to 28.6 pc.

We have masked all values in the maps with relative errors $\geq 25\%$. This is applied to any quantity: flux, ratio or combination of lines used in empirical parameters.

3.4.3 Hα maps and morphology

From figure 3.14 it is clear that the morphology of the complex of HII regions is well recovered from the IFU data. The upper panel is an Hα flux map created from the RSS blue data as explained in section 3.4.2. The masked values follow the criteria explained in that section, as well as the orientation (north *down*, east left). The lower panel shows an Hα (not continuum-subtracted) image taken at the Kitt Peak National Observatory (KPNO) 2.1-meter telescope (same source as Figure 3.3) showing the PPak field and with the same orientation as the map of the upper panel.

Hodge and Kennicutt (1983) catalogued more than 10000 HII regions in 125 galaxies. This HK catalog contains 540 identified HII regions in NGC 6946. We have labelled all the important knots following the HK identification. As it can be seen in the Hα map, only the most intense knots are clearly defined, and for this reason we have labelled them with the first four alphabetical letters. Interestingly, is not identified in Hodge and Kennicutt (1983). Since they have enough signal-to-noise, we will present the main measured properties of these four knots when discussing the integrated properties in section 3.4.8. It has to be remarked that the lower panel image has not been continuum-subtracted, so some knots are seen more intense since their continuum sources are included in the image, but their Hα emission is not so strong. This is the case of knots HK83-013, HK83-014, HK83-009 and HK83-006.

Figure 3.15 shows the continuum emission near Hα (*top*) and Hβ (*bottom*) maps together with the corresponding emission line intensity isocontours overplotted, while Figure 3.16 shows the continuum emission map near 8500 Å together with the Hα isocontours overplotted as reference. The red continuum comes from the first pointing. Maps of the continua are representative of the stellar emission, free of contamination from the gaseous emission lines. From the Hα and Hβ isocontours it can be seen that both emission structures are quite similar, with the four main intense knots (A, B, C and, D) well demarcated. The bightest

[12]The grid parameter represents the resolution of the triangulation.

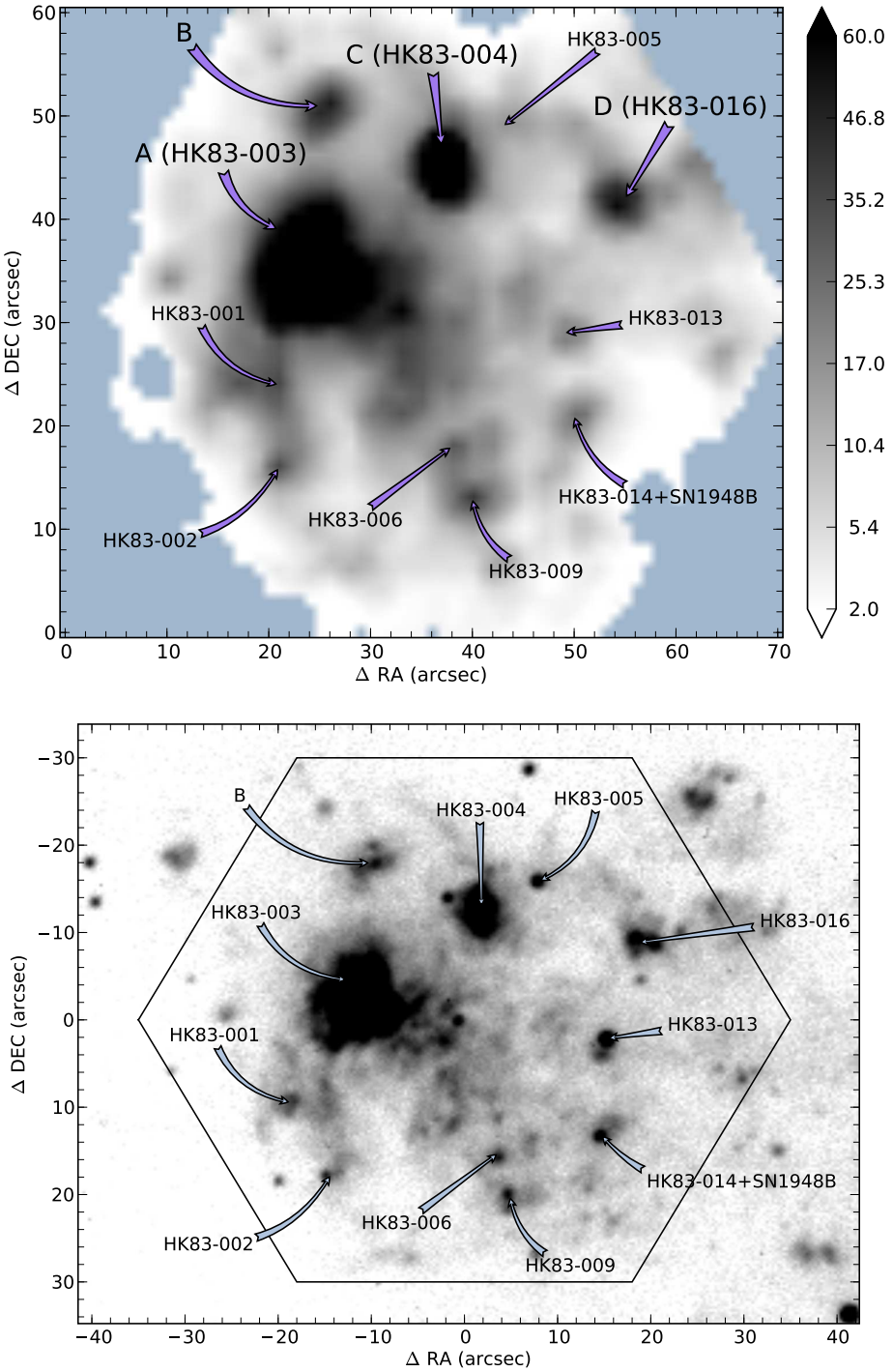

Figure 3.14: *Upper panel:* Hα flux map (not corrected for reddening) obtained from the IFU data. The scale bar (valid only for the upper panel) is given in units of 10^{-16} erg s^{-1} cm^{-2}. North is *down* and east is left. The masked values follow the criteria explained in section 3.4.2. *Lower panel:* Hα image taken at the Kitt Peak National Observatory (KPNO) 2.1-meter telescope (same source as Figure 3.3). The image has not been continuum-subtracted. The hexagon shows the position of the PPak FOV. The orientation is the same as the image of the upper panel. The most important knots are labelled following the identification by Hodge and Kennicutt (1983). The four main intense knots are also labelled with the first alphabet letters. Knot B is not identified in Hodge and Kennicutt (1983).

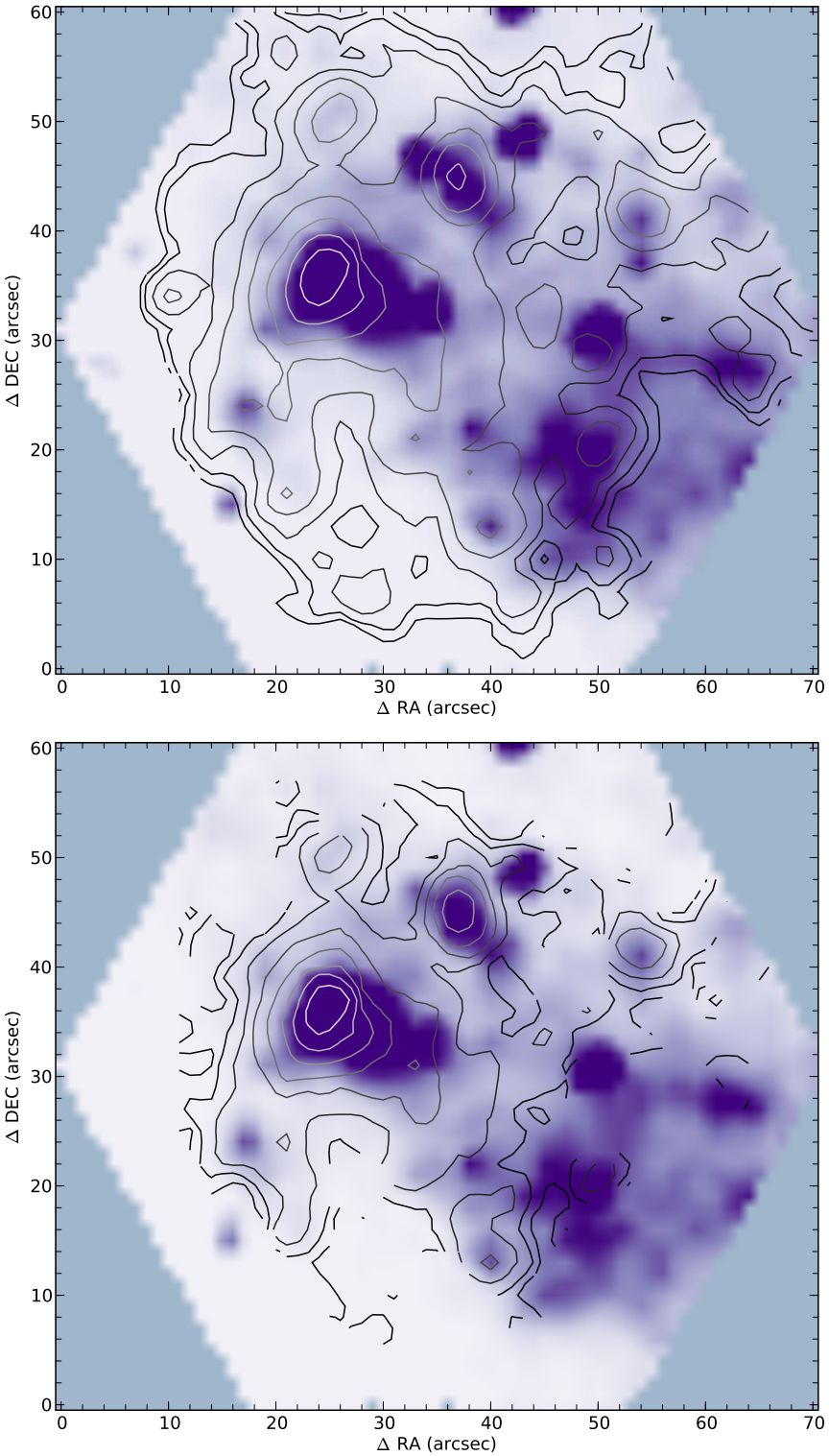

Figure 3.15: Maps in the continuum near Hα (*top*) and Hβ (*bottom*) emission lines together with the isocontours of the corresponding emission line flux overplotted. Maps are displayed in linear scale, while isocontours are in logarithmic scale. Contours are masked according to their emission line flux.

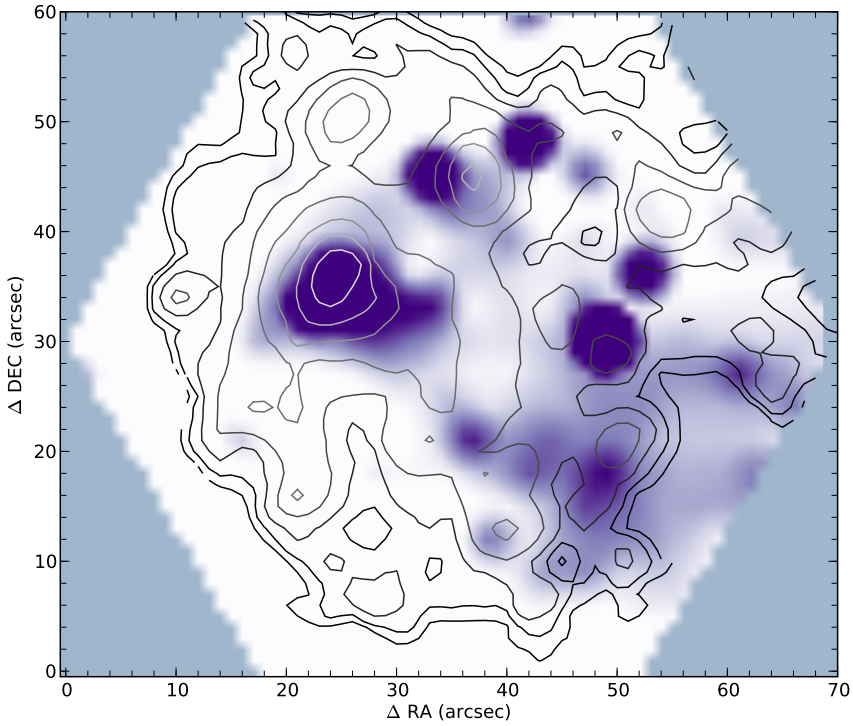

Figure 3.16: Maps in the continuum near 8500 Å together with the isocontours of Hα overplotted. Map displayed in linear scale, while the isocontour in logarithmic scale. Contours are masked accordingly to their emission line flux. The continuum map source comes from the (red) first pointing.

knot, A, has the most extended structure, with a tail pointing to the north-west. This structure seems to be formed following the continua morphology. There are not many differences between the continuum maps of Hα and Hβ. The peak intensity of the continuum in knot A corresponds to the same position in both emission line maps. From the continuum emission, it can be seen that the structure of knot A defines that of the Hα map, with a small concentration to the west of the knot, probably being the source of the north-west tail of this knot.

Although the rest of knots have their equivalence between their emission line maps and continua, their maximum position is not the same. A remarkable structure is the one of knot C, which has an elongated continuum in a south-east to north-west direction, while the emission line morphology is egg-like (ellipsoidal). The continua structure near this knot has associated the HK83-005 identification, but in our emission line maps it has only a little tail that is hardly seen.

The other way around happens to knot B. Although in the emission line maps it is seen some structure, in the continuum maps only a weak contribution is present. Knot D has a clear correspondence between the continuum and the Hα emission.

Interestingly, knots HK83-013 and HK83-014 have strong continuum contribution, but

very low Hα and Hβ emission, and their emission peaks have an offset as compared to their respective continua. This effect may be due to the fact that the underlying population of these knots is slightly older. Note that knot HK83-014 has a supernova associated.

As for the continuum emission near 8500 Å of Figure 3.16, the morphology is very similar to that of the blue part of Figure 3.15. In fact, the continuum peak of the most important knots in the red matches the ones from the blue. In some structures, the intensity of the red continuum is more marked, as the case of the source between knots HK83-013 and HK83-016.

Nevertheless, the overall continuum morphology of the whole region matches the one of the emission line maps, where the complex extends through the west region of the FOV, while the surroundings of the east (south and north) region have very low surface brightness. This is clear in Figure 3.3, where it is seen that the region is located at the end of the NE arm of NGC 6946.

3.4.4 Reddening correction and c(Hβ) map

We have used the value of the Balmer decrement derived from Hα/Hβ to estimate the reddening coefficient, c(Hβ) for each fiber spectrum. The HI series are used to determine the extinction, comparing the observed line ratios with the expected theoretical values. Case B (optically thick in all the Lyman lines) is the best simple approximation to describe the physical conditions in the ionization of the gas. This method takes advantage of the fact that the ratio between the emissivities of two hydrogen recombination lines, which depends on electron temperature and density, is almost constant. As an example, the ratio between the emissivity of Hα and Hβ is 2.86 for the case B with $n_e = 100\ cm^{-3}$ and $T_e = 10000$ K, and this value varies less than 10% in the range of interest of temperatures and densities for an HII region. Although the variation of these values is small, we have used an iterative method to estimate them, taking as starting values those derived from the measured [SII] $\lambda\lambda$ 6717,6731 Å and [OIII] $\lambda\lambda$ 4959,5007 Å. The theoretical values have been calculated based on the data by Storey and Hummer (1995). We have used a mean value of $n_e = 10^2\ cm^{-3}$ and $T_e = 8000$ K as characteristic values for the region to obtain the reddening map and the extinction law given by Cardelli et al. (1989) with $R_V = 3.1$.

Normally, all the available Balmer lines are used to estimate c(Hβ), an then a least square fit of the measured ratios, F(λ)/F(Hβ), to the theoretical ones is performed. Nevertheless, Hγ and Hδ lines have very low signal-to-noise in zones of low surface brightness, and are very difficult to measure for automatic fitting routines, yielding high uncertainties in the computed c(Hβ) value. Thus, we have used only the ratio Hα/Hβ to derive the extinction, since these two lines are very easily detected and measured. See Appendix A for a detailed explanation on the reddening correction and equations involved in the relation between c(Hβ) and the visual extinction A_V.

The reddening map, computed as explained above, is shown in Figure 3.17. The mean

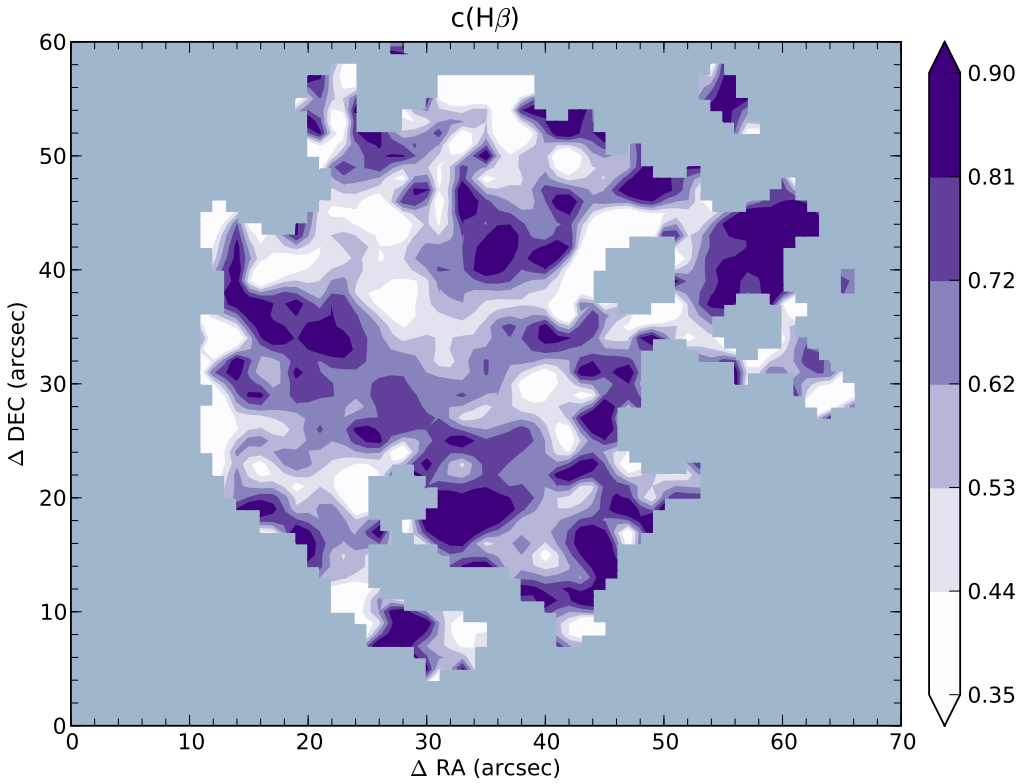

Figure 3.17: c(Hβ) map derived comparing the measured Hα/Hβ line ration map with the calculated for case B recombination, and assuming the Cardelli et al. (1989) extinction law.

and standard deviation for c(Hβ) over the FOV is 0.61 $\pm$ 0.19. In this, we are assuming a significant amount of reddening comes from a Galactic foreground screen. As mentioned before, the galaxy is located at a relative low Galactic latitude, and it has slightly more than one magnitude visual extinction, which is around 0.4 in terms of c(Hβ) (see Appendix A for details on conversions). Our mean value is remarkably close to the value found by Ferguson et al. (1998) for knot D (HK16 or FGW 6946B in their identification) of 0.68 $\pm$ 0.11. The reddening distribution is consistent with the distribution of the main four knots, where these knots exhibit high values of extinction. Interestingly, high values are also found in the north-west side of knot A, not correlating with any important feature in continua or emission line maps. It is also remarkable a "stream" of low reddening values which goes in east-west direction between knot A and the other 3 knots.

For each fiber spectrum we derived its corresponding reddening coefficient and all fluxes of the emission lines (for each fiber) were corrected for extinction using their corresponding c(Hβ) value, which is an important point when deriving the ionization structure and physical-chemical parameters.

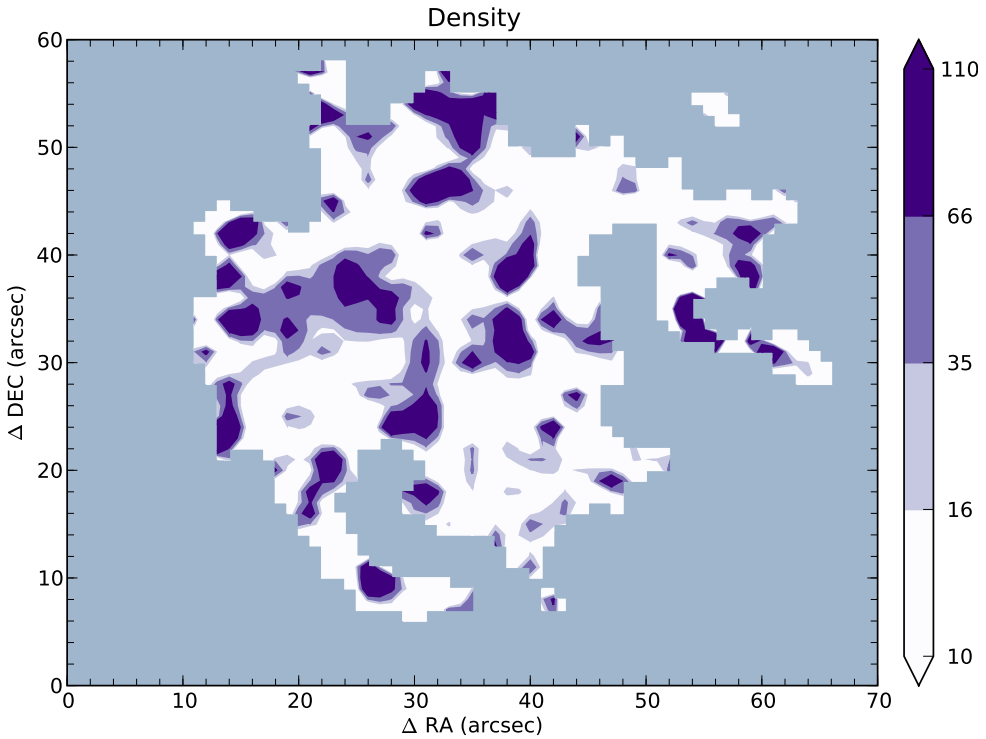

Figure 3.18: Map of the electron density, n_e, calculated from the ratio of [SII] $\lambda\lambda$ 6717,6731 Å lines. The scale is in units of cm^{-3}.

3.4.5 Electron density

The electron density of the ionized gas, and other physical conditions (such as temperatures when available), have been derived from the emission line data using the same procedures as in Pérez-Montero and Díaz (2003), based on the five-level statistical equilibrium atom approximation in the task `temden`, of the software package IRAF (De Robertis et al., 1987; Shaw and Dufour, 1995). See Appendix B for a detailed description of the relations of the physical conditions of the gas and ionic abundances. We have taken as sources of error the uncertainties associated with the measurement of the emission-line fluxes and the reddening correction, and we have propagated them through our calculations.

Figure 3.18 shows a plot of the spatial variation of electron density, n_e, as derived from the ratio of the [SII] $\lambda\lambda$ 6717,6731 lines (representative of the low-excitation zone of the ionized gas), assuming a temperature of 8000K. The map shows an overall low density through all the region, with most of the values below 100 cm^{-3}, an presenting a few denser knots. One of them shows the extended region of knot A, while two denser zones surround knot C. At any rate, the errors involved in some of the other regions are compatible with a general constant density, well below the critical value for collisional de-excitation. This low nominal value is consistent with other values from the literature (Ferguson et al., 1998). In terms of the [SII] $\lambda\lambda$ 6717/6731 ratio, the field average ratio is 1.41 $\pm$ 0.12 (1 σ error).

3.4.6 Ionization structure and excitation

The hardness (fraction of high energy photons) of the radiation and density of the gas are two of the main factors that drive the different ionization states of the metals. A "hard" spectrum increases the ionization degree, and this hardness increases with the temperature of the star. Since at higher number of electrons there are more recombinations and, as a result, more low ionization species, density is also an important variable.

The ionization degree should be measured estimating the ionic abundance of an element. Nevertheless, this implies the estimation of temperature, and measurement of very low intensity lines. To study the ionization degree throughout the nebula, the calculation of the ionic abundance at each point is not feasible. An alternative is to measure the so-called diagnostic ratios. These diagnostics involve two or three strong emission lines which result depends strongly on the ionization degree and, to a lesser extent, on temperature or abundance. The most common ones are [OIII] λ 5007/Hβ, [NII] λ 6584/Hα and, [SII] $\lambda\lambda$ 6717,6731/Hα.

The ionization potential of OIII is high (54.89 eV) as compared with that of HI (13.6 eV). Thus, the emission of [OIII] λ 5007 Å is related to highly ionized gas. On the other hand, the ionization potential of SI is low (10.36 eV) while SII has a intermediate value (23.40 eV). Therefore, the emission coming from [SII] λ 6717 Å and [SII] λ 6731 Å is related to low ionization and the ratio to Hα will decrease with the degree of ionization. The behaviour of the [NII] λ 6584/Hα is similar to [SII] $\lambda\lambda$ 6717,6731/Hα, but care has to be taken when dealing with gas of very low ionization degree. The ionization potential of NI (14.53 eV) is slightly higher than that of HI, so [NII] λ 6584/Hα could decrease when the ionization degree increases. Summing up, the flux ratio [OIII] λ 5007/Hβ is a good indicator of the mean level of ionization (radiation field strength) and temperature of the gas, whereas [NII] λ 6584/Hα or [SII] $\lambda\lambda$ 6717,6731/Hα are indicators of the number of ionizations per unit volume (ionization parameter).

Diagnostic diagrams (BPT, Baldwin et al., 1981; Veilleux and Osterbrock, 1987) can be used to distinguish two possible ionization sources, AGN or massive stars in star-forming regions, by comparing the ratios mentioned before. It is known that different objects populate quite different regions on these diagnostic diagrams depending on the ionization source.

Figure 3.19 shows [OIII] λ 5007/Hβ versus [NII] λ 6584/Hα and [OIII] λ 5007/Hβ versus [SII] $\lambda\lambda$ 6717,6731/Hα nebular diagnostic diagrams for all measurements in all IFU positions. On these plots, we also show the theoretical "maximum starburst line" derived by Kewley et al. (2001), indicating a conservative theoretical limit for pure photoionization from the hardest starburst ionizing spectrum that can be produced. For points to exist above or to the right-hand side of this threshold, and additional contribution to the excitation from non-photoionization processes is required. From these classical BPT diagnostic diagrams it is clear that the line ratios for all the position in the region are located in the general locus of HII -region like objects.

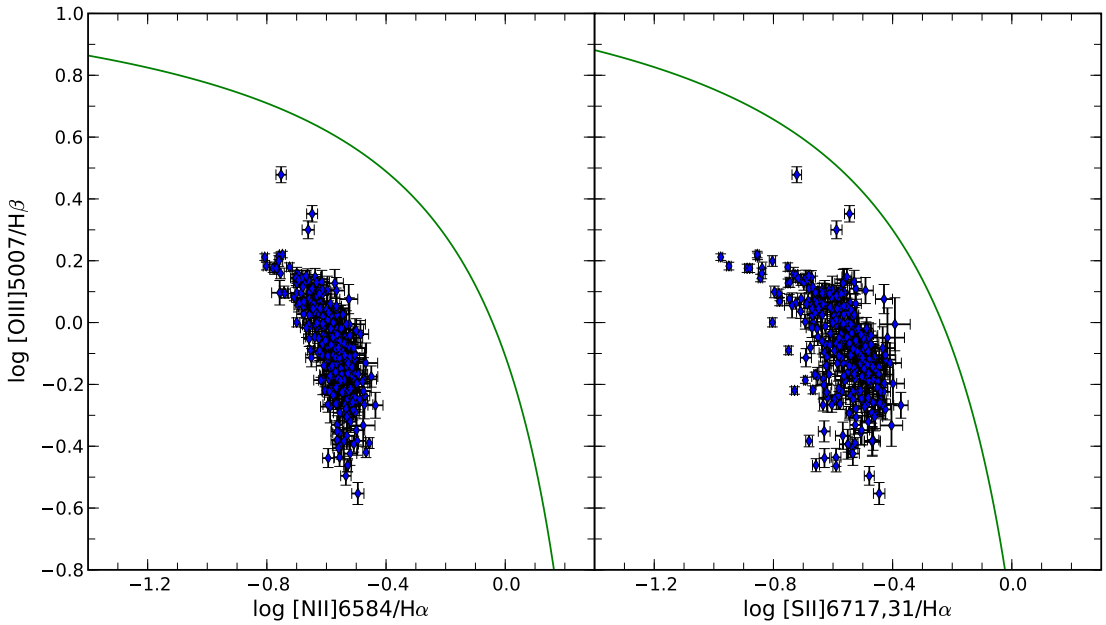

Figure 3.19: Diagnostic diagrams derived from different line ratios. *Left panel:* Relation between [OIII] λ 5007/Hβ and [NII] λ 6584/Hα. *Right panel:* Relation between [OIII] λ 5007/Hβ and [SII] $\lambda\lambda$ 6717,6731/Hα. The solid curve represents the theoretical maximum starburst line (Kewley et al., 2001).

It should be noted the variation of the [OIII] λ 5007/Hβ ratio across the region, of about 0.8 dex. This is comparable with the spread found in HII galaxies, as in the case of IIZw70 (Kehrig et al., 2008). On the other hand, the variation in the [NII] λ 6584/Hα and [SII] $\lambda\lambda$ 6717,6731/Hα ratios are lower. Numerically, the field average ratio of log([OIII] λ 5007/-Hβ) = -0.08 $\pm$ 0.16, log([NII] λ 6584/Hα) = -0.58 $\pm$ 0.07 and log([SII] $\lambda\lambda$ 6717,6731/Hα) = -0.54 $\pm$ 0.10 (1σ errors).

A spatial representation of these three line ratios is shown in Figure 3.20. For the sake of clarity and comparison, Hα is also included in the upper left panel, corrected for reddening. Unlike the reddening map, the structures that appear in the excitation maps are much simpler. In terms of the main four knots, particularly knot A, there is a very good correlation between the value of the intensity of Hα and the value of the ratio, being negative the sign of the correlation for ratios log([SII] $\lambda\lambda$ 6717,6731/Hα) and log([NII] λ 6584/Hα) and positive for the ratio log([OIII] λ 5007/Hβ). As it was mentioned before, this is the expected behaviour if in the central zones of the HII region the sulphur, nitrogen and, oxygen were twice ionized, while only once in the surroundings due to the increasing distance from the young stellar cluster or ionizing source.

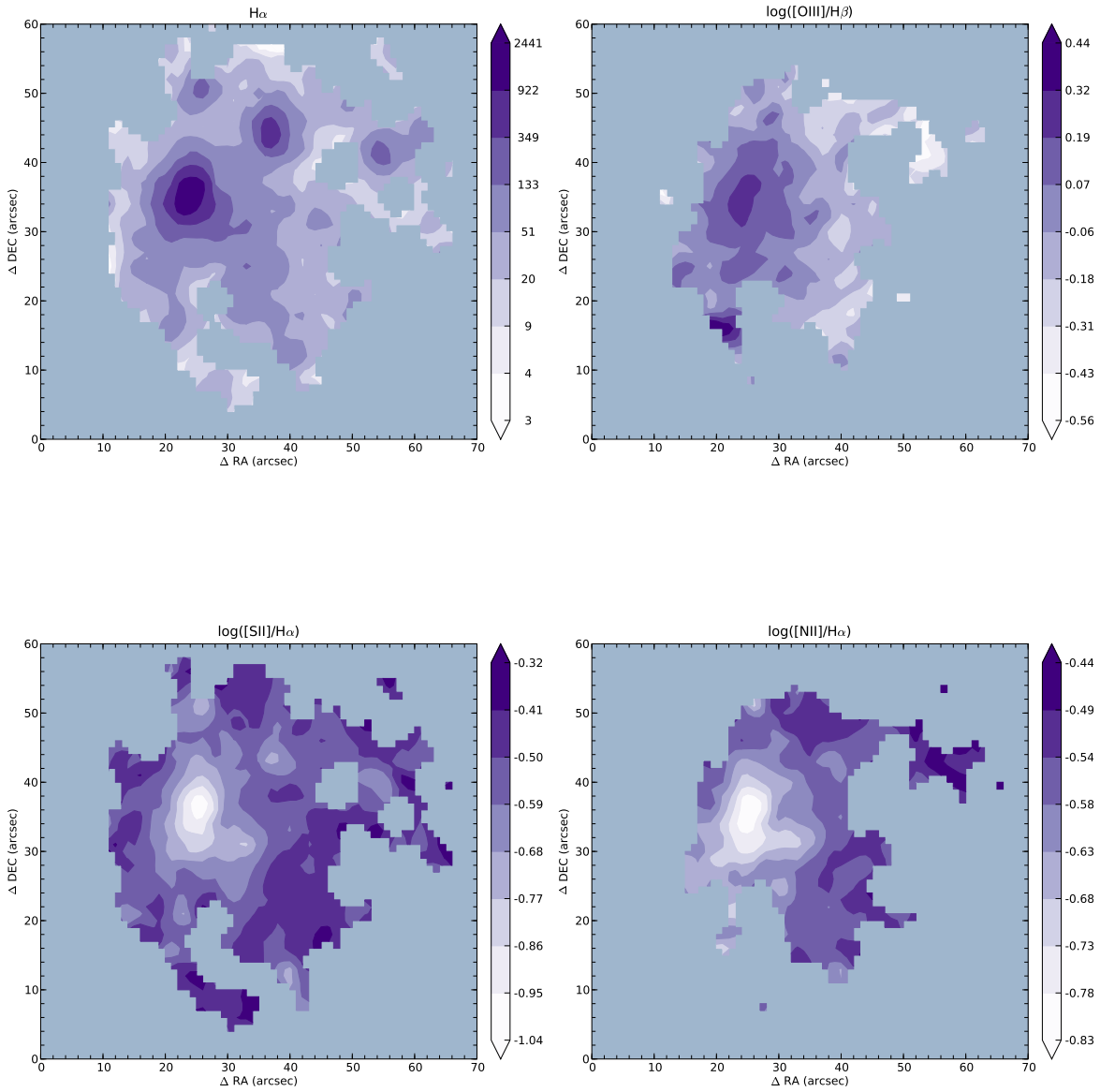

Figure 3.20: *Upper left panel:* Hα flux map (corrected for reddening). The scale bar is given in units of 10^{-16} erg s^{-1} cm^{-2}. This map is included as reference for the excitation maps. *Upper right panel:* Flux ratio map of log([OIII] λ 5007/Hβ). *Lower left panel:* Flux ratio map of log([SII] $\lambda\lambda$ 6717,6731/Hα). *Lower right panel:* Flux ratio map of log([NII] λ 6584/Hα).

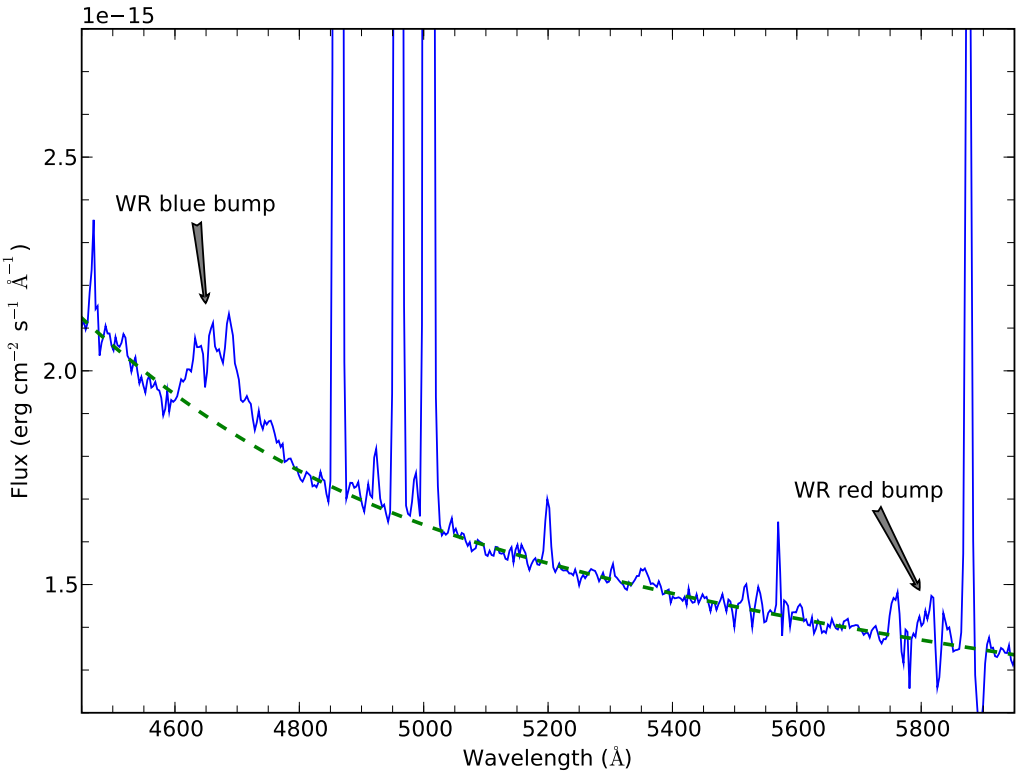

Figure 3.21: Detail of the integrated spectrum of knot A with the identification of both the blue (4650Å) and red (5808Å) Wolf-Rayet bumps over the adopted continuum, marked as a dashed (green) line.

3.4.7 Wolf-Rayet stellar population

Wolf-Rayet (WR) stars appear in the first stages after the main sequence of massive stars, so they are already visible early after the beginning of the burst of star formation (approximately 2 Myr). The WR phase lasts on average until $\sim$ 5 Myr. The strength of the stellar winds produced by these stars is sometimes measured in the integrated spectra of the starburst galaxies, which are identified as WR galaxies (Conti, 1991). The presence of the bumps produced by WR stars are therefore associated with the existence of processes of intense star formation. The existence of this WR stellar population can be very useful for the study and characterization of the ionizing stellar population in starburst galaxies (*e.g.* Pérez-Montero and Díaz, 2007). These WR features are the blue bump, centred at 4650 Å and produced mainly by broad emission lines of NV at 4605, 4620 Å, NIII 4634, 4640 Å, CIII/IV 4650, 4658 Å and HeII at 4686 Å. The red bump, usually fainter, is centred at 5808 Å and is emitted mainly by CIII/IV.

In addition to the initial mass of the star, another fundamental parameter in WR stars is metallicity. Increasing the content of heavy elements, increases the ratio of mass loss due to winds. Thus, the more metall rich is the star, the lower will be the initial mass needed

to become a WR star. To estimate the number of WR stars in a resolved cluster it is only necessary to count them. For an unresolved cluster, the equivalent width of the blue bump (WR λ 4650) or the ratio between this bump and the Hβ emission line are used as diagnostics. The values of these quantities in the range of interest (2-6 Myr) depends strongly on metallicity.

We have detected the blue bump in several fibers on the IFU data, while the red bump was only marginally detected when summing the emission of the whole knot A. In Figure 3.21 we show the broad emission of both the blue and red bumps (the last one very weakly detected) for the integrated flux for knot A. The blue bump is remarkably strong in the integrated spectrum of this knot. In section 3.4.8 the integrated properties of the knots are described.

Figure 3.22 shows the WR spatial distribution in the PPak field. The filled dark (violet) regions represent the fiber detections of the blue WR bump. On the upper panel the Hα contours are overplotted, while in the lower panel the continuum contours near the WR emission ($\sim \lambda$ 4500 Å) are shown. The filled regions only represents positions of the WR stars in the field, not intensity. Clear detections where found in 10 fibers of knot A, corresponding to the extended region in that location. On the other hand, only in one fiber of knot B was found a weak blue bump, while in knot C two fibers showed a medium-intensity feature. As it is clearly seen, the location of the bumps follow very well the morphology of the continuum emission adjacent to the WR blue bump. We also verified that the maximum of the continuum emission adjacent to Hβ corresponds spatially to the WR bumps intensity maximum. Interestingly, knot B shows a weak WR blue bump. Although the continuum there has very low surface brightness, the local peak intensity matches as well the position or the detected feature. As we see from top panel of Figure 3.22, the location of the WR blue bump coincides with the morphology of the Hα emission, although there are slight offsets from their peak intensity, particularly in knots B and C.

The bumps have been measured in the following way. First a continuum shape has been adopted and we have measured the broad emission over this continuum in the wavelengths of the blue bump, at 4650 Å. Finally, we have subtracted the emission of the narrower lines not emitted by the WR winds, which are [FeIII] 4658 Å, HeII 4686 Å, HeI + [ArIV] 4711 Å and [ArIV] 4740 Å in the blue bump (although these last two lines present very small contribution). The dereddened relative intensities and the equivalent widths of the blue bump are shown in Table 3.3. Although some contribution of the red bump was found in knots A and C, the flux could not be measured with an acceptable accuracy. No detection of blue or red bump was founded in knot D. All measurements were performed in the integrated spectra from the mosaic, so that the reported values have been derived from absolute fluxes.

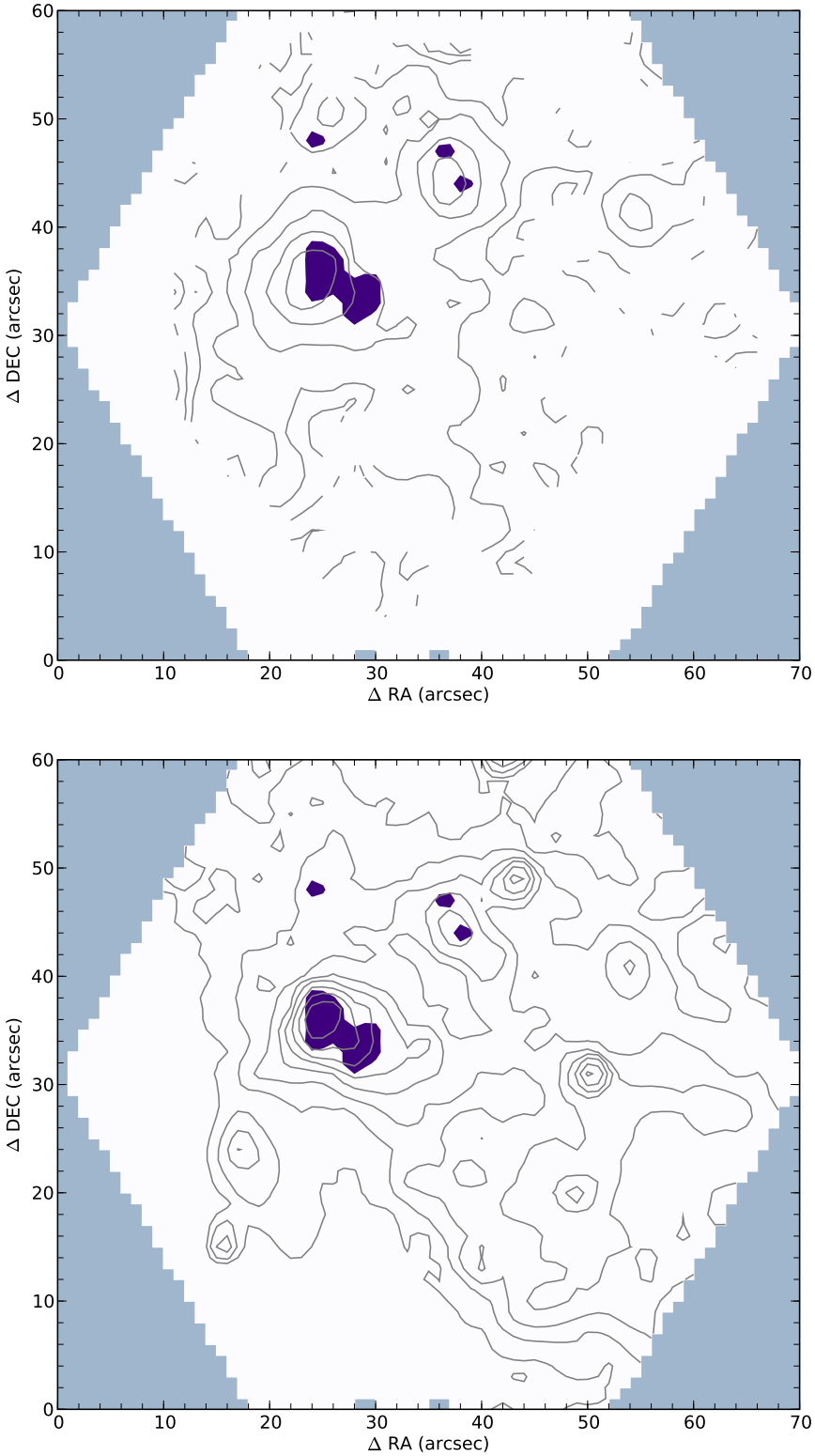

Figure 3.22: Wolf-Rayet (WR) spatial distribution. The filled dark (violet) regions represent the fiber detections of the blue WR bump. On the upper panel the Hα contours are overplotted, while in the lower panel the continuum contours near the WR emission ($\sim \lambda$ 4500 Å) are shown. The filled regions only represent positions of the WR stars in the field, not intensity.

ID	log L(bb) (erg · s^{-1})	I(bb)[a]	-EW(bb) Å
Knot A	38.58 ± 0.04	20.3 ± 1.7	14.0 ± 1.2
Knot B	37.41 ± 0.06	27.4 ± 3.5	25.5 ± 3.3
Knot C	37.90 ± 0.05	22.7 ± 2.8	16.4 ± 2.9
Knot D	...	...	...

[a] In units of 100 · I(Hβ)

Table 3.3: Luminosities, relative intensities and equivalent widths of the Wolf-Rayet features measured on the integrated spectra of four knots at 4650 Å (blue bump, bb). All quantities have been corrected for reddening.

3.4.8 Physical properties and chemical abundances from the integrated spectra

In order to study the mean properties of the HII complex, several integrated spectra were obtained from the PPak-field. As we have seen in Figure 3.14, there are four main Hα intense knots. These structures have enough signal-to-noise to perform an analysis of the physical properties of the gas and their abundances. Unfortunately, auroral lines with acceptable errors were not found in individual fibers; enough signal-to-noise to measure these weak lines was achieved only in the integrated spectrum of each knot.

In section 3.3.8 we have seen that a complete mosaic of 993 spectra was accomplished for the blue range (3700-7000 Å), while for the red data (7000-10000 Å) we had only one pointing of 331 spectra, since there was a problem with the guiding and de-rotator. Therefore, in order to take advantage of all the relevant emission lines available, we had to build the integrated spectrum for each knot from the first blue and red pointing. Since the FOV for one pointing is not completely covered by all the fibers (see Figure 3.8, for example), we cannot expect to obtain absolute fluxes. Nevertheless, we can assume that the relative intensities of the lines should be similar, so that the derived properties and abundances should not be different within the errors.

The spatial limits of each of the four knots were defined in the Hα map by means of visual inspection with the help of isocontour plots. The limit contour is at the 20-30% of the maximum peak. In order to have a better definition, we used the Hα map built from the mosaic (3 pointings). Then, once the knots were defined, we co-added all the fibers belonging to each knot in the mosaic exposure, obtaining four, absolute flux calibrated, integrated spectra. It is important to ensure that the integrated spectra of each knot in the one dithering exposure is built coming from exactly the same area. Performing this task is another advantage of IFU data, since each fiber is perfectly identified. From the mosaic integrated spectra we had the ID of the fibers, and therefore the fibers coming from each of the three ditherings. Thus, we co-added the fibers coming from the first blue and red

pointing for each knot. Finally, we built an integrated spectrum over the full FOV of our IFS dataset, both from the mosaic and from the one pointing data. Therefore, we ended up with ten spectra: five absolute flux calibrated spectra from the mosaic data covering the range 3700-7000 Å for the four main knots and the whole FOV, and other five spectra of the same areas coming from the blue and red first pointing covering the range 3700-10000 Å. All the fibers containing WR features were included in these integrated spectra, since the WR positions are near the peak of Hα, as shown in Figure 3.22.

The spectra of the four knots (labelled from A to D) and the integrated spectrum of the whole PPak-field with some of the relevant identified emission lines are shown in Figures 3.23 (Knot A an B), 3.24 (Knot C and D) and 3.25 (PPak-field). The spectrum of each knot is split into two panels. All of them come from the blue and red first pointing.

Line intensity ratios for the most relevant emission lines were measured in each spectrum using the `splot` task in IRAF following the procedure described in Hägele et al. (2006). A pseudo-continuum has been defined at the base of the hydrogen emission lines to measure the line intensities and minimize the errors introduced by the underlying population. As we have seen in section 3.4.1, this procedure gives the same results, within the observational errors, as fitting synthetic SSP models to the continuum. Since we had to measure auroral lines, we decided to measure manually all the lines. The statistical errors associated with the observed emission fluxes have been calculated using the same procedure as described in section 3.4.2 (see expression there).

As reported in section 3.3.9, the [SIII] λ 9532 Å line is affected by strong narrow water vapour lines and therefore its value has been set to 2.44, its theoretical ratio to the weaker [SIII] λ 9069 Å.

The reddening coefficient c(Hβ) has been calculated using the same procedures as described in section 3.4.4. The only difference is that an iterative method to estimate the temperature and density has been used in each case when the appropriate lines were available. To minimize the errors and to follow a similar approach as when deriving the maps, we have estimated c(Hβ) only by means of Hα and Hβ.

Tables 3.4, 3.5 and 3.6 give the equivalent widths and the reddening-corrected emission line fluxes for six integrated spectra together with the reddening constant and its error, taken as the uncertainty of the least-squares fit and the reddening-corrected Hβ intensity. The adopted reddeningcurve, $f(\lambda)$, normalized to Hβ, is given in column 2 of each table. The errors in the emission lines were obtained by propagating in quadrature the observational errors in the emission-line fluxes and the reddening constant uncertainties.

Table 3.4 presents the results for the integrated spectra from the entire PPak FOV for the mosaic exposure (PPak field Mosaic) and for the blue and red first pointing (PPak field Mosaic). As it can be seen, the relative intensities and equivalent widths are in very good agreement, within the errors, confirming the previous assumption.

Tables 3.5 and 3.6 show the results for the integrated spectra from the blue and red first

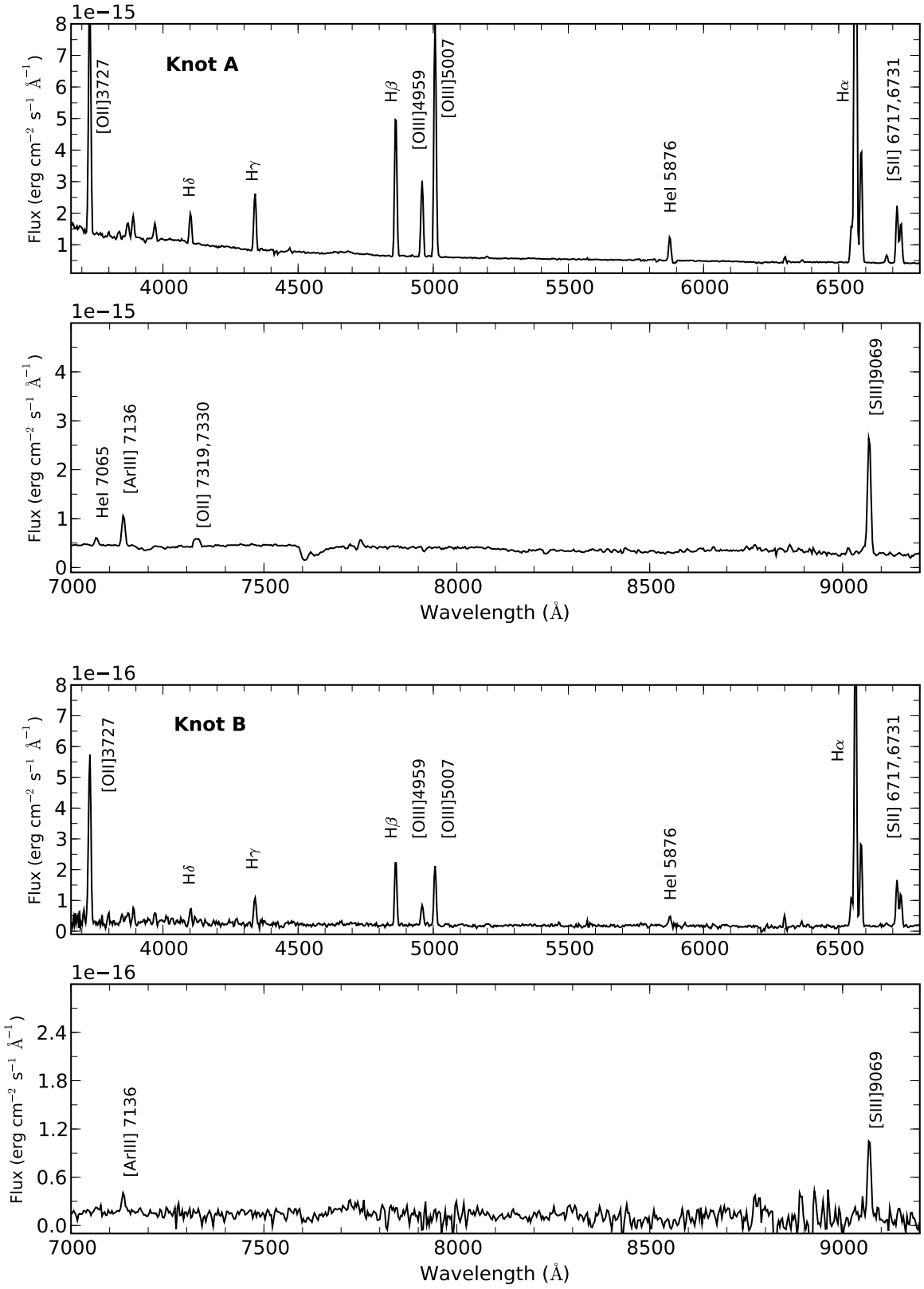

Figure 3.23: Blue and red spectra for the knots A and B.

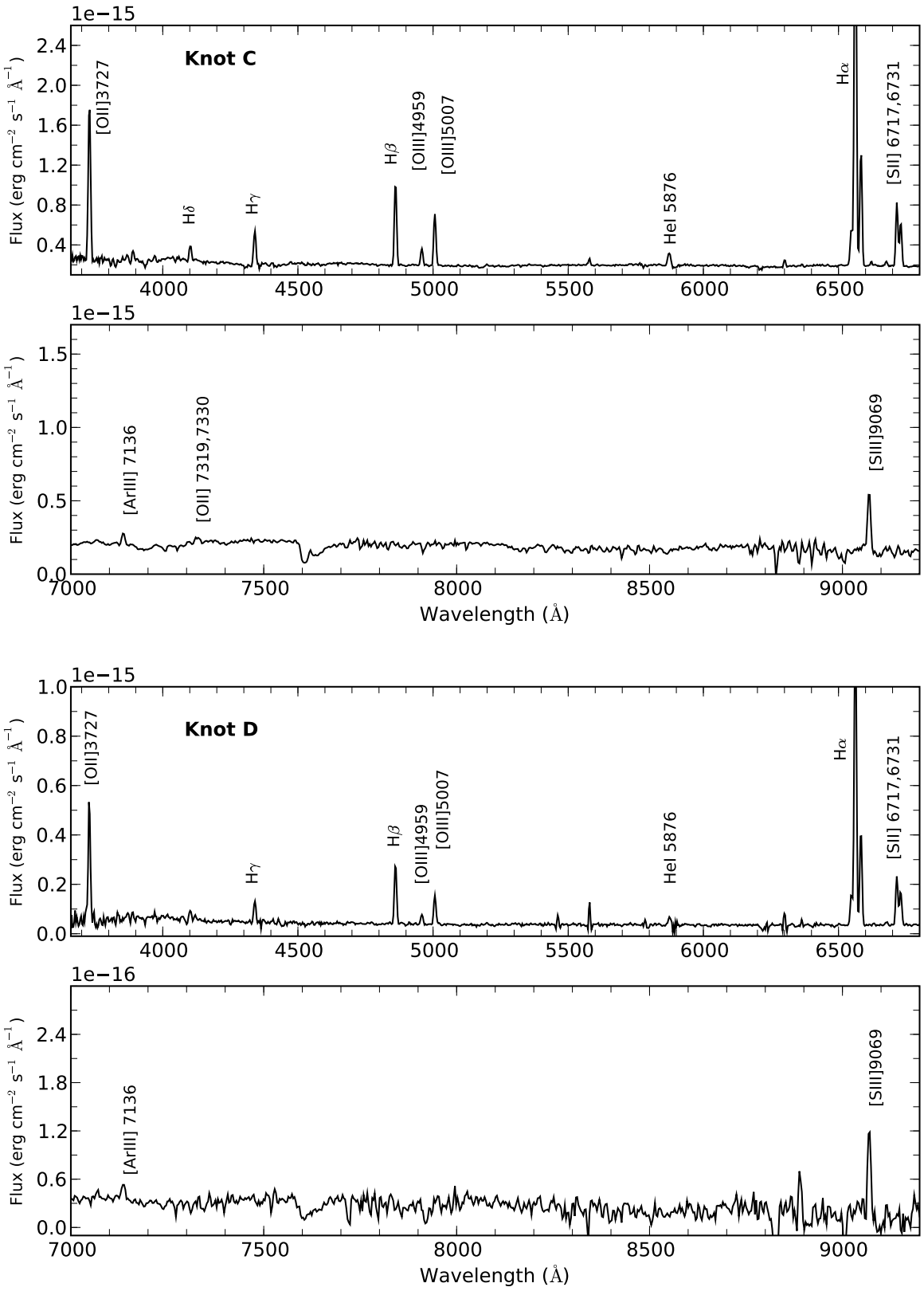

Figure 3.24: Blue and red spectra for the knots C and D.

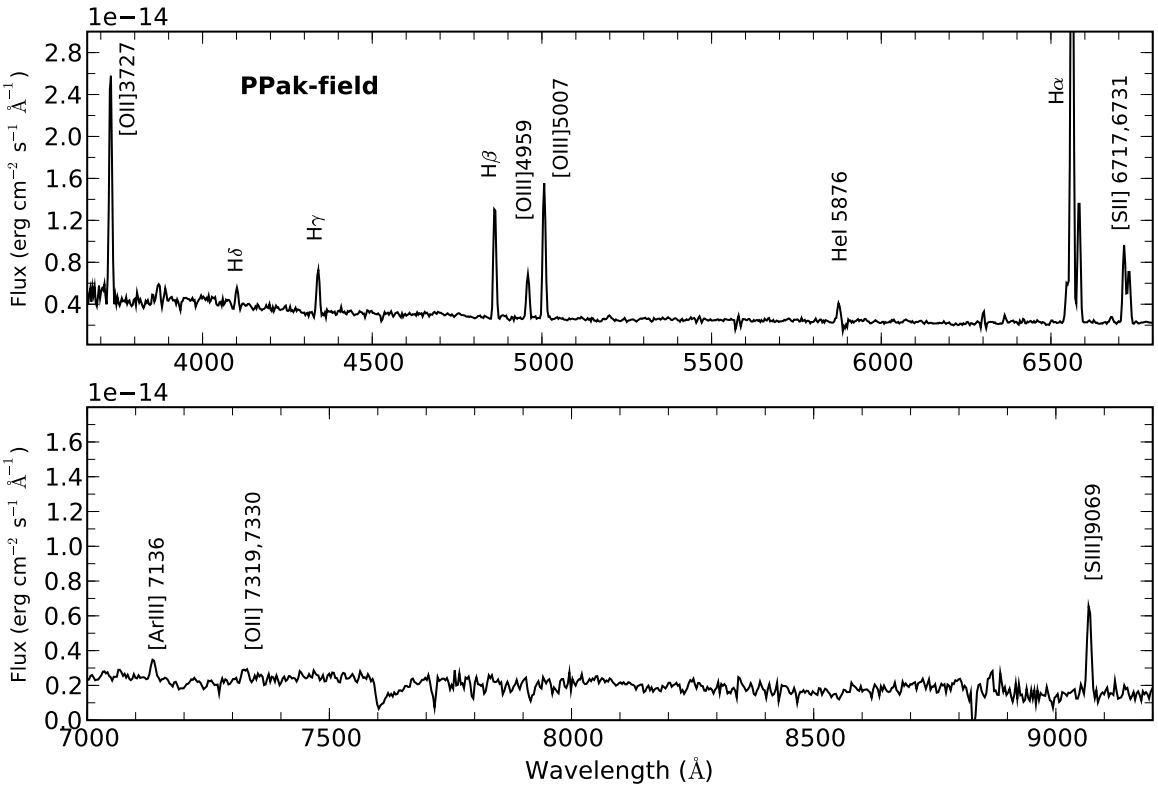

Figure 3.25: Blue and red spectra for the whole PPak-field.

pointing of the knots A and B, and C and D, respectively. Their ratios, as compared with the ones obtained from the mosaic exposure are, again, in good agreement. Thus, we only show the measured line intensities coming from the first pointing exposure. In Tables 3.5 and 3.6 the total reddening-corrected Hβ intensity (I_{tot}(Hβ)) measured in the mosaic is also given. As it can be appreciated, the total flux is between a factor of 2 or 3 higher than the value measured in the one single pointing.

The Hβ flux of the emission knots amounts to about 50% of the total PPak field-of-view flux, with knot A, B, C, and D contributing 38%, 2%, 7%, and 3% to the total flux, respectively. Knot A is the brightest of them and provides 75% of the combined flux from the four knots.

Electron densities and temperatures

The physical conditions of the ionized gas, including electron temperature and electron density, have been derived using the five-level statistical equilibrium atom approximation in the task `temden` of the STSDAS package of the software IRAF. For details of the equations involved, the reader is referred to Appendix B. We have taken as sources of error the uncertainties associated with the measurement of the emission-line fluxes and the reddening

		PPak-field Pointing-1			PPak-field Mosaic		
λ (Å)	f(λ)	F(λ)	-EW(Å)	I(λ)	F(λ)	-EW(Å)	I(λ)
3727 [OII][a]	0.322	1995 ± 65	-55.0	3459 ± 230	2078 ± 55	-60.2	3568 ± 262
3868 [NeIII]	0.291	146 ± 31	-3.7	240 ± 53	128 ± 25	-3.4	209 ± 43
4102 Hδ	0.229	163 ± 16	-4.9	241 ± 27	135 ± 18	-4.0	198 ± 29
4340 Hγ	0.157	426 ± 24	-15.6	557 ± 42	420 ± 20	-15.8	547 ± 42
4363 [OIII]	0.149	2 ± 1	-0.1	2 ± 1	2 ± 1	-0.1	3 ± 1
4686 HeII	0.050	9 ± 3	-0.3	9 ± 4	8 ± 1	-0.3	9 ± 1
4861 Hβ	0.000	1000 ± 13	-40.6	1000 ± 46	1000 ± 15	-41.6	1000 ± 54
4959 [OIII]	-0.026	395 ± 12	-16.0	378 ± 20	403 ± 12	-16.6	386 ± 23
5007 [OIII]	-0.038	1198 ± 14	-48.1	1123 ± 49	1214 ± 17	-51.6	1139 ± 59
5876 HeI	-0.203	166 ± 11	-7.8	117 ± 9	163 ± 20	-7.8	116 ± 15
6548 [NII]	-0.296	309 ± 8	-15.2	186 ± 8	333 ± 8	-17.7	203 ± 9
6563 Hα	-0.298	4857 ± 9	-238.6	2921 ± 90	4859 ± 7	-257.6	2948 ± 107
6584 [NII]	-0.300	1123 ± 9	-55.1	672 ± 21	1127 ± 12	-59.8	681 ± 26
6678 HeI	-0.313	52 ± 7	-2.6	31 ± 4	53 ± 7	-2.7	31 ± 4
6717 [SII]	-0.318	690 ± 3	-34.7	401 ± 12	683 ± 5	-36.2	400 ± 14
6731 [SII]	-0.320	484 ± 3	-24.4	280 ± 9	484 ± 6	-25.7	283 ± 10
7065 HeI	-0.364	33 ± 7	-1.5	18 ± 4	···	···	···
7136 [ArIII]	-0.374	112 ± 16	-5.1	59 ± 9	···	···	···
7325 [OII][b]	-0.398	76 ± 17	-4.3	39 ± 9	···	···	···
9069 [SIII]	-0.594	460 ± 20	-32.1	167 ± 8	···	···	···
I(Hβ)(erg s^{-1} cm^{-2})			6.05×10^{-13}			1.72×10^{-12}	
c(Hβ)			0.74 ± 0.02			0.73 ± 0.02	

[a] [OII] $\lambda\lambda$ 3726 + 3729
[b] [OII] $\lambda\lambda$ 7319 + 7330

Table 3.4: Relative observed and reddening corrected line intensities [F(Hβ)=I(Hβ)=1000] with their corresponding errors for the integrated spectrum of the PPak-field using the blue and red one-pointings (PPak-field Pointing-1) and the blue mosaic (PPak-field Mosaic). The adopted reddening curve, $f(\lambda)$ (normalized to Hβ), the equivalent width of the emission lines, the reddening-corrected Hβ intensity, and the constant of reddening are also given.

		Knot A			Knot B		
λ (Å)	f(λ)	F(λ)	-EW(Å)	I(λ)	F(λ)	-EW(Å)	I(λ)
3727 [OII][a]	0.322	1730 ± 19	-61.9	2883 ± 78	2782 ± 126	-175.8	5085 ± 572
3868 [NeIII]	0.291	97 ± 11	-3.6	154 ± 18	121 ± 32	-8.2	208 ± 58
4102 Hδ	0.229	207 ± 4	-9.2	298 ± 9	231 ± 38	-22.7	354 ± 67
4340 Hγ	0.157	395 ± 4	-22.1	507 ± 12	500 ± 52	-61.4	670 ± 92
4363 [OIII]	0.149	7 ± 3	-0.4	9 ± 4	5 ± 2	-0.3	7 ± 3
4471 HeI	0.115	33 ± 4	-2.1	40 ± 5	...	...	...
4658 [FeIII]	0.058	4 ± 1	-0.3	5 ± 1	...	...	...
4686 HeII	0.050	6 ± 2	-0.4	6 ± 2	...	...	...
4861 Hβ	0.000	1000 ± 5	-77.9	1000 ± 19	1000 ± 23	-99.3	1000 ± 81
4959 [OIII]	-0.026	538 ± 3	-40.3	517 ± 10	329 ± 13	-32.5	313 ± 27
5007 [OIII]	-0.038	1652 ± 6	-123.4	1556 ± 28	938 ± 13	-96.3	874 ± 67
5876 HeI	-0.203	160 ± 7	-15.0	116 ± 5	157 ± 14	-18.1	108 ± 12
6312 [SIII]	-0.264	8 ± 1	-0.9	6 ± 1	...	...	...
6548 [NII]	-0.296	217 ± 4	-23.5	136 ± 3	430 ± 13	-60.8	247 ± 16
6563 Hα	-0.298	4634 ± 5	-503.6	2890 ± 38	5090 ± 11	-711.0	2915 ± 160
6584 [NII]	-0.300	801 ± 2	-87.4	497 ± 7	1335 ± 10	-184.0	760 ± 42
6678 HeI	-0.313	51 ± 3	-5.6	31 ± 2	51 ± 12	-6.6	29 ± 7
6717 [SII]	-0.318	380 ± 2	-42.8	230 ± 3	722 ± 13	-94.0	398 ± 22
6731 [SII]	-0.320	280 ± 2	-31.6	169 ± 2	514 ± 13	-67.4	282 ± 17
7065 HeI	-0.364	32 ± 3	-3.3	18 ± 1	46 ± 15	-6.6	23 ± 8
7136 [ArIII]	-0.374	131 ± 3	-13.6	73 ± 2	109 ± 18	-13.5	54 ± 9
7319 [OII][b]	-0.398	54 ± 9	-6.2	29 ± 5	...	...	...
9069 [SIII]	-0.594	561 ± 16	-96.1	219 ± 6	437 ± 46	-62.6	144 ± 16
I(Hβ)(erg s^{-1} cm^{-2})			2.29×10^{-13}			1.37×10^{-14}	
I_{tot}(Hβ)(erg s^{-1} cm^{-2})			6.63×10^{-13}			3.69×10^{-14}	
c(Hβ)			0.69 ± 0.01			0.81 ± 0.03	

[a] [OII] $\lambda\lambda$ 3726 + 3729; [b] [OII] $\lambda\lambda$ 7319 + 7330

Table 3.5: Relative observed and reddening corrected line intensities [F(Hβ)=I(Hβ)=1000] with their corresponding errors for the integrated spectrum of the knots A and B using the blue and red one-pointings. The adopted reddening curve, $f(\lambda)$ (normalized to Hβ), the equivalent width of the emission lines, the reddening-corrected Hβ intensity, the reddening-corrected Hβ intensity measured in the blue mosaic (I_{tot}(Hβ)) and the constant of reddening are also given.

		Knot C			Knot D		
λ (Å)	f(λ)	F(λ)	-EW(Å)	I(λ)	F(λ)	-EW(Å)	I(λ)
3727 [OII][a]	0.322	2064 ± 51	-93.2	3676 ± 215	1711 ± 86	-54.2	3290 ± 299
3868 [NeIII]	0.291	53 ± 16	-1.8	89 ± 28	100 ± 29	-4.5	180 ± 55
4102 Hδ	0.229	181 ± 22	-6.4	273 ± 36	189 ± 39	-9.4	301 ± 66
4340 Hγ	0.157	453 ± 20	-20.7	600 ± 38	359 ± 23	-20.1	494 ± 45
4363 [OIII]	0.149	3 ± 1	-0.1	4 ± 1	···	···	···
4658 [FeIII]	0.058	5 ± 2	-0.2	5 ± 2	···	···	···
4686 HeII	0.050	4 ± 2	-0.1	4 ± 2	···	···	···
4861 Hβ	0.000	1000 ± 12	-76.2	1000 ± 42	1000 ± 17	-60.6	1000 ± 60
4959 [OIII]	-0.026	198 ± 6	-8.6	189 ± 9	170 ± 13	-11.2	161 ± 16
5007 [OIII]	-0.038	622 ± 9	-27.5	581 ± 24	488 ± 14	-31.5	452 ± 28
5876 HeI	-0.203	196 ± 16	-8.7	136 ± 12	137 ± 31	-9.5	91 ± 21
6548 [NII]	-0.296	428 ± 9	-19.2	252 ± 9	469 ± 10	-34.4	257 ± 12
6563 Hα	-0.298	4981 ± 8	-223.9	2921 ± 82	5232 ± 11	-382.2	2859 ± 115
6584 [NII]	-0.300	1378 ± 9	-62.0	804 ± 23	1588 ± 9	-115.8	863 ± 35
6678 HeI	-0.313	43 ± 4	-2.0	25 ± 3	53 ± 11	-3.7	28 ± 6
6717 [SII]	-0.318	727 ± 5	-33.2	411 ± 12	808 ± 7	-58.4	423 ± 17
6731 [SII]	-0.320	523 ± 5	-23.9	295 ± 9	588 ± 7	-42.6	307 ± 13
7065 HeI	-0.364	30 ± 6	-1.2	16 ± 3	26 ± 6	-1.7	12 ± 3
7136 [ArIII]	-0.374	82 ± 15	-3.5	42 ± 8	76 ± 12	-5.2	36 ± 6
7319 [OII]	-0.398	58 ± 13	-2.7	29 ± 6	···	···	···
9069 [SIII]	-0.594	451 ± 26	-24.0	156 ± 9	442 ± 22	-89.1	132 ± 7
I(Hβ)(erg s^{-1} cm^{-2})			5.13×10^{-14}			1.88×10^{-14}	
I_{tot}(Hβ)(erg s^{-1} cm^{-2})			1.28×10^{-13}			5.28×10^{-14}	
c(Hβ)			0.78 ± 0.02			0.88 ± 0.02	

[a] [OII] $\lambda\lambda$ 3726 + 3729

Table 3.6: Relative observed and reddening corrected line intensities [F(Hβ)=I(Hβ)=1000] with their corresponding errors for the integrated spectrum of the knots C and D using the blue and red one-pointings. The adopted reddening curve, $f(\lambda)$ (normalized to Hβ), the equivalent width of the emission lines, the reddening-corrected Hβ intensity, the reddening-corrected Hβ intensity measured in the blue mosaic (I_{tot}(Hβ)) and the constant of reddening are also given.

correction, and we have propagated them through our calculations.

Electron densities have been derived from the [SII] λ 6717,6731 Å line ratio, which is representative of the low-excitation zone of the ionized gas. In all cases, they were found to be lower than 100 particles per cubic centimetre, well below the critical density for collisional de-excitation. As compared with the map of Figure 3.18, the densities derived from the integrated spectra match well the ones obtained from the map for each particular region.

Several electron temperatures for three spectra have been measured: t([OII]), t([OIII]) and t([SIII]). For knot D, no auroral line was found in its integrated spectrum.

The spectral resolution is at limit to resolve the [OII] $\lambda\lambda$ 7319,7330 Å lines, so we measured the integrated flux of the doublet. This lines can have a contribution by direct recombination which increases with temperature (see Appendix B). Using the calculated [OIII] electron temperatures, we have estimated this contribution to be less than 3 per cent in all cases and therefore we have not corrected for this effect. For knot B, the [OII] $\lambda\lambda$ 7319,7330 Å lines did not have enough intensity to be measured with precision, so we derived its [OII] temperature from t([OIII]) using the relations based on the photoionization models described in Pérez-Montero and Díaz (2003), which take into account explicitly the dependence of t([OII]) on the electron density:

$$t([\mathrm{OII}]) = \frac{1.2 + 0.002 \cdot n + \frac{4.2}{n}}{t([\mathrm{OIII}])^{-1} + 0.08 + 0.003 \cdot n + \frac{2.5}{n}}$$

Although the [OIII] λ 4363 Å auroral line was detected in the one dithering exposure, the signal-to-noise of the mosaic was higher and the estimated errors lower. For this reason, we have used the t([OIII]) derived from the mosaic in the abundance analysis. At any rate, the [OIII] temperatures calculated from both sets of data coincide within the errors.

In the case of the sulphur, the [SIII] λ 6312 Å auroral line could only be measured with enough precision in the integrated spectra of knot A. For the rest of the knots, the [SIII] temperature has been estimated from the empirical relation:

$$t([\mathrm{SIII}]) = (1.19 \pm 0.08) t([\mathrm{OIII}]) - (0.32 \pm 0.10)$$

found by Hägele et al. (2006).

The electron densities and temperatures derived for the integrated spectra of the PPak-field and the four knots are listed in Table 3.7 along with their corresponding errors.

Chemical abundances

We have derived the ionic chemical abundances of the different species using the stronger emission lines available detected in the spectra and the task `ionic` of the STSDAS package in IRAF (see Appendix B). The total abundances have been derived by taking into account,

	PPak-field	Knot A	Knot B	Knot C	Knot D
n([SII])	55:	61 ± 20	98:	77:	73:[a]
t([OIII])[b]	0.78 ± 0.06	0.87 ± 0.06	0.80 ± 0.13	0.78 ± 0.10	···
t([OII])	0.83 ± 0.11	0.80 ± 0.07	0.87 ± 0.13[c]	0.78 ± 0.15	···
t([SIII])	0.61 ± 0.13[d]	0.71 ± 0.12	0.63 ± 0.20[d]	0.61 ± 0.17[d]	···

[a] Assuming a mean temperature from the temperature measured in the other knots
[b] [OIII] temperatures measured in the mosaic
[c] From a relation with T([OIII]) based on photoionization models
[d] From an empirical relation with T([OIII])

Table 3.7: Electron densities and temperatures for the integrated spectra of the PPak-field and the four knots. Densities in cm^{-3} and temperatures in 10^4 K.

when required, the unseen ionization stages of each element, resorting to the most widely accepted ICFs for each species:

$$\frac{X}{H} = ICF(X^i)\frac{X^{+i}}{H^{+i}}$$

Helium abundance

We have measured emission fluxes for 3 lines of HeI and one of HeII. The spectra presented other helium lines, although all of them were blended with another emission line or were so weak that they cannot be used to derive the helium abundance with the necessary accuracy. We have therefore used the HeI $\lambda\lambda$ 4471 (only found in knot A), 5876, 6678 and 7065, and HeII λ 4686 lines to estimate the abundances of helium once and twice ionized, respectively.

Helium lines arise mainly from pure recombination; however, they could have some contribution from collisional excitation as well as be affected by self-absorption and, if present, by underlying stellar absorption (see Olive and Skillman, 2001, for a complete treatment). We have taken the electron temperature of [OIII] as representative of the zone where the He emission arises and we have used the equations given by Olive and Skillman (2001) to derive the He^+/H^+ value (see Appendix B). We have not taken into account, however, the underlying stellar population and the corrections for fluorescence, since the involved helium lines have a negligible dependence with optical depth effects and the observed objects have low densities. As we have seen in section 3.4.7, the integrated spectra of the PPak-field and three of the four knots show in their spectra the signature of the presence of WR stars by the blue bump around λ 4600. For this reason, we have taken care when measuring the emission-line flux of HeII λ 4686. To calculate the abundance of twice ionized helium, we have resorted to the work by Kunth and Sargent (1983). Then, for the total abundance, we have directly added the two ionic abundances:

	PPak-field	Knot A	Knot B	Knot C
He^+/H^+ (λ4471)	···	0.079 ± 0.010	···	···
He^+/H^+ (λ5876)	0.082 ± 0.007	0.083 ± 0.004	0.075 ± 0.010	0.094 ± 0.009
He^+/H^+ (λ6678)	0.074 ± 0.011	0.078 ± 0.005	0.070 ± 0.018	0.060 ± 0.007
He^+/H^+ (λ7065)	0.084 ± 0.018	0.079 ± 0.007	0.110 ± 0.038	0.074 ± 0.016
He^+/H^+ (Adopted)	0.080 ± 0.007	0.080 ± 0.004	0.076 ± 0.035	0.073 ± 0.025
He^{2+}/H^+ (λ4686)	0.0008 ± 0.0003	0.0005 ± 0.0002	···	0.0003 ± 0.0001
(He/H)	0.080 ± 0.007	0.081 ± 0.004	···	0.073 ± 0.025

Table 3.8: Ionic and total chemical abundances for helium.

$$\frac{He}{H} = \frac{He^+ + He^{2+}}{H^+}$$

The results obtained for each line and their corresponding errors are presented in Table 3.8, along with the adopted value for He^+/H^+ (a weighted average of the values deduced from each of the lines).

Ionic and total chemical abundances from forbidden lines

The oxygen ionic abundance ratios, O^+/H^+ and O^{2+}/H^+, were derived from the [OII] $\lambda\lambda$ 3727,3729 Å and [OIII] $\lambda\lambda$ 4959, 5007 Å lines, respectively using the appropriate electron temperature for each ion. The total abundance of oxygen was derived assuming

$$\frac{O}{H} \approx \frac{O^+ + O^{2+}}{H^+}$$

Regarding the sulphur, we derived S^+ abundances from the fluxes of the [SII] emission lines at $\lambda\lambda$ 6717, 6731 Å assuming that T([SII]) ≈ T([OII]); S^{2+} abundances have been derived from the fluxes of the near-IR [SIII] λ 9069 line and the directly measured T([SIII]) for knot A and its estimated value for the other knots. The total sulphur abundance was calculated using an ionization correction factor (ICF) for S^++S^{2+} according to Barker (1980) formula, which is based on the photoionization models of Stasińska (1978):

$$ICF(S^+ + S^{2+}) \approx \left[1 - \left(\frac{O^{2+}}{O^+ + O^{2+}}\right)^{\alpha}\right]^{-1/\alpha}$$

where $\alpha = 2.5$ provides the best fit to the scarce observational data on S^{3+} abundances (Pérez-Montero et al., 2006). Taking this ICF as a function of the ratio O^{2+}/O instead of O^+/O reduces the propagated error for this quantity.

The ionic abundance of nitrogen, N^+/H^+, was derived from the intensities of the $\lambda\lambda$ 6548,

6584 Å lines assuming that T([NII]) ≈ T([OII]). Then, the total N abundance was derived under the following assumption:

$$\frac{N}{O} \approx \frac{N^+}{O^+}$$

Neon is only visible in the spectra via the [NeIII] emission line at λ3869 Å. For this ion, we took the electron temperature of [OIII], as representative of the high excitation zone. The total abundance of neon was calculated using the following expression for the ICF (Pérez-Montero et al., 2007):

$$ICF(Ne^{2+}) \approx 0.753 + 0.142 \cdot \frac{O^{2+}}{O^+ + O^{2+}} + 0.171 \cdot \frac{O^+ + O^{2+}}{O^{2+}}$$

This formula considers the overestimate of Ne/H in objects with low excitation, where the charge transfer between O^{2+} and H^0 becomes important (Izotov et al., 2004).

The only accessible emission lines of argon in the optical spectra of ionized regions correspond to Ar^{2+} and Ar^{3+}. However, in the integrated spectra of the knots only [ArIII] λ 7136 Å was measured and the abundance of Ar^{2+} was calculated assuming that T([ArIII]) ≈ T([SIII]) (Garnett, 1992). As already described in section 3.4.7, [ArIV] λ 4741 Å was present in some knots and subtracted to their WR blue bump flux, but their contribution was small to yield any accurate abundance determination. The total abundance of Ar was then calculated using the ICF(Ar^{2+}) derived from photo-ionization models by Pérez-Montero et al. (2007):

$$ICF(Ar^{2+}) = 0.749 + 0.507 \cdot \left(1 - \frac{O^{2+}}{O^+ + O^{2+}}\right) + +0.0604 \cdot \left(1 - \frac{O^{2+}}{O^+ + O^{2+}}\right)^{-1}$$

Finally, for iron the [FeIII] λ 4658 Å emission line was used and the electron temperature of [OIII]. We have taken the ICF(Fe^{2+}) from Rodríguez and Rubin (2004), which yields

$$ICF(Fe^{2+}) = \left(\frac{O^+}{O^{2+}}\right)^{0.09} \left(1 + \frac{O^{2+}}{O^+}\right)$$

The ionic and total abundances for each observed element for knots A, B, and, C are given in Table 3.9, along with their corresponding errors.

3.5 Discussion

3.5.1 Mass of the ionized gas

We have calculated the Hα luminosities for the four knots from our observed values, correcting for extinction according to the values found from the spectroscopic analysis. The

	PPak-field	Knot A	Knot B	Knot C
$12 + \log(O^+/H^+)$	8.50 ± 0.26	8.50 ± 0.18	8.56 ± 0.24	8.67 ± 0.24
$12 + \log(O^{2+}/H^+)$	7.98 ± 0.13	7.89 ± 0.10	7.84 ± 0.26	7.69 ± 0.21
12 + log(O/H)	8.62 ± 0.23	8.60 ± 0.16	8.63 ± 0.24	8.71 ± 0.24
$12 + \log(S^+/H^+)$	6.40 ± 0.15	6.22 ± 0.10	6.34 ± 0.14	6.50 ± 0.14
$12 + \log(S^{2+}/H^+)$	6.87 ± 0.29	6.79 ± 0.17	6.76 ± 0.38	6.84 ± 0.35
$ICF(S^+ + S^{2+})$	1.01 ± 0.11	1.01 ± 0.11	1.01 ± 0.12	1.00 ± 0.11
12 + log(S/H)	7.01 ± 0.25	6.89 ± 0.16	6.90 ± 0.31	7.01 ± 0.29
log(S/O)	-1.61 ± 0.34	-1.70 ± 0.23	-1.73 ± 0.39	-1.70 ± 0.37
$12 + \log(N^+/H^+)$	7.34 ± 0.15	7.25 ± 0.10	7.34 ± 0.14	7.51 ± 0.14
$ICF(N^+)$	1.30 ± 1.03	1.25 ± 0.69	1.18 ± 1.00	1.11 ± 0.87
12 + log(N/H)	7.45 ± 0.37	7.35 ± 0.26	7.42 ± 0.37	7.55 ± 0.37
log(N/O)	-1.17 ± 0.30	-1.25 ± 0.21	-1.23 ± 0.28	-1.16 ± 0.28
$12 + \log(Ne^{2+}/H^+)$	7.92 ± 0.18	7.49 ± 0.13	7.80 ± 0.34	7.49 ± 0.29
$ICF(Ne^{2+})$	1.52 ± 0.44	1.65 ± 0.38	1.85 ± 0.67	2.54 ± 1.30
12 + log(Ne/H)	8.10 ± 0.22	7.71 ± 0.16	8.08 ± 0.39	7.89 ± 0.37
log(Ne/O)	-0.52 ± 0.24	-0.89 ± 0.18	-0.57 ± 0.43	-0.82 ± 0.39
$12 + \log(Ar^{2+}/H^+)$	6.37 ± 0.31	6.22 ± 0.18	6.27 ± 0.41	6.22 ± 0.38
$ICF(Ar^{2+})$	1.22 ± 0.07	1.24 ± 0.04	1.23 ± 0.09	1.28 ± 0.04
12 + log(Ar/H)	6.45 ± 0.31	6.31 ± 0.18	6.36 ± 0.41	6.33 ± 0.38
log(Ar/O)	-2.16 ± 0.35	-2.28 ± 0.22	-2.27 ± 0.43	-2.38 ± 0.40
$12 + \log(Fe^{2+}/H^+)$	···	5.64 ± 0.14	···	5.94 ± 0.27
$ICF(Fe^{2+})$	···	1.41 ± 0.14	···	1.35 ± 0.13
12 + log(Fe/H)	···	5.79 ± 0.14	···	6.08 ± 0.27

Table 3.9: Ionic chemical abundances derived from forbidden emission lines, ICFs and total chemical abundances for elements heavier than helium.

Hα flux has been calculated in the mosaic, where no flux loss is expected. The resulting values are listed in Table 3.10.

The total number of hydrogen ionizing photons from the extinction corrected Hα flux has been derived in the same way as in Chapter §2

$$Q(H^0) = \frac{\alpha_B}{\alpha_{H\alpha}^{eff}} \times \frac{L_{H\alpha}}{h\nu_{H\alpha}}$$

From the number of Lyman α photons, $Q(H^0)$, it is possible to derive the corresponding mass of ionized hydrogen, M(HII) as

	Radius (pc)	F(Hα) (erg cm^{-2}s^{-1})	L(Hα) (erg s^{-1})	Q(H^0) (photon s^{-1})	M(HII) (M$_\odot$)
Knot A	190	1.93×10^{-12}	8.03×10^{39}	7.9×10^{51}	2.5×10^5
Knot B	95	1.08×10^{-13}	4.52×10^{38}	4.5×10^{50}	1.5×10^4
Knot C	115	3.76×10^{-13}	1.55×10^{39}	1.5×10^{51}	5.0×10^4
Knot D	100	1.51×10^{-13}	6.28×10^{38}	6.2×10^{50}	2.0×10^4

Table 3.10: Hα flux and derived parameters for the (mosaic) integrated spectra of the four knots.

$$M_{HII} = Q(H^0)\frac{m_p}{n_e \alpha_B}$$

The values are also listed in Table 3.10. All of them, given the assumptions of no dust absoption or photon leakage, represent lower limits.

Table 3.10 also gives the estimated radius, in parsecs, of a circular aperture covering the spatial distribution of the fibers used in the integrated spectra of each knot. This value is not intended to be accurate, but to give an order of magnitude of the sizes involved.

As it can be seen, the luminosities and masses of H^+ from this four knots are typical of *giant* HII regions and can be compared to the case of NGC 5471. Knot A of NGC 6946 is about a factor of 2 more luminous than Knot 1 in NGC 5471, while Knot C is similar to Knot 2 and the other two knots are of the same order of magnitude as Knot 4 or 10. It should be noted that the spatial scales involved in each case are very different. While the effective radius of the knots of NGC 5471 are around 60 pc, in NGC 6946 the radii can be 2 o 3 times larger.

3.5.2 Derived properties of the WR population

The detection and measurement of the WR blue bump in three of the four knots can be very useful for the study of the ionizing stellar population.

In this way, it is possible to compare the observed relative intensities and equivalent widths of the WR bumps with the predictions of Starburst 99 (Leitherer et al., 1999) population synthesis models as a function of the metallicity, age and star formation law of the cluster. For this purpose, we have run a Starburst 99 model based on stellar model atmospheres from Smith et al. (2002), Geneva evolutionary tracks with high stellar mass loss (Meynet et al., 1994), a Kroupa Initial Mass Function (IMF; Kroupa, 2002) in two intervals (0.1-0.5 and 0.5-100 M$_\odot$) with different exponents (1.3 and 2.3 respectively), a metallicity of Z = 0.02, the theoretical wind model (Leitherer et al., 1992) and a supernova cut-off of 8 M$_\odot$.

In Figure 3.26 we show the predicted equivalent width and relative intensity to Hβ for

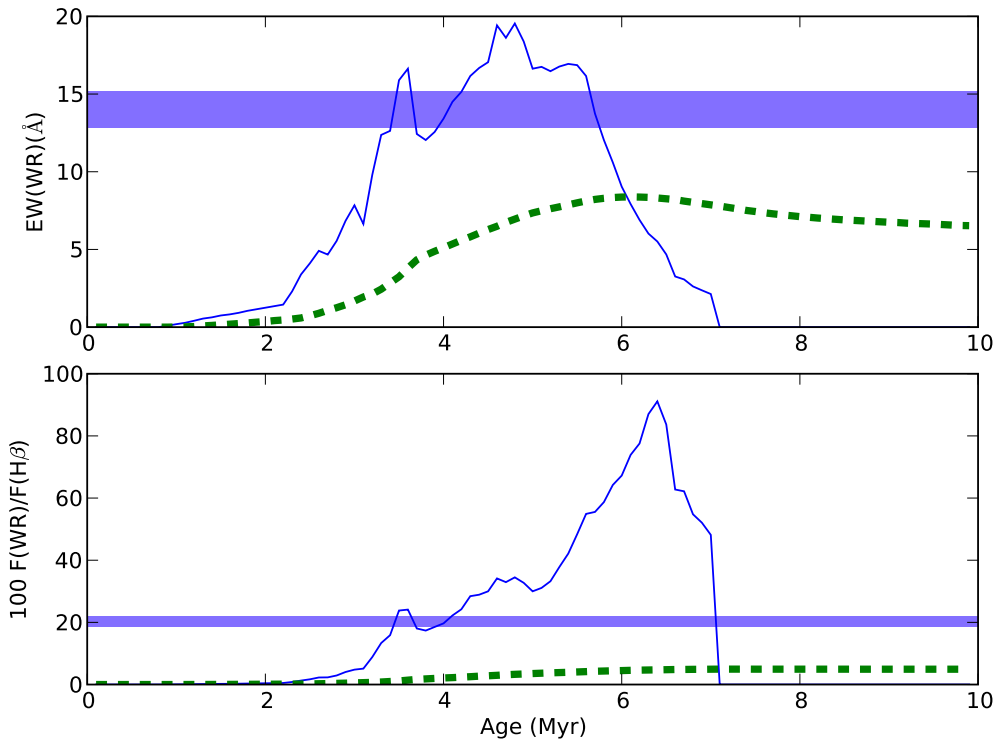

Figure 3.26: Relation between intensities and equivalent widths of the Wolf-Rayet blue bump as a function of the age of the cluster for a Z = 0.02 metallicity, according to Starburst 99 predictions. In both panels, (blue) solid lines represent instantaneous star formation and (green) dashed lines continuous star formation. The (light blue) horizontal band represents the error in the measurement of the appropriate quantity for knot A.

the blue bump as a function of the cluster age for a metallicity Z = 0.02 ($Z_{\odot}$), the closest value according with the total oxygen abundances derived. The (blue) solid lines represent in both plots the evolution of an instantaneous burst, while the (green) dashed lines do for a continuous star formation history with a constant star formation rate. The (light blue) horizontal bands in both panels represents the error in the measurement of the appropriate quantity for knot A. As noted in section 3.4.7, the quantities plotted depend strongly on metallicity. The models predict brightest and most prominent features for higher metallicity, according with the stellar model atmospheres for WR stars (Crowther, 2007). At the same time, we notice that in the instantaneous star formation the WR features appear during the interval between 2 and 5 Myr and they reach higher intensities. On the other hand, for a continuous star formation history, the WR features appear at the same age and, despite of reaching lower intensities, they converge to a non-zero value at older ages.

By comparing the relative intensities and equivalent widths of the three knots, shown in Table 3.3, we see that all of them are larger than the model-predicted values for a constant star formation law, but match fairly well with the values predicted for an instantaneous burst

Object ID	N(WR)	WR/O
Knot A	125 ± 10	0.047 ± 0.008
Knot B	5 ± 2	0.002 ± 0.001
Knot C	22 ± 3	0.008 ± 0.001

Table 3.11: Derived number of WR stars and ratios between WR and O stars.

of star formation. The only exception is knot B, were the equivalent width is slightly higher than predicted by the models. However, the observed relative intensities are inside in the expected range of theoretical values. From both quantities, an age around 4 Myr fits well for the three knots, indicating that these bursts are very young.

As already told in section 3.4.7, a red bump has been marginally detected in knot A, indicating the existence of WC stars, but no accurate measurements were made due the low signal-to-noise, so only the total number of WR (WN+WC) can be estimated.

Table 3.11 shows the number of O and WR stars. We have derived these numbers by comparing the dereddened luminosities of Hα and of the WR blue bump with the predictions of the instantaneous model of Starburst 99. As it can be seen, knot A contains more than one hundred WR stars, as expected from the strong blue bump feature from its integrated spectra. Interestingly, Knot B has a few WR stars, despite its weak contribution in the continuum map of Figure 3.15.

Other way to estimate the number of WR stars is by means of calibration of WR stars. Smith (1991) estimates that a single WN7 star emits 3.2 $\times$ 10^{36} ergs s^{-1} at 4650Å, which yields a total number of 120 ± 10 WR stars, very close to the value derived from the Starburst 99 model. On the other hand, Vacca and Conti (1992) estimate that one WN7 star emits 1.7 $\times$ 10^{36} ergs s^{-1}, rising the number of WR stars almost by a factor of 2.

3.5.3 Metal content

We derived oxygen, sulphur, nitrogen, neon, argon and iron chemical abundances in the integrated spectrum of the PPak-field and in three of the four knots, where auroral lines of [OIII], [OII] and [SIII] have been measured and thus their respective electron temperature derived. Due to the quality of the data, the electron temperatures derived and thus, the metallicities, have associated errors comparable to the dispersion found in empirical calibrations.

The derived temperatures (see Table 3.7) for the three knots and the integrated spectrum of the PPak-field show values very similar for all of them, centered in 8000K for t([OIII]). Knot A shows a higher temperature, as expected from its Hα luminosity, but similar to the other measurements within the errors. Similarly, all the values for t([OII]) are very close. The only exception is the one estimated for knot B from a relation with t([OIII]) based on

photoionization models. This value is a little bit higher than the mean value of the other direct measurements. It is known that the relation between t([OII]) and t([OIII]) does not present a clear trend, showing a large scatter. The [OII] temperature derived from relations based on the photoionization models described in Pérez-Montero and Díaz (2003) covers the range of values for a sample of HII galaxies, GEHRs and diffuse HII regions in the Galaxy and the Magellanic Clouds, as shown in Hägele et al. (2006). Higher density models show lower values of t([OII]) for a given t([OIII]), being this effect more notable at high electron temperatures (see Figure 4.12 of Chapter §4). Our objects lie in the low temperature region, where $N_e = 100$ and $N_e = 500$ models are very close. The derivation from t([OIII]) gives a slightly higher temperature than the directly derived, but still within the errors for our sample. A worse situation is presented for the relation based on the photoionization models by Stasińska (1990), which could yield a higher [OII] temperature by 2000 K for the regime of our data. These differences may translate into lower O^+/H^+ ratios, and therefore lower total abundances by an amount of 0.35 dex, taking as an example knot A. Nevertheless, the differences between the derived temperatures from Pérez-Montero and Díaz (2003) and the directly measured give abundances compatible within the errors.

Regarding the [SIII] temperature, the only direct temperature available we have is for Knot A, 7300 ± 1200 K. The value derived from the empirical relation found by Hägele et al. (2006) using t([OIII]) is 7400 ± 1300 K, which matches perfectly the direct measurement. In this case, the relation found by Garnett (1992) gives a [SIII] temperature 1400 K higher. As it has been told, we have used the former relation to estimate t([SIII]) for the other knots, in which the [SIII] λ 6312 Å auroral line could not be measured.

The abundances derived for the integrated spectra show values near the solar ones. The abundances of various elements in HII regions in NGC 6946 have been studied by McCall et al. (1985) and Ferguson et al. (1998). At the distance of the HII complex discussed in this paper studies find oxygen abundances very similar to solar. The galaxy shows a clear abundance gradient as a function of distance from the center. Belley and Roy (1992) estimated the global oxygen abundance gradient of NGC 6946 by means of imaging spectrophotometry in the nebular lines Hα, Hβ, [NII], and [OIII]. Using the empirical calibration of Edmunds and Pagel (1984), they calculated O/H abundances for HII distributed throughout the disc of the galaxy. For NGC 6946, they found that the global gradient is given by Δ log (O/H) / ΔR = -0.089 ± 0.003 dex kpc^{-1}, and extrapolated central abundances of 9.36 ± 0.02. This value is the same as the one estimated by Ferguson et al. (1998) using emission line spectra and the empirical relation of McGaugh (1991). At the projected galactocentric distance of our HII complex (6.85 kpc), this corresponds to 12 + log(O/H) = 8.75, 0.1 dex higher than our mean direct measurement, but within the errors. Larsen et al. (2006), by means of H and K band spectra for a young luminous super star cluster at 4.8 kpc, derived an (direct) abundance of 12 + log(O/H) = 8.76, about 0.2 dex lower values of HII regions at their galactocentric distance. To our knowledge, there is no other direct abundance determinations of our HII

complex in the literature.

The logarithmic N/O ratios found for Knot A, B, and C are -1.25 ± 0.21, -1.23 ± 0.28 and -1.16 ± 0.28 respectively. They point to a constant value within the errors. It is worth noting that an analysis of the data via a derivation of the [OII] temperature from t([OIII]) according to Stasińska (1990) models, would provide a N/O ratio larger than the directly derived. An overprediction of this temperature by 1500 K at t([OII]) = 8000K would increase the N/O ratio by 0.25 dex.

Finally, the log(S/O) ratios found for the three knots are -1.75 ± 0.23, -1.73 ± 0.39 and -1.70 ± 0.37, which are lower by a factor of 2.2 as compared with log (S/O) = -1.39, the solar value (Grevesse and Sauval, 1998). Nevertheless, they are consistent with this value within the large observational errors. Both log(N/O) and log(S/O) ratios are very similar to values found for the high metallicity HII regions analyzed by Castellanos et al. (2002).

The analysis discussed above was possible since we could derived temperatures for some of the most important ions. This is not the case of Knot D. The calculation of metallicities in this knot can only be carried out with calibrations based on the strongest emission lines because no auroral lines were detected and the direct method cannot be used.

The different strong-line methods for abundance derivations, which have been widely studied in the literature, are based on the direct calibration of the relative intensity of some bright emission lines against the abundance of some relevant ions present in the nebula. For the case of oxygen, we take the calibrations studied by Pérez-Montero and Díaz (2005), who obtain different uncertainties for each parameter in a sample of ionized gaseous nebulae with accurate determinations of chemical abundances in the whole range of metallicity.

We have applied these empirical calibrators to all the integrated spectra, the ones with auroral lines and knot D, from which no direct abundance determination has been made. The reader is referred to Appendix C for the definitions and detailed equations involved in each of the empirical calibrators used in this analysis.

Among the strong-line parameters available, we have used the O_{23} parameter (also known as R_{23}, originally defined by Pagel et al. (1979) and based on [OII] and [OIII] strong emission lines), which is characterised by its double-valued relation with metallicity. According to the values measured in other knots, we use the analytic expressions for the McGaugh (1991) upper branch given by Kobulnicky et al. (1999).

The N2 parameter (defined by Storchi-Bergmann et al., 1994) is based on the strong emission lines of [NII]. It remains single-valued up to high metallicities in its relation to oxygen abundance, and it is almost independent of reddening and flux calibration. We used the empirical calibration of this parameter from Denicoló et al. (2002) to derive the oxygen abundance.

The parameter O3N2, defined by Alloin et al. (1979) depends on strong emission lines of [OIII] and [NII]. We used the calibration due to Pettini and Pagel (2004).

The measurement of the [SII] and [SIII] infrared lines allows the use of the S_{23} parameter,

defined by Vilchez and Esteban (1996). We used the calibration done by Pérez-Montero and Díaz (2005).

The combination of the S_{23} and O_{23} parameters gives S_{23}/O_{23}, defined by Díaz and Pérez-Montero (2000), a parameter that increases monotonically with the oxygen abundance up to oversolar regime and which is very useful to study variations over wide ranges of metallicity. We applied the calibration found in Pérez-Montero and Díaz (2005).

The S_3O_3 and Ar_3O_3 parameters were defined and calibrated by Stasińska (2006). They used the ratio of [ArIII] 7136 Å and [OIII] 5007 Å, and [SIII] 9069 Å and [OIII] 5007 Å emission lines, respectively.

Finally, the N_2O_2 parameter, defined by Pérez-Montero and Díaz (2005) as the ratio between [NII] and [OII] emission lines, can be used to obtain the N/O ratio. In this case, we have used the calibration by Díaz et al. (2007), which includes high metallicity HII regions.

In Table 3.12 we present the oxygen and nitrogen abundances and their uncertainties for each integrated spectra as derived using the empirical calibrators listed above. As it can be seen, the estimated oxygen abundances coincides well with those obtained from the direct method, all of them around the solar value.

The parameters involving the sulphur lines give slightly lower abundance values. In this case, it should be noted that the near IR sulphur lines relative to the hydrogen recombination lines are more affected by reddening than in the case of oxygen when no Paschen lines are observed, which is the case. Moreover, as we showed in section 3.3.9, the near infrared spectra are affected by atmospheric absorption. Although we corrected for this effect, we concluded that only the [SIII] λ 9069 Å could be used. Even after the correction, if this line would still be affected by some absorption, this would increase the derived metallicity. Nevertheless, as well as the rest of calibrators, the abundances are consistent taken into account the errors in the calibrations and in the measurements.

Regarding the N_2O_2 parameter, very little difference is found in N/O among the four knots, which are also consistent with the ratio derived directly.

Both from the direct method and empirical calibrators, we can conclude that the four knots have very similar abundances, with no evidence of abundance variations.

3.5.4 Ionization structure

Table 3.12 gives some general properties of the integrated spectra as the ratio of lines representative of the ionization structure and derived ionization parameters.

Figure 3.27 shows the BPT diagrams as Figure 3.19, but including the five data from the integrated spectra. The (red) circle points represent the values of the knots, while the (yellow) square point the position in the diagram of the whole PPak field. As it can be appreciated, the integrated measurements span over the point-to-point values, with the same large spread in $\log([\text{OIII}]\,\lambda\,5007/\text{H}\beta)$ as compared with the relative small variation in the other two line

	PPak-field	Knot A	Knot B	Knot C	Knot D
$\log(O_{23})$	0.70 ± 0.03	0.70 ± 0.01	0.80 ± 0.05	0.65 ± 0.03	0.59 ± 0.04
12 + log(O/H) (O_{23}-upper)	8.67 ± 0.19	8.69 ± 0.19	8.51 ± 0.19	8.69 ± 0.19	8.75 ± 0.19
N_2	-0.66 ± 0.02	-0.79 ± 0.01	-0.59 ± 0.03	-0.57 ± 0.02	-0.54 ± 0.02
12 + log(O/H) (N_2)	8.49 ± 0.25	8.40 ± 0.25	8.55 ± 0.25	8.56 ± 0.25	8.60 ± 0.25
O3N2	0.69 ± 0.03	0.96 ± 0.01	0.53 ± 0.06	0.32 ± 0.03	0.18 ± 0.04
12 + log(O/H) (O3N2)	8.51 ± 0.25	8.42 ± 0.25	8.56 ± 0.25	8.63 ± 0.25	8.67 ± 0.25
$\log(S_{23})$	0.10 ± 0.02	0.06 ± 0.01	0.07 ± 0.04	0.09 ± 0.02	0.07 ± 0.03
12 + log(O/H) (S_{23})	8.34 ± 0.20	8.27 ± 0.20	8.28 ± 0.20	8.33 ± 0.20	8.29 ± 0.20
$\log(S_{23}/O_{23})$	-0.60 ± 0.04	-0.63 ± 0.01	-0.73 ± 0.07	-0.55 ± 0.03	-0.52 ± 0.05
12 + log(O/H) (S_{23}/O_{23})	8.39 ± 0.27	8.34 ± 0.27	8.22 ± 0.27	8.45 ± 0.27	8.50 ± 0.27
$\log(S_3O_3)$	-0.83 ± 0.03	-0.85 ± 0.01	-0.78 ± 0.06	-0.57 ± 0.03	-0.53 ± 0.04
12 + log(O/H) (S_3O_3)	8.43 ± 0.25	8.42 ± 0.25	8.45 ± 0.25	8.53 ± 0.25	8.54 ± 0.25
$\log(AR_3O_3)$	-1.28 ± 0.07	-1.33 ± 0.01	-1.21 ± 0.08	-1.14 ± 0.08	-1.10 ± 0.07
12 + log(O/H) (AR_3O_3)	8.50 ± 0.23	8.46 ± 0.23	8.54 ± 0.23	8.58 ± 0.23	8.59 ± 0.23
N_2O_2	-0.61 ± 0.03	-0.66 ± 0.01	-0.70 ± 0.05	-0.54 ± 0.03	-0.47 ± 0.04
log(N/O) (N_2O_2)	-1.18 ± 0.14	-1.22 ± 0.14	-1.25 ± 0.14	-1.14 ± 0.14	-1.09 ± 0.14
log([OII]/[OIII])	0.36 ± 0.03	0.14 ± 0.01	0.63 ± 0.06	0.68 ± 0.03	0.73 ± 0.05
log(u) ([OII]/[OIII])	-3.31	-3.13	-3.53	-3.56	-3.60
log([SII]/[SIII])	0.07 ± 0.02	-0.28 ± 0.01	0.14 ± 0.04	0.12 ± 0.02	0.21 ± 0.02
log(u) ([SII]/[SIII])	-3.11	-2.53	-3.22	-3.19	-3.34
log([OIII]5007/Hβ)	0.08 ± 0.01	0.22 ± 0.01	-0.03 ± 0.01	-0.21 ± 0.01	-0.31 ± 0.01
log([SII]6717,31/Hα)	-0.62 ± 0.01	-0.85 ± 0.01	-0.61 ± 0.01	-0.60 ± 0.01	-0.57 ± 0.01
log([NII]/[SII])	0.15 ± 0.02	0.22 ± 0.01	0.18 ± 0.03	0.19 ± 0.02	0.20 ± 0.02
$\log(O^+/O2+)$	0.52 ± 0.29	0.61 ± 0.20	0.74 ± 0.35	0.97 ± 0.32	···
$\log(S^+/S^{2+})$	-0.47 ± 0.33	-0.57 ± 0.20	-0.40 ± 0.41	-0.35 ± 0.38	···
log(η)	0.99 ± 0.43	1.18 ± 0.29	1.14 ± 0.54	1.32 ± 0.50	···
log(η')	0.29 ± 0.04	0.42 ± 0.02	0.49 ± 0.07	0.56 ± 0.04	0.52 ± 0.05

Table 3.12: Oxygen and nitrogen abundances and their uncertainties for each integrated spectrum as derived using different empirical calibrators. The line ratios representative of the ionization structure, the ionization parameter (u) and the η and η' parameters, are also included.

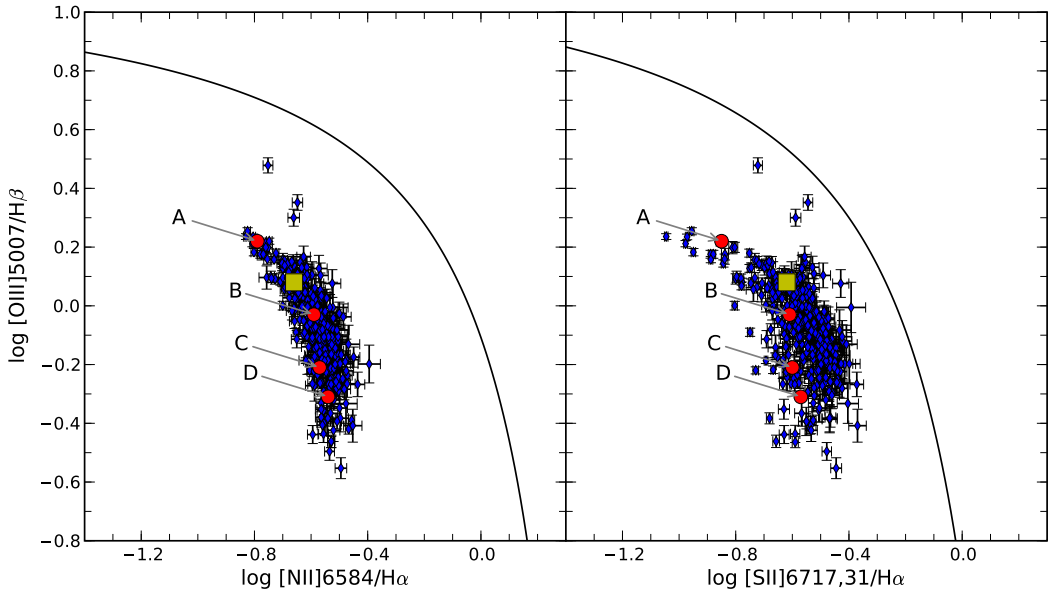

Figure 3.27: BPT diagrams including the values of the integrated spectra. The (red) circle points represents the values of the knots, while the (yellow) square point the position in the diagram of the whole PPak field.

ratios. As expected, the integrated value of the whole PPak field appears as a relative high excitation value, implying that Knot A is weighting in the integrated spectrum being the most important contribution to the total spectrum.

The volume-averaged ionization parameter u is defined as

$$u = \frac{Q}{4\pi R^2 nc}$$

where Q is the ionizing photon luminosity, R is the radius of the Strömgren sphere, n the number density of the gas, and c the speed of light. This parameter is essentially the local ratio of Lyman continuum photons to gas density, which determines the degree of ionization at any particular location within the nebula. Table 3.12 contains the ionization parameter as estimated from the [OII]/[OIII] and [SII]/[SIII] ratios. For the last one, Diaz et al. (1991) gives

$$log\, u = -1.68\, log([SII]/[SIII]) - 2.99$$

For the former ratio, the ionization parameter can be calculated from (Díaz et al., 2000)

$$log\, u = -0.80\, log([OII]/[OIII]) - 3.02$$

As it can be appreciated, the value of u derived from the [OII]/[OIII] ratio is systematically lower than the one obtained from the [SII]/[SIII] ratio. This could imply low effective

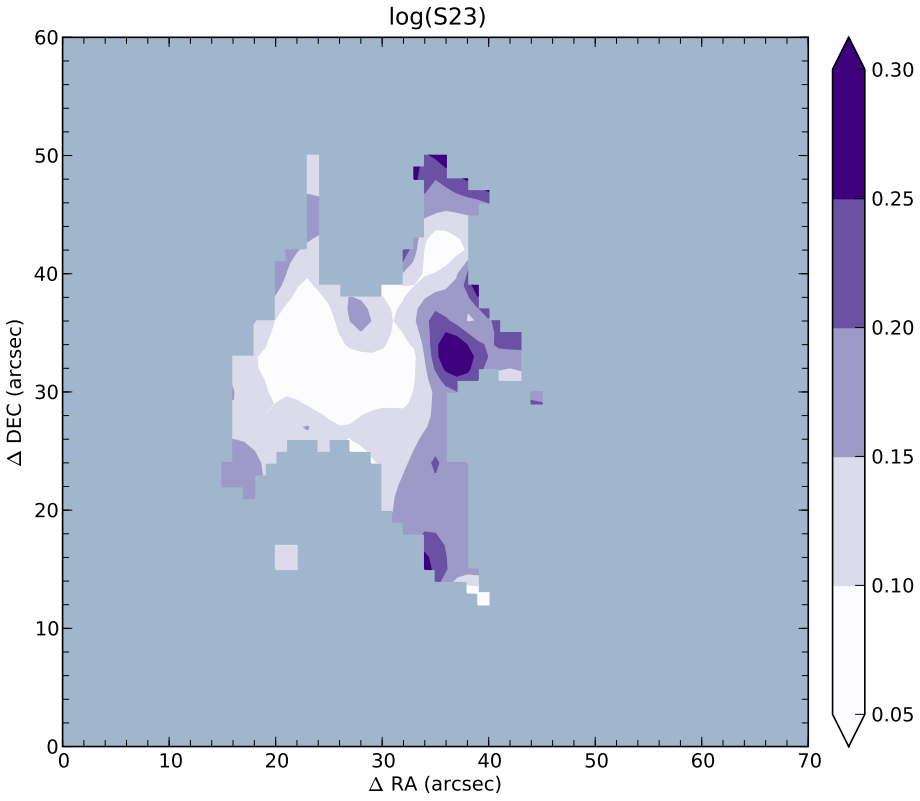

Figure 3.28: Map of the parameter S_{23}.

temperatures for the ionizing stars. As expected, the highest ionization parameter is given by Knot A.

The values of both ratios found for each knot are typical of high metallicity HII regions, which are found to be between -0.3 and 0.2 for log([SII]/[SIII]) and between 0.1 and 1 for log([OII]/[OIII]) (see the distribution of these ratios for high metallicity disc HII regions in Figure 17 of Díaz et al., 2007).

As mentioned in section 3.4.8, the Hα luminosity of the emission knots amounts to about 50% of the total PPak field of view. Knot A is the brightest of them and provides 75% of the combined flux from the knots and 38% of the total Hα flux. This knot has the highest excitation as characterised by the [OII]/[OIII] ratio and dominates the excitation deduced for the PPak field integrated spectrum. On the other hand the measured Hβ equivalent width for this entire region is about 40 Å, much lower than the ones measured for the individual knots that range from 60 to 100 Å. That is, the integrated spectra shows high excitation and a relatively evolved age which does not correspond to the individual knot evolutionary stages.

The ionization structure of a nebula depends essentially on the shape of the ionizing continuum and the nebular geometry. Figure 3.29 shows the point-to-point behaviour of the

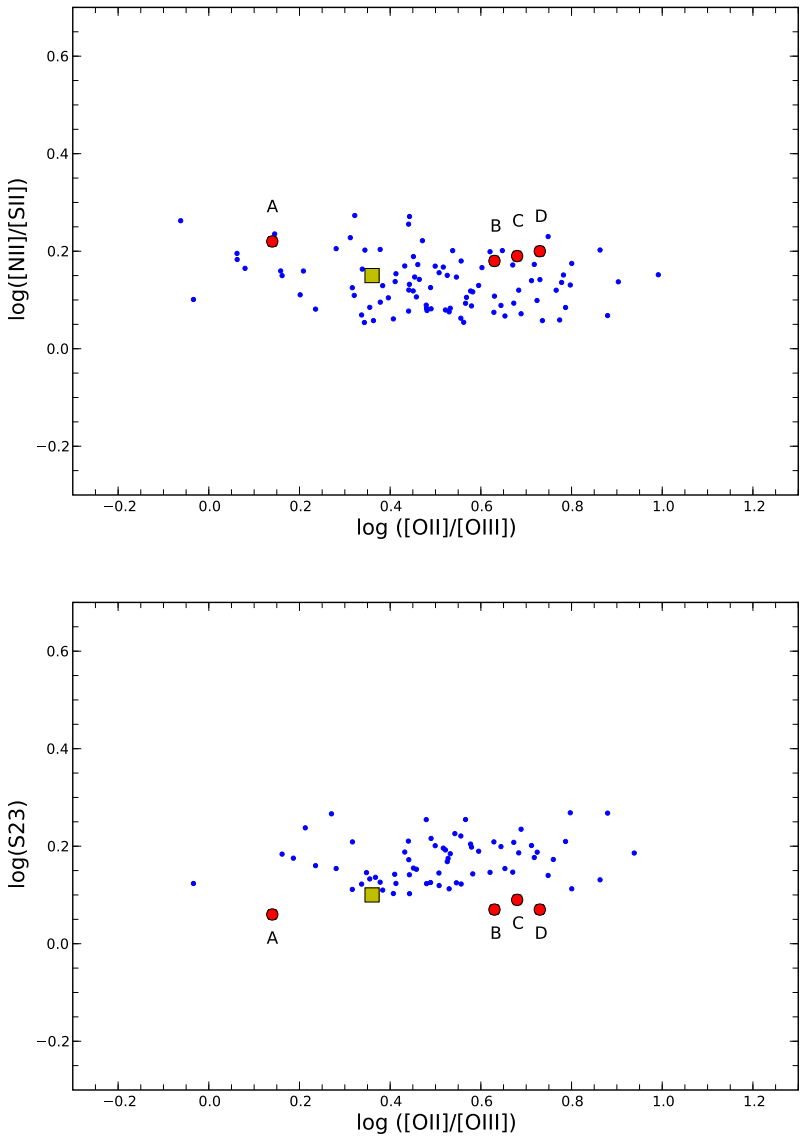

Figure 3.29: Point-to-point variations of the line ratio [NII]/[SII] (*upper*) and S_{23} parameter (*lower*) versus the excitation measured as [OII]/[OIII]. The (red) circle points represents the integrated values of the knots, while the (yellow) square point the position in the diagram of the whole PPak field.

observed line ratios [NII] $\lambda\lambda$ 6585,6584/[SII] $\lambda\lambda$ 6717,6731 and the S_{23} parameter as a function of the degree of excitation measured by [OII]/[OIII]. All values were obtained from the first pointing set, since the quantities represented involve the infrared sulphur lines. Although the first ratio contains only lines present in the blue part of the spectra, we have decided to use for this ratio only the first dithering instead of the mosaic for consistency in the comparison. In this case, for each point, the accuracy of the ratios is typically better than 20 percent.

The ratio [NII] $\lambda\lambda$ 6585,6584/[SII] $\lambda\lambda$ 6717,6731 versus the excitation seems fairly constant, although it can be appreciated a slight relative decrease with [OII]/[OIII]. This effect was also

found for several HII regions in M101 by McCall et al. (1985) and in NGC 604 by Diaz et al. (1987). According to these authors, this effect can be understood as an excitation effect due to the lower ionization potential of S^+ with respect to to N^+ combined with the relative low S^+/S^{++} ratio.

Regarding the S_{23} parameter (see map in Figure 3.28), as it can be appreciated in the lower panel of Figure 3.29, despite the large range of values for the excitation, this parameter seems to remain uniform. Nevertheless, due to the low signal-to-noise of the infrared sulphur lines of our data set, more data is needed to test this behaviour.

Chapter 4

Long-slit spectrophotometry of multiple knots of H II galaxies

4.1 Introduction

HII galaxies are low mass irregular galaxies with, at least, a recent episode of violent star formation (Melnick et al., 1985) concentrated in a few parsecs close to their cores. The intense processes of star formation occurring in the luminous knots of HII galaxies make them easily detected in surveys based on strong emission lines. In fact, these knots present spectra similar to those of giant extragalactic HII regions (GEHRs; Sargent and Searle, 1970; French, 1980). Therefore, we can apply the same measurement techniques as for HII regions. In this way, it is possible to use these knots to ascertain the basic properties of the host galaxy, such as extinction, metallicity, star formation rates, and from them derive the chemical evolution and the star formation history of the whole galaxy.

In some cases, it is possible to detect in these objects, intermediate-to-old stellar populations which have a more uniform spatial distribution than the bright and young stellar populations associated with the ionizing clusters (Schulte-Ladbeck et al., 1998). This older population produces a characteristic spectrum with absorption features which mainly affect the hydrogen recombination emission lines (see Diaz, 1988). In some cases, the underlying stellar absorption can severely affect the ratios of HI line pairs and hence the determination of the reddening constant.

HII galaxies are a subset of blue compact dwarf galaxies (BCDs), which are selected by their compact aspect and blue colour. A considerable number of the objects observed at

intermediate and high redshifts seems to have properties similar to that of HII galaxies we know in the Local Universe. This type of objects is thought to be more frequent in a younger Universe and they are possible building blocks for the largest galaxies that we can detect at low redshifts (Kauffmann et al., 1993). If interactions among dwarf irregular galaxies was a basic mechanism of galaxy formation in the past, it is important to study the cases taking place in the nearby Universe now and the links between dwarf interactions and the star formation history of BCDs. Moreover, it is important to know the true distribution functions of the properties of theses objects, among which the chemical abundances are of the greatest relevance.

Hägele et al. (2006) and Hägele et al. (2008) performed a detailed analysis of a sample of 10 HII galaxies in the Local Universe, deriving precise elemental abundances from high signal-to-noise spectra. Their spectral range included from the UV [OII] $\lambda\lambda$ 3727,29 Å doublet, to the near IR [SIII] $\lambda\lambda$ 9069,9532 Å lines. This allowed the derivation of the different line temperatures: T_e([OII]), T_e([SII]), T_e([OIII]), T_e([SIII]), T_e([NII]), needed in order to study the temperature and ionization structure of each HII galaxy considered as a multizone ionized region.

From this sample, some of these objects presented several bright knots. We selected one galaxy, J1657 (we follow the ID used in that work), at a redshift of 0.038 (161.2 Mpc, from Mould et al., 2000), whose knots have enough signal-to-noise to perform a precise analysis similar to the one done for the main knot and in which the slit covers their lineal spacial distribution.

To complete this study, we observed another HII galaxy which presents a similar morphology. Although IIZw71 is catalogued as a BCD galaxy it is, in fact, characterised by several very luminous Hα knots distributed along a ring that is rotating around the host galaxy. It has been catalogued as a probable polar-ring galaxy (B17) in the Polar-Ring Catalogue (Whitmore et al., 1990). Polar ring galaxies (PRGs) are systems with two kinematically separated components. The central component (the host galaxy) is usually a lenticular galaxy or occasionally an elliptical galaxy. The other component, the polar ring, follows an approximately circumpolar orbit around the host and it is characterised by the presence of stars, molecular gas ,and dust, inside another larger ring composed of neutral hydrogen. Thus, this ring becomes an appropriate place for star formation. It is thought that these objects are formed as a consequence of the interaction between galaxies with a small impact parameter (Bournaud and Combes, 2003). In the case of IIZw71, there are proofs from interferometric observations of interaction with IIZw70, another BCD. In fact, although clearly separated on optical images, both galaxies share a common HI envelope with a gaseous bridge or streamer connecting both structures (see Figure 3 of Cox et al., 2001). This points to an ongoing interaction between the two galaxies. Therefore this system becomes an ideal scenario for studying the effects of interactions in the formation and evolution of BCDs in the Local Universe. A distance of 18.1 Mpc to the system is adopted by Cox et al. (2001), taking a

value of $H_o = 75$ Km s^{-1} Mpc^{-1}. This implies a linear scale of 90 pc/arcsec on the sky.

It is important to realize that the combination of accurate spectrophotometry and wide spectral coverage cannot be achieved using single-arm spectrographs where, in order to reach the necessary spectral resolution, the wavelength range must be split into several independent observations. In those cases, the quality of the spectrophotometry is at best doubtful mainly because the different spectral ranges are not observed simultaneously. This problem applies to both objects and calibrators. Furthermore, one can never be sure of observing exactly the same region of the nebula in each spectral range. To avoid all these problems, the use of double-arm spectrographs is required.

In this chapter we present simultaneous blue and red observations the galaxy J1657 observed with the double arm TWIN spectrograph at the 3.5m telescope of the Calar Alto Observatory at the Complejo Astronómico Hispano Alemán (CAHA). Similarly, in a single long-slit exposition, we have observed the main bursts of star formation along the direction of the polar ring of IIZw71 with the ISIS double-beam spectrograph mounted on the 4.2m William Herschel Telescope (WHT). The analysis of the obtained spectra were used to make a comparative analysis of the different bursts of star formation. In the next section we describe the long-slit spectroscopic observations of the two objects. In section 4.3, we present the results of our study, including the determination of physical properties, such as electron density and reddening in the observed knots, and of chemical abundances. In section 4.4 we discuss our results, including a study of the kinematics of the polar ring, the determination of metallicity, the reddening, the stellar properties by means of fitting synthesis stellar populations and the star formation rates in the individual knots.

4.2 Observations and reduction

4.2.1 CAHA observations

Blue and red spectra were obtained simultaneously using the double beam Cassegrain Twin Spectrograph (TWIN) mounted on the 3.5m telescope of the Calar Alto Observatory at the Complejo Astronómico Hispano Alemán (CAHA), Spain. This galaxy was part of a four night observing run in 2006 June and they were acquired under excellent seeing and photometric conditions. Site#22b and Site#20b, 2000×800 px 15 μm, detectors were attached to the blue and red arms of the spectrograph, respectively. The T12 grating was used in the blue covering the wavelength range 3400-5700 Å (centered at $\lambda_c = 4550$ Å), giving a spectral dispersion of 1.09 Å pixel^{-1} (R $\simeq$ 4170). On the red arm, the T11 grating was mounted providing a spectral range from 5800 to 10400 Å ($\lambda_c = 8100$ Å) and a spectral dispersion of 2.42 Å pixel^{-1} (R $\simeq$ 3350). The pixel size for this set-up configuration is 0.56 arcsec for both spectral ranges. The slit width was $\sim$1.2 arcsec, which, combined with the spectral dispersions, yielded spectral resolutions of about 3.2 and 7.0 Å FWHM in the blue and the

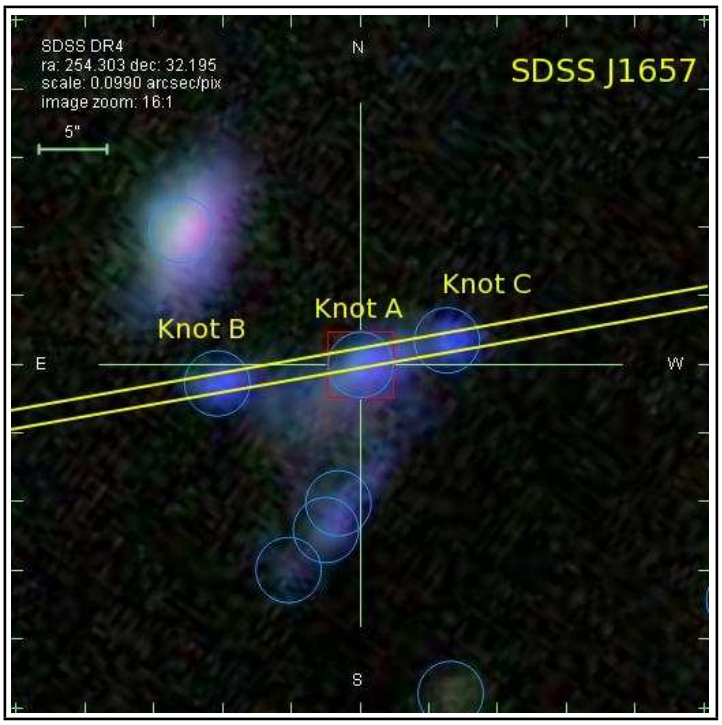

Figure 4.1: False colour image of J1657. This image was obtained using the SDSS explore tools. Circles and squares represent the photometric and spectroscopic SDSS targets, respectively. Note the alignment of the three knots along the parallactic angle.

red respectively. The observations were made at paralactic angle to avoid effects of differential refraction in the UV. As it can be seen in Figure 4.1, three knots of J1657 are almost perfectly aligned along the paralactic angle. The instrumental configuration, summarized in Table 4.1, covers the whole spectrum from 3400 to 10400 Å (with a gap between 5700 and 5800 Å) providing at the same time a moderate spectral resolution. As in the case of IIZw71, this guarantees the simultaneous measurement of the nebular lines from [OII] $\lambda\lambda$ 3727,29 to [SIII] $\lambda\lambda$ 9069,9532 Å at both ends of the spectrum, in the very same region of the galaxy, with a good signal-to-noise ratio that allows the measurement of the weak lines. Typical values of signal-to-noise ratios are 64 for [OIII] λ 4363 and 21 for [SII] λ 4068. Unfortunately, although the spectral range allowed the observation of the Balmer discontinuity, not enough signal-to-noise ratio was achieved to measure this jump with an acceptable accuracy.

4.2.2 WHT observations

The long-slit spectrophotometric observations of IIZw71 were obtained using the ISIS double-beam spectrograph mounted on the 4.2m William Herschel Telescope (WHT) of the Isaac Newton Group (ING) at the Roque de los Muchachos Observatory on the Spanish island of La Palma. They were acquired on 2005 July 8 during one single night's observing run and under photometric conditions, with an average seeing of 0.7 arcsec. The EEV12 and

Spectral range (Å)	Disp. (Å px^{-1})	FWHM (Å)	Spatial res. ($''$ px^{-1})	Exposure Time s
		WHT - ISIS		
3670-5070	0.45	1.0	0.2	4× 1200
5500-7800	0.86	3.5	0.2	2× 1200
7600-9900	0.86	3.5	0.2	2× 1200
		CAHA - TWIN		
3400-5700	1.09	2.8	0.56	5× 1800
5800-10400	2.42	6.9	0.56	5× 1800

Table 4.1: WHT and CAHA instrumental configuration

Marconi2 detectors were attached to the blue and red arms of the spectrograph, respectively. The R600B grating was used in the blue covering the wavelength range 3670-5070 Å (centred at $\lambda_c = 4370$ Å), giving a spectral dispersion of 0.45 Å pixel^{-1}. On the red arm, the R316R grating was mounted in two different central wavelengths providing a spectral range from 5500 to 7800 Å ($\lambda_c = 6650$ Å) and from 7600 to 9900 Å ($\lambda_c = 8750$ Å) with a spectral dispersion of 0.86 Å pixel^{-1}. To reduce the readout noise of our images, the observations were taken with the 'SLOW' CCD speed. The pixel size for this set-up configuration is 0.2 arcsec for both spectral ranges. The slit width was ∼1 arcsec, which, combined with the spectral dispersions, yields spectral resolutions of about 1.0 and 3.5 Å FWHM in the blue and red arms, respectively. The instrumental configuration, summarized in Table 4.1, was planned to cover the whole spectrum from about 3500 to 10000 Å, at the same time providing the required moderate spectral resolution. Unfortunately, the signal-to-noise achieved was by far not as good as in the CAHA observations. The value of signal-to-noise ratio is 10 for [OIII] λ 4363.

To cover all knots along the polar ring at the same exposure, all the spectra were taken at PA= 30°, an average of 56° off paralactic angle, and the spectra are thus somehow affected by atmospheric differential refraction. Taking the mean air mass into account during the observations of this object (≈ 1.25) and following the curves by Filippenko (1982), we calculated that the displacement between [OII] 3727 Å and [SIII] 9069 Å, which are the emission lines the most separated in wavelength, is no greater than 0.9 arcsecs.

4.2.3 Data reduction

Several bias and sky flat field frames were taken at the beginning and at the end of the night in both arms. In addition, two lamp flat fields and one calibration lamp exposure were performed at each telescope position. The calibration lamp used was CuNe+CuAr for

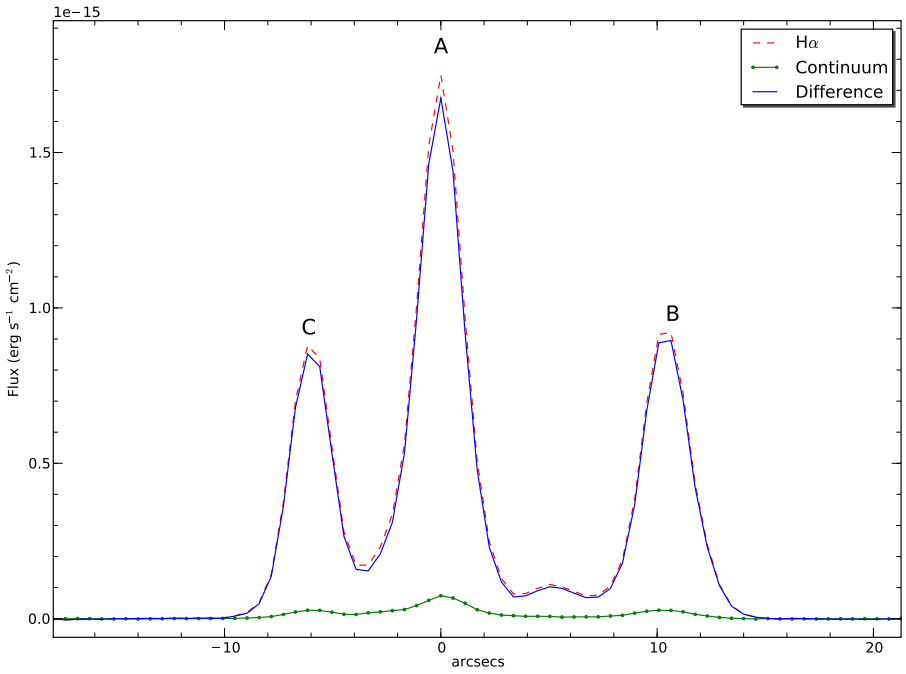

Figure 4.2: Spatial profile of the light distribution along the slit for the observed Hα emission (dashed red line), the adjacent continuum (thick green line), and the difference between the two (thin blue line).

IIZw71 and He-Ar for J1657. The images were processed and analysed with IRAF[1] routines in the usual manner. This procedure includes the removal of cosmic rays, bias subtraction, division by a normalised flat field, and wavelength calibration. Typical wavelength fits were performed using 30-35 lines in the blue and 20-25 lines in the red and polynomials of second to third order. These fits were made at 117 different locations along the slit in each arm for the WHT-ISIS observations (beam size of 10 pixels) and at 80 different locations for the CAHA-Twin observations (beam size of 10 pixels) obtaining rms residuals between ∼0.1 and ∼0.2 pix for the WHT data and between ∼0.1 and ∼0.3 pix for the CAHA data.

In the last step, the spectra were corrected for atmospheric extinction and flux-calibrated. For both arms of WHT, two standard star observations were used, allowing a good spectrophotometric calibration with an estimated accuracy of about 5%. For the CAHA data, four standard star observations were performed each night at the same time for both arms, allowing a good spectrophotometric calibration with an estimated accuracy of about 3% between the different standard star flux calibration curves.

Figure 4.2 and the left panel of Figure 4.3 show the spatial distribution of the Hα flux along the slit for IIZw71 and J1657. The emission line profile in these plots have been generated by collapsing 11 pixels of the spectra in the direction of the resolution at the central

[1]IRAF: the Image Reduction and Analysis Facility is distributed by the National Optical Astronomy Observatories, which is operated by the Association of Universities for Research in Astronomy, In. (AURA) under cooperative agreement with the National Science Foundation (NSF).

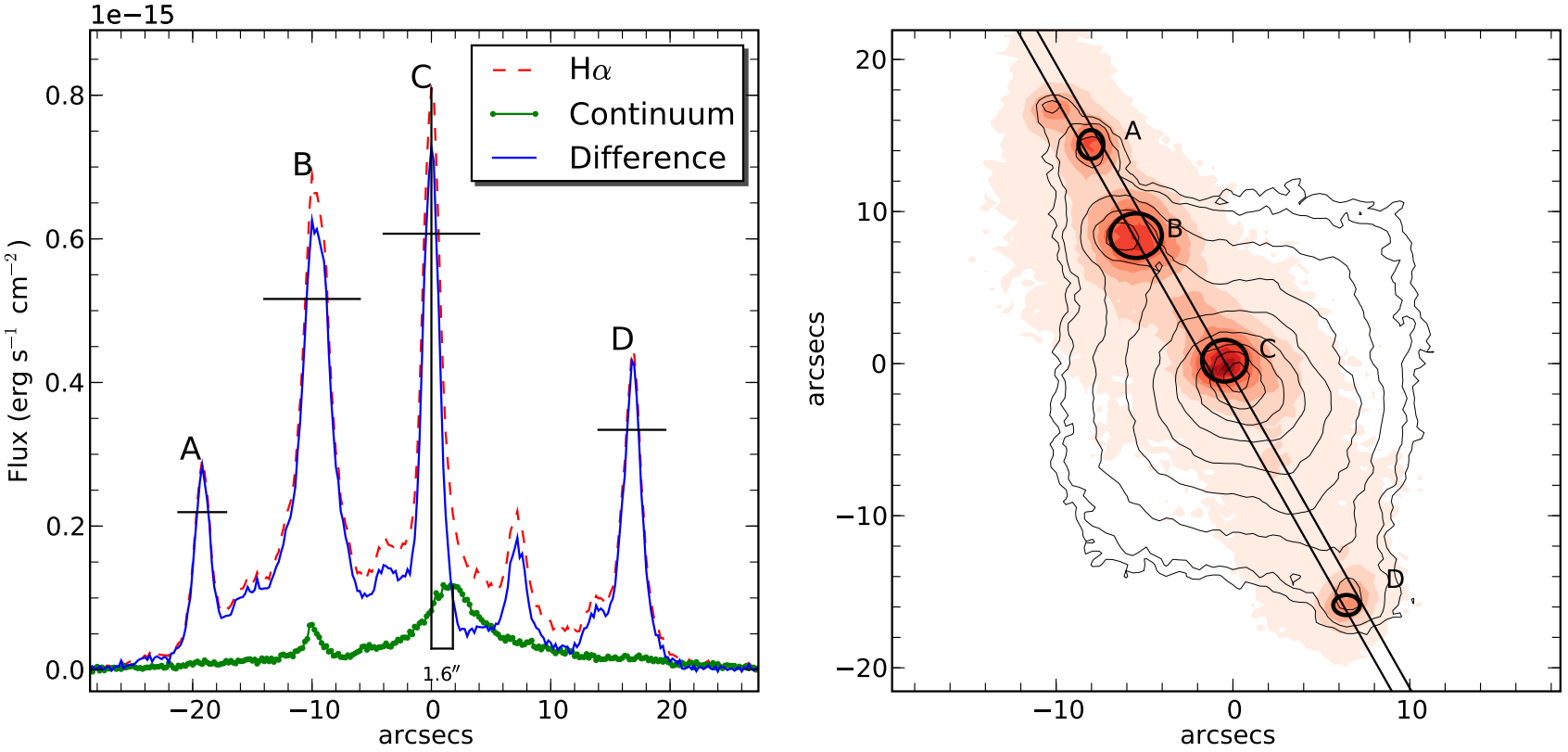

Figure 4.3: In left panel, spatial profile of the light distribution along the slit for the observed Hα emission (dashed red line), the adjacent continuum (thick green line), and the difference between the two (thin blue line). The horizontal lines show the spatial pixels that have been compressed to produce the one dimensional spectra corresponding to each emission knot. In the right panel, we show the Hα image from Gil de Paz et al. (2003) with the identification of the observed knots and the regions for which the broad band magnitudes and the narrow Hα flux have been measured. In the same image, we show the position of the slit for the observations described in the text and the elliptical regions measured to correct for aperture effects in each knot. We show the R-band contours as well, as taken from the same source, which show the position of the host galaxy.

position of the line in the rest frame, $\lambda\,6563$ Å. A continuum profile was also generated by collapsing 11 resolution pixels centred at $\lambda\,6593$ Å. The difference between the two, corresponds to the pure Hα emission. It can be seen from the profiles that in knot C of IIZw71, the most intense one, the peaks of the continuum and line emission do not coincide spatially but are separated by 1.6 arcsec. Also the width of the continuum profile is larger than that of the line emission. This suggests that most of this continuum is coming from the host galaxy behind the knot. From Figure 4.2 it is clear than the continuum emission is not very strong.

The regions of the frames to be extracted into one-dimensional spectra corresponding to each of the knots were selected on the Hα line and are marked by horizontal lines in the left panel of Figure 4.3. In the right panel of the same figure we show the Hα image and continuum contours in the R-band from Gil de Paz et al. (2003) in order to illustrate the position of the bursts of star formation and the relative position of the host galaxy. We also show elliptical regions in Hα taken to measure the total Hα flux of the knots for an aperture correction of the slit measurements. The different emission knots are labelled in both figures.

4.3 Results

4.3.1 Line intensities and reddening correction

The spectra of the four knots of IIZw71 (labelled from A to D) and the three knots of J1657 (labelled from A to C) with some of the relevant identified emission lines are shown in Figures 4.4 (Knot A and B of IIZw71), 4.5 (Knot C and D of IIZw71), 4.6 (Knot A and B of J1657) and 4.7 (Knot C of J1657). The spectrum of each observed knot is split into two panels. Knot A of J1657corresponds to the one analyzed by Hägele et al. (2008). In the case of IIZw71, Knot C, as expected, shows the greatest contribution from an underlying stellar population.

The emission line fluxes were measured on the spectra using the `splot` task of IRAF. We used two different ways to integrate the flux of a given line. (1) In the case of an isolated line, the intensity was calculated by integrating between two points given by the position of a local continuum placed by eye. (2) In the case of the two lines of [OII] at $\lambda\lambda$ 3727, 29 Å, which are partially blended, a multiple Gaussian fit procedure to estimate individual fluxes was used. This procedure is illustrated in Figure 4.8 for the particular case of the doublet [OII] $\lambda\lambda\,3727$,2729 Å in the spectra of Knot B of IIZw71. The statistical errors associated with the measured emission line fluxes were calculated, as in Chapter §3, using the expression:

$$\sigma_l = \sigma_c \sqrt{N\left(1 + \frac{EW}{N\Delta}\right)}$$

where σ_l is the error in the measured line flux, σ_c represents the standard deviation in a box near the measured emission line and stands for the error in the continuum placement, N is

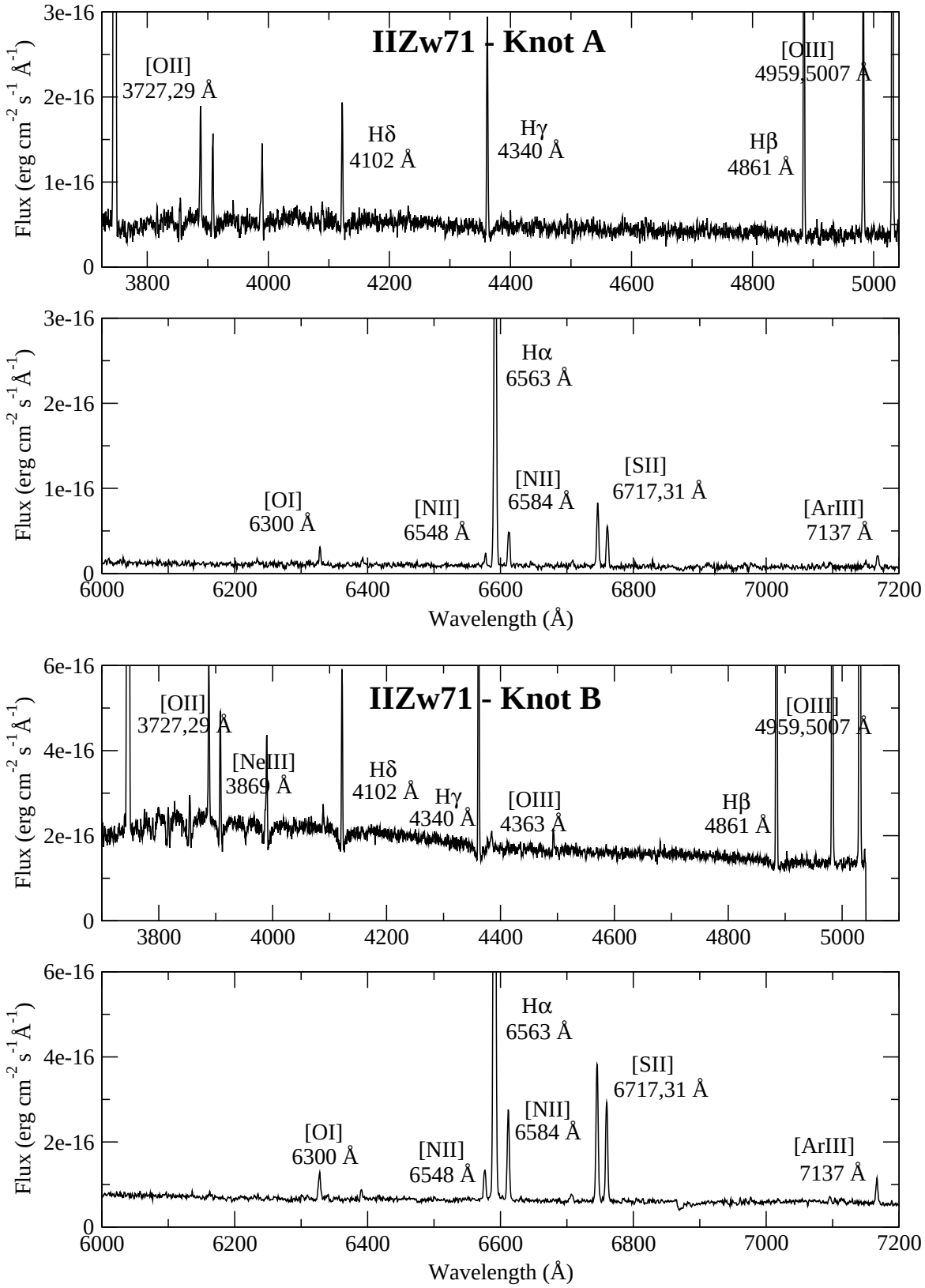

Figure 4.4: Blue and red spectra up to 7200 Å for the knots A and B of IIZw71.

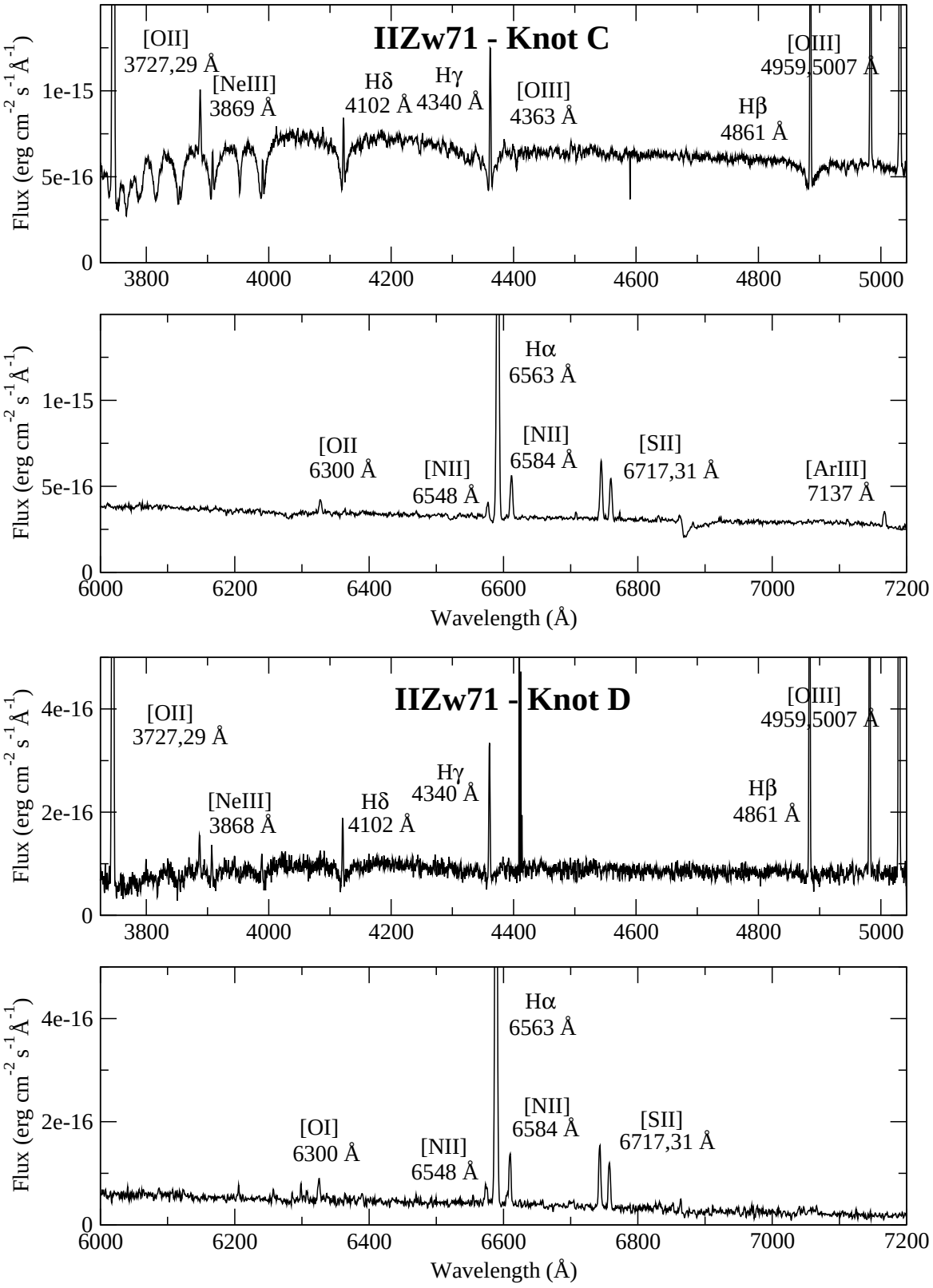

Figure 4.5: Blue and red spectra up to 7200 Å for the knots C and D of IIZw71.

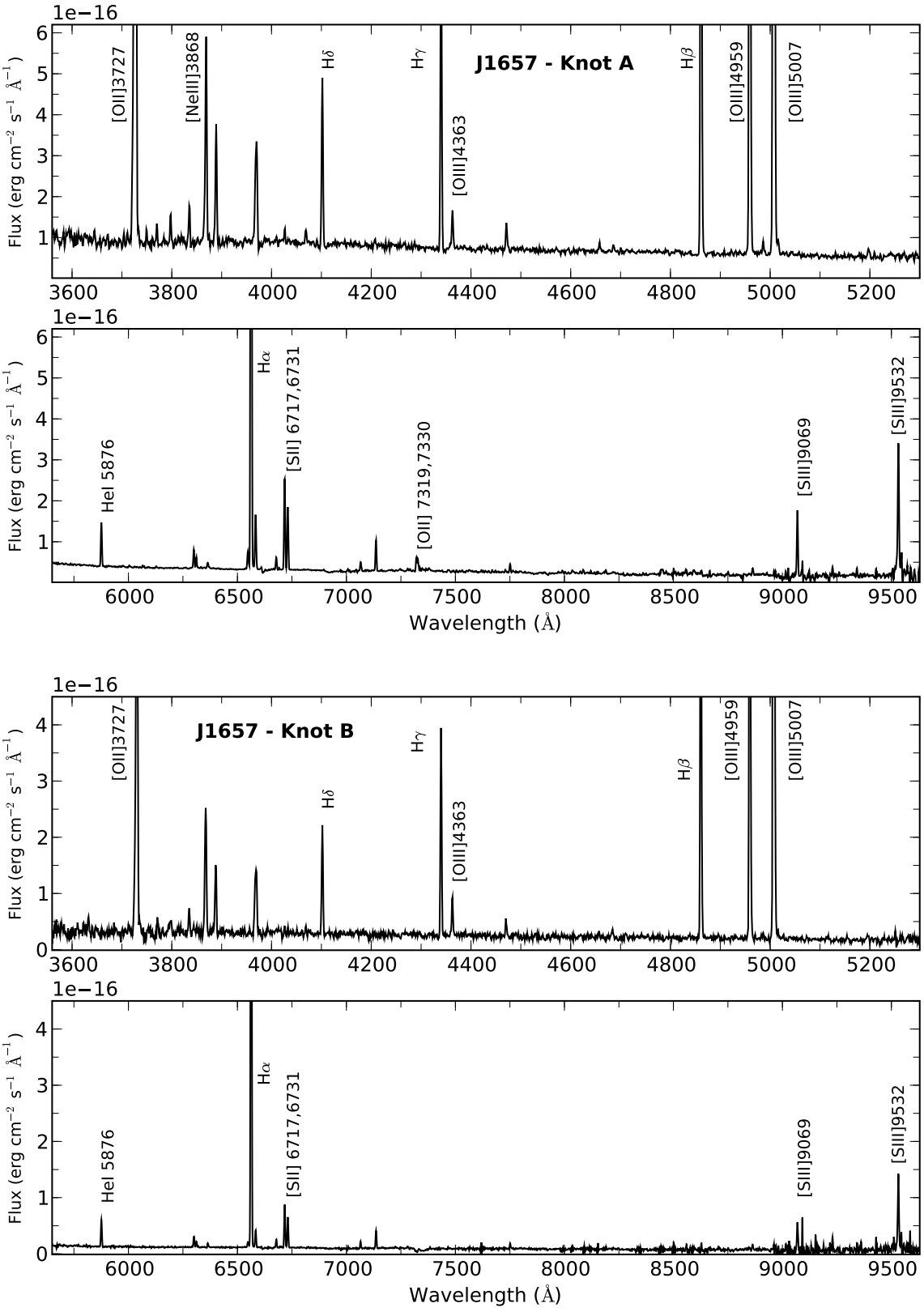

Figure 4.6: Blue and red spectra up to 9600 Å for the knots A and B of J1657.

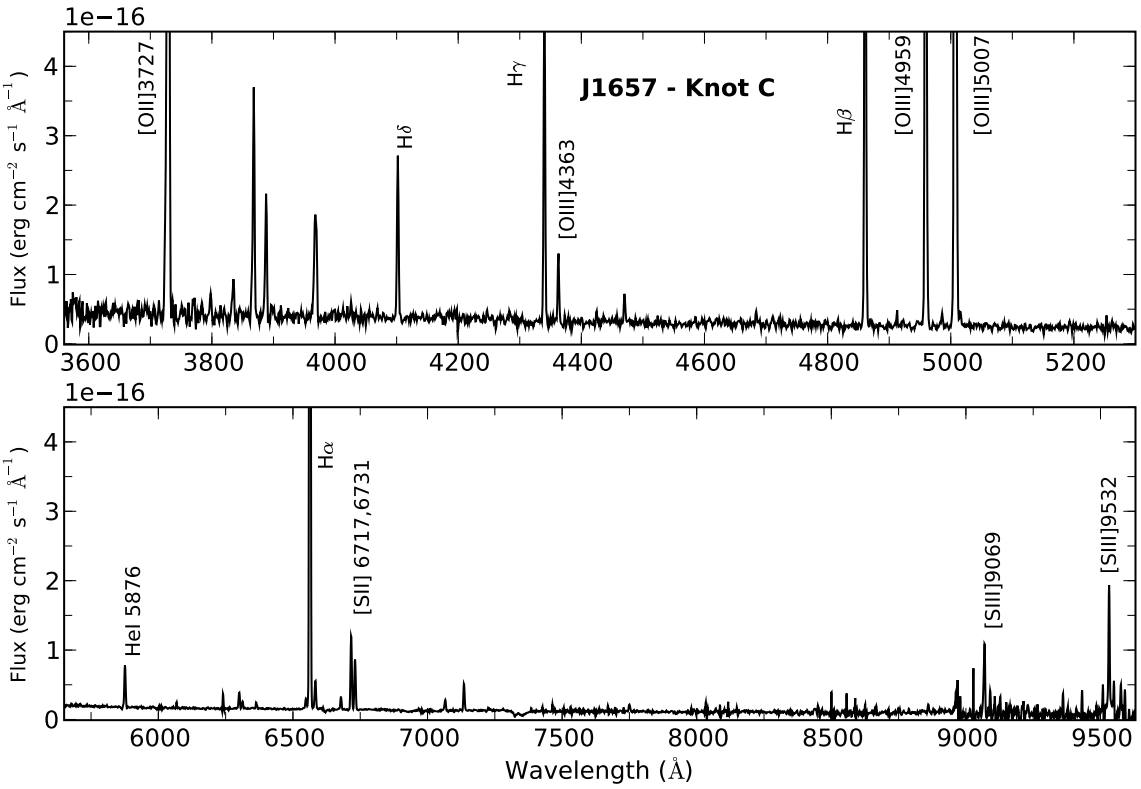

Figure 4.7: Blue and red spectra up to 9600 Å for the knot C of J1657.

the number of pixels used in the measurement of the line flux, EW is the line equivalent width, and Δ is the wavelength dispersion in Ångstroms per pixel.

There are several lines affected by bad pixels, internal reflections or charge transfer in the CCD, telluric emission lines or atmospheric absorption lines. These cause the errors to increase, and, in some cases, they are impossible to quantify. In these cases we do not include these lines in the Tables nor in our calculations, and these lines were excluded from any subsequent analysis. In the case of IIZw71, the emission line [SIII] λ 9532 Å is affected by the strong narrow water-vapor lines present in the λ 9300 - 9500 wavelength region (Diaz et al., 1985). All physical parameters depending on its intensity were calculated using the theoretical ratio between this line and [SIII] λ 9069 Å, I(9069) $\approx$ 2.44 $\times$ I(9532) (Osterbrock, 1989), as we did in Chapter §3.

In some cases there is an observable line (e.g., [ClIII] $\lambda\lambda$ 5517,5537, several carbon recombination lines, Balmer or Paschen lines) for which it is impossible to give a precise measurement. This might be due to a low signal to noise between the line and the surrounding continuum. This is also the case for the Balmer and Paschen jump for the CAHA data, that could not be measured even though it was observed, because it was very difficult to locate the continuum at both sides of the discontinuity with an acceptable accuracy.

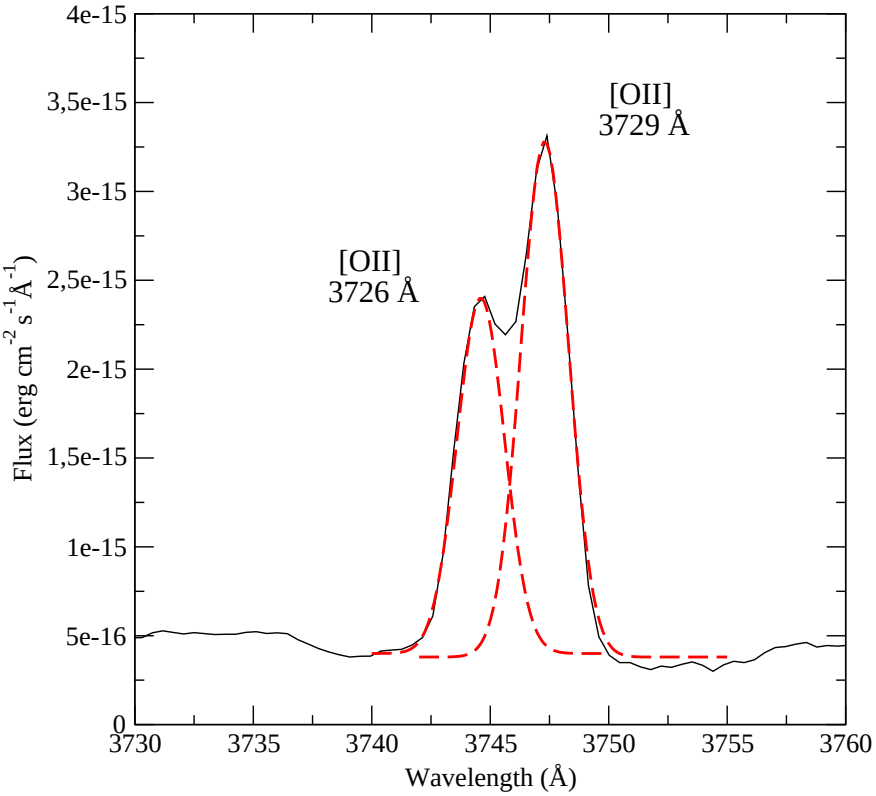

Figure 4.8: Deblending of the [OII] $\lambda\lambda$ 3727, 3729 Å lines for IIZw71. Their ratio allows to put lower limits to the electron density in the observed ionized regions.

A conspicuous underlying stellar population is easily appreciable in the spectra of IIZw71 by the presence of absorption features that depress the Balmer and Paschen emission lines. This effect does not allow the measurement of their fluxes with an acceptable accuracy (Diaz, 1988). To account for this, we subtracted from the four spectra of IIZw71 the best-fitting found by the spectral synthesis code STARLIGHT[2] (Cid Fernandes et al., 2004; Mateus et al., 2006). STARLIGHT fits an observed continuum spectral energy distribution using a combination of multiple simple stellar population (SSPs; also known as instantaneous burst) synthetic spectra using a χ^2 minimisation procedure. We chose for our analysis the SSP spectra from Bruzual and Charlot (2003), based on the STELIB library of Le Borgne et al. (2003), Padova (1994) evolutionary tracks, and a Chabrier (2003) initial mass function between 0.1 and 100 $M_\odot$. We fixed the metallicity to Z = 0.004 (= 1/5 $Z_\odot$) for all models, which is the metallicity in the Bruzual and Charlot (2003) library closest to those corresponding to the oxygen abundances measured in knots B and C, as explained later. The code simultaneously finds the ages and the relative contributions of the different present SSPs and the average reddening. The reddening law from Cardelli et al. (1989) was used. Prior to the fitting procedure, the spectra were shifted to the rest frame, and sampled again to a resolution of 1 Å.

[2]The STARLIGHT project is supported by the Brazilian agencies CNPq, CAPES and FAPESP and by the France-Brazil CAPES/Cofecub program

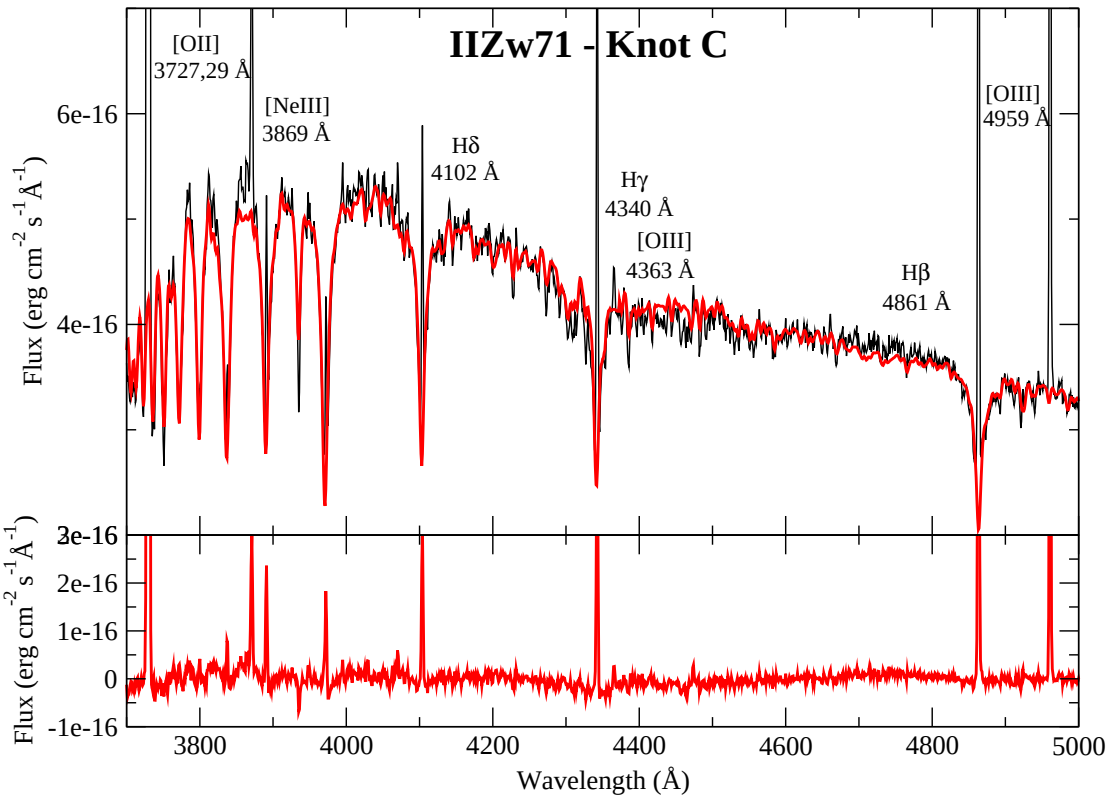

Figure 4.9: Results of the STARLIGHT fit to the continuum spectral energy distribution for knot C of IIZw71, the one most affected by underlying stellar population contribution. The lower panel shows the emission line spectrum once this contribution has been removed.

Bad pixels and emission lines were excluded from the final fits. The percentage of the mean deviation over all fitted pixels between observed and model spectra ranges between 7.3% in knots A and D, which have the lowest signal, to 2.9 % in knot B and 1.9% in knot C.

Figure 4.9 illustrates the results of the model fitting to the spectrum of knot C. The upper panel shows the observed spectrum and the model spectrum. The lower panel shows the subtraction of the fitted stellar continuum. We measured the Balmer emission line fluxes over a linear continuum derived by hand from the observed spectra. We then compared these with the same measurements over the continuum derived from the model SSPs. This allows the equivalent widths to be corrected by the presence of absorption stellar features in these lines that cause the measured EWs to be underestimated.

In Table 4.2 we summarise our results for the four brightest Balmer emission lines. For each Balmer line, the first row gives the measured equivalent width of the emission line, while the third row gives the corresponding value after the removal of the underlying absorption. The second row gives the ratio between the two. Knot C is the most affected indicating a larger contribution by the underlying stellar population, although the correction for the Hβ line only amounts to 13%, reaching 24% for the Hδ line. For the rest of the knots, only B presents a significant contribution of 13 % for the Hδ line.

Knot	A	B	C	D
EW(Hα) (Å)	270±30	130±10	40±2	140±5
f_c	1.00	1.00	1.05	1.00
EW(Hα)$_c$ (Å)	270±30	130±10	42±2	140±5
EW(Hβ) (Å)	34.9±4.5	30.0±1.7	10.7±1.1	32.2±4.7
f_c	1.01	1.03	1.13	1.00
EW(Hβ)$_c$ (Å)	35.2±4.7	30.9±1.8	12.1±1.3	32.2±4.9
EW(Hγ) (Å)	17.2±1.7	12.8±0.9	5.0±0.9	10.8±1.7
f_c	1.03	1.03	1.19	1.00
EW(Hγ)$_c$ (Å)	17.7±1.3	13.2±1.0	6.0±1.0	10.8±0.9
EW(Hδ) (Å)	8.1±0.6	6.2±0.7	1.8±1.0	8.0±0.8
f_c	1.09	1.13	1.24	1.03
EW(Hδ)$_c$ (Å)	8.8±0.6	7.0±1.0	2.3±1.0	8.2±1.0

Table 4.2: Equivalent widths of the hydrogen recombination lines Hβ, Hγ and Hδ as measured directly in the spectra of the observed knots of IIZw71 once the underlying stellar populations have been removed, with the corresponding correction factors.

In the case of J1657, the effect of the underlying population is not so strong. Following the procedures by Hägele et al. (2008), a pseudo-continuum has been defined at the base of the hydrogen emission lines to measure the line intensities and minimize the errors introduced by the underlying population. Hägele et al. (2008) compared the results obtained from this method with a multi-Gaussian fit to the absorption and emission components of the galaxy, finding that the difference between both methods for all Balmer lines is, within the observational errors, almost inappreciable for the stronger lines. Nevertheless, for this galaxy, the absorption wings in the Balmer lines were not prominent enough as to provide sensible results by the later method. Therefore, we have doubled the error derived using the expression for the statistical errors associated with the observed emission fluxes, (σ_l), as a conservative approach to include the uncertainties introduced by the presence of the underlying stellar population.

We also applied STARLIGHT code in J1657 to separate the emission spectra from the underlying stellar absorptions, but for the strongest emission lines the differences between the measurements made after the subtraction of the STARLIGHT fit and the the ones made using the pseudo-continuum are well bellow the observational errors.

The absorption features of the underlying stellar population may also affect the helium emission lines to some extent. However, these absorption lines are narrower than those of hydrogen (González Delgado et al., 2005). Therefore it is difficult to set adequate pseudo-continua at both sides of the lines to measure their fluxes.

The reddening coefficients c(Hβ) were calculated from the measured Balmer decrements, $F(\lambda)/F(H\beta)$. For consistency with the work by Hägele et al. (2008), we adopted the galactic

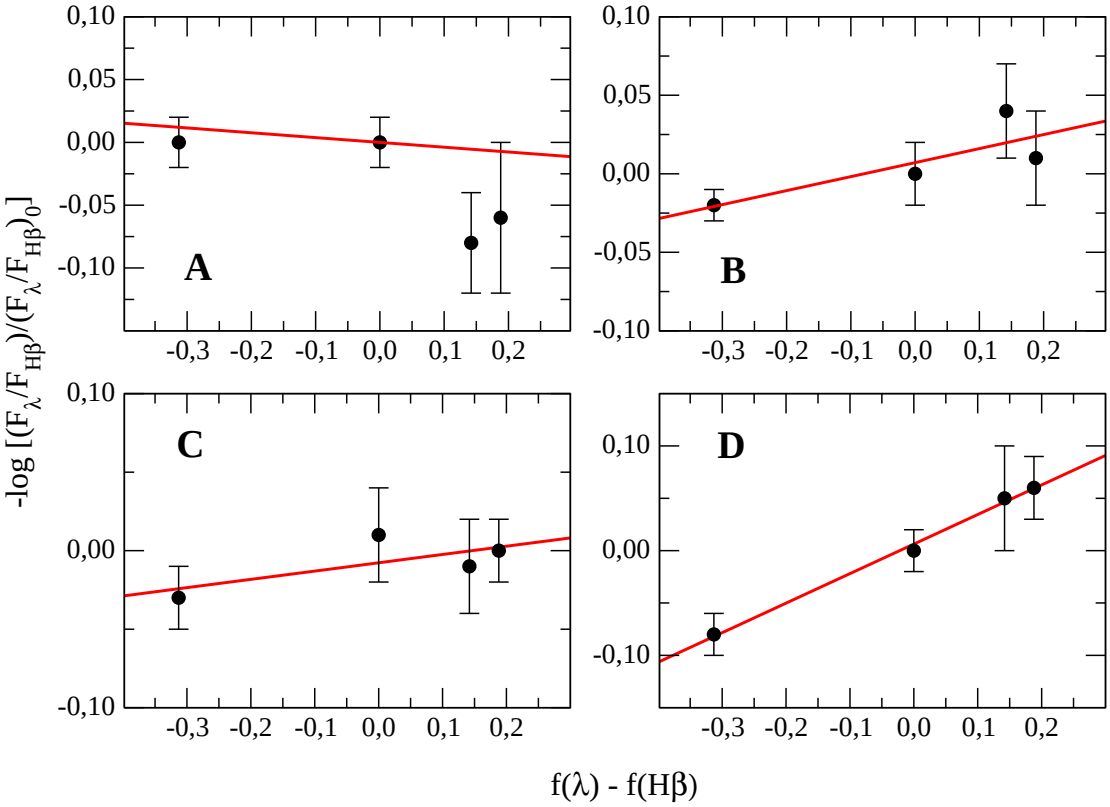

Figure 4.10: Representation for each observed knot of IIZw71 of the ratio of the expected and observed ratios of the Balmer hydrogen lines and the extinction curve. The slope of the obtained fit is the constant of reddening.

extinction law of Miller and Mathews (1972) with R_v=3.2. As explained in Chapter §3, a least square fit of the measured decrements to the theoretical ones, $(F(\lambda)/F(H\beta))_0$, computed based on the data by Storey and Hummer (1995), was performed that provides the value of $c(\mathrm{H}\beta)$. The theoretical Balmer decrements depend on electron temperature and density. We used an iterative method to estimate them, taking as starting values those derived from the measured [SII] $\lambda\lambda$ 6717,6731 Å and [OIII] $\lambda\lambda$ 4363, 4959, 5007 Å line fluxes. Only the strongest Balmer emission lines (Hα, Hβ, Hγ and Hδ) have been used.

In Figure 4.10 we show the actual fits for each of the observed knots of IIZw71. The Galactic extinction for this object is negligible, so we can be sure that internal reddening is the unique source of extinction. All the observed knots present positive values of c(Hβ), except knot A in which the extinction is consistent with zero value. The highest value of c(Hβ) is found for knot D.

For the sake of comparison, along the following sections we have included all the results found by Hägele et al. (2008) for knot A of J1657.

In Tables 4.3 and 4.4 are listed the reddening corrected emission lines for each knot of IIZw71 and J1657 respectively, together with the reddening constant and its error taken as

the uncertainties of the least square fit and the reddening corrected Hβ intensity. Column 1 of the table shows the wavelength and the name of the measured lines. The adopted reddening curve, $f(\lambda)$, normalized to Hβ, is given in column 2 of Table 4.4. The errors in the emission lines, as explained in previous chapters, were obtained by propagating in quadrature the observational errors in the emission line fluxes and the reddening constant uncertainties. We have not taken into account errors in the theoretical intensities since they are much lower than the observational ones. Finally, to compare the high quality of the data of J1657 achieved by Hägele et al. (2008) for Knot A, we have listed in Column 5 of Table 4.4 the fractional error in the line intensities calculated as explained above.

4.3.2 Physical conditions of the gas

The physical conditions of the ionized gas, including electron temperatures and electron density, have been derived from the emission line data using the same procedures as in Chapter §3, based on the five-level statistical equilibrium atom approximation in the task `temden`, of the software package IRAF. See Appendix B for a detailed description of the relations of the physical conditions of the gas and ionic abundances. As usual, we have taken as sources of error the uncertainties associated with the measurement of the emission-line fluxes and the reddening correction, and we have propagated them through our calculations.

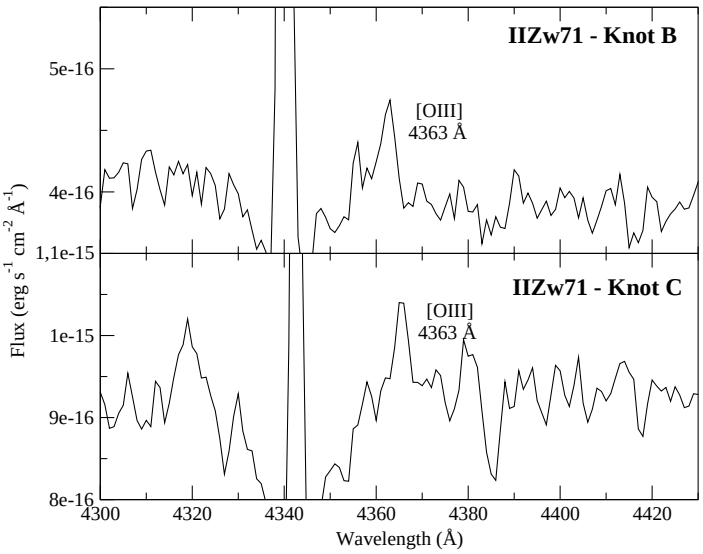

Figure 4.11: Detail of the rest-frame spectra of the knots B and C of IIZw71 around the [OIII] 4363 Å emission line.

Electron densities were derived in the four knots of IIZw71 from [OII] $\lambda\lambda$ 3726 / 3729 Å line ratios and in all the knots of both galaxies from [SII] $\lambda\lambda$ 6717 / 6731 Å line ratios, which are representative of the low-excitation zone of the ionized gas.

In all knots of IIZw71 the density values provide upper limits, which are lower when the [OII] lines are used. In the case of these lines, however, the spectral dispersion of our data do not allow total resolution of the lines, and they were deconvolved by fitting two Gaussian components as shown in Figure 4.8. The values for the electron density are lower in both galaxies than the critical density for collisional de-excitation.

	A		B		C		D	
λ (Å)	$F(\lambda)$	$I(\lambda)$	$F(\lambda)$	$I(\lambda)$	$F(\lambda)$	$I(\lambda)$	$F(\lambda)$	$I(\lambda)$
3726 [OII][a]	2018±62	2070±240	1545±43	1667±132	1497±60	1561±133	1225±107	1552±227
3729 [OII][a]	2936±289	2767±377	2271±61	2450±163	1990±74	2076±156	1758±150	2227±290
3869 [NeIII]	321±37	328±93	242±23	258±50	297±23	307±53	183±25	224±68
4102 Hδ	303±29	307±75	242±15	254±40	257±19	263±42	233±32	270±67
4340 Hγ	584±91	570±117	466±13	480±43	483±31	491±52	417±43	458±75
4363 [OIII]	...	...	29±5	30±11	43±10	44±16	...	...
4861 Hβ	1000±39	1000±39	1000±37	1000±37	1000±47	1000±47	1000±118	1000±118
4959 [OIII]	734±42	733±54	818±27	814±34	937±34	934±41	850±75	837±80
5007 [OIII]	2101±69	2096±99	2411±67	2393±79	2770±95	2759±106	2608±119	2550±223
6300 [OI]	83±19	81±30	92±7	87±16	77±6	74±15	100±13	84±25
6548 [NII]	101±19	99±19	92±7	86±8	93±13	90±17	100±13	82±15
6563 Hα	2752±126	2693±269	2895±93	2713±161	3000±120	2894±183	3333±324	2724±320
6584 [NII]	303±21	296±24	250±18	234±21	230±14	222±18	250±15	204±19
6717 [SII]	514±41	502±59	405±17	378±29	297±12	285±24	267±15	215±29
6731 [SII]	339±30	332±47	292±12	272±24	217±14	208±24	200±9	161±24
7137 [ArIII]	138±19	134±46	68±7	63±18	77±6	73±20	...	...
9069 [SIII]	92±28	88±42	124±15	110±43	107±14	100±43	250±43	174±80
F(Hβ)(10^{-15}erg seg^{-1} cm^{-2})	0.89±0.05		3.61±0.10		4.19±0.10		3.49±0.10	
c(Hβ)	<0.05		0.09±0.03		0.05±0.02		0.28±0.02	

[a] Partially blended (see text and Figure 4.8)

Table 4.3: Relative observed and reddening corrected line intensities [F(Hβ)=I(Hβ)=1000] for the different observed knots of IIZw71. For each knot we also give the flux of Hβ, once reddening corrected and after subtraction of the underlying absorption and the constant of reddening, with their corresponding errors.

Table 4.4: Relative reddening corrected line intensities [$F(H\beta)$=$I(H\beta)$=10000] for the three knots of J1657.

		SDSS J1657 Knot A			SDSS J1657 Knot B			SDSS J1657 Knot C		
λ (Å)	f(λ)	-EW (Å)	$I(\lambda)$	Error (%)	-EW (Å)	$I(\lambda)$	Error (%)	-EW (Å)	$I(\lambda)$	Error (%)
3727 [OII][a]	0.271	120.1	18832 ± 230	1.2	107.8	13266 ± 420	3.2	112.2	14809 ± 282	1.9
3750 H12	0.266	1.9	232 ± 47	20.2	···	···	···	···	···	···
3770 H11	0.261	2.3	293 ± 40	13.8	9.7	617 ± 146	23.7	···	···	···
3798 H10	0.254	4.1	500 ± 68	13.5	···	···	···	4.9	465 ± 141	30.4
3835 H9	0.246	7.1	780 ± 93	11.9	8.9	783 ± 180	23.0	7.5	761 ± 140	18.4
3868 [NeIII]	0.238	23.1	3262 ± 132	4.0	30.7	3663 ± 132	3.6	28.6	3533 ± 118	3.3
3889 HeI+H8	0.233	14.0	1826 ± 95	5.2	22.3	1954 ± 208	10.7	26.2	2192 ± 267	12.2
3968 [NeIII]+H7	0.216	22.4	2456 ± 121	4.9	30.1	2705 ± 221	8.2	29.9	2699 ± 237	8.8
4026 [NII]+HeI	0.203	1.1	155 ± 16	10.4	4.3	327 ± 105	32.1	···	···	···
4068 [SII]	0.195	1.4	198 ± 15	7.4	1.4	153 ± 36	23.7	1.2	130 ± 35	26.9
4102 Hδ	0.188	20.9	2432 ± 65	2.7	30.2	2667 ± 163	6.1	29.2	2619 ± 173	6.6
4340 Hγ	0.142	43.1	4417 ± 97	2.2	76.5	4813 ± 219	4.5	68.7	4712 ± 140	3.0
4363 [OIII]	0.138	4.5	524 ± 24	4.6	8.3	846 ± 67	7.9	8.9	838 ± 59	7.0
4471 HeI	0.106	4.2	443 ± 33	7.4	4.7	405 ± 44	11.0	5.3	445 ± 41	9.3
4658 [FeIII]	0.053	1.0	107 ± 16	14.9	···	···	···	···	···	···
4686 HeII	0.045	1.2	126 ± 14	11.0	4.3	313 ± 68	21.9	2.1	170 ± 24	14.2

continued on next page

Table 4.4 continued

λ (Å)	f(λ)	SDSS J1657 Knot A			SDSS J1657 Knot B			SDSS J1657 Knot C		
		-EW (Å)	$I(\lambda)$	Error (%)	-EW (Å)	$I(\lambda)$	Error (%)	-EW (Å)	$I(\lambda)$	Error (%)
4861 Hβ	0.000	117.8	10000 ± 79	0.8	153.3	10001 ± 178	1.8	167.2	10001 ± 128	1.3
4921 HeI	-0.014	0.8	75 ± 14	18.6	···	···	···	···	···	···
4959 [OIII]	-0.024	152.5	14333 ± 127	0.9	218.5	16118 ± 129	0.8	199.2	14940 ± 114	0.8
4986 [FeIII][b]	-0.030	1.4	135 ± 28	20.5	2.4	163 ± 57	35.1	3.2	215 ± 39	18.3
5007 [OIII]	-0.035	455.1	43082 ± 240	0.6	705.5	48653 ± 256	0.5	613.2	44727 ± 129	0.3
5015 HeI	-0.037	2.4	222 ± 23	10.1	3.2	205 ± 35	17.3	3.2	220 ± 28	12.6
5199 [NI]	-0.078	2.0	157 ± 26	16.4	···	···	···	···	···	···
5876 HeI	-0.209	18.9	1116 ± 44	3.9	23.4	991 ± 29	2.9	29.0	1149 ± 47	4.1
6300 [OI]	-0.276	8.1	438 ± 16	3.7	9.6	393 ± 26	6.7	8.6	366 ± 14	3.9
6312 [SIII]	-0.278	3.7	201 ± 9	4.3	4.3	175 ± 10	5.8	3.5	148 ± 10	6.4
6364 [OI]	-0.285	2.8	152 ± 18	11.8	3.6	141 ± 20	14.4	3.0	124 ± 12	10.0
6548 [NII]	-0.311	9.4	464 ± 23	5.0	5.5	216 ± 23	10.7	6.7	266 ± 14	5.4
6563 Hα	-0.313	571.3	27772 ± 153	0.5	772.5	28159 ± 105	0.4	730.5	27919 ± 133	0.5
6584 [NII]	-0.316	28.8	1428 ± 47	3.3	16.2	632 ± 50	8.0	17.0	680 ± 29	4.3
6678 HeI	-0.329	6.7	315 ± 18	5.7	7.3	272 ± 11	4.1	7.9	296 ± 20	6.9
6717 [SII]	-0.334	47.4	2207 ± 57	2.6	39.4	1489 ± 35	2.3	45.1	1699 ± 56	3.3
6731 [SII]	-0.336	32.2	1598 ± 43	2.7	28.1	1060 ± 25	2.3	30.7	1154 ± 40	3.4

continued on next page

Table 4.4 continued

λ (Å)	f(λ)	SDSS J1657 Knot A			SDSS J1657 Knot B			SDSS J1657 Knot C		
		-EW (Å)	$I(\lambda)$	Error (%)	-EW (Å)	$I(\lambda)$	Error (%)	-EW (Å)	$I(\lambda)$	Error (%)
7065 HeI	-0.377	5.6	235 ± 10	4.4	7.5	226 ± 12	5.1	8.8	279 ± 26	9.3
7136 [ArIII]	-0.385	16.4	717 ± 26	3.6	18.4	584 ± 19	3.3	17.6	581 ± 17	2.9
7281 HeI[c]	-0.402	0.9	41 ± 7	18.2	3.0	90 ± 14	15.9	1.4	46 ± 13	28.6
7319 [OII][d]	-0.406	12.3	302 ± 17	5.6	4.8	165 ± 15	9.2	6.1	196 ± 18	9.2
7330 [OII][e]	-0.407	8.8	211 ± 14	6.5	7.2	251 ± 21	8.4	7.9	254 ± 26	10.1
7751 [ArIII]	-0.451	4.6	177 ± 22	12.3	5.5	163 ± 13	8.0	5.8	170 ± 17	9.9
8665 P13	-0.531	7.7	144 ± 53	37.1	···	···	···	8.9	133 ± 38	28.3
8751 P12	-0.537	4.2	101 ± 29	28.2	···	···	···	···	···	···
8865 P11	-0.546	8.5	211 ± 34	16.3	17.9	277 ± 73	26.2	11.3	228 ± 46	20.2
9014 P10	-0.557	15.4	167 ± 36	21.5	···	···	···	···	···	···
9069 [SIII]	-0.561	59.2	1400 ± 99	7.1	68.2	984 ± 122	12.4	81.9	1577 ± 134	8.5
9229 P9	-0.572	16.9	263 ± 47	18.0	26.1	364 ± 129	35.6	···	···	···
9532 [SIII]	-0.592	157.3	3674 ± 257	7.0	85.1	2700 ± 152	5.6	238.7	2915 ± 162	5.6
I(Hβ)(erg seg^{-1} cm^{-2})			6.3×10^{-15}			2.6×10^{-15}			3.4×10^{-15}	
c(Hβ)			0.05 ± 0.01			0.15 ± 0.02			0.13 ± 0.02	

[a] [OII] $\lambda\lambda\,3726+3729$; [b] [FeIII] $\lambda\lambda\,4986+4987$; [c] possibly blend with an unknown line; [d] [OII] $\lambda\lambda\,7318+7320$; [e] [OII] $\lambda\lambda\,7330+7331$.

	n([OII])	n([SII])	T([OIII])	T([OII])	T([SIII])	T([SII])
J1657 Knot A	···	30:	1.23 ± 0.02	1.33 ± 0.07	1.45 ± 0.08	0.88 ± 0.05
J1657 Knot B	···	11:	1.43 ± 0.05	1.52 ± 0.12	1.64 ± 0.11	1.00 ± 0.17
J1657 Knot C	···	10:	1.48 ± 0.05	1.50 ± 0.13	1.29 ± 0.07	0.83 ± 0.15
IIZw71 Knot A	<200	< 230	···	···	···	···
IIZw71 Knot B	<85	< 160	1.24 ± 0.17	1.25 ± 0.13[a]	1.16 ± 0.11[b]	···
IIZw71 Knot C	<180	< 210	1.37 ± 0.20	1.28 ± 0.13[a]	1.32 ± 0.12[b]	···
IIZw71 Knot D	<190	< 350	···	···	···	···

[a] From a relation with T([OIII]) based on photoionization models
[b] From an empirical relation with T([OIII])

Table 4.5: Electron densities and temperatures for the knots of J1657 and IIZw71. Densities in cm^{-3} and temperatures in 10^4 K.

For all three knots of J1657 we have derived the electron temperatures of [OII], [OIII], [SII] and [SIII]. As we saw in Chapter §3, the [OII] $\lambda\lambda$ 7319,7330 Å lines have a contribution by direct recombination which increases with temperature. Using the calculated [OIII] electron temperatures, we have estimated these contributions to be less than 4 % in all cases and therefore we have not corrected for this effect. The expression for the correction of direct recombination (see Appendix B), however, is valid only in the range of temperatures between 5000 and 10000 K, so the found temperatures are slightly over that range. At any rate, the relative contribution of recombination to collisional intensities decreases rapidly with increasing temperature, therefore for the high T_e values found in our objects this contribution is expected to be small.

For knots B and C of IIZw71, for which the intensity of the [OIII]λ 4363 Å was measured with sufficient signal-to-noise (see Figure 4.11 for a more detailed plot of this line in these knots), the [OIII] electron temperature was derived directly from the ratio (I(4959Å) + I(5007Å)) / I(4363Å). Then we derived T([OII]) from T([OIII]) using the relations based on the photoionization models described in Pérez-Montero and Díaz (2003), which take explicitly into account the dependence of T([OII]) on the electron density (see Chapter §3), and T([SIII]) has been estimated from the empirical relation:

$$T([SIII]) = (1.19 \pm 0.08)\, T([OIII]) - (0.32 \pm 0.10)$$

found by Hägele et al. (2006).

The derived electron densities and temperatures for Knots A, B, and C of J1657 and for Knots B and C of IIZw71 are given in Table 4.5 along with their corresponding errors.

4.3.3 Chemical abundance derivation

We have derived the ionic chemical abundances of the different species using the strongest available emission lines detected in the analyzed spectra and the task `ionic` of the STSDAS package in IRAF, as described in Chapter §3. For details on the derived equations, see Appendix B.

The total abundances have been calculated by taking into account, when required, the unseen ionization stages of each element, using the appropriate ionization correction factor (ICF) for each species:

$$\frac{X}{H} = ICF(X^{+i})\frac{X^{+i}}{H^{+}}$$

Helium

Neither J1657 not IIZw71 show in their spectra the signature of the presence of Wolf-Rayet (WR) stars, as traced by the blue 'bump' around $\lambda\,4600$ Å, and for the red 'bump' around $\lambda\,5808$ Å.

Not enough signal-to-noise was achieved in the spectra of IIZw71 in order to derive helium abundances. Thus, this section is devoted to the results of J1657.

We have used the well detected and measured HeI $\lambda\lambda$ 4471, 5876, 6678 and 7065 Å lines, to calculate the abundances of once ionized helium. For the three knots also the HeII λ 4686 Å line was measured allowing the calculation of twice ionized He. The He lines arise mainly from pure recombination, although they could have some contribution from collisional excitation and be affected by self-absorption. We have taken the electron temperature of [OIII] as representative of the zone where the He emission arises since at any rate ratios of recombination lines are weakly sensitive to electron temperature. All the details of the equations used in the calculation of the helium abundance are presented in Appendix B. We have not made any corrections for fluorescence since three of the used helium lines have a small dependence with optical depth effects but the observed objects have low densities. Neither for the presence of an underlying stellar population.

The total abundance of He has been found by adding directly the two ionic abundances:

$$\frac{He}{H} = \frac{He^{+} + He^{2+}}{H^{+}}$$

The results obtained for each line and the total He abundances, along with their corresponding errors are presented in Table 4.6. The adopted value for He^{+}/H^{+} that is the average, weighted by the errors, of the different ionic abundances derived from each HeI emission line, is also given.

	J1657 Knot A	J1657 Knot B	J1657 Knot C
He^+/H^+ (λ4471)	0.093±0.007	0.085±0.009	0.094±0.009
He^+/H^+ (λ5876)	0.085±0.003	0.079±0.002	0.093±0.003
He^+/H^+ (λ6678)	0.086±0.005	0.077±0.003	0.084±0.005
He^+/H^+ (λ7065)	0.093±0.005	0.086±0.006	0.105±0.010
He^+/H^+ (Adopted)	0.087±0.005	0.080±0.005	0.092±0.009
He^{2+}/H^+ (λ4686)	0.0011±0.0001	0.0028±0.0006	0.0015±0.0002
(He/H)	0.088±0.008	0.080±0.008	0.092±0.009

Table 4.6: Ionic and total chemical abundances for helium for the knots of J1657.

Ionic and total chemical abundances from forbidden lines

The oxygen ionic abundance ratios, O^+/H^+ and O^{2+}/H^+, have been derived from the [OII] $\lambda\lambda$ 3727,29 Å and [OIII] $\lambda\lambda$ 4959, 5007 Å lines respectively using for each ion its corresponding temperature[3].

At the temperatures derived for our observed galaxies, most of the oxygen is in the form of O^+ and O^{2+}, therefore the approximation:

$$\frac{O}{H} = \frac{O^+ + O^{2+}}{H^+}$$

has been used.

In the same way, we have derived S^+/H^+ and S^{2+}/H^+, abundances using t([SII]) and t([SIII]) values and the fluxes of the [SII] emission lines at $\lambda\lambda$ 6717,6731 Å and the near-IR [SIII] $\lambda\lambda$ 9069, 9532 Å lines respectively. For IIZw71, we have assumed that T([SII]) ≈ T([OII]).

Unlike oxygen, for sulphur a relatively important contribution from S^{3+} may be expected depending on the nebular excitation. The total sulphur abundance has been calculated using an ICF for S^++S^{2+} according to the formula by Barker (1980), which is based on the photoionization models by Stasińska (1978):

$$ICF(S^+ + S^{2+}) = \left[1 - \left(1 - \frac{O^{2+}}{O^+ + O^{2+}}\right)^{\alpha}\right]^{-1/\alpha}$$

where $\alpha = 2.5$ gives the best fit to the scarce observational data on S^{3+} abundances (Pérez-Montero et al., 2006). Taking this ICF as a function of the ratio O^{2+}/O instead of O^+/O reduces the propagated error for this quantity.

The ionic abundance of nitrogen, N^+/H^+ has been derived from the intensities of the $\lambda\lambda$ 6548,6584 Å lines and along with the assumption $T_e([NII]) \approx T_e([OII])$.

The N/O abundance ratio has been derived under the assumption that

[3] As in Chapter 3, we have used fittings to the `ionic` task results. Again, see Appendix B for details.

$$\frac{N}{O} = \frac{N^+}{O^+}$$

and the N/H ratio as:

$$log\frac{N}{H} = log\frac{N}{O} + log\frac{O}{H}$$

Neon is only visible in all the spectra via the [NeIII] emission line at λ3868 Å, then Ne^{2+} has been derived using this line. For this ion we have taken the electron temperature of [OIII], as representative of the high excitation zone ($(T_e([NeIII]) \approx T_e([OIII])$; Peimbert and Costero, 1969). Classically, the total abundance of neon has been calculated assuming that

$$\frac{Ne}{O} = \frac{Ne^{2+}}{O^{2+}}$$

Izotov et al. (2004) point out that this assumption can lead to an overestimate of Ne/H in objects with low excitation, where the charge transfer between O^{2+} and H^0 becomes important. Thus, we have used the following expression for the ICF (Pérez-Montero et al., 2007):

$$ICF(Ne^{2+}) \approx 0.753 + 0.142 \cdot \frac{O^{2+}}{O^+ + O^{2+}} + 0.171 \cdot \frac{O^+ + O^{2+}}{O^{2+}}$$

Given the high excitation of the observed objects there are no significant differences between the total neon abundance derived using this ICF and those estimated using the classical approximation: $Ne/O \approx Ne^{2+}/O^{2+}$.

The only accessible emission lines of argon in the optical spectra of ionized regions correspond to Ar^{2+} and Ar^{3+}. The abundance of Ar^{2+} has been calculated from the measured [ArIII] λ 7136 Å line emission assuming that $T_e([ArIII]) \approx T_e([SIII])$ (Garnett, 1992). No [ArIV] line has been found in the spectra.

The total abundance of Ar was then calculated using the ICF(Ar^{2+}) derived from photoionization models by Pérez-Montero et al. (2007):

$$ICF(Ar^{2+}) = 0.749 + 0.507 \cdot \left(1 - \frac{O^{2+}}{O^+ + O^{2+}}\right) + +0.0604 \cdot \left(1 - \frac{O^{2+}}{O^+ + O^{2+}}\right)^{-1}$$

Finally, for iron (only measured in Knot A of J1657) we have used the emission line of [FeIII] λ 4658 Å to calculate Fe^{2+} assuming $T_e([FeIII]) \approx T_e([OIII])$.

The ICF for iron twice ionized has been taken from Rodríguez and Rubin (2004):

$$ICF(Fe^{2+}) = \left(\frac{O^+}{O^{2+}}\right)^{0.09} \cdot \left[1 + \frac{O^{2+}}{O^+}\right]$$

	J1657 Knot A	J1657 Knot B	J1657 Knot C
$12 + \log(O^+/H^+)$	7.37 ± 0.09	7.03 ± 0.12	7.10 ± 0.12
$12 + \log(O^{2+}/H^+)$	7.87 ± 0.02	7.74 ± 0.04	7.67 ± 0.04
12 + log(O/H)	7.99 ± 0.04	7.82 ± 0.05	7.78 ± 0.06
$12 + \log(S^+/H^+)$	6.07 ± 0.08	5.76 ± 0.19	6.02 ± 0.24
$12 + \log(S^{2+}/H^+)$	6.00 ± 0.06	5.79 ± 0.07	6.02 ± 0.07
$ICF(S^+ + S^{2+})$	1.32 ± 0.05	1.51 ± 0.10	1.38 ± 0.09
12 + log(S/H)	6.46 ± 0.07	6.25 ± 0.13	6.46 ± 0.16
log(S/O)	-1.53 ± 0.08	-1.57 ± 0.14	-1.32 ± 0.17
$12 + \log(N^+/H^+)$	6.15 ± 0.06	5.68 ± 0.10	5.74 ± 0.09
12 + log(N/H)	6.76 ± 0.28	6.47 ± 0.39	6.42 ± 0.39
log(N/O)	-1.23 ± 0.11	-1.35 ± 0.16	-1.36 ± 0.15
$12 + \log(Ne^{2+}/H^+)$	7.22 ± 0.04	7.06 ± 0.06	7.00 ± 0.05
ICF(Ne)	1.09 ± 0.00	1.08 ± 0.00	1.08 ± 0.01
12 + log(Ne/H)	7.25 ± 0.04	7.09 ± 0.06	7.04 ± 0.05
log(Ne/O)	-0.74 ± 0.06	-0.73 ± 0.08	-0.74 ± 0.08
$12 + \log(Ar^{2+}/H^+)$	5.49 ± 0.06	5.31 ± 0.06	5.49 ± 0.06
$ICF(Ar^{2+})$	1.13 ± 0.02	1.23 ± 0.06	1.16 ± 0.04
12 + log(Ar/H)	5.54 ± 0.06	5.39 ± 0.06	5.55 ± 0.06
log(Ar/O)	-2.45 ± 0.07	-2.43 ± 0.08	-2.22 ± 0.08
$12 + \log(Fe^{2+}/H^+)$	5.54 ± 0.08	···	···
ICF(Fe)	3.55 ± 0.50	···	···
12 + log(Fe/H)	6.08 ± 0.11	···	···

Table 4.7: Ionic chemical abundances derived from forbidden emission lines, ICFs and total chemical abundances for elements heavier than helium for the knots of J1657.

The ionic abundances of the different elements heavier than helium with respect to ionized hydrogen, ICFs and total abundances along with their corresponding errors are given in Table 4.7 and 4.8 for J1657 and IIZw71, respectively.

	IIZw71 Knot B	IIZw71 Knot C
$12 + \log(O^+/H^+)$	7.67 ± 0.23	7.63 ± 0.23
$12 + \log(O^{2+}/H^+)$	7.63 ± 0.19	7.57 ± 0.19
12 + log(O/H)	7.95 ± 0.21	7.90 ± 0.21
$12 + \log(S^+/H^+)$	5.94 ± 0.12	5.83 ± 0.13
$12 + \log(S^{2+}/H^+)$	6.00 ± 0.26	5.85 ± 0.26
ICF($S^+ + S^{2+}$)	1.15 ± 0.13	1.14 ± 0.12
12 + log(S/H)	6.33 ± 0.24	6.20 ± 0.24
log(S/O)	-1.62 ± 0.31	-1.70 ± 0.31
$12 + \log(N^+/H^+)$	5.87 ± 0.28	5.63 ± 0.23
12 + log(N/H)	6.15 ± 0.40	5.90 ± 0.38
log(N/O)	-1.48 ± 0.37	-1.68 ± 0.32
$12 + \log(Ne^{2+}/H^+)$	7.12 ± 0.29	7.06 ± 0.28
ICF(Ne^{2+})	1.22 ± 0.13	1.23 ± 0.14
12 + log(Ne/H)	7.19 ± 0.35	7.13 ± 0.35
log(Ne/O)	-0.75 ± 0.30	-0.77 ± 0.30
$12 + \log(Ar^{2+}/H^+)$	5.61 ± 0.22	5.57 ± 0.19
ICF(Ar^{2+})	1.16 ± 0.03	1.16 ± 0.04
12 + log(Ar/H)	5.65 ± 0.26	5.60 ± 0.26
log(Ar/O)	-2.29 ± 0.30	-2.29 ± 0.30

Table 4.8: Ionic chemical abundances derived from forbidden emission lines, ICFs and total chemical abundances for elements heavier than helium for knots B and C of IIZw71.

4.4 Discussion

4.4.1 Gaseous physical conditions and element abundances

Densities and temperatures

Four electron temperatures – T_e([OIII]), T_e([OII]), T_e([SIII]) and T_e([SII])– have been estimated in all the knots of J1657. [NII] λ5755 is detected, but has poor signal. The good quality of the data allows us to reach accuracies, for Knot A, of the order of 2%, 4%, 5% and 7% for T_e([OIII]), T_e([OII]), T_e([SIII]), and T_e([SII]), respectively.

Unfortunately, for IIZw71 only T_e([OIII]) could be estimated directly. Thus, in this section we are going to discuss only the results obtained for J1657 when comparing with models.

The knots of J1657 and IIZw71 show temperatures within a relatively narrow range, between 12000 and 14800 K for T_e([OIII]). It is worth to remember that the adopted selection

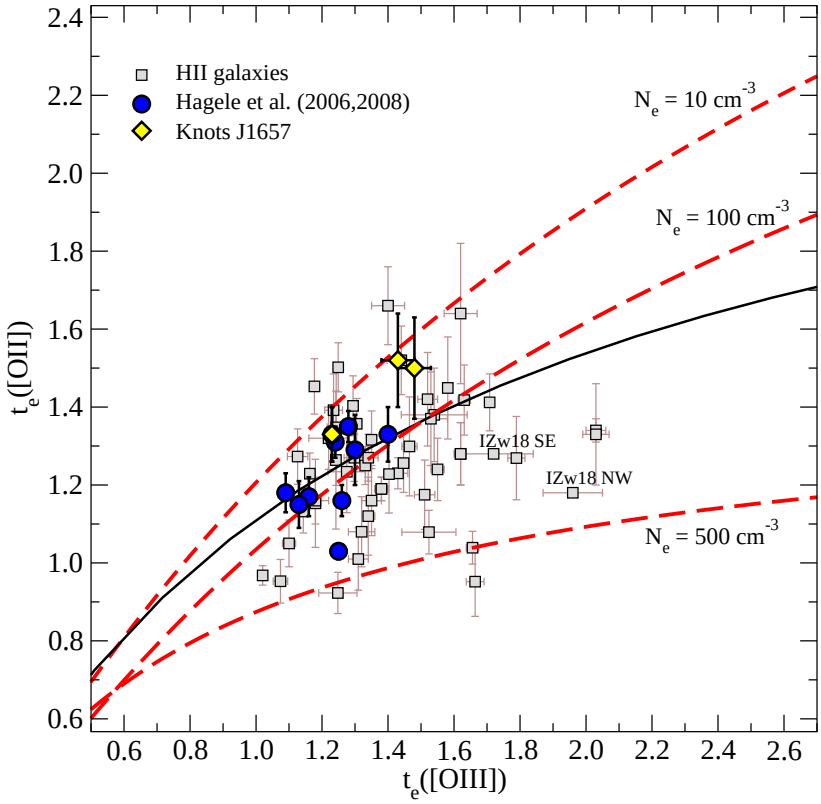

Figure 4.12: Relation between t_e([OII]) and t_e([OIII]), for the knots of J1657, the objects studied by Hägele et al. (2006) and Hägele et al. (2008), and HII galaxies from the literature. The red dashed lines correspond to photo-ionization models from Pérez-Montero and Díaz (2003) for electron densities $N_e = 10$, 100 and 500 cm^{-3}. The model sequences from (Stasińska, 1990, solid line) are also shown. Temperatures are in units of 10^4 K.

criteria for J1657 (see Hägele et al., 2008) was high Hβ flux and large equivalent width of Hα, which tends to select objects with abundances and electron temperatures close to the median values shown by HII galaxies. To our knowledge, there is no previous reported t_e([OIII]) for this galaxy in the literature. Figure 4.12 shows the relation between the [OII] and [OIII] temperatures measured in the three knots of J1657. Also shown in the Figure are the corresponding values for HII galaxies as derived from the emission line intensities compiled from the literature and the objects studied by Hägele et al. (2006) and Hägele et al. (2008). In Table 13 of Hägele et al. (2008) are listed the values together with the references that have been used. This compilation is restricted to objects for which the temperatures could be derived with an accuracy better than 10%. An exception has been made for IZw18. In this case, the large errors in the derived [OII] temperatures (30% and 40% for T_e([OII]) in the NW and SE knots respectively), are probably related to the low oxygen abundance in this galaxy and hence the weakness of the involved emission lines. These points are labelled in the Figure and, due to their large values, no error bars in t_e([OII]) are shown.

The relation between the [OII] and [OIII] temperatures does not show a clear trend, show-

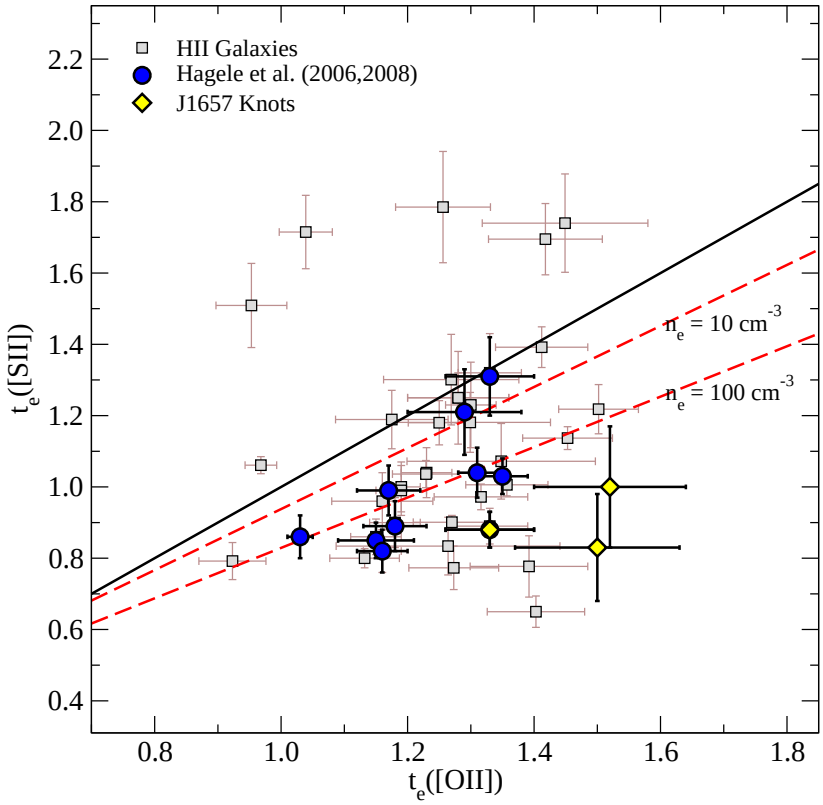

Figure 4.13: Relation between t_e([SII]) and t_e([OII]) for knots of J1657, the objects studied by Hägele et al. (2006) and Hägele et al. (2008) and HII regions from the literature. The solid line represents the one to one relation. The red dashed lines correspond to the photo-ionization models from Pérez-Montero and Díaz (2003) for electron densities $N_e = 10$ and $100\,cm^{-3}$. Temperatures are in units of 10^4 K.

ing a scatter which is larger than observational errors. As it was mentioned in Chapter §3, the [OII] temperature is somewhat dependent on density. The density effect can be seen by looking at the model sequences which are overplotted and which correspond to photo-ionization models from Pérez-Montero and Díaz (2003) for electron densities $N_e = 10$, 100 and $500\,cm^{-3}$. This relationship was used to derived the [OII] temperature for Knot B in NGC 6946 and for IIZw71. Higher density models show lower values of t_e([OII]) for a given t_e([OIII]). The effect is more noticeable at high electron temperatures. The data points populate the region of the diagram spanned by model sequences with most objects located between the model sequences corresponding to N_e 100 and 500 cm^{-3}. The three knots of J1657, however, lie between the model sequences for N_e 10 and 100 cm^{-3} (in fact, very close to the first one), which is consistent with the derived values of the density.

The standard procedure in principle adopted for the analysis of low resolution and poor signal-to-noise data is to used the (not unique) relation between the [OII] and [OIII] temperatures which is now extended to data of much higher quality. The solid line in Figure 4.12 shows the relation based on the photo-ionization models by Stasińska (1990), adopted

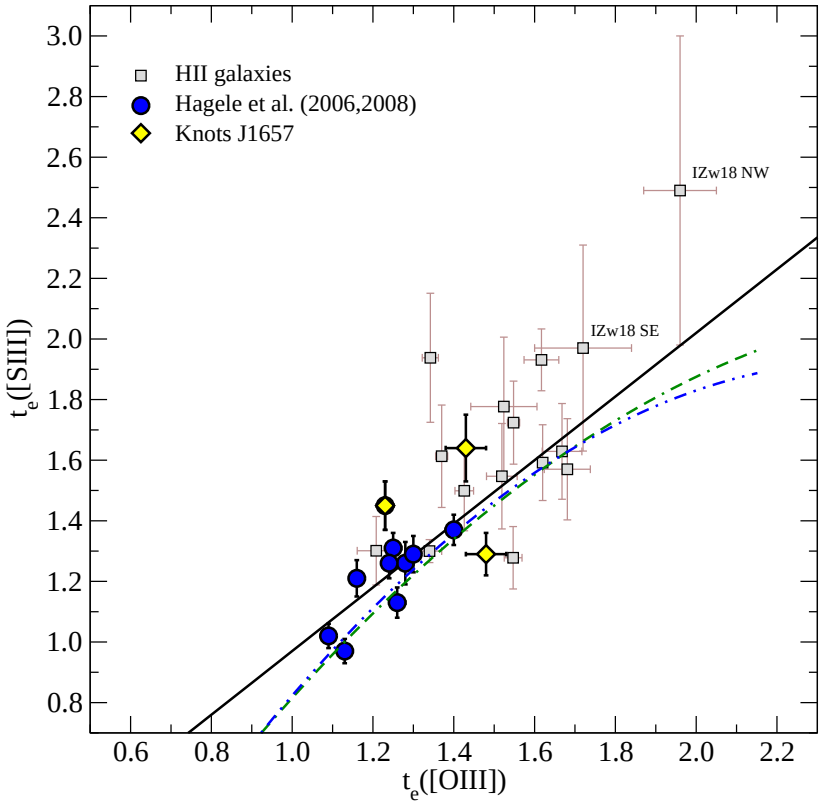

Figure 4.14: Relation between t_e([SIII]) and t_e([OIII]) for the knots of J1657 and those from the literature. The solid line corresponds to the photo-ionization model sequence of Pérez-Montero and Díaz (2005). The (green) double dashed-dotted line and the (blue) dashed-double dotted line represent the models presented by Izotov et al. (2006) for low and intermediate metallicity HII regions. The temperatures are in units of 10^4 K.

in many abundance studies of ionized nebulae. A substantial part of the sample objects show [OII] temperatures which are lower or higher than predicted by this relation for as much as 3000 K. As an example, at a value of T_e([OIII]) of 14300 K for Knot B of J1657, the models by Stasińska (1990) predicts a lower temperature for T_e([OII]) by an amount of 2000 K, which translate into a higher O^+/H^+ ionic ratio by 0.2 dex and a final higher total oxygen abundance by ±0.05 dex. Moreover, when using model sequences to predict [OII] temperatures no uncertainties are attached to the t_e([OII]) vs. t_e([OIII]) relation and the outcome is a reported T_e([OII]) which carries only the usually small observational error of T_e([OIII]) which translates into very small errors in the oxygen ionic and total abundances.

In general, model predictions overestimate t_e([OII]) and hence underestimate the O^+/H^+ ratio. This is of relatively little concern in objects of high excitation for which O^+/O is less than $\sim$ 10%, but this differences could be more marked on higher metallicity objects, as we have seen for the NGC 6946 complex studied in this work, where total oxygen abundances could be underestimated by up to 0.2 dex.

In the usually assumed structure of ionized nebulae, low ionization lines arise from the

same region and therefore the temperatures of [OII], [SII] and [NII] are expected to show similar values, once allowance is made for a possible density effect for the first two. In Figure 4.13 we show the relation between t_e([SII]) and t_e([OII]) for the knots of J1657, the objects studied by Hägele et al. (2006) and Hägele et al. (2008) and those from the literature. The relations derived by Pérez-Montero and Díaz (2003) using photo-ionization models for electron densities $N_e = 10$ and $100\,cm^{-3}$ are also shown. Any dependence on density is difficult to appreciate. The measurements for the knots of J1657 of the [SII] and [OII] temperatures are located bellow the model sequence for $N_e = 100\,cm^{-3}$. Nevertheless, due to the large errors associated to knots B and C, the values for both t_e([OII]) and t_e([SII]) are consistent with a similar temperature for each ion for the three knots.

The situation, in general, seems to be better for the [SIII] temperature. Figure 4.14 shows the relation between t_e([SIII]) and t_e([OIII]) for the knots of J1657 and the compilation of published data on HII galaxies for which measurements of the nebular and auroral lines of [OIII] and [SIII] exist, thus allowing the simultaneous determination of T_e([OIII]) and T_e([SIII]). The solid line in the figure shows the model sequence from Pérez-Montero and Díaz (2005), which differs slightly from the semi-empirical relation by Garnett (1992), while the other two lines correspond to the relations given by Izotov et al. (2006) for low and intermediate metallicity HII regions. The three model sequences are coincident for temperatures in the range from 12000 and 17000 K, and very little, if any, metallicity dependence is predicted. The three knots of J1657, however, lie at both sides of the one to one relation. As can be seen, although Knots B and C have similar T_e([OIII]) temperature, they have a difference in T_e([SIII]) of 2500 K. Since the number of objects is small, more high quality data are needed in order to confirm the relation between the [OIII] and [SIII] temperatures and obtain an empirical fit with well determined *rms* errors.

Abundances

The abundances derived for the three knots of J1657 and knots B and C of IIZw71 show the characteristic low values found in strong line HII galaxies. These values are between 7.78 and 7.99. From the high quality data of J1657 the mean error values for the oxygen and neon abundances are 0.05 dex, 0.12 for sulphur and 0.07 for argon. Knots B and C of J1657 show a similar value of 12+log(O/H), while Knot A is almost 0.2 dex higher than the other pair. In the case of IIZw71, the derived ionic abundances in knots B and C are very similar, leading to total O/H abundances of 12+log(O/H) = 7.90 in knot C and 7.95 in knot B. These values deviate slightly from the metallicity reported in the literature for the integrated object, which is 12+log(O/H) = 8.24 (Shi et al., 2005; Kewley et al., 2005) and the difference is even greater than the value for the nuclear region, which could be considered as knot C, given by Kewley et al. (2005), which is 12+log(O/H) = 8.55. The value reported by Shi et al. (2005) are based on the direct method, while those reported by Kewley et al.

(2005) were derived using empirical calibrations since no temperature sensitive lines were observed.

The logarithmic N/O ratios found for J1657 are -1.23 ± 0.11, -1.35 ± 0.16 and -1.36 ± 0.15 for knots A, B, and C, respectively, which are remarkably constant. The derived values are on the high log(N/O) side of the distribution for this kind of objects (see Figure 4.15). For IIZw71, although the difference between knots B and C is of 0.2 dex, due to the large errors, it can be consider as well fairly constant.

In general, the common procedure of obtaining t_e([OII]) from t_e([OIII]) using Stasińska (1990) relation and assuming $t_e([OII]) = t_e([NII])$, yields N/O ratios larger than using the measured t_e([OII]) values since, in most cases, the model sequence over-predicts t_e([OII]). In our particular case, as we have seen, for the three knots of J1657 t_e([OII]) is under-predicted by Stasińska (1990) models; for Knot B the difference is more than 2000 K. This would decrease the N/O ratio by more than 0.1 dex.

The log(S/O) ratios found are the quite similar for Knots A and B of J1657, with -1.53 and -1.57, respectively, and higher for Knot C, with -1.32. The average error is 0.12. For IIZw71, both knots shows a very similar value. They are consistent with $\log(S/O)_\odot = -1.36$, the solar value (Grevesse and Sauval, 1998) within the observational errors (see Figure 4.15).

The logarithmic Ne/O ratio is remarkably constant of both objects, with a mean value of 0.75, despite, for example, the differences in oxygen abundances between knot A and the other two in J1657. They are consistent with solar value, log(Ne/O) = -0.61 dex[4], as shown in Figure 4.16.

Finally, the Ar/O ratios found show a very similar value for Knot A and B, while Knot C has a ratio higher by 0.2 dex. Both knots of IIZw71 have the same ratio. The mean value is consistent with solar[5] (see Figure 4.16).

4.4.2 Chemical abundances from empirical calibrators for Knots A and D of IIZw71

The emission-line spectra of the four star-forming knots in IIZw71 are remarkably similar, implying similar values for ionization parameter, ionization temperature, and chemical abundances. We derived the ionization parameters from the ratio of the [OII] and [OIII] lines according to the expression given in Díaz et al. (2000) (see Chapter §3). They are similar in all the knots ranging from 6.42×10^{-4} for knot A to 9.67×10^{-4} for knot C. Using these values, the corrected Hα fluxes, and the sizes of the regions from Hα images we can calculate the density of the emitting gas (Diaz et al., 1991). This is similar for the four knots with a value of about 20 particles $\cdot$ cm^{-3}, consistent with the upper limits we derived from the ratio of the [SII] lines and providing filling factor for the gas of a few times 10^{-2}, values common

[4]Oxygen from Allende Prieto et al. (2001) and neon from Grevesse and Sauval (1998).
[5]Oxygen from Allende Prieto et al. (2001) and argon from Grevesse and Sauval (1998).

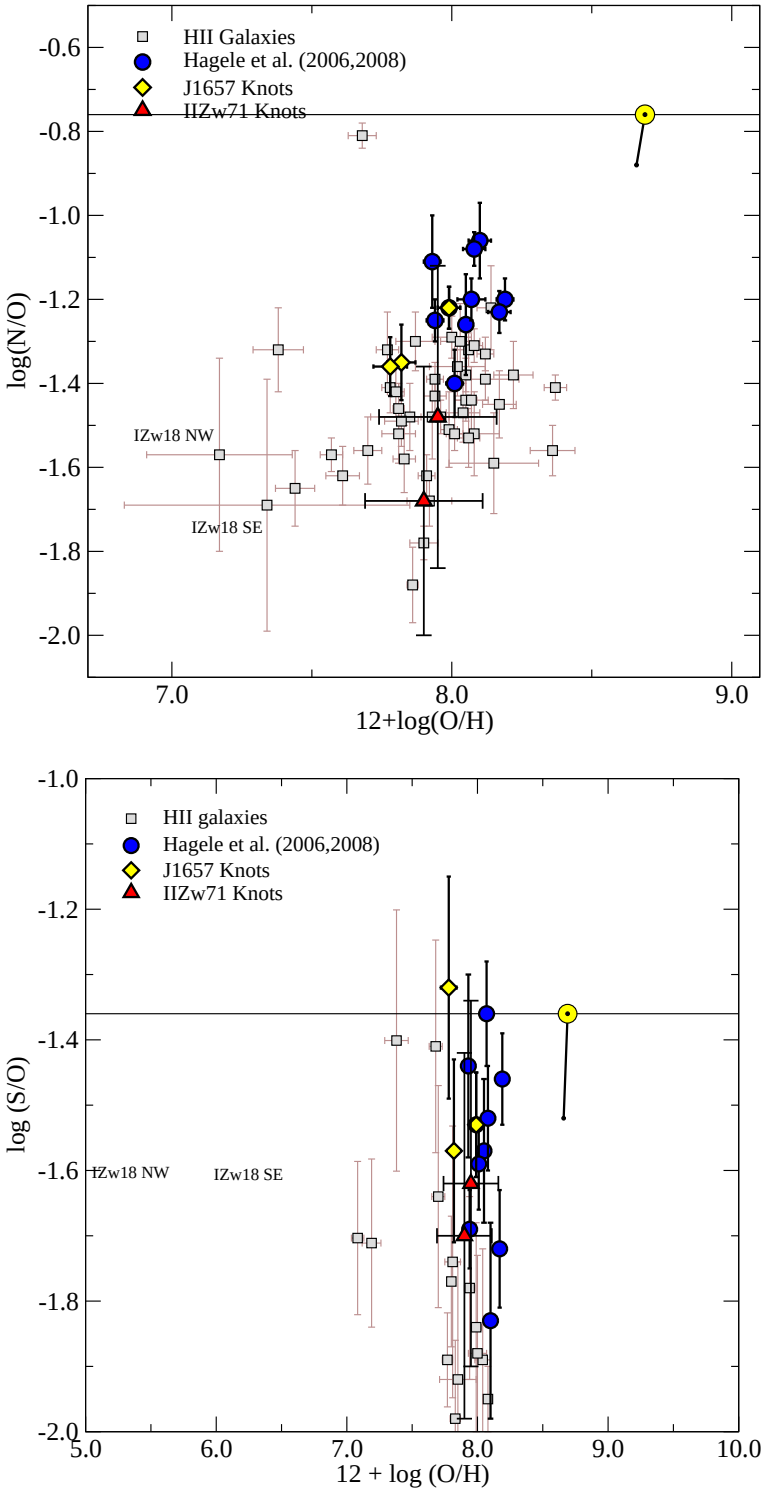

Figure 4.15: N/O (*upper panel*) and S/O (*lower panel*) ratios as a function of 12+log(O/H) for the knots of J1657 (filled yellow diamonds), knots of IIZw71 (filled red triangles), the objects of Hägele et al. (2006) and Hägele et al. (2008) (blue circles) and the HII galaxies (open squares) from the literature. The solar values are shown with the sun symbol; oxygen from Allende Prieto et al. (2001), nitrogen from Holweger (2001) and Grevesse and Sauval (1998) for sulphur. These values are linked by a solid line with the solar ratios from Asplund et al. (2005).

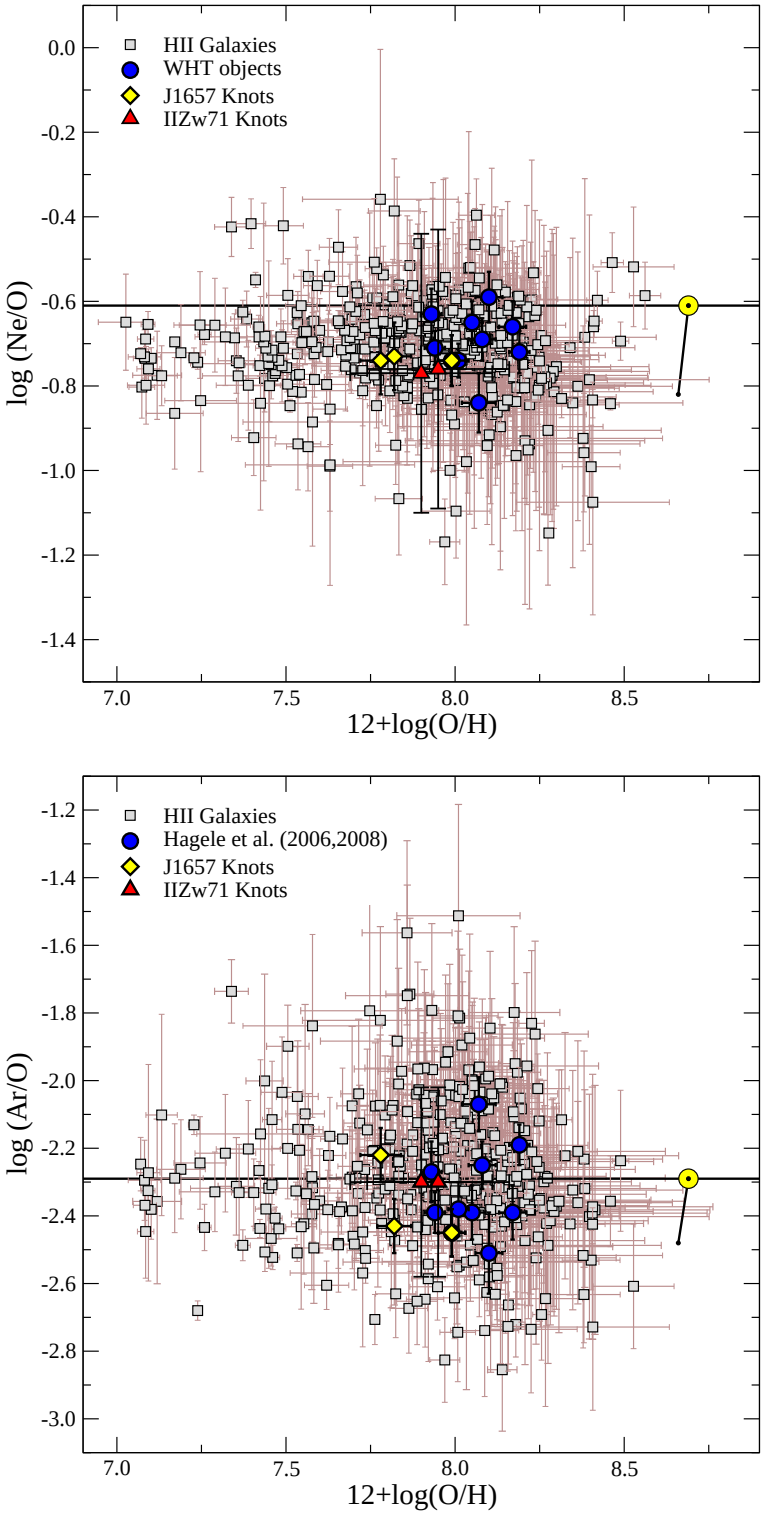

Figure 4.16: Ne/O (*upper panel*) and Ar/O (*lower panel*) ratios as a function of 12+log(O/H) for the knots of J1657 (filled yellow diamonds), knots of IIZw71 (filled red triangles), the objects of Hägele et al. (2006) and Hägele et al. (2008) (blue circles) and the HII galaxies (open squares) from the literature. The solar values are shown with the sun symbol; oxygen from Allende Prieto et al. (2001) and from Grevesse and Sauval (1998) for neon and argon. These values are linked by a solid line with the solar ratios from Asplund et al. (2005).

to giant HII regions.

As we have seen from previous sections, the derived ionic abundances knots B and C are very similar. However, due to the lack of auroral lines in the spectra of knots A and D, no temperatures have been derived and therefore, no ionic abundances. The calculation of metallicities in these two knots can only be carried out with calibrations based on the strongest emission lines, as we did in Chapter §3 for knot D of NGC 6946.

The different strong-line methods for abundance derivations, which have been widely studied in the literature, are based on directly calibrating the relative intensity of some bright emission lines against the abundance of some relevant ions present in the nebula (see Appendix C for details on the definition and equations of the parameters used in this work). For the case of oxygen, we take the calibrations studied by Pérez-Montero and Díaz (2005), who obtain different uncertainties for each parameter in a sample of ionized gaseous nebulae with accurate determinations of chemical abundances in the whole range of metallicity.

In Figure 4.17, we show the corresponding total abundances as derived from several strong-line methods and the oxygen abundances calculated from the electron temperatures measured in knots B and C. Among the available strong-line parameters we studied the O_{23} parameter (also known as R_{23} and originally defined by Pagel et al. (1979) and based on [OII] and [OIII] strong emission lines). This parameter is characterised by its double-valued relation with metallicity, with a very large dispersion in the turnover region. According to the values measured in knots B and C, we used the McGaugh (1991) calibration for the lower branch, obtaining similar values for the oxygen abundance in the four observed knots.

The N2 parameter (defined by Storchi-Bergmann et al., 1994) is based on the strong emission lines of [NII]. It remains single-valued up to high metallicities in its relation to oxygen abundance, and it is almost independent of reddening and flux calibrations. Nevertheless, it has the high dispersion associated to the functional parameters of the nebula (ionization parameter and ionizing radiation temperature) and to N/O variations. We used the empirical calibration of this parameter from Denicoló et al. (2002) to derive the oxygen abundance in the four knots of this galaxy. We can see in Figure 4.17 that the abundances predicted by this parameter are quite similar for all the knots although higher than the values derived from the direct method in knots B and C.

The S_{23} parameter was defined by Vilchez and Esteban (1996) and is based on the strong emission lines of [SII] and [SIII]. The calibration done by Pérez-Montero and Díaz (2005) yields oxygen abundances comparable for the four observed knots, slightly higher than the directly derived abundances of knots B and C, but still consistent with them within the errors. In the case of sulphur, both the directly and empirically derived abundances of knots B and C are slightly different with knot C showing a lower abundance. However it should be remembered that the near IR sulphur lines relative to the hydrogen recombination lines are more affected by reddening than in the case of oxygen when no Paschen lines are observed, which is the case.

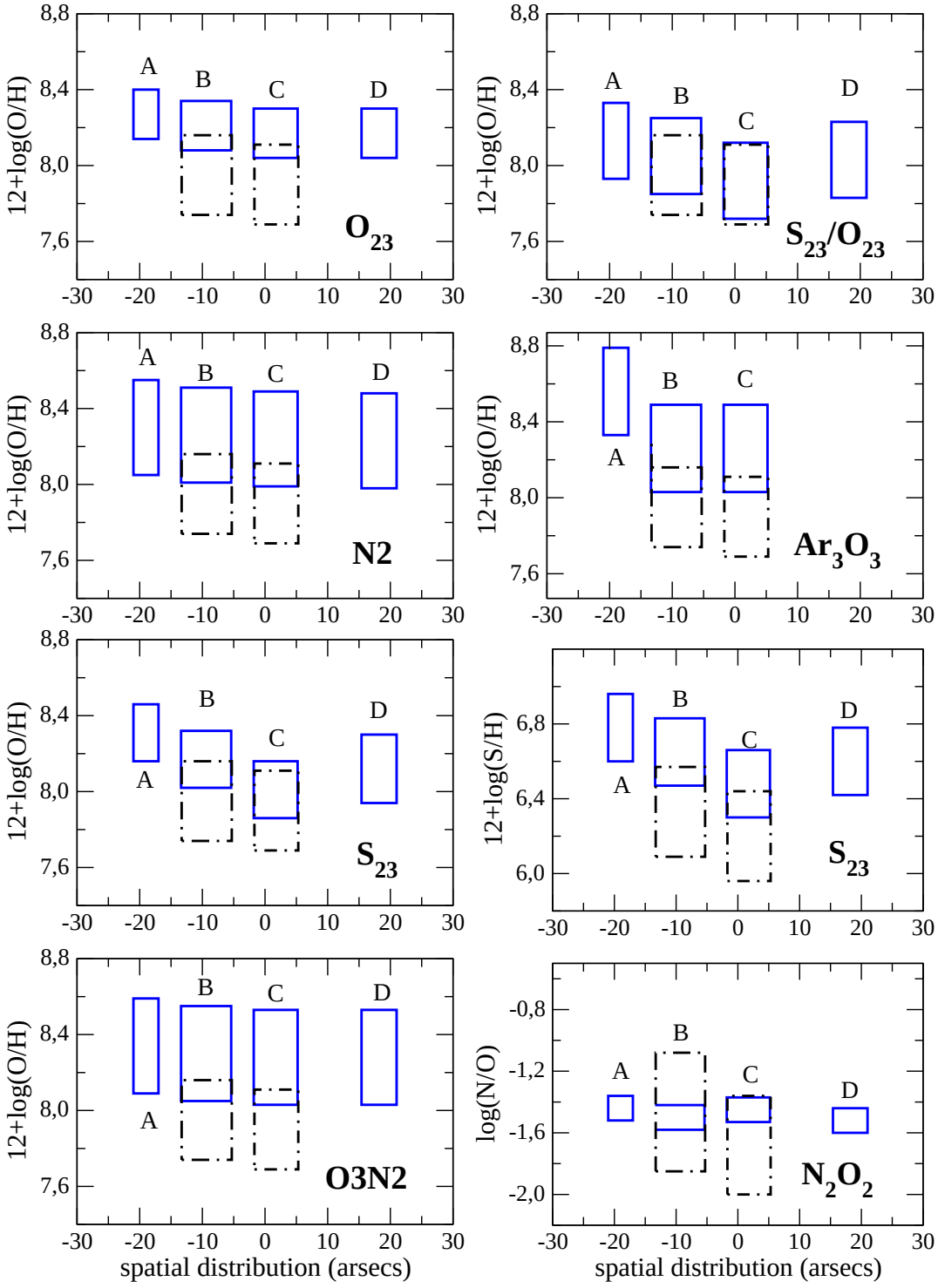

Figure 4.17: The oxygen abundances and their uncertainties for each observed knot of IIZw71, as derived using different empirical calibrators. From upper to lower panel: O_{23}, N2, S_{23} and O3N2, at left and Ar_3O_3 and S_{23}/O_{23} at right. The lower panels of right column represent the sulphur abundance as derived from the S_{23} parameter and the N/O ratio as derived from the N_2O_2 parameter. The dash-dotted line represent the abundances and their uncertainties as derived from the direct method in knots B and C.

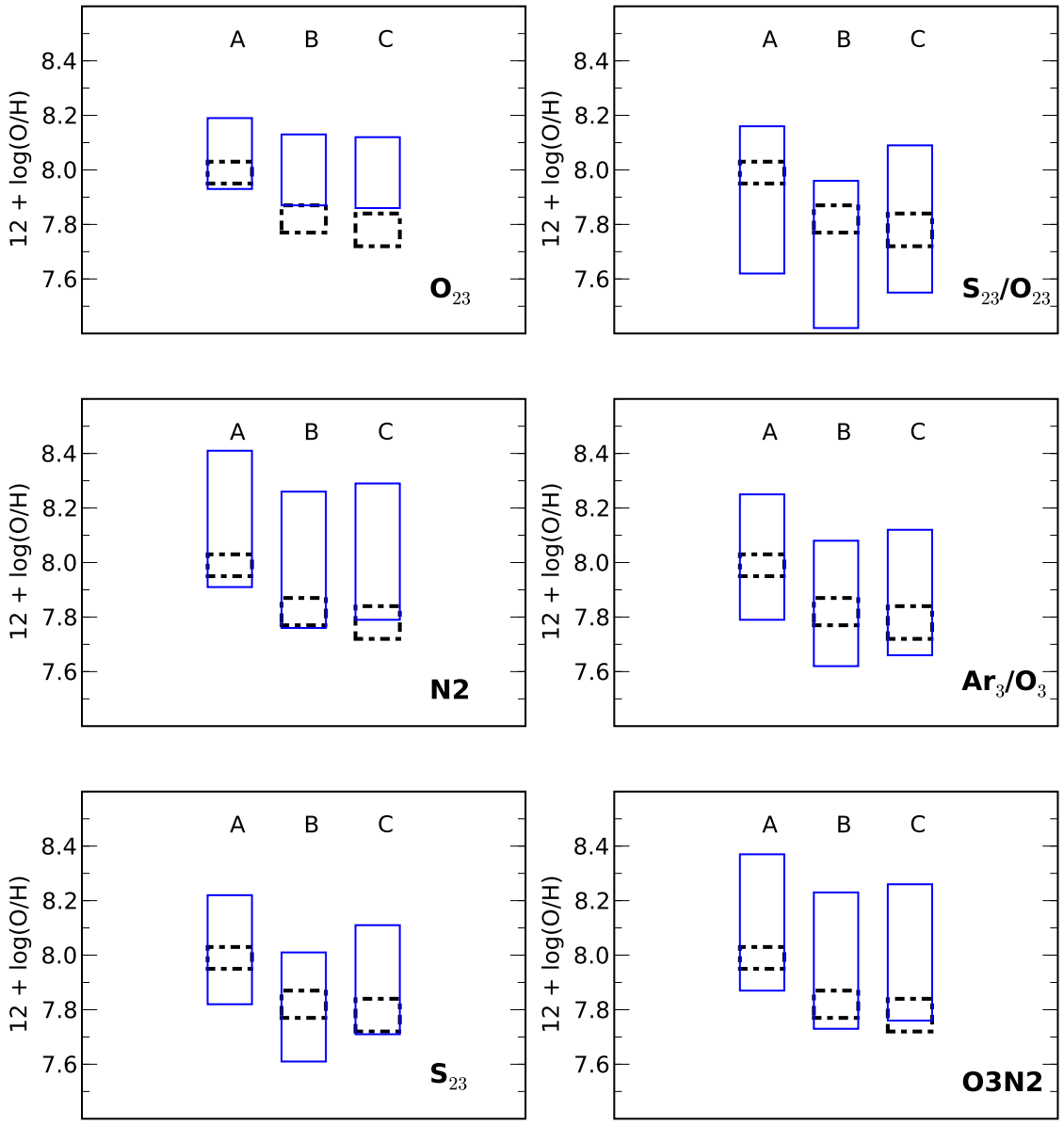

Figure 4.18: The oxygen abundances and their uncertainties for each observed knot of J1657, as derived using different empirical calibrators. From upper to lower panel: O_{23}, N2, and S_{23}, at left and S_{23}/O_{23}, Ar_3O_3 and O3N2 at right. The dash-dotted line represent the abundances and their uncertainties as derived from the direct method.

The parameter O3N2, defined by Alloin et al. (1979) depends on strong emission lines of [OIII] and [NII]. We used the calibration due to Pettini and Pagel (2004) and, as we can see in Figure 4.17 it has a very similar behaviour to that of N2.

The combination of the S_{23} and O_{23} parameters gives S_{23}/O_{23}, defined by Díaz and Pérez-Montero (2000), a parameter that increases monotonically with the oxygen abundance up to oversolar regime and which is very useful to study variations over wide ranges of metallicity (*e.g.* disks). We applied the calibration found in Pérez-Montero and Díaz (2005) and, in this case, there is almost a perfect coincidence with the values found by the direct method in knots B and C. Again, we find a similar value in knots D and A.

The Ar_3O_3 parameter, defined and calibrated by Stasińska (2006) as the ratio of [ArIII] 7136 Å and [OIII] 5007 Å emission lines, predicts identical values for the metallicity in knots B and C, although noticeably higher than the directly derived ones. A rather high value is found in knot A and no data on the [ArIII] line in knot D were available.

Finally, the N_2O_2 parameter, defined by Pérez-Montero and Díaz (2005) as the ratio between [NII] and [OII] emission lines, can be used to obtain the N/O ratio. Using this parameter, very little difference is found in N/O among the four observed knots, which are also consistent with the directly derived ratio.

For the sake of comparison, Figure 4.18 shows the corresponding total oxygen abundances as derived from the strong-line methods used in the previous case and the oxygen abundances calculated from the electron temperatures measured in the three knots of J1657. As it can be seen, O_{23} and N2 parameters clearly overestimate the oxygen abundance, particularly in the case of knots B and C. The behaviour of the rest of the parameters is very similar as for IIZw71, except for Ar_3O_3, which has a better estimation of the abundance for all the knots.

4.4.3 The stellar population

The study of the stellar content in the observed knots of J1657 and IIZw71 was carried out using the STARLIGHT code, which calculates the combination of stellar libraries and the extinction law that reproduces the spectral distribution of energy, to derive the properties of the stellar population in each of the knots. The used Population Synthesis stellar libraries and the method to fit the observed spectra of each of the knots is described in section 4.3.1.

In Figures 4.19 and 4.20 we show the age distributions of the mass fraction (upper) and the visual light fraction (bottom) for the knots of IIZw71 and J1657, respectively. All of them present a very young stellar population with ages below 10 Myr (IIZw71) or around this value (J1657), responsible for the ionization of the surrounding gas, although most of the stellar mass belongs to populations older than 100 Myr in almost all cases for IIZw71. Interestingly, for J1657, practically all the mass of the knots comes from a very old population of 8.3 Gyr. The estimated total stellar mass and the fraction by mass of the stellar population with an age younger than 10 million years, responsible for the ionization of the gas, are listed in

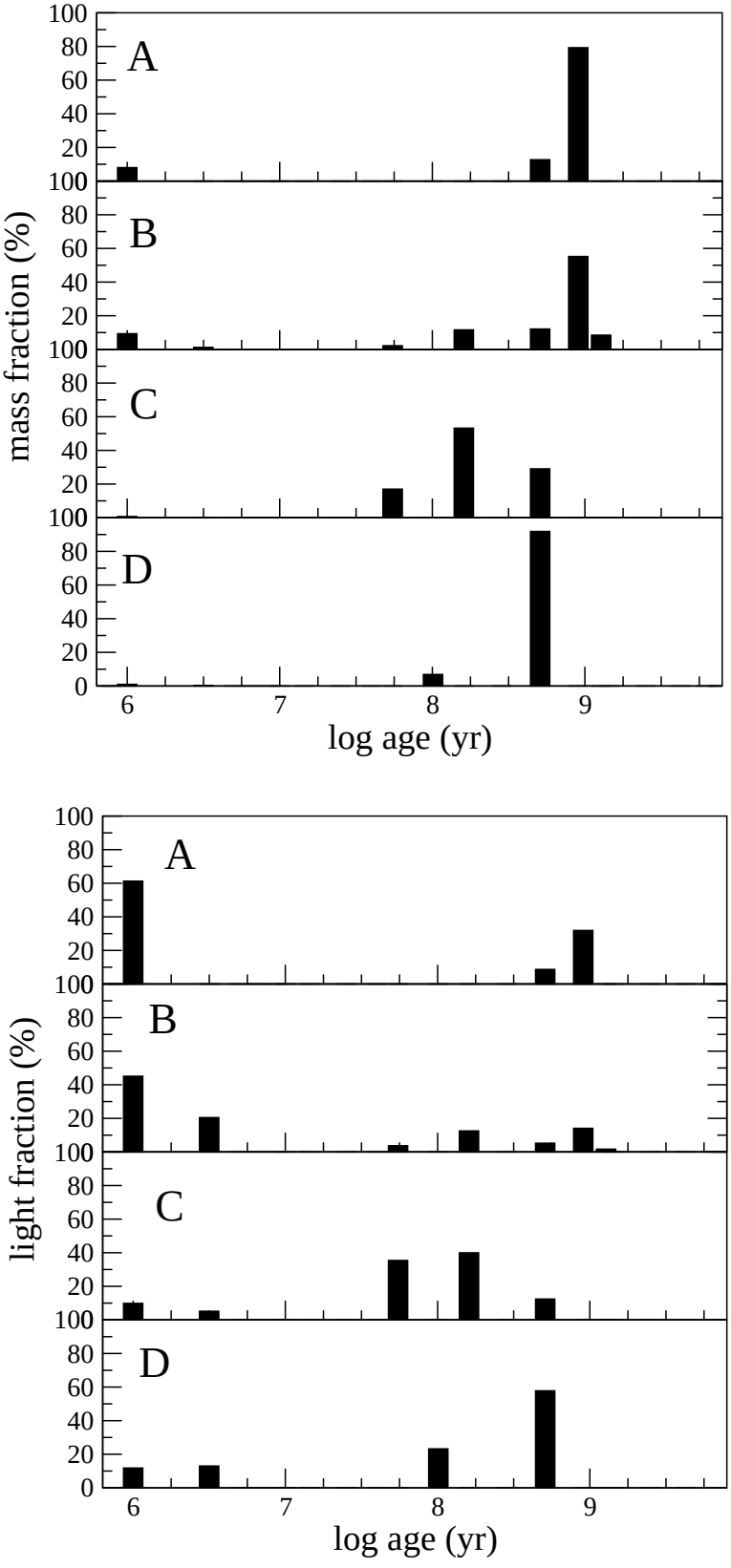

Figure 4.19: Histogram of the distribution in mass fraction (*upper*) and visual light (*bottom*) of the most probable stellar population models fitted by STARLIGHT for each of the observed knots of IIZw71.

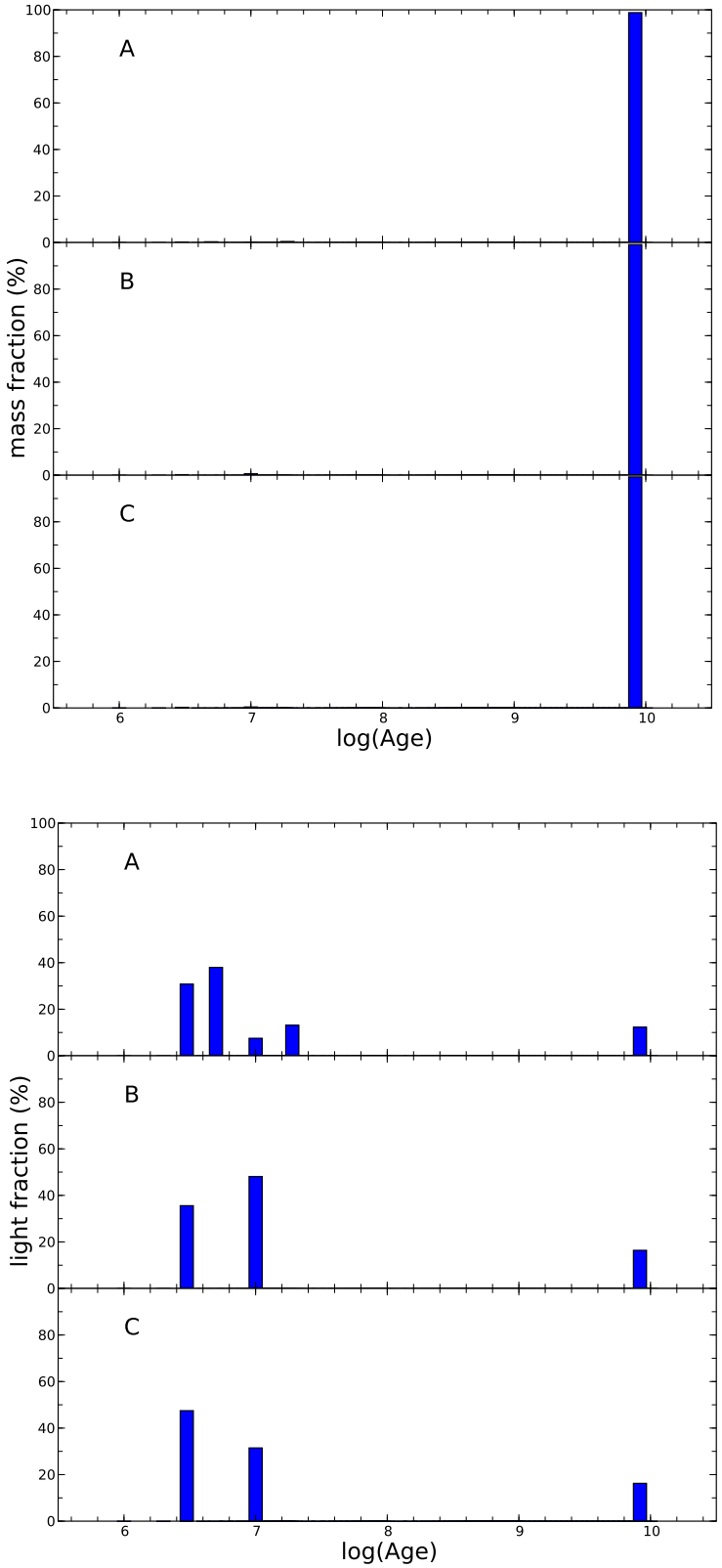

Figure 4.20: Histogram of the distribution in mass fraction (*upper*) and visual light (*bottom*) of the most probable stellar population models fitted by STARLIGHT for each of the observed knots of J1657.

ID	A(V) (mag)	c(Hβ)	M_* ($M_\odot$)	f(age < 10 Myr) (%)
IIZw71 Knot A	0.41	0.19	1.4×10^6	0.08
IIZw71 Knot B	0.99	0.46	8.3×10^6	0.11
IIZw71 Knot C	0.09	0.04	3.3×10^7	0.008
IIZw71 Knot D	0.54	0.25	2.9×10^6	0.013
J1657 Knot A	0.18	0.08	2.8×10^8	0.58
J1657 Knot B	0.00	0.00	1.0×10^8	0.21
J1657 Knot C	0.00	0.00	1.4×10^8	0.28

Table 4.9: Values of the extinction, total stellar mass, and fraction of the mass in stars younger than 10 Myr for each knot of IIZw71 and J1657 in the best-fit model predicted by STARLIGHT.

Table 4.9 for all the knots, together with the internal extinction, represented by A(V) (as given by STARLIGHT) and the reddening constant (using the transformations of Appendix A), estimated by the model. For IIZw71, the masses were corrected using an aperture factor, which takes into account the light not collected by the slit and which was calculated as the weighted mean of the ratios of the light in the whole region as measured in the Hα image and in the regions covered by the slit. In the case of J1657, no aperture correction factors have been taken into account for the Hα luminosities, due to the compact nature of the object. Indeed, the discrepancy factors between our Hα luminosities for Knot A and those measured in the SDSS catalogue using a 3 arcsec fiber is not larger than 1.3.

Although it is not expected to find the same values of extinction in the gas and the stellar population, there is a very good agreement between the values of the extinction estimated by STARLIGHT in knots C and D of IIZw71 in relation to the values obtained from the decrement of Balmer. In J1657, although the behaviour of the extinction is inverted, being larger in knot A that in B and C, the opposite from the derived values using the decrement of Balmer, the general result is consistent with low extinction. In knots A and B of IIZw71, the values are higher than those derived for the ionized gas. In these two knots the specific weight of the youngest population is higher. Since STARLIGHT assumes a common source of extinction for all the stellar populations entering the fit, the degeneracy between age and extinction tends to overestimate the extinction derived for the optimal fit. On the other hand, in knots C and D, which are probably contaminated by the light coming from the host galaxy, the contribution by the young stellar population is much lower, and the light at longer wavelengths is dominated by the older stellar population and the estimated average extinction is more representative.

ID	R_{eq} (arcsec)	F(Hα) (erg s^{-1} cm^{-2})	L(Hα) (erg s^{-1})	Q(H^o) (s^{-1})	M_{ion} ($M_\odot$)	M(HII) ($M_\odot$)	SFR $M_\odot$/yr
IIZw71 A	1.64	1.25×10^{-14}	4.9×10^{38}	3.6×10^{50}	5.6×10^{4}	7.3×10^{3}	0.004
IIZw71 B	2.94	4.83×10^{-14}	1.9×10^{39}	1.4×10^{51}	2.4×10^{5}	3.3×10^{4}	0.015
IIZw71 C	2.65	3.96×10^{-14}	1.6×10^{39}	1.1×10^{51}	4.4×10^{5}	2.3×10^{4}	0.012
IIZw71 D	1.43	1.10×10^{-14}	4.3×10^{38}	3.2×10^{50}	5.3×10^{4}	6.4×10^{3}	0.003
J1657 A	···	1.75×10^{-14}	5.4×10^{40}	3.9×10^{52}	2.2×10^{6}	1.3×10^{6}	0.430
J1657 B	···	7.32×10^{-15}	2.3×10^{40}	1.6×10^{52}	7.3×10^{5}	1.7×10^{6}	0.180
J1657 C	···	9.49×10^{-15}	2.9×10^{40}	2.2×10^{52}	8.8×10^{5}	2.2×10^{6}	0.233

Table 4.10: Derived properties of the observed knots using the extinction-corrected Hα fluxes measured in the images from Gil de Paz et al. (2003) for IIZw71 and in the spectra for J1657.

4.4.4 Ionising stellar populations

Some properties of the emission knots can be obtained from the measured Hα flux, such as Hα luminosity, number of ionizing photons, mass of ionizing stars and mass of ionized hydrogen (see Díaz et al., 2000). In order to obtain these quantities, for IIZw71 we analysed the Hα image of the galaxy, retrieved from the Palomar/Las Campanas atlas of blue compact dwarf galaxies (Gil de Paz et al., 2003). We defined elliptical apertures on this image for each of the four knots extracted in the spectroscopic observations and we measured all the flux inside the elliptical apertures up to the isophote corresponding to the 30% of the light in the brightest knot. These regions are shown in the right panel of Figure 4.3 and their sizes are given in the first column of Table 4.10, as the radius of a circular aperture of area equal to that encompassed by the refereed isophote. For J1657, due to the reasons given in the previous section, we have used the values obtained directly from the spectra, so no radius is given. The observed Hα flux was corrected in each knot for reddening using the values of the reddening constants, c(Hβ), given in Table 4.3 and 4.4. The derived values are given in Table 4.10.

The derived values of the masses of the ionizing clusters can be compared with those provided by the STARLIGHT fit. For J1657 STARLIGHT gives slightly lower values than the ones we derive by a factor of 2. For IIZw71 STARLIGHT gives also lower values by a factor of 2 for knots A, C and, D, but by a factor of 4 for knot B. If we take the masses derived from the Hα fluxes for IIZw71 as an example, which are, in principle, lower limits since neither dust absorption nor a possible escape of photons are taken into account, and we use the calculated proportions of young to total mass given in Table 4.9 we obtain total masses between 7 $\times$ 10^7 and 4$\times$ 10^8 $M_\odot$ for knots A, B, and D and 5$\times10^9$ $M_\odot$ for knot C. This high value points to a large contribution to the older population by the bulge of the host galaxy. This is consistent with the continuum light distribution shown in Figure 4.3

which is wider than that associated with cluster C and peaks at a region displaced from that of the cluster by 1.6 arcsec (about 144 pc). On the other hand for knot B the cluster shows a significant continuum of the same spatial extent as the line emission and the maxima of both distributions coincide. Knots A and D show very little continua of their own, so their underlying population probably corresponds to the outer parts of the host galaxy.

Since the differences in metallicity among the different knots of IIZw71 are not significant and the age distributions are also similar, this could indicate a common chemical evolution of these knots, probably related to the process of interaction with the companion galaxy IIZw70.

In the case of J1657, since all the values of proportions of young to total mass are very similar, the same exercise yield a mass of about 3×10^8 $M_\odot$ for the three knots.

The star formation rate (SFR) for each knot was derived from the Hα luminosity using the expression given by Kennicutt (1998):

$$SFR = 7.9 \times 10^{-42} \times L(H\alpha)$$

The derived values are also given in Table 4.10. In the case of J1657, the values for SFR range from 0.180 $M_\odot$ yr^{-1} for knot B to 0.430 $M_\odot$ yr^{-1} for knot A, between one and two orders of magnitude larger than in IIZw71. For the polar ring, they vary from 0.003 $M_\odot$ yr^{-1} for knot D to 0.015 $M_\odot$ yr^{-1} for knot B and provide a total SFR for the ring of 0.035 $M_\odot$ yr^{-1}, about half of the values quoted by Kewley et al. (2005) for the integrated object, which is 0.066 $M_\odot$ yr^{-1}. Using the sizes of the emitting regions obtained from the Hα images and listed in Table 4.10, we obtain a rather constant SFR per unit area, of the order of $7{\times}10^{-8}$ $M_\odot$ yr^{-1} pc^{-2}. This is higher than the average value of individual HII regions in polar rings given in Reshetnikov and Combes (1994) which is 3.2 $\times 10^{-9}$ $M_\odot$ yr^{-1} pc^{-2}.

It is worth to compare the luminosities and masses of H^+ of these two objects to those derived for the GEHRs in previous chapters. As it can be appreciated from Tables 2.4, 3.10 and 4.10, the values derived for knot A and B of NGC 5471 or knot A and C of NGC 6946 are of the same order of knot B of IIZw71, the most luminous one. Thus, one knot of this galaxy can be treated as a knot of a GEHR. Regarding J1657, the properties one knot of this galaxy can be compared with those of a whole GEHR. It should be noted that HII galaxies present a wide variety of luminosities, some of them presenting knots of the same order as individual knots of GEHRs.

4.4.5 Kinematics and dynamics of the polar ring

We have analysed the differential radial velocity along the slit using the Hα and [SII] 6717 Å emission lines. The heliocentric velocities are displayed in Figure 4.21 superimposed on the observed Hα profile. We find an asymmetric rotation, as it was already stated by Reshetnikov and Combes (1994), possibly affected by the expanding velocities of the bubbles of ionized

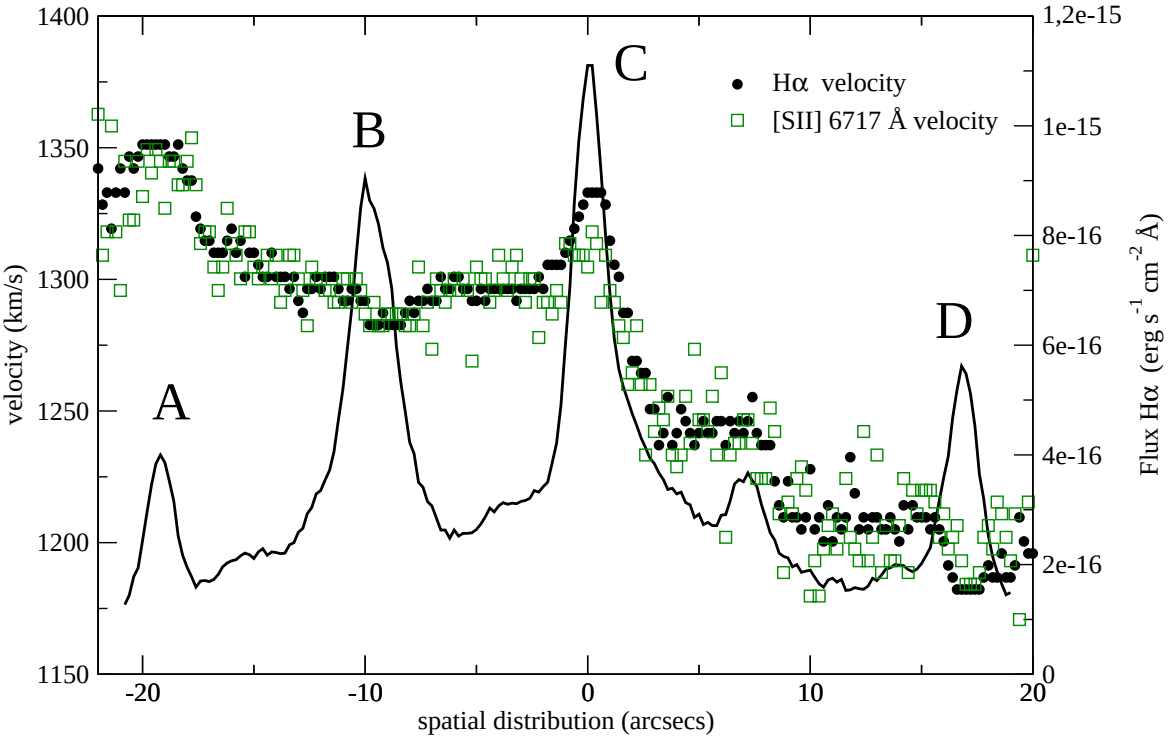

Figure 4.21: Rotation curve of IIZw71. Filled circles represent heliocentric velocity derived from Hα and open squares from [SII] 6717 Å. Solid line represents the spatial distribution of flux of Hα to be compared with the rotation curve.

gas surrounding the knots of star formation which reaches 60 km/s in the case of knot C.

Assuming that we see the polar ring of the galaxy edge-on, with a radial velocity of 85 km/s, and considering an optical radius of 20 arcsec, which is where we can measure the emission lines with a good enough signal-to-noise ratio, we calculated a dynamical mass inside this radius of (2.8 $\pm$ 0.2) $\times 10^9$ $M_\odot$. We then calculated the L_B luminosity inside the radius of 20 arcsec, internal to the polar ring, from the B brightness distribution given in Cairós et al. (2001), obtaining $L_B = 7.2 \times 10^8$ $L_\odot$. Therefore, we obtain a value of 3.9 for the M/L_B ratio inside the star forming-ring. This is close to the value of 2.8 found by Reshetnikov and Combes (1994) from optical observations within a distance of 30 arcsec from the centre. Considering that their blue light probably encompasses the light coming from the emission knots in the ring, that luminosity probably constitutes an upper limit and provides a lower limit to the M/L_B.

Chapter 5

Conclusions and future work

In the present thesis we have studied star formation processes in galaxies at different scales: looking inside giant HII regions of the Local Universe and individual starburst knots in HII galaxies.

For NGC 5471, a GEHR in the outskirts of the spiral galaxy M101, we have performed a cluster and resolved stellar photometry study to derive the star formation history of this complex. Integrated photometry of the whole region, using data from GALEX (ultraviolet), HST/WFPC2 (optical) and TNG (near infrared), yields two possible solutions for a single stellar population: one that corresponds to an age of $\sim$ 8 Myr with moderate extinction and one with an age around 50 Myr and very low extinction. This degeneration is typical of this kind of approach when spatially integrated data are used and reflects the complexity of GEHR which include clusters with different ages and extinction values.

From the photometric analysis of the eleven clusters defined on the IR H image a clear correlation emerges in the sense that redder knots have less Hα flux, showing a clear aging trend. The ages range from 3 Myr for the youngest cluster, up to 10 Myr for the oldest one.

The complex history of star formation of NGC 5471 revealed by the cluster analysis is confirmed by the resolved stellar analysis. From the CMD it is clear that star formation has been proceeding more or less continuously for the last 100 Myr. The well-defined main-sequence gives a youngest age of about 4 Myr, while red stars, which span a range of 3-4 magnitudes, indicate that star formation has occurred during the last 15-70 Myr.

We have found that the masses of the ionized gas and of the stellar cluster in the current star formation event are both of the same order of magnitude, close to 10^6 $M_\odot$, which may be understood in terms of a very high efficiency in star formation. This implies that there

has to be a large reservoir of gas to maintain this star formation rate, something that is confirmed by the huge HI concentration in which the region is located.

From the spatial distribution of the stars, we can conclude that the star formation in NGC 5471 has proceeded in an general spatio-temporal sequence from the halo innwards to the core, something also seen in 30 Doradus (Walborn and Blades, 1997). The current event of ionizing clusters is contained within a large bubble, which is likely to have been produced by the stars that formed $\sim$ 20 Myr ago. This leads to the general question of if a low density "seed" generation of evolved intermediate mass stars is in fact a prerequisite to trigger a starburst event (Brandner, 2002). More data of similar kind are obviously needed in order to have an answer.

The total oxygen abundances of the four resolved knots analysed spectroscopically (Skillman, 1985; Kennicutt et al., 2003) show a similar value with only one of them showing a slightly lower oxygen content. No more detailed studies for this region have been yet done.

The recently developed technique of Integral Field Spectroscopy offers the opportunity to perform a spatially resolved study of the physical conditions of the ionized gas of GEHR exploring at the same time the properties of their ionizing stellar populations. This has been done in this work for the giant HII region complex in NGC 6946 using PPak attached to the 3.5m telescope of the CAHA observatory. The configuration was chosen to cover the whole spectrum from 3600 up to 10000 Å, allowing the measurement of the [SIII] lines in the near infrared. This is the first time to our knowledge that data of this kind have been obtained for such a wide spectral range.

From the created maps, we have selected four main knots, labelled from A to D, to perform a detailed integrated spectroscopic analysis of these structures and of the whole PPak field-of-view. For all the knots the density has been found to be very similar and below 100 cm^{-3}. The electron temperature of [OIII] was measured in knots A, B, C and the integrated PPak-field, and was found to be around 8000 K. The temperatures of [OII] and [SIII] were also measured in the four cases. The abundances derived from the "direct method" are typical of high metallicity disk HII regions, and very uniform among all knots, with a mean value of 8.65. This is comparable to what has been found by other authors for regions at similar galactocentric distance (Larsen et al., 2006). The S/O and N/O ratios are very similar in all structures. Therefore, a remarkable abundance uniformity is found despite the different excitations found throughout the nebula that can be appreciated in the [OIII] λ 5007/Hβ, [NII] λ 6584/Hα and, [SII] $\lambda\lambda$ 6717,6731/Hα maps. This uniformity is also supported by the behaviour of the S_{23} parameter which is approximately constant despite the wide range of excitation observed. This confirms the results found in the classical studies by Skillman (1985), Diaz et al. (1987), Rosa and Mathis (1987), and more recently in spatially resolved studies of HII galaxies (Kehrig et al., 2008; Lagos et al., 2009). On the other hand, there are stellar populations old enough as to produce supernovae since at least one is reported to exist in the region (Mayall, 1948). This implies either a very fast and effective

mixing with the surroundings or that, as suggested by Stasińska et al. (2007), the new metals processed and injected by the current star formation episode are not observed and reside in the hot gas phase. The metals from previous events, on the contrary, would be well mixed and homogeneously distributed through the whole extent of the region.

The Hα luminosity of the emission knots amounts to about 50% of the total PPak field of view. Knot A is the brightest of them and provides 75% of the combined flux from the knots and 38% of the total Hα flux. This knot has the highest excitation as characterised by the [OII]/[OIII] ratio and dominates the excitation deduced for the PPak field integrated spectrum. On the other hand the measured Hβ equivalent width for this entire region is about 40 Å, much lower than the ones measured for the individual knots that range from 60 to 100 Å. That is, the integrated spectra shows high excitation and a relatively evolved age which does not correspond to the individual knot evolutionary stages.

Wolf-Rayet features have been detected in knot A and C, and a weak contribution by these stars has been also found in knot B, leading to a derived total number of WR stars of 125, 22 and 5, respectively and provide O/WR number ratios which are consistent with SB99 models for an age of about 4 Myr for the metallicity of the region. Knot D, with no WR features, shows weak Hα emission, low excitation, and the lowest Hβ equivalent width value all of which points to a more evolved state.

Once the assumption of uniform abundance has been confirmed true for GEHR from IFS observations, spectrophotometric observations of two HII galaxies, IIZw71 and J1657, were carried out to study the physical properties of the individual bursts of star formation. The star formation processes in HII galaxies are found to occur in low density environments. In all the knots of J1657 the electron densities have been found to be lower than 30 cm^{-3}, well below the critical density for collisional de-excitation. For IIZw71, two densities were measured: n([OII]) and n([SII]), the latter one being slightly higher than the former. Although by factors between 5 and 10 larger than for J1657, the densities found are still bellow the critical value for collisional de-excitation.

We extracted information on the four brightest knots of IIZw71 in Hα that we labelled from A to D and of the three knots of J1657, labelled from A to C. In this latter galaxy, we have measured four line temperatures: T_e([OIII]), T_e([SIII]), T_e([OII]), and T_e([SII]), reaching high accuracies. For IIZw71, the electron temperature of [OIII] was measured in knots B and C, with an accuracy of 14%. The temperature of the main knot of J1657 has been found to be about 2000 K lower than the other two knots, while the [OIII] temperature of knot C of IIZw71 is 1000 K higher than B. The temperatures related to the high ionization zone ares similar for both galaxies, with a mean value of 13000 K.

The temperature measurements for both galaxies allowed the direct derivation of ionic abundances of oxygen, sulphur, nitrogen, neon and argon. The total abundances of these species are in the same range of metallicities measured in HII galaxies, between 7.78 and 7.99. Knot A of J1657 presents a slightly larger abundance by 0.1 dex with respect to the

other two, very similar. Knots B and C of IIZw71 have the same metallicity, within the errors, but they are slightly lower than the abundances previously reported from measurements of the integrated galaxy according to strong-line calibrations. The metallicity in the other two fainter knots of this galaxy, where the temperature sensitive line could not be detected, was estimated by means of different strong-line parameters. In all cases, the estimated abundances are consistent with those derived for knots B and C by the direct method with the parameter involving the sulphur lines providing the abundance closer to it. The rest of the parameters slightly overestimate the oxygen abundance. The N/O abundance, as derived from the N2O2 parameter (the ratio of the [NII] and [OII] intensities), is remarkably constant over the ring indicating that local pollution processes are absent. In the case of J1657, it has been found that oxygen abundances of knot B and C are very close, with knot A showing a slightly higher value. This behaviour is mirrored by the N/O ratio, but for the S/O and Ar/O, knots A and B have a similar value, knot C being the one with a different value. Regarding the Ne/O ratio, this is remarkably similar for all knots. Therefore, similar to what has been found for the GEHR, no conclusive spatial variations of the total elemental abundances throughout the two observed HII galaxies are found, so the same considerations made above apply here although at a different scale.

Although the underlying stellar population of the host galaxy of IIZw71 is detected in the spectrum of the central knot (knot C), the similarity of the star formation histories in the four knots, as deduced from the fitting of SSPs, as well as the derived metallicities, point to a common chemical evolution of the polar ring. In the case of J1657, the star formation history for the three knots derived from STARLIGHT are remarkably similar, with an old population of about 8 Gyr presenting more than the 95% contribution to the mass fraction. This result is somewhat unexpected and data on its surface brightness distribution would be very valuable to explore further this finding.

Regarding IIZw71, for the differential velocity, we used the wavelength position of Hα and [SII] to measure an asymmetric rotation of the ring with a mean value of 85 km s^{-1} at an optical radius of 20″. This gives a dynamical mass of $(2.8 \pm 0.2) \times 10^9$ M$_\odot$ and an M/L$_B$ ratio of 3.9, close to the value reported previously by Reshetnikov and Combes (1994). The kinematics of the ring is significantly affected by the expanding bubbles of ionised gas, which in the case of knot C reaches 60 km s^{-1}.

Future work

Several results of this work have revealed interesting new paths for futher investigation. This will entail the obtention of new data in a much wider wavelength range and the 3D modelling of HII regions, among others.

NGC 5471 is truly a very amazing object which deserves more detailed analysis. We have spectrophotometric data of this region with the aim to perform a kinematical study of

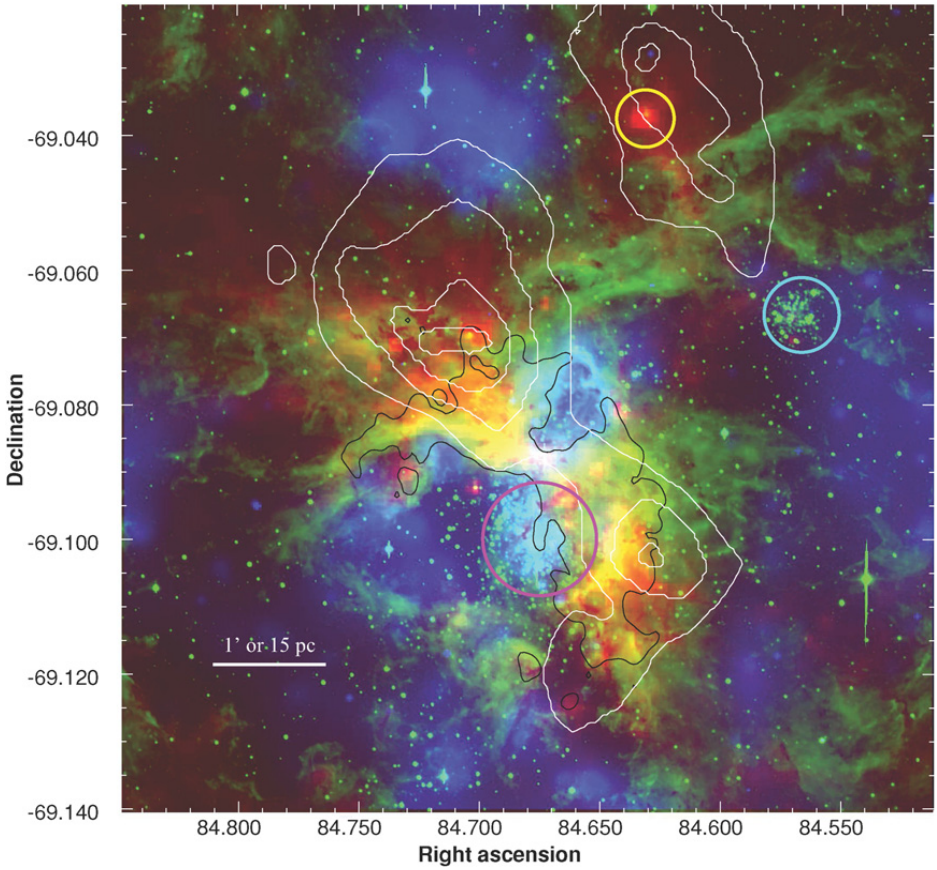

Figure 5.1: Multiwavelength 30 Doradus nebula image. Red: IRAC 8 μm image. Green: ESO B-band image. Blue: broadband soft X-ray image, 0.5-2 keV. White contours: ^{1}2CO(1-0) emission. Black contour: a single level of 3 cm radio emission. Magenta mark: the star cluster R136, core of NGC 2070. Cyan mark: the star cluster Hodge 301. Yellow mark: an IR point source in the molecular cloud Dor-06. Figure from Indebetouw et al. (2009).

the processes which are taking place in this gigantic bubble, without ruling out the use of IFS. Of great interest would be to obtain a complete SED with OSIRIS at the GTC, with tunable filters covering from the extreme ultraviolet up to the further infrared filter available. Obtaining the ionization structure, by means of narrow filters as [OII], HeII, Hβ, [OIII], HeI, Hα, [NII] and [SIII], would also be a priority. Radiocontinuum at 6 or 20 cm would allow to build an opacity map of the region.

One important issue is to extend the wavelength window and combine all available data. Observations at mid-infrared (MID) wavelengths offer several advantages for studying star formation and its interaction with circumcluster dust an gas (Indebetouw et al., 2009). This wavelength range can pierce cold molecular clouds and reveal the star-forming regions that they shroud. Thus, MIR, combined with ultraviolet and optical data, can provide a huge amount of information that will help us to understand star formation processes (see Figure 5.1). Therefore, XXI century starburst studies demands to undertake wide multiwavelength analysis.

The issue of the spatial variations of temperatures and abundances across a given HII region (or galaxy) is also one important point that deserves deeper study. For this purpose, IFS has been revealed as a powerful tool, as seen in this work. More data using this young technique is needed to enlarge the sample.

With the help of IFS, it is possible to detect and locate precisely, with two-dimensional information, the ionizing sources of a given region. Until the beginning of the XXI century, we had only one dimensional photo-ionization codes (*i.e.* CLOUDY, Ferland et al., 1998) to modelize ionized regions. However, 3D tools (*i.e.* MOCASSIN, Ercolano et al., 2003) have recently emerge as a powerful tool to unveil the processes of planetary nebula or HII regions. Due to its self-consistent treatment of asymmetries, density, chemical inhomogeneities as diffuse radiation, one of our future goals is to use MOCASSIN to modelize in a realistic way HII complexes.

Regarding stellar populations in HII galaxies, we are finishing a project to study the properties of the brightest knots of star formation in the HII galaxies studied by Hägele et al. (2006) and Hägele et al. (2008) using detailed photo-ionization models. In this way we study the properties of the ionizing stellar population, including the Wolf-Rayet stars following the analysis methodology explained in Pérez-Montero and Díaz (2007).

CONCLUSIONES

En esta tesis se han estudiado los procesos de formación estelar en galaxias a diferentes escalas: en regiones gigantes HII del Universo Local y en nodos individuales de formación estelar en galaxias HII .

Para NGC 5471, una Región HII Extragaláctica Gigante (RHEG) en las afueras de la galaxia espiral M101, se ha realizado un estudio fotométrico de sus cúmulos y un análisis estelar resuelto para obtener la historia de formaci'on estelar de este complejo. La fotometría integrada de la región como un todo, empleando para ello datos de GALEX (ultravioleta), HST/WFPC2 (óptico) y TNG (infrarrojo cercano), da dos posibles soluciones par una población estelar simple: una que corresponde a una edad de unos 8 Ma con una extinción moderada y otra con una edad de alrededor de 50 Ma con baja extinción. Esta degeneración es típica en este de métodos en los que se emplean datos integrados espacialmente, y reflejan la complejidad de las RHEG que contienen cúmulos de distintas edades y con extinción diferente.

Del análisis fotométrico de los once cúmulos definidos sobre la imagen infrarroja H, se deriva una clara correlación en la que los nodos más rojos muestran menos flujo Hα, mostrando una evidente curva de edad. Las edades se comprenden entre 3 Ma para los cúmulos más jóvenes, hasta 10 Ma para los más viejos.

La compleja historia de formación estelar de NGC 5471 mostrada por el análisis de sus cúmulos es confirmada por el estudio estelar resuelto. Del CMD, se desprende que la formación estelar se ha venido dando lugar de forma más o menos continua durante los últimos 100 Ma. En el CMD se puede apreciar una bien definida secuencia principal de unos 4 Ma, mientras que las estrellas rojas, extendidas sobre un rango de 3-4 magnitudes, indican que han ocurrido procesos de formación estelar durante los últimos 15-70 Ma.

De la distribución espacial de las estrellas, se puede concluir que la formación estelar en NGC 5471 ha seguido una secuencia general espacio-temporal desde el halo hacia el núcleo, un hecho también observado en 30 Doradus (Walborn and Blades, 1997). Los cúmulos ionizantes actuales están contenidos dentro de una gran burbuja, la cual, probablemente, se ha formado por las estrellas que se formaron hace unos 20 Ma. Este fenómeno se relaciona con la cuestión general sobre si una semilla de baja densidad de estrellas evolucionadas de masa intermedia es un prerrequisito para disparar el evento de la formación estelar (Brandner, 2002). Sin embargo, para contestar a esta pregunta son necesarios más datos de este tipo.

Las abundancias totales de oxígeno para los cuatro nodos resueltos derivadas de análisis espectroscópicos (Skillman, 1985; Kennicutt et al., 2003) muestran un valor muy similar; sólo uno de ellos tiene una abundancia ligeramente menor al resto. Hasta ahora, no se han realizado estudios más detallados de esta región.

La Espectroscopía de Campo Integral (ECI), una técnica desarrollada recientemente, ofrece la oportunidad de realizar un estudio espacialmente resuelto de las condiciones físicas del gas ionizado de las RHEG, permitiendo al mismo tiempo explorar las propiedades de las poblaciones estelares ionizantes. Esta técnica se ha empleado para el análisis del complejo de regiones gigantes HII en la galaxia NGC 6946, usando para ello PPak, un instrumento acoplado al telescopio de 3.5m del observatorio CAHA. La configuración se escogió para cubrir el rango espectral de 3600 a 10000 Å, permitiendo la medida de las líneas de [SIII] en el infrarrojo cercano. Esta es la primera vez que se utiliza un rango espectral tan amplio para este tipo de datos.

De los mapas creados, se han seleccionado cuatro nodos principales, etiquetados de A a D, para realizar un análisis espectroscópico integrado detallado de estas estructuras, así como de todo el campo de PPak. Para todos los nodos se ha encontrado una densidad muy similar, por debajo de los 100 cm^{-3}. Se pudo medir la temperatura electrónica de [OIII] en los nodos A, B, C y en el campo completo de PPak, siendo el valor medio de unos 8000 K. También se midieron las temperaturas de [OII] y [SIII] en estos cuatro casos. Las abundancias que se desprenden del "método directo" son típicas de regiones HII de disco de alta metalicidad, con un valor bastante uniforme para todos los nodos, con un valor medio de 8.65. Esto es similar a lo encontrado por otros autores para regiones situadas a una distancia galactocéntrica parecida (Larsen et al., 2006). Los cocientes de abudancias S/O y N/O son bastante parecidos en todos los nodos. Así pues, se encuentra una una abundancia bastante uniforme a pesar de la alta dispersión en excitación a lo largo de toda la nebulosa, obtenida de los mapas de los cocientes [OIII] $\lambda\,5007/\mathrm{H}\beta$, [NII] $\lambda\,6584/\mathrm{H}\alpha$ y [SII] $\lambda\lambda\,6717{,}6731/\mathrm{H}\alpha$. Esta uniformidad es apoyada por el comportamiento del parámetro S_{23}, el cual es aproximadamente constante a pesar del amplio rango de excitación observado. Estos hechos confirman el resultado encontrado por los estudios clásicos de Skillman (1985), Diaz et al. (1987), Rosa and Mathis (1987), y más recientemente por estudios espacialmente resueltos en galaxias HII (Kehrig et al., 2008; Lagos et al., 2009). Por otro lado, deben estar presentes poblaciones estelares de edad avanzada como para producir supernovas, puesto que al menos hay una detectada en este complejo (Mayall, 1948). Esto implica que, o se produce un mezclado muy rápido y efectivo, o que, como sugiere Stasińska et al. (2007), los nuevos metales inyectados en el medio por el episodio reciente de formación estelar no son observados y residen en la fase de gas caliente. Por el contrario, los metales que provienen de eventos anteriores se mezclarían y distribuirían homogéneamente por toda la región.

La luminosidad Hα de la emisión de los nodos es de aproximadamente el 50% de la totalidad de la emisión del campo de PPak. El nodo A, el más brillante, da cuenta del 75%

de flujo combinado de los 4 nodos, y un 30% del total. Este nodo tiene la mayor excitación, obtenida del cociente [OII]/[OIII], y domina en el espectro integrado de todo el campo. Por otro lado, la anchura equivalente de Hβ de toda la región es de unos 40 Å, mucho menor que la medida para cada nodo individual, cuyo margen está comprendido entre 60 y 100 Å. Es decir, el espectro integrado muestra una gran excitación y una edad relativamente avanzada, algo que no se corresponde con el estado evolutivo de los nodos individuales.

Se han detectado rasgos de Wolf-Rayet en los nodos A y C, y una contribución más débil en el B, dando como resultado un número total de estrellas WR de 125, 22 y 5, respectivamente, y cocientes O/WR consitentes con modelos SB99 para una edad de unos 4 Myr. El nodo D, sin muestras de WR, tiene una débil emisión Hα, baja excitación, y la anchura equivalente más baja de todos los nodos, lo que induce a pensar que se encuentra en un estado evolutivo más avanzado.

Una vez que se ha comprobado la hipótesis de la uniformidad de la abundancia para las RHEG mediante las observaciones ECI, se ha realizado un análisis espectrofotométrico de los nodos individuales de dos galaxias HII , IIZw71 (una galaxia con anillo polar) y J1657. Los procesos de formación estelar en galaxias HII parece ocurrir en ambientes de baja densidad. En todos los nodos de J1657 las densidades electrónicas son menores que 30 cm^{-3}, muy por debajo de la densidad crítca para la deexcitación colisional. Para IIZw71 se consiguieron medir dos densidades: n([OII]) y n([SII]), siendo la primera es ligeramente superior a la última. A pesar de que la densidad es entre 5 y 10 veces mayor que para J1657, sigue estando por debajo del valor para deexcitación colisional.

Se analizaron los cuatro nodos más brillantes de IIZw71, etiquetados de A a D, y tres, de A a C, de J1657. En esta última galaxia se midieron con gran precisión cuatro temperaturas de línea: T_e([OIII]), T_e([SIII]), T_e([OII]) y T_e([SII]). Para IIZw71, se consiguió medir la temperatura electrónica de [OIII] en los nodos B y C, con una precisión de un 14%. La temperatura del nodo principal de J1657es unos 2000K más baja que el resto de los dos nodos, mientras que la temperatura de [OIII] para el nodo C de IIZw71 es unos 1000K superior al B. Las temperaturas relacionadas con la zona de alta excitación es similar para ambas galaxias, con valor medio de unos 13000K.

Las medidas de las temperaturas para ambas galaxias ha permitido la obtención directa de las abundancias iónicas de oxígeno, azufre, nitrógeno, neón y argón. Las abundancias totales para estas especies se encuentra en el mismo rango de metalicidades que las medidas para galaxias HII , entre 7.78 y 7.99. El nodo A de J1657 presenta una abundancia ligeramente superior, de unos 0.1 dex, con respecto a los otros dos, los cuales son muy parecidos. Los nodos B y C de IIZw71 tiene la misma metalicidad, dentro de los errores. Sin embargo, sus valores son ligeramente menores que las abudancias encontradas en la literatura derivadas de medidas de la galaxia integrada o de calibraciones de líneas intensas. La metalicidad en los dos nodos más débiles de esta galaxia fue estimada a partir de varios parámetros empíricos, ya que no detectó ninguna línea auroral. En todos los casos, las abundancias estimadas son

consistentes con las obtenidas para B y C a partir del método directo, siendo el parámetro que contiene las líneas de azufre el más cercano. El resto de parámetros sobreestima ligeramente las abundancias de oxígeno. El cociente N/O, obtenido a partir del parámetro N2O2, es bastante constante a lo largo del anillo, sugiriendo que no hay procesos de polución local. Para J1657, las abundancias del nodo B y C son muy similares, mostrando el nodo A un valor ligeramente superior. Este comportamiento también es reflejado por el cociente N/O, mientras que para los cocientes S/O y Ar/O, son los nodos A y B los que tienen un valor similar. El cociente Ne/O muestra un valor marcadamente constante para todos los nodos. De estos resultados se desprende que, al igual que para las RHEG, no se aprecian variaciones espaciales para las abundancias totales a lo largo de las galaxias HII observadas. Las mismas consideraciones que se han hecho para las RHEG pueden hacerse para las galaxias HII , aunque a una escala diferente.

Aunque se detecta la población subyacente de la galaxia anfitriona de IIZw71 en el espectro del nodo central (C), la similitud de la historia de formación estelar, obtenida a partir de ajustes de Poblaciones Estelares Simples, así como de las metalicidades, apuntan hacia una evolución química común para todo el anillo. La historia de formación estelar para los tres nodos de J1657 son muy parecidas, con una población vieja de unos 8 Gyr sumando el 95% de la masa total. Este resultado es de algún modo inesperado, y sería necesario un anaálisis en términos de brillo superficial para aclarar este punto.

Con respecto a la cinemática de IIZw71, se han empleado las líneas de Hα y [SII] para medir la rotación del anillo, obteniendo un valor medio de 85 km s^{-1} a un radio óptico de 20$''$. La masa dinámica derivada de estos datos es de unos $(2.8 \pm 0.2) \times 10^9$ M$_\odot$ y un cociente M/L$_B$ de 3.9, cerca del valor encontrado por Reshetnikov and Combes (1994). La cinemática del anillo está afectada por las burbujas en expasión de gas ionizado, donde para el nodo C alcanza un valor de 60 km s^{-1}.

Appendix A

Interstellar Reddening Corrections

We summarize here the standard procedure specifying the nomenclature used to avoid confusion.

The extinction at a wavelength λ is

$$F_\lambda = F_{\lambda 0} 10^{-0.4 A_\lambda} \tag{A.1}$$

where F_λ and $F_{\lambda 0}$ are the observed and intrinsic fluxes, respectively.

The extinction A_λ is related to A_V by means of the reddening curve by $\zeta(x; R_V) = A_\lambda / A_V$, where $x = 1/\lambda$ with λ in microns, and A_λ is the extinction in magnitudes. This relation is parametrized in terms of $R_V = A_V / E_{B-V}$, where $E_{B-V} = A_B - A_V$ is the color excess. To simplify notation, we write the reddening curve as $\zeta(\lambda)$.

If the intrinsic flux passes through a medium of optical depth τ_λ the observed flux is $F_\lambda = F_{\lambda 0} e^{-\tau_\lambda}$; it is assumed that the interstellar extinction has the same wavelength dependence, so that $\tau_\lambda = C f(\lambda)$.

As the Balmer lines are strong and the line ratios are relative insensitive to electron temperature, they can be used to determine interstellar extinction with a rough estimation of the temperature. The measured ratio of two or more H I Balmer lines (Hα/Hβ, Hγ/Hβ, ...) can be compared with the theoretical ratio of the recombination theory. This can be expressed in the usual form

$$\frac{F_\lambda}{F_{H\beta}} = \frac{F_{\lambda 0}}{F_{H\beta 0}} 10^{-c[f(\lambda) - f(H\beta)]} \tag{A.2}$$

where c=0.434C. This value is the reddening constant, and is found in the literature as c(Hβ), the logarithmic extinction at Hβ ($F_{H\beta} = F_{H\beta 0}10^{-c}$). We can rearrange equation A.2 as

$$F_\lambda = F_{\lambda 0}10^{-c(\lambda)} = F_{\lambda 0}10^{-c(H\beta)(1+g(\lambda))} \tag{A.3}$$

where g(λ) = f(λ) - f(Hβ) and c(Hβ) the logarithmic extinction at Hβ, which can be written as c(Hβ) = 0.4$A_{H\beta}$. Comparing equation A.3 with A.1 and taking into account the reddening curve $\zeta(\lambda)$,

$$g(\lambda) = \frac{A_\lambda}{A_\beta} - 1 = \frac{\zeta(\lambda)}{\zeta(\lambda_{H\beta})} - 1 \tag{A.4}$$

Finally, we can write the logarithmic extinction at any wavelength c(λ) as a function of the reddening curve

$$c(\lambda) = c(H\beta)(1 + g(\lambda)) = c(H\beta)\frac{\zeta(\lambda)}{\zeta(\lambda_{H\beta})} \tag{A.5}$$

We can also write the constant of reddening in terms of the color excess

$$c(H\beta) = 0.4A_{H\beta} = 0.4\zeta(\lambda_{H\beta})R_V E(B-V) \tag{A.6}$$

Taking into account the reddening law of Cardelli et al. (1989) and a value of $R_V = 3.1$, we obtain $A_{H\beta}/A_V = \zeta(\lambda_{H\beta}) = 1.164$, which allows to write the reddening constant as a function of the color excess as c(Hβ) = 1.443 E(B-V).

Another way of estimating the extinction is by relating the visual extinction to the observed ratio of two lines. This method is useful when only Hα and Hβ are available. The relation is given by:

$$\frac{F_{H\alpha}}{F_{H\beta}} = \frac{F_{H\alpha 0}\cdot 10^{-0.4A_{H\alpha}}}{F_{H\beta 0}\cdot 10^{-0.4A_{H\beta}}} = \frac{F_{H\alpha 0}}{F_{H\beta 0}}\cdot 10^{0.4\frac{A_{H\beta}-A_{H\alpha}}{A_V}\cdot A_V} \tag{A.7}$$

and re-arranging it gives

$$A_V = 2.5\cdot \frac{log_{10}\left(\frac{F_{H\alpha}/F_{H\beta}}{F_{H\alpha 0}/F_{H\beta 0}}\right)}{\frac{A_{H\beta}-A_{H\alpha}}{A_V}} \tag{A.8}$$

Appendix B

Physical conditions of the gas and abundances

All equations employed in the calculation of the physical conditions of the gas and abundances are reproduced in this Appendix. Only the temperatures and elements involved in this work are listed.

B.1 Physical conditions of the gas

The electron density and temperatures of the ionized gas have been derived using the same procedures as in Pérez-Montero and Díaz (2003), based on the five-level statistical equilibrium atom approximation in the task *temden*, of the software package IRAF (De Robertis et al., 1987; Shaw and Dufour, 1995). The atomic coefficients used here are the same as in Pérez-Montero and Díaz (2003), except in the case of O^+ for which the transition probabilities from Zeippen (1982) and the collision strengths from Pradhan (1976) have been used, which offer more reliable nebular diagnostic results for this species (Wang et al., 2004).

Adequate fitting functions have been derived from the `temden` task. They are given below.

B.1.1 Density

Sulphur

The electron density can be derived from the [SII] $\lambda\lambda$ 6717 / 6731 Å line ratio, through the R_{S2} parameter, which is defined as:

$$R_{S2} = \frac{I(6717\text{Å})}{I(6731\text{Å})}$$

R_{S2} is related with the density in the following way:

$$n([S\,\textsc{ii}]) = 10^3 \cdot \frac{R_{S2} \cdot a_0(t) + a_1(t)}{R_{S2} \cdot b_0(t) + b_1(t)}$$

where

$$\begin{aligned} a_0(t) &= 2.21 - 1.3/t - 1.25t + 0.23t^2 \\ a_1(t) &= -3.35 + 1.94/t + 1.93t - 0.36t^2 \\ b_0(t) &= -4.33 + 2.33/t + 2.72t - 0.57t^2 \\ b_1(t) &= 1.84 - 1/t - 1.14t + 0.24t^2 \end{aligned}$$

here t is generally t([Oiii]), where $\mathrm{t} = 10^{-4}\,\mathrm{T}_e$, although an iterative process could be used to calculate it with t([Sii]) given that this temperature, like t([Oii]), a type np^3 ion, is density dependent.

Oxygen

In the case that enough spectral resolution is available to resolve the [Oii] doublet, we can use the ratio:

$$R'_{O2} = \frac{I(3727\text{Å})}{I(3729\text{Å})}$$

Therefore, the density can be calculated through the expression:

$$n([O\,\textsc{ii}]) = 10^2 \cdot \frac{R'_{O2} \cdot a_0(t) + a_1(t)}{R'_{O2} \cdot b_0(t) + b_1(t)}$$

where

$$\begin{aligned} a_0(t) &= 4.99 + 7.12/t - 4.71t \\ a_1(t) &= -3.69 - 4.54/t + 3.27t \\ b_0(t) &= 0.29 - 0.52/t - 0.011t \\ b_1(t) &= -0.88 + 1.85/t - 0.052t \end{aligned}$$

where t can be t([Oiii]), although an iterative process can be used to calculate it by means of t([Oii]).

B.1.2 Temperature

The following expressions are valid in the temperature range between 7000 and 23000 K and the errors involved in the fit are always lower than observational errors by factors between 5 and 10.

Oxygen

[OIII] temperature is calculated from the ratio:

$$R_{O3} = \frac{I(4959\text{Å}) + I(5007\text{Å})}{I(4363\text{Å})}$$

The fit, as for the rest of the np^2 ions, is independent of the electron density:

$$t([O\text{III}]) = 0.8254 - 0.0002415\, R_{O3} + \frac{47.77}{R_{O3}}$$

For [OII] the ratio for the electron temperature is calculated from:

$$R_{O2} = \frac{I(3727\text{Å}) + I(3729\text{Å})}{I(7319\text{Å}) + I(7330\text{Å})}$$

The [OII] $\lambda\lambda$ 7319,7330 Å lines have a contribution from direct recombination which increases with temperature. Such emission, however, can be quantified and corrected for as:

$$\frac{I_R(7319 + 7330)}{I(H\beta)} = 9.36\, t^{0.44}\, \frac{O^{2+}}{H^+}$$

where t denotes the electron temperature in units of 10^4 K (Liu et al., 2000). This expression is valid only in the range of temperatures between 5000 and 10000 K.

The ratio of the [OII] lines depends on the electron density:

$$t([O\text{II}]) = a_0(n) + a_1(n) \cdot R_{O2} + \frac{a_2(n)}{R_{O2}}$$

where the coefficients are respectively:

$$a_0(n) = 0.23 - 0.0005 \cdot n - \frac{0.17}{n}$$
$$a_1(n) = 0.0017 - 0.000009 \cdot n - \frac{0.0064}{n}$$
$$a_2(n) = 38.3 - 0.021 \cdot n - \frac{16.4}{n}$$

Sulphur

As in the case of [OII], the temperature of [SII] depends on density (np^3 ions). The ratio used to estimate t(S[II]) is

$$R'_{S2} = \frac{I(6717\text{Å}) + I(6731\text{Å})}{I(4068\text{Å}) + I(4076\text{Å})}$$

If one of the [SII] auroral lines cannot be measured, the theoretical ratio can be used, I(4068Å) $\approx 3 \cdot$ I(4067Å). Then, the temperature is calculated

$$t([S\text{II}]) = a_0(n) + a_1(n) \cdot R'_{S2} + \frac{a_2(n)}{R'_{S2}} + \frac{a_3(n)}{R'_{S2}}$$

where

$$a_0(n) = 1.92 - 0.0017 \cdot n - \frac{0.848}{n}$$
$$a_1(n) = -0.0375 - \frac{0.0185}{n}$$
$$a_2(n) = -14.15 + 0.019 \cdot n - \frac{10.4}{n}$$
$$a_3(n) = -105.64 + 0.019 \cdot n - \frac{58.52}{n}$$

Direct measurements of the [SIII] temperature have been possible with the availability of the collisional lines in the near IR. The ratio is:

$$R_{S3} = \frac{I(9069\text{Å}) + I(9532\text{Å})}{I(6312\text{Å})}$$

This expression can be simplified in case of lacking one of the near IR lines, using the theoretical ratio I(9532Å) $\approx 2.44 \cdot$ I(9069Å). The temperature can be calculated by the fit:

$$t([S\text{III}]) = \frac{R_{S3} + 36.4}{1.8 \cdot R_{S3} - 3.01}$$

B.2 Ionic abundances

The derived fittings to the `ionic` task results following the functional form given by Pagel et al. (1992) for each element are listed below. In all relations t denotes the appropriate line electron temperature, in units of 10^4 K, corresponding to the assumed ionization structure, and n the electron density.

Oxygen

The chemical abundance of O^+ can be determined from the intensity of the [OII] $\lambda\lambda$ 3727, 3729 Å lines:

$$12+log(O^+/H^+) = log\left(\frac{I(3727+3729)}{I(H\beta)}\right)+5.992+\frac{1.583}{t}-0.681\cdot log\,t+log(1+0.00023\cdot n)$$

For the O^{2+} abundance, [OIII] $\lambda\lambda$ 4959,5007 Å lines are used:

$$12+log(O^{2+}/H^+) = log\left(\frac{I(4959+5007)}{I(H\beta)}\right)+6.144+\frac{1.251}{t}-0.55\cdot log\,t$$

Sulphur

The abundance of the S^+ is obtained from the 6717,6731 Å lines:

$$12+log(S^+/H^+) = log\left(\frac{I(6717+6731)}{I(H\beta)}\right)+5.423+\frac{0.929}{t}-0.28\cdot log\,t+0.0001\cdot n$$

When the [SII] auroral lines are not available, it is usually assumed that t[SII] $\approx$ t[OII], although there is evidence suggesting a somewhat lower value.

The abundance is obtained from the 9069,9532 Å lines for S^{2+}:

$$12+log(S^{2+}/H^+) = log\left(\frac{I(9069+9532)}{I(H\beta)}\right)+5.8+\frac{0.771}{t}-0.22\cdot log\,t$$

Nitrogen

The N^+ abundance can be calculated from the 6548 and 6584 Å lines:

$$12+log(N^+/H^+) = log\left(\frac{I(6548+6584)}{I(H\beta)}\right)+6.273++\frac{0.894}{t}-0.592\cdot log\,t$$

Given the proximity to Hα, if one of them cannot be measured the theoretical relation I(6584Å) $\approx 2.9 \cdot$ I(6548Å) can be used.

Neon

The [NeIII] line at 3868 Å is used for neon:

$$12+log(Ne^{2+}/H^+) = log\left(\frac{I(3868)}{I(H\beta)}\right)+6.486+\frac{1.558}{t}-0.504\cdot log\,t$$

For this ion, the assumption t([NeIII]) $\approx$ t([OIII]) is usually adopted.

Argon

For argon, the [ArIII] 7136 Å line is used:

$$12 + log(Ar^{2+}/H^{+}) = log\left(\frac{I(7136)}{I(H\beta)}\right) + 6.157 + \frac{0.808}{t} - 0.508 \cdot log\, t$$

In this case, the approximation t([ArIII] ≈ t([SIII]) is normally followed.

Iron

In the case of iron, the [FeIII] λ 4658 Å emission line is used to derive the ionic abundance of the iron twice ionized, using the electron temperature of [OIII]. Care has to be taken because this line is in the region where the blue bump of the Wolf-Rayet feature lies. Izotov et al. (1994), using emissivities by Garstang et al. (1978), derived:

$$\frac{N(Fe^{++})}{N(H^{+})} = 2.3 \times 10^{-6}\, 1.387\, t^{-0.983}\, 10^{-0.0424/t} \sqrt{t}\, 10^{1.34/t}\, \frac{I(\lambda 4658)}{I(H\beta)}$$

which can be written in the functional form given by Pagel et al. (1992) as:

$$12 + log(Fe^{2+}/H^{+}) = log\left(\frac{I(4658)}{I(H\beta)}\right) + 6.504 + \frac{1.298}{t} - 0.483 \cdot log\, t$$

Helium

Helium lines, as hydrogen ones in the visible spectrum, arise mainly from pure recombination, although they have some contribution from collisional excitation and be affected by self-absorption. There are many of them, but usually blended with other lines. The ones generally used are HeI $\lambda\lambda$ 4471, 5876, 6678 and 7065Å, and HeII λ 4686Å to estimate the helium abundances once and twice ionized respectively. Normally, the [OIII] temperature is adopted as representative of the helium zone.

Olive and Skillman (2001) carried out a very thorough study to determinate all the contributions to the helium lines. In that work, the helium intensities are scaled to Hβ and the singly ionized helium abundance is given by:

$$y^{+}(\lambda) = \frac{I(\lambda)}{I(H\beta)} \frac{E(H\beta)}{E(\lambda)} \left(\frac{W(\lambda) + a_{\mathrm{HeI}})}{W(\lambda)}\right) \frac{1}{1+\gamma} \frac{1}{f(\tau)}$$

where E(λ)/E(Hβ) is the theoretical emissivity scaled to Hβ and W(λ) the equivalent width. The last expression also contains a correction factor for underlying stellar absorption, parametrized by a_{HeI}, a density dependent collisional correction factor, $(1 + \gamma)^{-1}$, and a fluorescence correction which depends on the optical depth τ.

The theoretical emissivities scaled to Hβ are taken from Smits (1996):

$$E(H\beta)/E(4471) = 2.0094T^{0.1259}$$
$$E(H\beta)/E(5876) = 0.7355T^{0.2298}$$
$$E(H\beta)/E(6678) = 2.5861T^{0.2475}$$
$$E(H\beta)/E(7065) = 4.3588T^{-0.3456}$$

For the collisional correction γ, the expressions taken from Kingdon and Ferland (1995):

$$\gamma(4471) = (6.95T^{0.15}e^{-4.545/T} + 0.22T^{-0.55}e^{-4.884/T} + 0.98T^{-0.45}e^{-4.901/T})/D$$
$$\gamma(5876) = (6.78T^{0.07}e^{-3.776/T} + 1.67T^{-0.15}e^{-4.545/T} + 0.60T^{-0.34}e^{-4.901/T})/D$$
$$\gamma(6678) = (3.15T^{-0.54}e^{-3.776/T} + 0.51T^{-0.51}e^{-4.545/T} + 0.20T^{-0.66}e^{-4.901/T})/D$$
$$\gamma(7065) = (38.09T^{-1.09}e^{-3.364/T} + 2.80T^{-1.06}e^{-3.699/T})/D$$

where D = 1 + $3130n^{-1}T^{-0.50}$. The corrections for fluorescence are given in terms of the optical depth:

$$f(4471) = 1 + 0.001\tau$$
$$f(5876) = 1 + 0.0049\tau$$
$$f(6678) = 1$$
$$f(7065) = 1 + 0.4\tau^{0.55}$$

which, as it can be seen, are close to 1.

For the helium twice ionized, the equation found by Kunth and Sargent (1983) can be used:

$$y^{2+}(4686) = (0.065 + 0.024t - 0.0052t^2)\frac{I(\lambda 4686)}{I(H\beta)}$$

Appendix C

Empirical calibrators

In this Appendix we list all the empirical metallicity calibrators used in this work, their definitions and calibrations. For a review on some of the metallicity calibrators described here and its uncertainties see Pérez-Montero and Díaz (2005) and Kewley and Ellison (2008).

The O_{23} parameter

The O_{23} parameter, also known as R_{23}, was defined as:

$$O_{23} \equiv \frac{[O\textsc{ii}]\,\lambda3727 + [O\textsc{iii}]\,\lambda4959 + [O\textsc{iii}]\,\lambda5007}{H\beta}$$

by Pagel et al. (1979). The major drawback to using O_{23} is that is doubled valued with metallicity. Three different regions can be distinguished: a lower branch in which O_{23} increases with increasing abundance, an upper branch in which the opposite occurs and a turnover region. McGaugh (1991) produced a calibration based on theoretical models in which the ionization is provide by stellar clusters of different metallicities, including a correction for ionization parameter variations. In this work we used the analytic expressions for the McGaugh (1991) lower an upper branches given in Kobulnicky et al. (1999):

$$\begin{aligned} 12 + log(O/H)_{lower} =& 12 - 4.944 + 0.767x + 0.602x^2 - y(0.29 + 0.332x - 0.331x^2), \\ 12 + log(O/H)_{upper} =& 12 - 2.939 - 0.2x - 0.237x^2 - 0.305x^3 - 0.0283x^4 - \\ & - y(0.0047 - 0.0221x - 0.102x^2 - 0.0817x^3 - 0.00717x^4) \end{aligned}$$

where x = log O_{23} and

$$y = log\left(\frac{[O\textsc{iii}]}{[O\textsc{ii}]}\right) = log\left(\frac{[O\textsc{iii}]\,\lambda4959 + [O\textsc{iii}]\,\lambda5007}{[O\textsc{ii}]\,\lambda3727}\right)$$

The estimated accuracy of the calibration is 0.13 dex for the lower branch and 0.19 for the upper branch.

The N2 parameter

The N2 parameter was defined by Storchi-Bergmann et al. (1994) as

$$N2 \equiv log\left(\frac{[N\textsc{ii}]\,\lambda6584}{H\alpha}\right)$$

The relationship between N2 and oxygen abundance is single-valued and this parameter is almost free of uncertainties introduced by reddening corrections. Nevertheless, it has it has the high dispersion associated to the functional parameters of the nebula (ionization parameter and ionizing radiation temperature) and to N/O variations. The used empirical calibration of this parameter is from Denicoló et al. (2002):

$$12 + log(O/H) = 9.12 + 0.73 \times N2$$

with an associated uncertainty of 0.25 dex.

The O3N2 parameter

The O3N2 parameter was defined by Alloin et al. (1979) as

$$O3N2 \equiv log\left(\frac{([O\textsc{iii}]\,\lambda5007/H\beta)}{([N\textsc{ii}]\,\lambda6584/H\alpha)}\right)$$

which again is almost independent of reddening correction or flux calibration. Pettini and Pagel (2004) fitted the observed relationship between this ratio and the T_e-based metallicity for a sample of 137 Hii regions. This fit is

$$12 + log(O/H) = 8.73 - 0.32 \times 03N2$$

Last equation is only valid for O3N2 ¡ 2 and its estimated accuracy is of 0.25 dex.

The S_{23} parameter

The S_{23} parameter was defined by Vilchez and Esteban (1996) as

$$S_{23} \equiv \frac{[S\textsc{ii}]\,\lambda6717 + [S\textsc{ii}]\,\lambda6731 + [S\textsc{iii}]\,\lambda9069 + [S\textsc{iii}]\,\lambda9532}{H\beta}$$

One advantage of this parameter is that the sulphur lines remain intense even for the highest metallicity objects. The calibration done by Pérez-Montero and Díaz (2005) is

$$12 + log(O/H) = 8.15 + 1.85\, logS_{23} + 0.58\, (logS_{23})^2$$

The dispersion is 0.2 dex in all the abundance ranges, although it decreases to 0.10 dex for the HII galaxy sample.

The S_{23}/O_{23} parameter

The combination of the S_{23} and O_{23} parameters gives S_{23}/O_{23}, defined by Díaz and Pérez-Montero (2000), which increases monotonically with the oxygen abundance up to oversolar regime. The relation is:

$$12 + log(O/H) = 9.09 + 1.03\, log\left(\frac{S_{23}}{O_{23}}\right) - 0.23\left[log\left(\frac{S_{23}}{O_{23}}\right)\right]^2$$

with a dispersion of 0.27 dex.

The S_3O_3 parameter

The S_3O_3 parameter was defined by Stasińska (2006) as:

$$S_3O_3 \equiv \frac{[S\,\textsc{iii}]\,\lambda 9069}{[O\,\textsc{iii}]\,\lambda 5007}$$

seeking a metallicity index with several properties, as to be single valued, have a behaviour dominated by a well understood "physical" reason, be unaffected by the presence of diffuse ionized gas and be independent of chemical evolution. Its calibration is

$$12 + log(O/H) = 8.70 + 0.28x + 0.03x^2 + 0.1x^3$$

where x = log S_3O_3. The standard deviation is 0.25 dex.

The Ar_3O_3 parameter

Stasińska (2006) also defined and calibrated the Ar_3OO_3 parameter, seeking for the same good properties as the ones enumerated for the S_3OO_3. The index is:

$$Ar_3O_3 \equiv \frac{[Ar\,\textsc{iii}]\,\lambda 9069}{[O\,\textsc{iii}]\,\lambda 5007}$$

while is calibration is:

$$12 + log(O/H) = 8.91 + 0.34x + 0.27x^2 + 0.20x^3$$

where x = log Ar_3O_3. Its standard deviation is 0.23 dex.

The N_2O_2 parameter

The N_2O_2 parameter was defined by Pérez-Montero and Díaz (2005) as:

$$N_2O_2 \equiv \frac{[N\textsc{ii}]\lambda6548 + [N\textsc{ii}]\lambda6584}{[O\textsc{ii}]\lambda3727 + [O\textsc{ii}]\lambda3729}$$

A tight relation exists between N_2O_2 and $\log(N^+/O^+)$, and hence, it can be used as an indicator of log(N/O). Its calibration is

$$log\left(\frac{N}{O}\right) = 1.144\ log\left(\frac{[N\textsc{ii}]}{[O\textsc{ii}]}\right) - 0.232$$

The uncertainty involved in the determination of the N/O ratio is 0.14 dex, bur decreases to only 0.08 for HII galaxies.

Díaz et al. (2007) recalibrated this relation including high metallicity regions and circumnuclear star-forming regions. The data yields the expression:

$$log\left(\frac{N}{O}\right) = (0.65 \pm 0.02)\ log\left(\frac{[N\textsc{ii}]}{[O\textsc{ii}]}\right) - (0.79 \pm 0.01)$$

which is shallower than that found by Pérez-Montero and Díaz (2005).

Appendix D

Stellar photometry results of NGC 5471

This Appendix includes the stellar photometry results of the NGC 5471 CMD.

ID	X pixel	Y pixel	R.A. (J2000)	Decl. (J2000)	m_{F547M} (mag)	$m_{F675W'}$ (mag)	m_{F547M} - $m_{F675W'}$ (mag)
1	359.56	562.57	14:04:27.50	54:23:41.53	24.24 ± 0.07	23.45 ± 0.05	0.79 ± 0.09
2	324.75	512.37	14:04:27.56	54:23:47.59	24.57 ± 0.10	23.93 ± 0.07	0.65 ± 0.12
3	352.44	544.56	14:04:27.57	54:23:43.36	24.05 ± 0.07	23.95 ± 0.06	0.09 ± 0.09
4	332.62	514.12	14:04:27.61	54:23:46.96	24.59 ± 0.09	24.88 ± 0.19	-0.30 ± 0.21
5	378.56	569.56	14:04:27.62	54:23:39.79	24.04 ± 0.06	23.62 ± 0.06	0.42 ± 0.08
6	323.33	496.44	14:04:27.66	54:23:48.91	24.07 ± 0.06	24.13 ± 0.12	-0.06 ± 0.14
7	373.56	553.15	14:04:27.69	54:23:41.37	24.18 ± 0.07	23.24 ± 0.05	0.94 ± 0.09
8	293.29	455.69	14:04:27.69	54:23:53.94	23.62 ± 0.05	22.57 ± 0.03	1.05 ± 0.06
9	351.67	523.45	14:04:27.71	54:23:45.04	23.85 ± 0.07	23.87 ± 0.11	-0.02 ± 0.13
10	290.75	449.59	14:04:27.71	54:23:54.57	23.86 ± 0.06	23.02 ± 0.04	0.84 ± 0.07
11	368.80	540.45	14:04:27.74	54:23:42.65	23.14 ± 0.03	23.24 ± 0.04	-0.10 ± 0.05
12	346.68	513.49	14:04:27.74	54:23:46.12	25.26 ± 0.15	24.89 ± 0.17	0.38 ± 0.23
13	381.63	555.86	14:04:27.75	54:23:40.66	24.08 ± 0.07	24.18 ± 0.11	-0.10 ± 0.13
14	360.90	530.61	14:04:27.75	54:23:43.91	23.96 ± 0.06	24.09 ± 0.09	-0.14 ± 0.10
15	318.82	469.76	14:04:27.81	54:23:51.25	25.22 ± 0.15	25.04 ± 0.20	0.18 ± 0.26
16	312.47	461.48	14:04:27.81	54:23:52.29	23.20 ± 0.04	23.22 ± 0.04	-0.02 ± 0.05
17	291.51	435.95	14:04:27.81	54:23:55.57	25.38 ± 0.21	25.23 ± 0.19	0.16 ± 0.28
18	359.87	517.56	14:04:27.83	54:23:44.98	24.20 ± 0.09	24.26 ± 0.10	-0.06 ± 0.13

continued on next page

· · · *continued from previous page*

ID	X pixel	Y pixel	R.A. (J2000)	Decl. (J2000)	m_{F547M} (mag)	$m_{F675W'}$ (mag)	m_{F547M} - $m_{F675W'}$ (mag)
19	354.84	509.85	14:04:27.84	54:23:45.89	24.02 ± 0.06	23.67 ± 0.05	0.34 ± 0.08
20	319.56	460.53	14:04:27.88	54:23:51.91	24.45 ± 0.08	24.87 ± 0.20	-0.42 ± 0.22
21	350.12	497.33	14:04:27.89	54:23:47.15	24.98 ± 0.20	24.76 ± 0.26	0.21 ± 0.33
22	406.64	562.32	14:04:27.92	54:23:38.59	25.39 ± 0.18	24.70 ± 0.12	0.69 ± 0.21
23	348.95	491.48	14:04:27.92	54:23:47.68	23.79 ± 0.07	23.54 ± 0.09	0.25 ± 0.12
24	345.50	486.03	14:04:27.93	54:23:48.31	23.10 ± 0.03	23.16 ± 0.06	-0.06 ± 0.07
25	353.28	491.53	14:04:27.96	54:23:47.40	24.58 ± 0.14	24.32 ± 0.15	0.27 ± 0.20
26	313.06	441.38	14:04:27.96	54:23:53.80	25.35 ± 0.18	25.15 ± 0.19	0.20 ± 0.26
27	394.59	541.04	14:04:27.97	54:23:40.98	24.42 ± 0.08	23.80 ± 0.10	0.62 ± 0.13
28	384.61	527.41	14:04:27.98	54:23:42.66	23.93 ± 0.06	23.82 ± 0.08	0.12 ± 0.10
29	352.15	487.10	14:04:27.98	54:23:47.81	23.63 ± 0.09	23.71 ± 0.12	-0.08 ± 0.15
30	360.69	495.71	14:04:27.99	54:23:46.61	22.05 ± 0.02	21.10 ± 0.02	0.95 ± 0.03
31	332.89	462.33	14:04:27.99	54:23:50.94	24.54 ± 0.09	24.79 ± 0.20	-0.24 ± 0.22
32	356.43	488.54	14:04:28.01	54:23:47.43	24.08 ± 0.09	24.32 ± 0.15	-0.24 ± 0.17
33	323.37	447.58	14:04:28.01	54:23:52.67	21.89 ± 0.02	21.64 ± 0.03	0.25 ± 0.03
34	392.42	528.60	14:04:28.04	54:23:42.08	24.69 ± 0.11	24.69 ± 0.13	0.00 ± 0.17
35	387.58	521.82	14:04:28.04	54:23:42.91	23.82 ± 0.06	23.70 ± 0.06	0.11 ± 0.08
36	360.29	487.82	14:04:28.05	54:23:47.25	24.22 ± 0.08	24.72 ± 0.15	-0.50 ± 0.17
37	337.13	458.39	14:04:28.05	54:23:50.97	24.20 ± 0.10	24.14 ± 0.15	0.06 ± 0.18
38	373.24	501.98	14:04:28.06	54:23:45.34	25.22 ± 0.18	24.80 ± 0.17	0.43 ± 0.24
39	355.34	479.74	14:04:28.06	54:23:48.18	23.75 ± 0.09	22.98 ± 0.06	0.78 ± 0.11
40	333.41	453.68	14:04:28.06	54:23:51.57	24.80 ± 0.14	24.72 ± 0.15	0.08 ± 0.20
41	359.38	483.76	14:04:28.07	54:23:47.62	24.04 ± 0.07	24.51 ± 0.16	-0.46 ± 0.17
42	352.51	475.53	14:04:28.07	54:23:48.68	21.55 ± 0.01	21.49 ± 0.01	0.06 ± 0.02
43	391.56	521.51	14:04:28.08	54:23:42.68	25.31 ± 0.17	25.10 ± 0.16	0.21 ± 0.23
44	349.19	469.10	14:04:28.08	54:23:49.39	25.31 ± 0.19	25.12 ± 0.20	0.18 ± 0.28
45	326.28	438.42	14:04:28.10	54:23:53.20	24.42 ± 0.08	24.31 ± 0.11	0.10 ± 0.14
46	303.72	410.72	14:04:28.10	54:23:56.75	23.36 ± 0.04	23.37 ± 0.04	-0.01 ± 0.06
47	349.14	464.75	14:04:28.11	54:23:49.73	25.40 ± 0.20	24.75 ± 0.20	0.64 ± 0.29
48	317.59	426.28	14:04:28.11	54:23:54.68	24.80 ± 0.15	24.86 ± 0.12	-0.07 ± 0.20
49	385.37	507.92	14:04:28.12	54:23:44.12	24.32 ± 0.08	23.69 ± 0.06	0.64 ± 0.10
50	376.97	497.79	14:04:28.12	54:23:45.43	23.96 ± 0.07	23.84 ± 0.06	0.12 ± 0.10
51	353.80	469.82	14:04:28.12	54:23:49.04	25.15 ± 0.18	24.84 ± 0.20	0.31 ± 0.27
52	319.41	425.47	14:04:28.13	54:23:54.63	24.69 ± 0.12	24.74 ± 0.17	-0.05 ± 0.21
53	365.35	481.36	14:04:28.14	54:23:47.43	25.17 ± 0.20	24.87 ± 0.18	0.30 ± 0.27
54	374.91	491.83	14:04:28.15	54:23:46.02	24.14 ± 0.07	24.37 ± 0.11	-0.23 ± 0.13
55	331.62	439.00	14:04:28.15	54:23:52.82	23.89 ± 0.17	23.75 ± 0.12	0.14 ± 0.21
56	361.59	474.44	14:04:28.16	54:23:48.20	22.67 ± 0.03	21.86 ± 0.02	0.81 ± 0.03
57	297.32	395.33	14:04:28.16	54:23:58.34	25.03 ± 0.15	24.73 ± 0.14	0.30 ± 0.20
58	413.53	536.77	14:04:28.17	54:23:40.12	25.23 ± 0.15	25.15 ± 0.17	0.08 ± 0.23
59	380.64	495.43	14:04:28.17	54:23:45.38	22.93 ± 0.06	22.09 ± 0.04	0.84 ± 0.07
60	373.70	487.06	14:04:28.17	54:23:46.46	24.65 ± 0.10	24.86 ± 0.21	-0.21 ± 0.23
61	345.98	453.89	14:04:28.17	54:23:50.76	23.84 ± 0.06	23.89 ± 0.09	-0.05 ± 0.11
62	341.90	448.61	14:04:28.17	54:23:51.43	25.20 ± 0.15	25.19 ± 0.21	0.01 ± 0.26

continued on next page

· · · *continued from previous page*

ID	X pixel	Y pixel	R.A. (J2000)	Decl. (J2000)	m_{F547M} (mag)	$m_{F675W'}$ (mag)	m_{F547M} - $m_{F675W'}$ (mag)
63	386.74	501.52	14:04:28.18	54:23:44.53	24.59 ± 0.14	24.49 ± 0.13	0.10 ± 0.19
64	338.27	442.38	14:04:28.18	54:23:52.14	24.30 ± 0.07	24.01 ± 0.09	0.29 ± 0.12
65	400.79	517.32	14:04:28.19	54:23:42.42	25.29 ± 0.21	24.58 ± 0.21	0.71 ± 0.30
66	359.90	467.43	14:04:28.19	54:23:48.84	24.58 ± 0.09	24.65 ± 0.15	-0.07 ± 0.18
67	384.41	495.92	14:04:28.20	54:23:45.11	22.16 ± 0.05	21.61 ± 0.04	0.56 ± 0.06
68	307.70	401.39	14:04:28.20	54:23:57.22	23.99 ± 0.06	24.22 ± 0.09	-0.23 ± 0.11
69	369.78	476.41	14:04:28.21	54:23:47.53	24.74 ± 0.14	24.31 ± 0.20	0.42 ± 0.24
70	303.51	395.28	14:04:28.21	54:23:57.95	24.96 ± 0.12	24.89 ± 0.16	0.07 ± 0.20
71	435.05	555.17	14:04:28.22	54:23:37.35	24.54 ± 0.11	24.40 ± 0.12	0.14 ± 0.16
72	365.12	469.93	14:04:28.22	54:23:48.32	24.87 ± 0.12	24.86 ± 0.13	0.02 ± 0.18
73	331.89	428.66	14:04:28.22	54:23:53.60	25.21 ± 0.17	24.81 ± 0.16	0.40 ± 0.23
74	424.33	540.80	14:04:28.23	54:23:39.13	25.13 ± 0.17	24.90 ± 0.16	0.23 ± 0.24
75	389.95	499.31	14:04:28.23	54:23:44.50	24.76 ± 0.13	24.39 ± 0.11	0.37 ± 0.17
76	351.09	450.86	14:04:28.23	54:23:50.68	24.43 ± 0.11	24.39 ± 0.12	0.04 ± 0.16
77	336.48	433.27	14:04:28.23	54:23:52.95	24.64 ± 0.10	23.60 ± 0.08	1.04 ± 0.13
78	402.29	512.46	14:04:28.24	54:23:42.70	24.08 ± 0.07	23.35 ± 0.05	0.73 ± 0.09
79	400.45	510.01	14:04:28.24	54:23:43.01	24.14 ± 0.08	23.39 ± 0.05	0.74 ± 0.09
80	356.20	456.53	14:04:28.24	54:23:49.92	23.95 ± 0.07	23.17 ± 0.07	0.78 ± 0.10
81	335.15	430.16	14:04:28.24	54:23:53.27	25.00 ± 0.13	24.53 ± 0.11	0.47 ± 0.17
82	316.50	407.74	14:04:28.24	54:23:56.18	24.45 ± 0.09	24.35 ± 0.10	0.10 ± 0.14
83	417.30	529.17	14:04:28.25	54:23:40.47	24.86 ± 0.15	24.80 ± 0.18	0.06 ± 0.23
84	393.07	500.03	14:04:28.25	54:23:44.24	23.96 ± 0.09	22.92 ± 0.05	1.04 ± 0.10
85	385.32	489.95	14:04:28.25	54:23:45.51	23.35 ± 0.14	22.89 ± 0.08	0.46 ± 0.16
86	452.19	571.24	14:04:28.26	54:23:35.03	24.94 ± 0.19	25.06 ± 0.14	-0.12 ± 0.24
87	356.65	453.44	14:04:28.26	54:23:50.13	24.09 ± 0.07	23.96 ± 0.13	0.13 ± 0.15
88	304.60	388.35	14:04:28.27	54:23:58.42	25.14 ± 0.14	24.93 ± 0.15	0.20 ± 0.20
89	424.25	533.45	14:04:28.28	54:23:39.70	24.32 ± 0.10	23.49 ± 0.05	0.83 ± 0.11
90	440.37	552.12	14:04:28.29	54:23:37.25	23.78 ± 0.07	23.75 ± 0.07	0.03 ± 0.09
91	389.07	489.74	14:04:28.29	54:23:45.29	23.06 ± 0.11	22.22 ± 0.08	0.83 ± 0.14
92	383.81	483.52	14:04:28.29	54:23:46.10	24.04 ± 0.10	24.33 ± 0.16	-0.29 ± 0.19
93	351.50	443.56	14:04:28.29	54:23:51.21	24.96 ± 0.14	24.74 ± 0.22	0.22 ± 0.26
94	399.99	501.86	14:04:28.30	54:23:43.67	23.65 ± 0.14	22.97 ± 0.12	0.68 ± 0.19
95	376.94	473.42	14:04:28.30	54:23:47.31	24.21 ± 0.07	24.45 ± 0.14	-0.24 ± 0.16
96	319.98	403.26	14:04:28.30	54:23:56.30	24.48 ± 0.09	24.55 ± 0.15	-0.07 ± 0.17
97	381.26	476.89	14:04:28.31	54:23:46.77	24.65 ± 0.15	25.05 ± 0.21	-0.40 ± 0.26
98	371.66	463.84	14:04:28.32	54:23:48.38	24.07 ± 0.08	24.44 ± 0.21	-0.37 ± 0.23
99	358.74	447.90	14:04:28.32	54:23:50.42	24.62 ± 0.12	24.32 ± 0.21	0.29 ± 0.24
100	356.78	444.56	14:04:28.33	54:23:50.80	25.32 ± 0.19	24.60 ± 0.12	0.72 ± 0.22
101	354.54	441.54	14:04:28.33	54:23:51.18	24.16 ± 0.14	23.87 ± 0.17	0.29 ± 0.22
102	389.69	483.64	14:04:28.34	54:23:45.72	22.52 ± 0.11	22.51 ± 0.06	0.01 ± 0.12
103	340.33	423.29	14:04:28.34	54:23:53.48	23.51 ± 0.04	22.99 ± 0.05	0.52 ± 0.07
104	402.19	497.79	14:04:28.35	54:23:43.84	23.16 ± 0.09	22.95 ± 0.10	0.21 ± 0.13
105	393.46	486.03	14:04:28.35	54:23:45.30	23.50 ± 0.13	22.70 ± 0.10	0.80 ± 0.17
106	365.76	452.22	14:04:28.35	54:23:49.65	23.44 ± 0.04	23.25 ± 0.07	0.19 ± 0.08

continued on next page

· · · *continued from previous page*

ID	X pixel	Y pixel	R.A. (J2000)	Decl. (J2000)	m_{F547M} (mag)	$m_{F675W'}$ (mag)	m_{F547M} - $m_{F675W'}$ (mag)
107	350.32	434.07	14:04:28.35	54:23:52.02	23.74 ± 0.08	22.80 ± 0.05	0.93 ± 0.09
108	410.35	505.25	14:04:28.36	54:23:42.75	23.66 ± 0.08	23.74 ± 0.11	-0.07 ± 0.13
109	378.62	466.94	14:04:28.36	54:23:47.70	23.95 ± 0.07	23.75 ± 0.14	0.20 ± 0.15
110	375.55	463.08	14:04:28.36	54:23:48.20	23.89 ± 0.06	24.32 ± 0.15	-0.42 ± 0.16
111	368.74	455.06	14:04:28.36	54:23:49.24	23.66 ± 0.05	23.79 ± 0.06	-0.12 ± 0.08
112	329.38	406.93	14:04:28.36	54:23:55.43	23.94 ± 0.07	24.07 ± 0.11	-0.13 ± 0.12
113	320.36	394.26	14:04:28.37	54:23:56.97	22.55 ± 0.02	22.56 ± 0.03	-0.01 ± 0.04
114	398.81	489.42	14:04:28.38	54:23:44.70	23.85 ± 0.08	23.10 ± 0.06	0.75 ± 0.10
115	361.43	442.34	14:04:28.38	54:23:50.68	23.79 ± 0.06	23.10 ± 0.10	0.69 ± 0.12
116	355.58	435.33	14:04:28.38	54:23:51.59	23.90 ± 0.08	23.45 ± 0.14	0.45 ± 0.16
117	443.46	542.56	14:04:28.39	54:23:37.79	24.77 ± 0.13	24.78 ± 0.17	-0.01 ± 0.21
118	403.66	493.83	14:04:28.39	54:23:44.06	23.71 ± 0.06	23.45 ± 0.12	0.27 ± 0.13
119	402.60	491.84	14:04:28.39	54:23:44.28	23.42 ± 0.04	23.23 ± 0.06	0.19 ± 0.07
120	369.49	451.45	14:04:28.39	54:23:49.47	24.24 ± 0.08	24.77 ± 0.15	-0.53 ± 0.17
121	338.23	413.09	14:04:28.39	54:23:54.40	23.17 ± 0.04	22.14 ± 0.02	1.03 ± 0.05
122	354.47	432.15	14:04:28.40	54:23:51.91	22.23 ± 0.04	21.15 ± 0.03	1.08 ± 0.05
123	344.61	420.20	14:04:28.40	54:23:53.45	24.84 ± 0.13	24.47 ± 0.23	0.36 ± 0.27
124	431.38	523.98	14:04:28.42	54:23:39.99	24.15 ± 0.08	24.41 ± 0.11	-0.26 ± 0.13
125	417.34	505.83	14:04:28.42	54:23:42.27	22.81 ± 0.05	22.78 ± 0.05	0.03 ± 0.07
126	409.21	496.82	14:04:28.42	54:23:43.48	21.22 ± 0.02	21.09 ± 0.03	0.12 ± 0.04
127	387.49	469.14	14:04:28.42	54:23:46.98	22.68 ± 0.04	22.48 ± 0.03	0.20 ± 0.05
128	444.22	537.15	14:04:28.43	54:23:38.16	24.55 ± 0.09	23.55 ± 0.08	0.99 ± 0.12
129	430.16	520.32	14:04:28.43	54:23:40.35	24.52 ± 0.09	24.60 ± 0.17	-0.08 ± 0.20
130	389.95	470.55	14:04:28.43	54:23:46.71	23.13 ± 0.06	22.78 ± 0.06	0.35 ± 0.09
131	385.00	465.61	14:04:28.43	54:23:47.41	24.66 ± 0.18	24.49 ± 0.14	0.17 ± 0.23
132	382.50	461.29	14:04:28.43	54:23:47.90	23.86 ± 0.09	23.77 ± 0.17	0.09 ± 0.19
133	351.10	423.96	14:04:28.43	54:23:52.75	25.22 ± 0.20	25.03 ± 0.20	0.19 ± 0.28
134	323.94	390.68	14:04:28.43	54:23:57.02	24.27 ± 0.09	24.27 ± 0.12	-0.01 ± 0.15
135	404.45	488.06	14:04:28.44	54:23:44.45	22.51 ± 0.03	22.33 ± 0.03	0.19 ± 0.04
136	380.90	459.14	14:04:28.44	54:23:48.16	23.64 ± 0.12	23.71 ± 0.17	-0.07 ± 0.21
137	338.46	406.09	14:04:28.44	54:23:54.92	24.03 ± 0.07	23.95 ± 0.09	0.08 ± 0.11
138	422.86	508.43	14:04:28.45	54:23:41.72	24.43 ± 0.14	24.56 ± 0.20	-0.13 ± 0.24
139	415.48	499.31	14:04:28.45	54:23:42.89	23.82 ± 0.06	22.93 ± 0.04	0.90 ± 0.07
140	400.69	481.70	14:04:28.45	54:23:45.18	23.82 ± 0.08	23.83 ± 0.07	-0.01 ± 0.10
141	371.48	445.74	14:04:28.45	54:23:49.79	24.11 ± 0.16	23.74 ± 0.28	0.37 ± 0.32
142	377.49	451.05	14:04:28.46	54:23:49.00	23.71 ± 0.13	23.58 ± 0.10	0.13 ± 0.16
143	405.06	482.12	14:04:28.48	54:23:44.87	24.65 ± 0.17	24.71 ± 0.17	-0.06 ± 0.24
144	368.75	437.65	14:04:28.48	54:23:50.58	23.13 ± 0.16	22.07 ± 0.08	1.06 ± 0.18
145	350.42	415.82	14:04:28.48	54:23:53.42	23.72 ± 0.16	22.95 ± 0.14	0.78 ± 0.21
146	343.72	408.04	14:04:28.48	54:23:54.44	23.48 ± 0.05	23.62 ± 0.09	-0.14 ± 0.10
147	449.14	535.41	14:04:28.49	54:23:37.99	22.59 ± 0.03	22.65 ± 0.03	-0.05 ± 0.04
148	386.26	458.71	14:04:28.49	54:23:47.86	23.80 ± 0.18	23.94 ± 0.36	-0.15 ± 0.40
149	399.37	472.98	14:04:28.50	54:23:45.93	23.59 ± 0.09	23.90 ± 0.15	-0.31 ± 0.17
150	374.87	442.30	14:04:28.50	54:23:49.84	22.36 ± 0.06	22.29 ± 0.07	0.07 ± 0.09

continued on next page

· · · *continued from previous page*

ID	X pixel	Y pixel	R.A. (J2000)	Decl. (J2000)	m_{F547M} (mag)	$m_{F675W'}$ (mag)	m_{F547M} - $m_{F675W'}$ (mag)
151	324.50	381.03	14:04:28.50	54:23:57.73	23.03 ± 0.08	22.24 ± 0.04	0.79 ± 0.09
152	414.39	490.19	14:04:28.51	54:23:43.66	24.60 ± 0.10	24.30 ± 0.20	0.30 ± 0.22
153	381.76	449.25	14:04:28.51	54:23:48.87	23.94 ± 0.27	23.47 ± 0.30	0.48 ± 0.40
154	363.72	427.52	14:04:28.51	54:23:51.68	22.32 ± 0.23	21.17 ± 0.12	1.16 ± 0.26
155	346.59	406.62	14:04:28.51	54:23:54.37	23.86 ± 0.08	23.01 ± 0.10	0.85 ± 0.13
156	380.50	446.98	14:04:28.52	54:23:49.13	24.16 ± 0.25	23.25 ± 0.15	0.91 ± 0.29
157	448.67	529.49	14:04:28.53	54:23:38.47	25.24 ± 0.16	24.90 ± 0.18	0.34 ± 0.24
158	389.65	457.06	14:04:28.53	54:23:47.77	23.64 ± 0.14	23.80 ± 0.14	-0.16 ± 0.20
159	367.79	429.85	14:04:28.53	54:23:51.25	22.56 ± 0.23	22.41 ± 0.25	0.15 ± 0.34
160	433.66	509.96	14:04:28.54	54:23:40.92	23.33 ± 0.04	23.20 ± 0.06	0.14 ± 0.07
161	385.70	450.93	14:04:28.54	54:23:48.49	23.34 ± 0.09	23.43 ± 0.21	-0.09 ± 0.23
162	331.19	383.93	14:04:28.54	54:23:57.09	24.84 ± 0.11	24.59 ± 0.14	0.26 ± 0.18
163	407.69	476.10	14:04:28.55	54:23:45.17	23.29 ± 0.05	23.16 ± 0.11	0.13 ± 0.12
164	394.25	460.16	14:04:28.55	54:23:47.24	23.91 ± 0.09	24.16 ± 0.17	-0.26 ± 0.19
165	467.38	548.42	14:04:28.56	54:23:35.84	25.18 ± 0.19	24.81 ± 0.18	0.37 ± 0.26
166	423.35	493.64	14:04:28.56	54:23:42.83	24.06 ± 0.10	24.05 ± 0.10	0.01 ± 0.14
167	385.91	447.66	14:04:28.56	54:23:48.73	24.39 ± 0.11	24.22 ± 0.12	0.17 ± 0.16
168	379.87	440.71	14:04:28.56	54:23:49.65	23.04 ± 0.12	21.96 ± 0.08	1.08 ± 0.14
169	374.11	433.63	14:04:28.56	54:23:50.56	23.93 ± 0.10	23.02 ± 0.04	0.92 ± 0.11
170	368.78	427.46	14:04:28.56	54:23:51.37	22.48 ± 0.04	22.34 ± 0.03	0.14 ± 0.05
171	439.61	512.11	14:04:28.57	54:23:40.38	24.79 ± 0.14	23.99 ± 0.10	0.80 ± 0.17
172	426.53	496.62	14:04:28.57	54:23:42.40	23.48 ± 0.05	22.59 ± 0.03	0.89 ± 0.05
173	412.97	479.29	14:04:28.57	54:23:44.59	24.91 ± 0.16	24.79 ± 0.16	0.13 ± 0.22
174	365.35	421.55	14:04:28.57	54:23:52.04	23.45 ± 0.06	22.72 ± 0.04	0.72 ± 0.07
175	429.17	498.74	14:04:28.58	54:23:42.07	24.19 ± 0.08	24.30 ± 0.09	-0.10 ± 0.12
176	421.71	489.08	14:04:28.58	54:23:43.29	24.43 ± 0.14	24.75 ± 0.15	-0.32 ± 0.20
177	379.28	436.50	14:04:28.58	54:23:50.01	23.33 ± 0.06	23.36 ± 0.06	-0.03 ± 0.09
178	407.94	471.02	14:04:28.59	54:23:45.55	23.32 ± 0.07	23.18 ± 0.06	0.14 ± 0.09
179	388.15	446.90	14:04:28.59	54:23:48.65	24.48 ± 0.10	24.65 ± 0.14	-0.16 ± 0.17
180	444.48	513.87	14:04:28.60	54:23:39.94	24.19 ± 0.15	24.97 ± 0.15	-0.78 ± 0.21
181	420.88	486.06	14:04:28.60	54:23:43.57	23.95 ± 0.13	22.99 ± 0.04	0.95 ± 0.13
182	404.14	464.36	14:04:28.60	54:23:46.30	23.63 ± 0.10	23.47 ± 0.08	0.16 ± 0.13
183	400.72	460.38	14:04:28.60	54:23:46.82	24.02 ± 0.15	24.27 ± 0.14	-0.25 ± 0.21
184	394.34	452.50	14:04:28.60	54:23:47.83	24.48 ± 0.12	24.53 ± 0.17	-0.05 ± 0.21
185	438.99	506.93	14:04:28.61	54:23:40.82	25.13 ± 0.15	24.97 ± 0.20	0.16 ± 0.25
186	411.53	472.58	14:04:28.61	54:23:45.20	21.60 ± 0.01	21.35 ± 0.02	0.25 ± 0.02
187	354.22	401.67	14:04:28.61	54:23:54.27	24.48 ± 0.10	23.93 ± 0.08	0.54 ± 0.13
188	344.19	389.25	14:04:28.61	54:23:55.86	24.97 ± 0.12	24.52 ± 0.19	0.45 ± 0.22
189	334.01	377.37	14:04:28.61	54:23:57.42	22.75 ± 0.03	22.78 ± 0.03	-0.03 ± 0.04
190	452.38	521.35	14:04:28.62	54:23:38.87	24.53 ± 0.09	24.34 ± 0.16	0.19 ± 0.18
191	364.06	412.46	14:04:28.62	54:23:52.82	23.14 ± 0.05	23.11 ± 0.05	0.03 ± 0.07
192	329.71	371.04	14:04:28.62	54:23:58.18	23.66 ± 0.10	23.57 ± 0.09	0.09 ± 0.13
193	406.96	463.64	14:04:28.63	54:23:46.18	23.85 ± 0.07	24.04 ± 0.07	-0.19 ± 0.10
194	394.50	449.03	14:04:28.63	54:23:48.09	23.47 ± 0.07	23.54 ± 0.09	-0.07 ± 0.11

continued on next page

· · · *continued from previous page*

ID	X pixel	Y pixel	R.A. (J2000)	Decl. (J2000)	m_{F547M} (mag)	$m_{F675W'}$ (mag)	m_{F547M} - $m_{F675W'}$ (mag)
195	444.08	508.45	14:04:28.64	54:23:40.39	24.45 ± 0.09	24.49 ± 0.13	-0.04 ± 0.16
196	391.62	444.18	14:04:28.64	54:23:48.64	22.50 ± 0.11	22.68 ± 0.20	-0.19 ± 0.23
197	384.49	435.77	14:04:28.64	54:23:49.74	23.46 ± 0.18	22.72 ± 0.19	0.74 ± 0.26
198	368.85	416.52	14:04:28.64	54:23:52.21	19.97 ± 0.12	19.01 ± 0.06	0.96 ± 0.13
199	486.38	559.26	14:04:28.65	54:23:33.81	25.26 ± 0.18	25.16 ± 0.17	0.10 ± 0.25
200	436.81	498.62	14:04:28.65	54:23:41.60	25.26 ± 0.17	24.81 ± 0.13	0.46 ± 0.21
201	428.68	487.95	14:04:28.65	54:23:42.94	25.10 ± 0.17	24.68 ± 0.12	0.41 ± 0.20
202	409.89	464.84	14:04:28.65	54:23:45.90	24.00 ± 0.08	24.04 ± 0.11	-0.04 ± 0.14
203	405.17	458.61	14:04:28.65	54:23:46.68	24.58 ± 0.21	24.53 ± 0.17	0.05 ± 0.28
204	402.31	455.06	14:04:28.65	54:23:47.13	23.51 ± 0.14	23.62 ± 0.17	-0.11 ± 0.22
205	374.38	420.99	14:04:28.65	54:23:51.51	21.79 ± 0.15	21.75 ± 0.17	0.04 ± 0.22
206	359.27	403.39	14:04:28.65	54:23:53.82	22.75 ± 0.12	22.56 ± 0.18	0.18 ± 0.22
207	433.11	492.47	14:04:28.66	54:23:42.31	24.23 ± 0.07	23.19 ± 0.04	1.04 ± 0.08
208	383.08	430.02	14:04:28.66	54:23:50.27	23.20 ± 0.13	22.09 ± 0.09	1.10 ± 0.16
209	450.66	512.97	14:04:28.67	54:23:39.62	23.94 ± 0.13	23.02 ± 0.11	0.92 ± 0.17
210	426.47	483.08	14:04:28.67	54:23:43.45	24.70 ± 0.16	24.55 ± 0.24	0.15 ± 0.29
211	416.10	469.41	14:04:28.67	54:23:45.16	23.35 ± 0.12	22.33 ± 0.05	1.02 ± 0.13
212	358.85	400.05	14:04:28.67	54:23:54.11	23.40 ± 0.05	23.56 ± 0.07	-0.16 ± 0.09
213	351.69	390.56	14:04:28.67	54:23:55.29	22.70 ± 0.12	22.47 ± 0.09	0.23 ± 0.15
214	363.84	404.50	14:04:28.68	54:23:53.45	24.31 ± 0.11	24.18 ± 0.11	0.14 ± 0.16
215	331.63	364.49	14:04:28.68	54:23:58.56	23.12 ± 0.03	23.21 ± 0.04	-0.08 ± 0.05
216	376.00	418.43	14:04:28.69	54:23:51.61	22.90 ± 0.04	23.08 ± 0.05	-0.18 ± 0.06
217	358.55	397.04	14:04:28.69	54:23:54.36	22.81 ± 0.12	22.71 ± 0.15	0.09 ± 0.19
218	353.40	389.38	14:04:28.69	54:23:55.27	21.80 ± 0.13	21.14 ± 0.07	0.66 ± 0.15
219	379.16	419.90	14:04:28.70	54:23:51.30	21.85 ± 0.12	21.92 ± 0.16	-0.06 ± 0.20
220	375.29	416.04	14:04:28.70	54:23:51.84	22.95 ± 0.04	23.23 ± 0.07	-0.28 ± 0.09
221	415.18	462.50	14:04:28.71	54:23:45.75	24.49 ± 0.12	24.42 ± 0.12	0.07 ± 0.17
222	401.63	446.40	14:04:28.71	54:23:47.84	23.06 ± 0.10	23.20 ± 0.14	-0.13 ± 0.17
223	451.33	506.56	14:04:28.72	54:23:40.08	23.60 ± 0.05	22.64 ± 0.03	0.96 ± 0.05
224	427.41	477.50	14:04:28.72	54:23:43.82	22.62 ± 0.07	22.48 ± 0.06	0.14 ± 0.10
225	392.75	433.81	14:04:28.72	54:23:49.37	23.52 ± 0.13	23.03 ± 0.08	0.49 ± 0.15
226	390.88	431.55	14:04:28.72	54:23:49.66	22.98 ± 0.23	23.10 ± 0.32	-0.12 ± 0.39
227	466.75	523.71	14:04:28.73	54:23:37.78	24.67 ± 0.10	23.86 ± 0.12	0.81 ± 0.15
228	419.62	466.44	14:04:28.73	54:23:45.16	24.17 ± 0.07	24.50 ± 0.10	-0.33 ± 0.12
229	384.91	422.75	14:04:28.73	54:23:50.72	23.06 ± 0.15	22.87 ± 0.22	0.19 ± 0.27
230	376.35	412.55	14:04:28.73	54:23:52.04	23.09 ± 0.05	22.94 ± 0.05	0.16 ± 0.07
231	436.88	485.16	14:04:28.74	54:23:42.64	24.43 ± 0.11	24.64 ± 0.18	-0.21 ± 0.21
232	411.16	452.85	14:04:28.75	54:23:46.74	21.93 ± 0.04	22.03 ± 0.05	-0.10 ± 0.06
233	398.84	437.61	14:04:28.75	54:23:48.69	22.75 ± 0.09	22.92 ± 0.20	-0.18 ± 0.21
234	379.30	413.11	14:04:28.75	54:23:51.81	22.51 ± 0.05	22.54 ± 0.07	-0.04 ± 0.08
235	374.28	406.91	14:04:28.75	54:23:52.61	21.56 ± 0.06	20.61 ± 0.01	0.95 ± 0.06
236	455.57	505.45	14:04:28.76	54:23:39.89	23.84 ± 0.08	22.59 ± 0.03	1.26 ± 0.09
237	368.91	399.23	14:04:28.76	54:23:53.54	24.07 ± 0.13	23.59 ± 0.13	0.48 ± 0.18
238	365.58	394.85	14:04:28.76	54:23:54.08	24.42 ± 0.11	24.07 ± 0.17	0.35 ± 0.20

continued on next page

· · · *continued from previous page*

ID	X pixel	Y pixel	R.A. (J2000)	Decl. (J2000)	m_{F547M} (mag)	$m_{F675W'}$ (mag)	m_{F547M} - $m_{F675W'}$ (mag)
239	482.22	537.22	14:04:28.77	54:23:35.77	24.84 ± 0.15	24.38 ± 0.13	0.47 ± 0.20
240	417.00	456.88	14:04:28.77	54:23:46.07	24.18 ± 0.16	23.32 ± 0.08	0.85 ± 0.17
241	407.25	445.69	14:04:28.77	54:23:47.54	23.32 ± 0.28	22.34 ± 0.11	0.98 ± 0.30
242	402.81	439.52	14:04:28.77	54:23:48.30	22.93 ± 0.22	21.75 ± 0.06	1.18 ± 0.22
243	392.55	427.71	14:04:28.77	54:23:49.85	22.61 ± 0.27	22.58 ± 0.31	0.03 ± 0.42
244	441.70	486.49	14:04:28.78	54:23:42.23	23.93 ± 0.13	24.09 ± 0.24	-0.16 ± 0.27
245	415.70	454.23	14:04:28.78	54:23:46.35	22.96 ± 0.06	22.13 ± 0.04	0.82 ± 0.07
246	359.63	384.63	14:04:28.78	54:23:55.25	24.44 ± 0.09	23.56 ± 0.11	0.89 ± 0.14
247	479.45	530.33	14:04:28.79	54:23:36.47	25.39 ± 0.18	25.32 ± 0.19	0.08 ± 0.26
248	414.17	450.81	14:04:28.79	54:23:46.71	22.64 ± 0.18	22.77 ± 0.16	-0.14 ± 0.24
249	447.44	490.09	14:04:28.80	54:23:41.59	24.29 ± 0.18	23.84 ± 0.15	0.45 ± 0.23
250	435.85	476.59	14:04:28.80	54:23:43.36	22.60 ± 0.03	22.31 ± 0.04	0.28 ± 0.05
251	432.67	471.56	14:04:28.80	54:23:43.95	22.89 ± 0.04	22.40 ± 0.04	0.49 ± 0.05
252	427.53	466.40	14:04:28.80	54:23:44.67	24.80 ± 0.12	24.79 ± 0.20	0.01 ± 0.23
253	403.19	436.01	14:04:28.80	54:23:48.54	22.55 ± 0.12	22.85 ± 0.15	-0.30 ± 0.20
254	398.76	430.48	14:04:28.80	54:23:49.25	22.83 ± 0.20	22.88 ± 0.29	-0.05 ± 0.35
255	380.68	408.75	14:04:28.80	54:23:52.06	22.37 ± 0.16	21.93 ± 0.07	0.44 ± 0.18
256	411.22	444.41	14:04:28.81	54:23:47.39	22.21 ± 0.26	22.28 ± 0.23	-0.07 ± 0.35
257	390.37	418.28	14:04:28.81	54:23:50.72	22.71 ± 0.11	21.50 ± 0.04	1.21 ± 0.12
258	376.30	402.12	14:04:28.81	54:23:52.85	23.16 ± 0.14	23.34 ± 0.13	-0.18 ± 0.19
259	357.47	378.54	14:04:28.81	54:23:55.85	24.96 ± 0.20	24.38 ± 0.29	0.58 ± 0.35
260	452.60	493.29	14:04:28.82	54:23:41.02	24.39 ± 0.13	24.10 ± 0.13	0.29 ± 0.18
261	446.76	487.02	14:04:28.82	54:23:41.87	23.73 ± 0.12	23.63 ± 0.17	0.10 ± 0.21
262	422.62	456.43	14:04:28.82	54:23:45.75	24.06 ± 0.14	23.23 ± 0.07	0.83 ± 0.16
263	371.74	394.75	14:04:28.82	54:23:53.70	22.58 ± 0.08	22.53 ± 0.05	0.05 ± 0.10
264	328.81	342.17	14:04:28.82	54:24:00.46	25.19 ± 0.21	24.16 ± 0.07	1.03 ± 0.22
265	465.65	508.76	14:04:28.83	54:23:39.01	24.67 ± 0.11	24.62 ± 0.19	0.06 ± 0.23
266	420.90	453.60	14:04:28.83	54:23:46.07	22.82 ± 0.11	22.89 ± 0.09	-0.08 ± 0.14
267	339.61	353.49	14:04:28.83	54:23:58.91	25.31 ± 0.17	25.19 ± 0.20	0.11 ± 0.26
268	400.09	426.74	14:04:28.84	54:23:49.45	23.57 ± 0.06	23.39 ± 0.07	0.17 ± 0.09
269	371.98	391.47	14:04:28.84	54:23:53.94	23.13 ± 0.13	23.24 ± 0.10	-0.11 ± 0.17
270	357.50	374.50	14:04:28.84	54:23:56.16	24.22 ± 0.07	24.12 ± 0.18	0.10 ± 0.19
271	484.96	529.63	14:04:28.85	54:23:36.18	23.63 ± 0.05	23.57 ± 0.06	0.06 ± 0.07
272	446.41	482.66	14:04:28.85	54:23:42.23	23.75 ± 0.10	23.43 ± 0.06	0.32 ± 0.12
273	437.06	470.65	14:04:28.85	54:23:43.74	24.25 ± 0.10	24.33 ± 0.17	-0.08 ± 0.20
274	418.84	448.14	14:04:28.85	54:23:46.62	22.53 ± 0.16	22.46 ± 0.23	0.07 ± 0.28
275	408.52	434.91	14:04:28.85	54:23:48.29	20.96 ± 0.02	21.18 ± 0.02	-0.22 ± 0.03
276	362.77	379.62	14:04:28.85	54:23:55.44	25.04 ± 0.23	24.40 ± 0.29	0.64 ± 0.37
277	382.11	401.25	14:04:28.86	54:23:52.55	23.55 ± 0.14	23.72 ± 0.07	-0.17 ± 0.15
278	332.76	340.89	14:04:28.86	54:24:00.31	24.53 ± 0.11	23.84 ± 0.08	0.69 ± 0.14
279	421.97	448.85	14:04:28.87	54:23:46.37	23.73 ± 0.06	23.38 ± 0.09	0.35 ± 0.11
280	447.76	479.88	14:04:28.88	54:23:42.36	22.25 ± 0.06	22.07 ± 0.05	0.18 ± 0.07
281	441.44	472.22	14:04:28.88	54:23:43.35	22.94 ± 0.04	22.27 ± 0.04	0.67 ± 0.06
282	412.86	436.52	14:04:28.88	54:23:47.90	19.37 ± 0.09	19.16 ± 0.05	0.21 ± 0.10

continued on next page

· · · *continued from previous page*

ID	X pixel	Y pixel	R.A. (J2000)	Decl. (J2000)	m_{F547M} (mag)	$m_{F675W'}$ (mag)	m_{F547M} - $m_{F675W'}$ (mag)
283	393.99	413.31	14:04:28.88	54:23:50.87	23.35 ± 0.12	23.30 ± 0.20	0.05 ± 0.23
284	337.80	345.13	14:04:28.88	54:23:59.67	22.89 ± 0.03	22.36 ± 0.03	0.52 ± 0.04
285	465.98	500.84	14:04:28.89	54:23:39.60	23.61 ± 0.05	23.33 ± 0.06	0.27 ± 0.08
286	459.53	491.98	14:04:28.89	54:23:40.68	22.47 ± 0.04	22.43 ± 0.05	0.03 ± 0.06
287	452.72	484.46	14:04:28.89	54:23:41.69	23.79 ± 0.11	22.92 ± 0.07	0.87 ± 0.13
288	385.19	401.06	14:04:28.89	54:23:52.37	23.44 ± 0.16	22.56 ± 0.06	0.88 ± 0.17
289	381.39	396.90	14:04:28.89	54:23:52.93	24.98 ± 0.15	24.99 ± 0.19	-0.01 ± 0.24
290	445.88	474.56	14:04:28.90	54:23:42.89	22.43 ± 0.04	22.51 ± 0.06	-0.08 ± 0.07
291	419.51	442.06	14:04:28.90	54:23:47.05	22.01 ± 0.09	21.95 ± 0.22	0.06 ± 0.24
292	410.64	431.31	14:04:28.90	54:23:48.44	18.92 ± 0.06	18.98 ± 0.07	-0.06 ± 0.09
293	404.39	423.47	14:04:28.90	54:23:49.44	21.91 ± 0.17	21.87 ± 0.28	0.04 ± 0.33
294	484.10	519.45	14:04:28.91	54:23:37.02	24.46 ± 0.09	23.96 ± 0.09	0.50 ± 0.12
295	456.89	487.19	14:04:28.91	54:23:41.22	23.67 ± 0.08	23.91 ± 0.12	-0.23 ± 0.15
296	441.19	467.00	14:04:28.91	54:23:43.76	23.78 ± 0.09	23.71 ± 0.08	0.06 ± 0.12
297	370.75	380.35	14:04:28.91	54:23:54.88	24.13 ± 0.07	24.35 ± 0.18	-0.22 ± 0.20
298	358.64	365.63	14:04:28.91	54:23:56.77	25.07 ± 0.15	24.73 ± 0.21	0.34 ± 0.26
299	400.79	415.95	14:04:28.92	54:23:50.24	21.13 ± 0.04	21.02 ± 0.03	0.10 ± 0.05
300	388.44	401.70	14:04:28.92	54:23:52.12	23.70 ± 0.09	23.82 ± 0.07	-0.13 ± 0.11
301	380.84	391.33	14:04:28.92	54:23:53.40	22.53 ± 0.04	22.76 ± 0.06	-0.24 ± 0.07
302	362.92	370.42	14:04:28.92	54:23:56.14	24.97 ± 0.16	24.55 ± 0.14	0.42 ± 0.21
303	451.52	476.61	14:04:28.93	54:23:42.37	24.52 ± 0.12	23.45 ± 0.07	1.07 ± 0.14
304	437.99	460.31	14:04:28.93	54:23:44.48	23.39 ± 0.07	23.56 ± 0.06	-0.17 ± 0.09
305	429.05	449.85	14:04:28.93	54:23:45.85	24.89 ± 0.16	24.21 ± 0.13	0.68 ± 0.21
306	498.75	533.57	14:04:28.94	54:23:35.01	24.04 ± 0.07	23.25 ± 0.04	0.79 ± 0.08
307	455.23	480.27	14:04:28.94	54:23:41.86	24.75 ± 0.12	23.76 ± 0.07	0.99 ± 0.14
308	436.69	457.46	14:04:28.94	54:23:44.78	23.36 ± 0.10	23.35 ± 0.11	0.01 ± 0.15
309	378.54	385.64	14:04:28.94	54:23:53.98	22.94 ± 0.10	23.20 ± 0.10	-0.26 ± 0.14
310	408.80	421.88	14:04:28.95	54:23:49.28	22.41 ± 0.03	22.22 ± 0.04	0.18 ± 0.05
311	435.81	454.26	14:04:28.96	54:23:45.09	23.93 ± 0.14	24.06 ± 0.14	-0.12 ± 0.20
312	423.01	437.91	14:04:28.96	54:23:47.15	23.64 ± 0.08	23.55 ± 0.11	0.09 ± 0.13
313	375.36	380.17	14:04:28.96	54:23:54.60	25.11 ± 0.15	24.84 ± 0.21	0.27 ± 0.26
314	343.43	339.82	14:04:28.96	54:23:59.72	23.26 ± 0.07	22.33 ± 0.04	0.92 ± 0.08
315	427.76	442.72	14:04:28.97	54:23:46.48	23.22 ± 0.23	22.74 ± 0.25	0.47 ± 0.34
316	400.00	408.54	14:04:28.97	54:23:50.86	24.48 ± 0.10	23.99 ± 0.10	0.49 ± 0.14
317	391.38	397.27	14:04:28.97	54:23:52.28	23.09 ± 0.14	22.86 ± 0.09	0.23 ± 0.16
318	468.69	491.15	14:04:28.98	54:23:40.17	21.69 ± 0.01	21.53 ± 0.01	0.16 ± 0.02
319	415.81	426.36	14:04:28.98	54:23:48.50	22.10 ± 0.22	22.23 ± 0.27	-0.12 ± 0.35
320	365.23	364.37	14:04:28.98	54:23:56.46	23.68 ± 0.06	22.71 ± 0.07	0.97 ± 0.09
321	363.03	361.51	14:04:28.98	54:23:56.82	23.49 ± 0.06	23.45 ± 0.10	0.05 ± 0.11
322	346.97	341.57	14:04:28.98	54:23:59.36	24.61 ± 0.10	24.51 ± 0.12	0.10 ± 0.15
323	486.76	512.21	14:04:28.99	54:23:37.41	24.96 ± 0.19	24.72 ± 0.20	0.25 ± 0.27
324	465.38	486.04	14:04:28.99	54:23:40.77	23.84 ± 0.13	24.24 ± 0.33	-0.39 ± 0.35
325	461.14	481.41	14:04:28.99	54:23:41.40	23.98 ± 0.07	24.16 ± 0.10	-0.18 ± 0.12
326	452.31	470.07	14:04:28.99	54:23:42.83	24.26 ± 0.11	24.61 ± 0.17	-0.36 ± 0.20

continued on next page

· · · *continued from previous page*

ID	X pixel	Y pixel	R.A. (J2000)	Decl. (J2000)	m_{F547M} (mag)	$m_{F675W'}$ (mag)	m_{F547M} - $m_{F675W'}$ (mag)
327	431.16	444.18	14:04:28.99	54:23:46.16	23.23 ± 0.12	22.89 ± 0.15	0.34 ± 0.19
328	419.16	429.23	14:04:28.99	54:23:48.06	22.66 ± 0.16	21.51 ± 0.09	1.15 ± 0.18
329	352.97	347.93	14:04:28.99	54:23:58.50	24.04 ± 0.06	23.17 ± 0.04	0.88 ± 0.07
330	424.72	434.55	14:04:29.00	54:23:47.30	22.76 ± 0.20	22.84 ± 0.31	-0.08 ± 0.37
331	388.40	389.37	14:04:29.00	54:23:53.07	22.36 ± 0.16	22.49 ± 0.12	-0.12 ± 0.20
332	433.63	443.97	14:04:29.01	54:23:46.02	22.93 ± 0.10	22.83 ± 0.19	0.10 ± 0.22
333	411.56	416.94	14:04:29.01	54:23:49.49	21.23 ± 0.05	21.18 ± 0.06	0.05 ± 0.07
334	404.90	409.40	14:04:29.01	54:23:50.49	23.82 ± 0.12	23.86 ± 0.15	-0.04 ± 0.19
335	458.82	474.28	14:04:29.02	54:23:42.09	22.88 ± 0.16	22.85 ± 0.32	0.02 ± 0.35
336	449.89	463.30	14:04:29.02	54:23:43.50	23.76 ± 0.12	23.45 ± 0.15	0.32 ± 0.20
337	385.81	383.64	14:04:29.02	54:23:53.68	21.61 ± 0.11	21.72 ± 0.07	-0.12 ± 0.13
338	369.81	365.02	14:04:29.02	54:23:56.12	24.59 ± 0.10	24.51 ± 0.17	0.08 ± 0.20
339	461.65	475.57	14:04:29.03	54:23:41.82	22.56 ± 0.17	22.66 ± 0.33	-0.10 ± 0.37
340	445.44	455.26	14:04:29.03	54:23:44.40	23.33 ± 0.11	23.08 ± 0.14	0.25 ± 0.18
341	382.36	378.16	14:04:29.03	54:23:54.32	24.44 ± 0.15	24.73 ± 0.17	-0.29 ± 0.23
342	360.25	351.44	14:04:29.03	54:23:57.77	25.24 ± 0.18	24.79 ± 0.20	0.45 ± 0.27
343	408.55	409.47	14:04:29.04	54:23:50.25	22.93 ± 0.10	21.81 ± 0.02	1.12 ± 0.10
344	501.47	521.33	14:04:29.05	54:23:35.78	24.69 ± 0.10	24.05 ± 0.08	0.64 ± 0.13
345	472.84	486.33	14:04:29.05	54:23:40.28	24.49 ± 0.14	24.42 ± 0.15	0.07 ± 0.21
346	460.80	471.44	14:04:29.05	54:23:42.19	23.03 ± 0.07	22.73 ± 0.04	0.30 ± 0.08
347	448.95	457.10	14:04:29.05	54:23:44.04	23.11 ± 0.07	23.34 ± 0.12	-0.23 ± 0.14
348	420.96	422.52	14:04:29.05	54:23:48.47	22.80 ± 0.10	23.08 ± 0.13	-0.28 ± 0.16
349	479.13	492.52	14:04:29.06	54:23:39.41	25.07 ± 0.18	24.85 ± 0.20	0.21 ± 0.27
350	473.93	486.23	14:04:29.06	54:23:40.22	24.70 ± 0.21	24.80 ± 0.20	-0.10 ± 0.29
351	457.70	466.81	14:04:29.06	54:23:42.74	24.18 ± 0.09	23.99 ± 0.09	0.19 ± 0.12
352	394.66	389.40	14:04:29.06	54:23:52.68	23.33 ± 0.17	22.43 ± 0.07	0.90 ± 0.18
353	350.88	335.52	14:04:29.06	54:23:59.58	23.63 ± 0.05	22.73 ± 0.03	0.90 ± 0.05
354	470.96	481.87	14:04:29.07	54:23:40.75	24.20 ± 0.08	24.53 ± 0.14	-0.33 ± 0.16
355	468.91	478.87	14:04:29.07	54:23:41.11	23.95 ± 0.07	23.63 ± 0.07	0.32 ± 0.10
356	407.20	403.30	14:04:29.07	54:23:50.82	23.01 ± 0.19	21.87 ± 0.08	1.14 ± 0.20
357	400.29	394.51	14:04:29.07	54:23:51.93	21.46 ± 0.10	20.60 ± 0.05	0.86 ± 0.11
358	370.29	357.31	14:04:29.07	54:23:56.68	24.20 ± 0.25	23.74 ± 0.20	0.47 ± 0.32
359	483.42	496.15	14:04:29.08	54:23:38.86	24.75 ± 0.11	24.58 ± 0.12	0.17 ± 0.17
360	475.23	483.65	14:04:29.09	54:23:40.34	24.33 ± 0.10	24.25 ± 0.14	0.08 ± 0.17
361	456.75	461.75	14:04:29.09	54:23:43.19	22.70 ± 0.09	22.67 ± 0.18	0.03 ± 0.20
362	446.37	449.26	14:04:29.09	54:23:44.81	22.89 ± 0.21	22.76 ± 0.31	0.13 ± 0.37
363	443.35	444.96	14:04:29.09	54:23:45.33	22.85 ± 0.07	22.94 ± 0.07	-0.09 ± 0.10
364	419.45	415.25	14:04:29.09	54:23:49.12	22.65 ± 0.07	22.15 ± 0.07	0.50 ± 0.10
365	374.22	360.32	14:04:29.09	54:23:56.20	24.26 ± 0.20	23.91 ± 0.20	0.35 ± 0.28
366	466.19	472.20	14:04:29.10	54:23:41.79	20.62 ± 0.09	20.68 ± 0.10	-0.06 ± 0.13
367	461.13	465.82	14:04:29.10	54:23:42.60	23.43 ± 0.07	23.41 ± 0.08	0.03 ± 0.10
368	433.40	430.91	14:04:29.10	54:23:47.04	23.08 ± 0.08	23.34 ± 0.09	-0.26 ± 0.12
369	394.75	384.19	14:04:29.10	54:23:53.07	23.75 ± 0.10	24.05 ± 0.15	-0.30 ± 0.18
370	389.50	377.60	14:04:29.10	54:23:53.91	23.04 ± 0.08	23.10 ± 0.10	-0.06 ± 0.13

continued on next page

· · · *continued from previous page*

ID	X pixel	Y pixel	R.A. (J2000)	Decl. (J2000)	m_{F547M} (mag)	$m_{F675W'}$ (mag)	m_{F547M} - $m_{F675W'}$ (mag)
371	386.60	374.03	14:04:29.10	54:23:54.37	22.85 ± 0.10	22.85 ± 0.11	-0.01 ± 0.15
372	383.48	369.61	14:04:29.10	54:23:54.91	22.84 ± 0.07	22.85 ± 0.10	-0.00 ± 0.12
373	437.84	435.10	14:04:29.11	54:23:46.44	22.02 ± 0.32	21.25 ± 0.19	0.78 ± 0.37
374	422.46	416.89	14:04:29.11	54:23:48.81	23.11 ± 0.09	22.56 ± 0.10	0.55 ± 0.14
375	392.41	380.14	14:04:29.11	54:23:53.53	22.40 ± 0.19	22.27 ± 0.18	0.13 ± 0.26
376	376.99	360.10	14:04:29.11	54:23:56.05	24.23 ± 0.10	24.39 ± 0.10	-0.16 ± 0.15
377	487.12	494.10	14:04:29.12	54:23:38.79	25.01 ± 0.17	25.11 ± 0.18	-0.10 ± 0.25
378	483.92	491.05	14:04:29.12	54:23:39.22	24.79 ± 0.14	24.76 ± 0.17	0.03 ± 0.22
379	451.29	450.67	14:04:29.12	54:23:44.39	23.40 ± 0.10	23.37 ± 0.09	0.03 ± 0.13
380	436.38	432.82	14:04:29.12	54:23:46.70	22.25 ± 0.29	21.26 ± 0.15	0.99 ± 0.33
381	406.62	395.36	14:04:29.12	54:23:51.46	22.74 ± 0.08	21.99 ± 0.19	0.76 ± 0.20
382	366.55	347.12	14:04:29.12	54:23:57.70	23.77 ± 0.05	22.76 ± 0.03	1.01 ± 0.06
383	354.04	330.66	14:04:29.12	54:23:59.76	25.52 ± 0.18	24.89 ± 0.17	0.63 ± 0.25
384	376.04	356.75	14:04:29.13	54:23:56.37	23.41 ± 0.06	23.20 ± 0.07	0.21 ± 0.09
385	345.66	319.28	14:04:29.13	54:24:01.17	23.70 ± 0.05	22.86 ± 0.03	0.84 ± 0.06
386	473.52	475.35	14:04:29.14	54:23:41.09	23.36 ± 0.05	22.95 ± 0.04	0.41 ± 0.07
387	449.49	445.32	14:04:29.14	54:23:44.91	23.58 ± 0.09	23.73 ± 0.11	-0.15 ± 0.14
388	400.98	385.54	14:04:29.14	54:23:52.58	23.34 ± 0.07	23.98 ± 0.14	-0.64 ± 0.15
389	391.65	374.44	14:04:29.14	54:23:54.02	23.41 ± 0.10	23.55 ± 0.13	-0.14 ± 0.17
390	458.86	456.24	14:04:29.15	54:23:43.48	23.46 ± 0.05	23.47 ± 0.06	-0.01 ± 0.08
391	443.12	436.36	14:04:29.15	54:23:46.01	20.63 ± 0.02	20.75 ± 0.01	-0.11 ± 0.03
392	429.93	419.50	14:04:29.15	54:23:48.14	23.55 ± 0.15	23.68 ± 0.18	-0.13 ± 0.24
393	395.79	378.75	14:04:29.15	54:23:53.43	21.79 ± 0.12	21.90 ± 0.08	-0.11 ± 0.14
394	387.33	368.42	14:04:29.15	54:23:54.75	23.49 ± 0.11	23.50 ± 0.14	-0.01 ± 0.18
395	434.33	424.79	14:04:29.16	54:23:47.45	22.93 ± 0.27	22.07 ± 0.07	0.86 ± 0.28
396	391.35	371.40	14:04:29.16	54:23:54.27	22.11 ± 0.07	22.25 ± 0.10	-0.15 ± 0.12
397	371.89	347.70	14:04:29.16	54:23:57.32	24.36 ± 0.11	24.47 ± 0.20	-0.11 ± 0.22
398	485.82	485.38	14:04:29.17	54:23:39.54	23.58 ± 0.05	23.52 ± 0.08	0.07 ± 0.10
399	448.14	439.24	14:04:29.17	54:23:45.47	20.92 ± 0.02	20.47 ± 0.02	0.45 ± 0.03
400	441.47	431.15	14:04:29.17	54:23:46.51	21.68 ± 0.02	22.15 ± 0.03	-0.47 ± 0.03
401	385.64	362.84	14:04:29.17	54:23:55.29	23.60 ± 0.06	23.58 ± 0.09	0.03 ± 0.11
402	377.71	352.84	14:04:29.17	54:23:56.56	23.97 ± 0.18	23.62 ± 0.15	0.35 ± 0.23
403	410.00	392.15	14:04:29.18	54:23:51.50	22.81 ± 0.10	22.73 ± 0.29	0.08 ± 0.31
404	365.66	337.12	14:04:29.18	54:23:58.53	25.42 ± 0.19	24.88 ± 0.20	0.53 ± 0.27
405	484.16	480.72	14:04:29.19	54:23:40.00	23.32 ± 0.06	23.40 ± 0.08	-0.07 ± 0.10
406	462.66	455.06	14:04:29.19	54:23:43.34	21.87 ± 0.05	22.13 ± 0.06	-0.26 ± 0.07
407	456.86	448.05	14:04:29.19	54:23:44.24	22.53 ± 0.10	21.45 ± 0.02	1.08 ± 0.10
408	405.71	385.21	14:04:29.19	54:23:52.30	23.25 ± 0.05	22.26 ± 0.06	0.99 ± 0.07
409	390.28	366.57	14:04:29.19	54:23:54.71	23.97 ± 0.20	24.11 ± 0.41	-0.15 ± 0.46
410	470.95	463.90	14:04:29.20	54:23:42.13	22.58 ± 0.17	21.47 ± 0.08	1.11 ± 0.18
411	442.63	429.09	14:04:29.20	54:23:46.60	21.37 ± 0.13	21.57 ± 0.16	-0.20 ± 0.20
412	421.16	402.31	14:04:29.20	54:23:50.01	24.03 ± 0.07	24.05 ± 0.08	-0.02 ± 0.11
413	480.69	474.09	14:04:29.21	54:23:40.73	24.30 ± 0.17	24.02 ± 0.25	0.28 ± 0.30
414	433.25	416.49	14:04:29.21	54:23:48.16	23.23 ± 0.07	23.07 ± 0.07	0.17 ± 0.10

continued on next page

· · · *continued from previous page*

ID	X pixel	Y pixel	R.A. (J2000)	Decl. (J2000)	m_{F547M} (mag)	$m_{F675W'}$ (mag)	m_{F547M} - $m_{F675W'}$ (mag)
415	401.44	376.48	14:04:29.21	54:23:53.25	22.38 ± 0.17	22.37 ± 0.34	0.01 ± 0.38
416	503.83	501.88	14:04:29.22	54:23:37.13	24.95 ± 0.13	24.54 ± 0.16	0.41 ± 0.21
417	478.88	471.12	14:04:29.22	54:23:41.08	24.52 ± 0.17	23.93 ± 0.16	0.58 ± 0.24
418	398.14	371.31	14:04:29.22	54:23:53.85	24.87 ± 0.14	24.24 ± 0.10	0.63 ± 0.17
419	386.88	355.99	14:04:29.23	54:23:55.74	24.08 ± 0.13	23.82 ± 0.19	0.26 ± 0.23
420	463.90	449.73	14:04:29.24	54:23:43.67	23.04 ± 0.21	22.25 ± 0.15	0.79 ± 0.26
421	430.21	407.64	14:04:29.24	54:23:49.03	22.79 ± 0.07	22.91 ± 0.11	-0.12 ± 0.12
422	421.05	396.09	14:04:29.24	54:23:50.50	24.56 ± 0.21	24.57 ± 0.17	-0.01 ± 0.27
423	478.92	466.86	14:04:29.25	54:23:41.40	25.03 ± 0.16	24.49 ± 0.14	0.54 ± 0.21
424	408.19	380.14	14:04:29.25	54:23:52.54	22.61 ± 0.05	21.88 ± 0.03	0.73 ± 0.06
425	385.81	352.06	14:04:29.25	54:23:56.11	24.50 ± 0.13	24.32 ± 0.16	0.18 ± 0.21
426	473.63	458.51	14:04:29.26	54:23:42.38	24.03 ± 0.07	24.13 ± 0.11	-0.09 ± 0.13
427	459.90	442.25	14:04:29.26	54:23:44.50	22.57 ± 0.05	22.89 ± 0.06	-0.32 ± 0.08
428	371.48	333.10	14:04:29.26	54:23:58.48	24.71 ± 0.12	23.85 ± 0.07	0.86 ± 0.14
429	494.75	482.56	14:04:29.27	54:23:39.20	23.67 ± 0.06	22.69 ± 0.03	0.97 ± 0.06
430	433.91	408.50	14:04:29.27	54:23:48.73	24.04 ± 0.08	24.46 ± 0.17	-0.42 ± 0.18
431	429.96	403.24	14:04:29.27	54:23:49.39	24.85 ± 0.14	24.75 ± 0.17	0.10 ± 0.22
432	417.65	388.10	14:04:29.27	54:23:51.33	19.65 ± 0.01	19.47 ± 0.01	0.18 ± 0.02
433	450.56	427.99	14:04:29.28	54:23:46.18	21.95 ± 0.15	21.88 ± 0.19	0.07 ± 0.24
434	403.46	369.94	14:04:29.28	54:23:53.62	23.94 ± 0.07	24.03 ± 0.10	-0.09 ± 0.12
435	397.08	362.28	14:04:29.28	54:23:54.62	22.45 ± 0.09	22.52 ± 0.16	-0.07 ± 0.18
436	509.61	498.02	14:04:29.29	54:23:37.07	23.93 ± 0.06	24.00 ± 0.09	-0.07 ± 0.11
437	487.20	470.81	14:04:29.29	54:23:40.58	24.39 ± 0.09	24.50 ± 0.17	-0.12 ± 0.19
438	442.23	415.88	14:04:29.29	54:23:47.64	22.44 ± 0.19	22.40 ± 0.28	0.04 ± 0.34
439	411.80	378.26	14:04:29.29	54:23:52.46	20.81 ± 0.02	21.03 ± 0.03	-0.23 ± 0.03
440	408.55	373.97	14:04:29.29	54:23:52.99	21.39 ± 0.03	21.44 ± 0.03	-0.05 ± 0.04
441	390.29	351.36	14:04:29.29	54:23:55.88	23.79 ± 0.06	24.02 ± 0.14	-0.23 ± 0.15
442	476.56	456.83	14:04:29.30	54:23:42.32	22.79 ± 0.07	22.70 ± 0.11	0.10 ± 0.13
443	468.10	446.39	14:04:29.30	54:23:43.66	22.18 ± 0.05	21.96 ± 0.07	0.21 ± 0.09
444	423.28	390.96	14:04:29.30	54:23:50.76	23.43 ± 0.11	23.79 ± 0.13	-0.36 ± 0.17
445	406.77	370.26	14:04:29.30	54:23:53.39	24.22 ± 0.10	23.61 ± 0.07	0.61 ± 0.12
446	480.36	460.38	14:04:29.31	54:23:41.81	23.08 ± 0.07	22.98 ± 0.12	0.09 ± 0.14
447	452.26	425.55	14:04:29.31	54:23:46.27	22.27 ± 0.15	22.31 ± 0.18	-0.04 ± 0.24
448	383.36	340.15	14:04:29.31	54:23:57.18	24.18 ± 0.10	24.36 ± 0.09	-0.17 ± 0.14
449	438.54	407.00	14:04:29.32	54:23:48.56	23.45 ± 0.10	22.64 ± 0.07	0.81 ± 0.12
450	408.45	369.50	14:04:29.32	54:23:53.34	24.30 ± 0.14	23.13 ± 0.05	1.18 ± 0.15
451	353.36	302.21	14:04:29.32	54:24:02.00	23.51 ± 0.04	23.68 ± 0.06	-0.17 ± 0.07
452	474.88	450.06	14:04:29.33	54:23:42.95	25.28 ± 0.19	24.47 ± 0.12	0.81 ± 0.22
453	459.61	431.69	14:04:29.33	54:23:45.33	21.79 ± 0.18	21.65 ± 0.22	0.14 ± 0.29
454	451.42	420.90	14:04:29.33	54:23:46.68	22.60 ± 0.42	22.37 ± 0.38	0.23 ± 0.57
455	447.60	416.30	14:04:29.33	54:23:47.27	19.89 ± 0.03	19.74 ± 0.04	0.15 ± 0.05
456	428.36	393.00	14:04:29.33	54:23:50.28	22.69 ± 0.08	22.84 ± 0.06	-0.15 ± 0.10
457	462.43	434.36	14:04:29.34	54:23:44.95	23.42 ± 0.10	23.55 ± 0.11	-0.13 ± 0.15
458	453.81	423.45	14:04:29.34	54:23:46.33	22.20 ± 0.08	22.27 ± 0.11	-0.07 ± 0.13

continued on next page

· · · *continued from previous page*

ID	X pixel	Y pixel	R.A. (J2000)	Decl. (J2000)	m_{F547M} (mag)	$m_{F675W'}$ (mag)	m_{F547M} - $m_{F675W'}$ (mag)
459	425.12	388.47	14:04:29.34	54:23:50.83	24.17 ± 0.15	23.84 ± 0.11	0.34 ± 0.18
460	406.37	364.25	14:04:29.34	54:23:53.88	23.03 ± 0.05	23.74 ± 0.10	-0.71 ± 0.11
461	402.67	360.54	14:04:29.34	54:23:54.40	22.54 ± 0.06	22.74 ± 0.11	-0.20 ± 0.13
462	486.49	461.47	14:04:29.35	54:23:41.34	23.74 ± 0.07	23.87 ± 0.16	-0.13 ± 0.17
463	412.61	370.91	14:04:29.35	54:23:52.97	23.93 ± 0.13	23.70 ± 0.09	0.23 ± 0.15
464	411.38	369.76	14:04:29.35	54:23:53.14	23.25 ± 0.05	23.43 ± 0.07	-0.18 ± 0.09
465	371.10	320.74	14:04:29.35	54:23:59.45	25.35 ± 0.16	24.77 ± 0.20	0.58 ± 0.26
466	492.35	468.06	14:04:29.36	54:23:40.47	24.72 ± 0.12	24.38 ± 0.16	0.34 ± 0.20
467	398.12	352.03	14:04:29.36	54:23:55.34	24.95 ± 0.15	24.94 ± 0.16	0.01 ± 0.22
468	393.29	346.02	14:04:29.36	54:23:56.11	24.70 ± 0.12	24.61 ± 0.17	0.09 ± 0.21
469	463.72	431.50	14:04:29.37	54:23:45.09	22.95 ± 0.06	23.03 ± 0.07	-0.08 ± 0.09
470	459.82	425.97	14:04:29.37	54:23:45.76	23.00 ± 0.04	22.88 ± 0.05	0.12 ± 0.07
471	454.39	419.39	14:04:29.37	54:23:46.61	20.87 ± 0.16	20.87 ± 0.18	0.00 ± 0.25
472	443.45	406.51	14:04:29.37	54:23:48.29	22.75 ± 0.10	21.82 ± 0.06	0.94 ± 0.12
473	473.70	442.12	14:04:29.38	54:23:43.64	23.86 ± 0.29	23.44 ± 0.22	0.43 ± 0.36
474	456.81	421.40	14:04:29.38	54:23:46.30	21.29 ± 0.29	21.15 ± 0.26	0.14 ± 0.39
475	435.39	395.18	14:04:29.38	54:23:49.67	23.11 ± 0.07	23.19 ± 0.07	-0.08 ± 0.10
476	467.93	433.50	14:04:29.39	54:23:44.67	23.30 ± 0.05	23.62 ± 0.09	-0.32 ± 0.10
477	447.38	408.45	14:04:29.39	54:23:47.89	22.46 ± 0.04	22.65 ± 0.04	-0.19 ± 0.05
478	439.65	398.40	14:04:29.39	54:23:49.15	22.02 ± 0.04	21.27 ± 0.03	0.75 ± 0.04
479	431.17	388.50	14:04:29.39	54:23:50.45	24.33 ± 0.14	24.64 ± 0.20	-0.31 ± 0.25
480	422.01	377.52	14:04:29.39	54:23:51.87	20.99 ± 0.05	20.50 ± 0.03	0.49 ± 0.06
481	418.99	372.13	14:04:29.40	54:23:52.48	23.82 ± 0.06	23.71 ± 0.07	0.10 ± 0.10
482	531.02	507.71	14:04:29.41	54:23:34.98	24.42 ± 0.10	24.27 ± 0.10	0.16 ± 0.14
483	408.74	357.53	14:04:29.41	54:23:54.25	23.61 ± 0.09	23.79 ± 0.19	-0.18 ± 0.21
484	484.36	448.86	14:04:29.42	54:23:42.45	24.83 ± 0.14	24.53 ± 0.18	0.29 ± 0.23
485	452.82	410.70	14:04:29.42	54:23:47.38	21.84 ± 0.02	21.83 ± 0.03	0.02 ± 0.04
486	432.45	385.20	14:04:29.42	54:23:50.62	23.47 ± 0.09	23.36 ± 0.14	0.11 ± 0.17
487	399.21	344.79	14:04:29.42	54:23:55.83	23.75 ± 0.06	23.58 ± 0.07	0.17 ± 0.09
488	530.68	505.23	14:04:29.43	54:23:35.19	23.74 ± 0.07	23.67 ± 0.06	0.07 ± 0.10
489	526.90	498.86	14:04:29.44	54:23:35.92	25.19 ± 0.15	24.96 ± 0.20	0.23 ± 0.25
490	450.40	404.46	14:04:29.44	54:23:48.01	22.97 ± 0.05	22.97 ± 0.04	0.00 ± 0.07
491	417.27	364.74	14:04:29.44	54:23:53.16	21.30 ± 0.05	21.32 ± 0.05	-0.02 ± 0.07
492	470.95	428.22	14:04:29.45	54:23:44.88	23.25 ± 0.04	23.33 ± 0.05	-0.08 ± 0.07
493	463.15	419.70	14:04:29.45	54:23:46.03	21.64 ± 0.02	22.00 ± 0.03	-0.36 ± 0.03
494	439.25	389.74	14:04:29.45	54:23:49.85	24.11 ± 0.13	24.34 ± 0.15	-0.23 ± 0.20
495	504.47	468.68	14:04:29.46	54:23:39.66	24.02 ± 0.08	23.64 ± 0.07	0.38 ± 0.11
496	484.83	444.38	14:04:29.46	54:23:42.76	24.96 ± 0.15	25.04 ± 0.20	-0.09 ± 0.25
497	427.60	373.62	14:04:29.46	54:23:51.82	23.34 ± 0.12	23.12 ± 0.10	0.23 ± 0.15
498	534.87	504.97	14:04:29.47	54:23:34.94	24.39 ± 0.10	24.58 ± 0.13	-0.18 ± 0.16
499	495.85	456.88	14:04:29.47	54:23:41.11	24.20 ± 0.09	24.10 ± 0.11	0.10 ± 0.14
500	477.69	434.26	14:04:29.47	54:23:43.99	23.55 ± 0.21	23.47 ± 0.30	0.08 ± 0.37
501	461.65	415.13	14:04:29.47	54:23:46.48	19.14 ± 0.14	19.25 ± 0.17	-0.10 ± 0.22
502	451.15	402.15	14:04:29.47	54:23:48.14	22.05 ± 0.14	22.15 ± 0.23	-0.10 ± 0.27

continued on next page

· · · *continued from previous page*

ID	X pixel	Y pixel	R.A. (J2000)	Decl. (J2000)	m_{F547M} (mag)	$m_{F675W'}$ (mag)	m_{F547M} - $m_{F675W'}$ (mag)
503	445.04	394.78	14:04:29.47	54:23:49.09	22.92 ± 0.07	22.10 ± 0.02	0.82 ± 0.07
504	488.22	445.42	14:04:29.48	54:23:42.47	24.54 ± 0.10	24.32 ± 0.14	0.22 ± 0.17
505	485.29	440.85	14:04:29.49	54:23:43.01	22.26 ± 0.07	21.21 ± 0.05	1.05 ± 0.09
506	422.61	364.50	14:04:29.49	54:23:52.84	24.91 ± 0.13	24.22 ± 0.10	0.69 ± 0.16
507	396.31	331.48	14:04:29.49	54:23:57.04	25.52 ± 0.19	24.95 ± 0.18	0.57 ± 0.26
508	448.21	393.84	14:04:29.50	54:23:48.97	22.61 ± 0.07	22.85 ± 0.16	-0.24 ± 0.18
509	438.50	382.71	14:04:29.50	54:23:50.43	23.46 ± 0.05	23.66 ± 0.11	-0.20 ± 0.12
510	412.77	350.74	14:04:29.50	54:23:54.52	24.74 ± 0.14	24.71 ± 0.13	0.02 ± 0.19
511	483.78	436.42	14:04:29.51	54:23:43.44	23.75 ± 0.06	23.62 ± 0.06	0.13 ± 0.08
512	473.43	424.21	14:04:29.51	54:23:45.04	23.42 ± 0.05	23.64 ± 0.09	-0.22 ± 0.10
513	470.95	419.97	14:04:29.51	54:23:45.52	22.90 ± 0.04	22.46 ± 0.04	0.44 ± 0.06
514	440.72	383.89	14:04:29.51	54:23:50.20	23.69 ± 0.15	23.70 ± 0.19	-0.01 ± 0.24
515	481.21	431.96	14:04:29.52	54:23:43.95	24.27 ± 0.09	24.09 ± 0.09	0.18 ± 0.13
516	420.06	356.64	14:04:29.52	54:23:53.60	24.57 ± 0.16	24.89 ± 0.21	-0.32 ± 0.27
517	467.72	413.44	14:04:29.53	54:23:46.23	21.50 ± 0.02	20.85 ± 0.01	0.65 ± 0.03
518	470.62	415.79	14:04:29.54	54:23:45.86	21.38 ± 0.02	20.54 ± 0.01	0.84 ± 0.02
519	450.57	391.01	14:04:29.54	54:23:49.04	21.19 ± 0.04	20.18 ± 0.01	1.01 ± 0.04
520	437.42	374.39	14:04:29.55	54:23:51.14	24.21 ± 0.18	23.77 ± 0.17	0.44 ± 0.24
521	496.70	444.56	14:04:29.56	54:23:42.00	25.08 ± 0.17	24.06 ± 0.13	1.02 ± 0.21
522	477.77	421.93	14:04:29.56	54:23:44.94	23.22 ± 0.04	23.45 ± 0.06	-0.24 ± 0.08
523	460.49	401.25	14:04:29.56	54:23:47.62	20.10 ± 0.07	19.87 ± 0.07	0.23 ± 0.10
524	446.91	384.06	14:04:29.56	54:23:49.80	24.32 ± 0.09	24.34 ± 0.12	-0.01 ± 0.15
525	435.71	368.36	14:04:29.57	54:23:51.72	24.32 ± 0.19	24.02 ± 0.26	0.30 ± 0.32
526	500.08	446.30	14:04:29.58	54:23:41.66	25.03 ± 0.16	24.39 ± 0.26	0.64 ± 0.30
527	471.97	411.44	14:04:29.58	54:23:46.11	23.73 ± 0.08	22.93 ± 0.07	0.80 ± 0.11
528	467.19	405.67	14:04:29.58	54:23:46.86	22.55 ± 0.03	22.90 ± 0.05	-0.35 ± 0.06
529	440.97	374.30	14:04:29.58	54:23:50.93	24.82 ± 0.12	24.66 ± 0.14	0.16 ± 0.19
530	481.66	421.99	14:04:29.59	54:23:44.69	24.22 ± 0.09	23.94 ± 0.09	0.28 ± 0.12
531	438.72	368.94	14:04:29.60	54:23:51.48	24.66 ± 0.12	24.35 ± 0.16	0.31 ± 0.20
532	414.60	338.10	14:04:29.60	54:23:55.38	24.82 ± 0.11	24.61 ± 0.20	0.21 ± 0.22
533	470.65	406.93	14:04:29.61	54:23:46.54	23.73 ± 0.07	23.47 ± 0.07	0.26 ± 0.10
534	445.40	373.76	14:04:29.62	54:23:50.69	23.95 ± 0.17	23.84 ± 0.21	0.11 ± 0.27
535	443.16	371.18	14:04:29.62	54:23:51.03	23.46 ± 0.07	23.51 ± 0.14	-0.05 ± 0.16
536	448.26	376.50	14:04:29.63	54:23:50.30	24.77 ± 0.37	24.02 ± 0.34	0.75 ± 0.51
537	437.07	361.45	14:04:29.64	54:23:52.16	24.39 ± 0.09	24.33 ± 0.13	0.05 ± 0.15
538	483.85	417.39	14:04:29.65	54:23:44.91	22.77 ± 0.16	22.70 ± 0.27	0.07 ± 0.31
539	471.64	402.09	14:04:29.65	54:23:46.86	22.81 ± 0.24	22.68 ± 0.24	0.13 ± 0.34
540	462.70	391.27	14:04:29.65	54:23:48.25	24.05 ± 0.08	24.36 ± 0.12	-0.31 ± 0.14
541	451.51	376.58	14:04:29.65	54:23:50.09	23.70 ± 0.16	22.82 ± 0.13	0.88 ± 0.20
542	481.32	412.72	14:04:29.66	54:23:45.43	24.90 ± 0.14	24.57 ± 0.14	0.32 ± 0.20
543	410.80	326.41	14:04:29.66	54:23:56.52	24.93 ± 0.12	24.57 ± 0.16	0.36 ± 0.20
544	446.87	368.62	14:04:29.67	54:23:50.99	24.64 ± 0.10	24.93 ± 0.19	-0.28 ± 0.22
545	441.18	361.88	14:04:29.67	54:23:51.87	23.58 ± 0.07	23.65 ± 0.08	-0.06 ± 0.10
546	494.20	425.06	14:04:29.68	54:23:43.67	23.42 ± 0.06	23.46 ± 0.10	-0.04 ± 0.11

continued on next page

· · · *continued from previous page*

ID	X pixel	Y pixel	R.A. (J2000)	Decl. (J2000)	m_{F547M} (mag)	$m_{F675W'}$ (mag)	m_{F547M} - $m_{F675W'}$ (mag)
547	450.44	371.25	14:04:29.68	54:23:50.57	24.43 ± 0.15	24.46 ± 0.23	-0.03 ± 0.28
548	400.74	310.93	14:04:29.68	54:23:58.35	25.18 ± 0.14	25.20 ± 0.16	-0.01 ± 0.22
549	474.94	399.51	14:04:29.70	54:23:46.85	23.95 ± 0.20	24.08 ± 0.40	-0.13 ± 0.44
550	488.52	411.67	14:04:29.73	54:23:45.06	22.43 ± 0.03	22.34 ± 0.07	0.09 ± 0.07
551	411.00	316.26	14:04:29.73	54:23:57.29	22.49 ± 0.02	21.24 ± 0.02	1.25 ± 0.03
552	382.28	280.49	14:04:29.73	54:24:01.85	23.31 ± 0.04	22.23 ± 0.03	1.09 ± 0.05
553	476.33	395.21	14:04:29.74	54:23:47.09	23.96 ± 0.09	23.00 ± 0.07	0.96 ± 0.11
554	417.30	320.79	14:04:29.75	54:23:56.54	24.63 ± 0.09	23.92 ± 0.12	0.72 ± 0.15
555	504.44	426.52	14:04:29.76	54:23:42.91	24.55 ± 0.13	23.75 ± 0.10	0.80 ± 0.17
556	459.62	371.41	14:04:29.76	54:23:49.98	25.30 ± 0.18	24.78 ± 0.18	0.52 ± 0.26
557	456.71	367.99	14:04:29.76	54:23:50.42	25.18 ± 0.18	24.15 ± 0.14	1.03 ± 0.23
558	440.97	347.24	14:04:29.77	54:23:53.01	22.92 ± 0.03	22.82 ± 0.03	0.10 ± 0.04
559	534.98	461.27	14:04:29.78	54:23:38.31	24.76 ± 0.10	24.10 ± 0.10	0.66 ± 0.14
560	489.69	406.15	14:04:29.78	54:23:45.41	24.59 ± 0.12	24.54 ± 0.19	0.05 ± 0.22
561	446.11	352.60	14:04:29.78	54:23:52.28	24.31 ± 0.08	24.17 ± 0.10	0.13 ± 0.13
562	439.28	344.24	14:04:29.78	54:23:53.35	23.76 ± 0.14	23.83 ± 0.16	-0.07 ± 0.21
563	519.88	441.53	14:04:29.79	54:23:40.78	24.49 ± 0.10	24.78 ± 0.17	-0.29 ± 0.19
564	415.37	313.83	14:04:29.79	54:23:57.20	22.84 ± 0.03	23.04 ± 0.04	-0.20 ± 0.05
565	545.18	471.02	14:04:29.80	54:23:36.91	24.28 ± 0.09	24.04 ± 0.12	0.24 ± 0.15
566	472.67	382.20	14:04:29.80	54:23:48.32	23.93 ± 0.11	24.00 ± 0.13	-0.07 ± 0.17
567	453.34	356.88	14:04:29.81	54:23:51.49	25.32 ± 0.17	25.24 ± 0.19	0.08 ± 0.25
568	510.30	426.40	14:04:29.82	54:23:42.55	23.31 ± 0.04	23.40 ± 0.06	-0.09 ± 0.07
569	449.48	351.10	14:04:29.82	54:23:52.18	24.14 ± 0.07	24.14 ± 0.10	0.00 ± 0.12
570	440.96	339.14	14:04:29.83	54:23:53.64	23.07 ± 0.03	23.08 ± 0.05	-0.02 ± 0.06
571	521.02	436.17	14:04:29.84	54:23:41.12	25.10 ± 0.14	24.85 ± 0.19	0.25 ± 0.24
572	504.47	415.39	14:04:29.84	54:23:43.77	25.35 ± 0.17	25.08 ± 0.18	0.26 ± 0.25
573	471.36	375.70	14:04:29.84	54:23:48.91	24.39 ± 0.19	24.35 ± 0.21	0.04 ± 0.28
574	410.64	299.12	14:04:29.85	54:23:58.63	25.16 ± 0.17	24.90 ± 0.18	0.26 ± 0.25
575	524.14	436.43	14:04:29.87	54:23:40.91	23.90 ± 0.05	23.74 ± 0.08	0.17 ± 0.10
576	475.68	376.04	14:04:29.87	54:23:48.61	24.54 ± 0.13	24.23 ± 0.16	0.31 ± 0.20
577	423.57	311.98	14:04:29.87	54:23:56.83	23.62 ± 0.07	23.63 ± 0.09	-0.01 ± 0.11
578	541.19	456.02	14:04:29.88	54:23:38.32	23.43 ± 0.04	22.46 ± 0.02	0.97 ± 0.05
579	491.48	393.51	14:04:29.89	54:23:46.27	25.36 ± 0.19	25.23 ± 0.18	0.13 ± 0.27
580	475.34	372.98	14:04:29.89	54:23:48.87	24.59 ± 0.10	23.80 ± 0.07	0.79 ± 0.13
581	469.09	365.05	14:04:29.89	54:23:49.87	24.57 ± 0.09	24.53 ± 0.11	0.04 ± 0.14
582	417.26	301.40	14:04:29.89	54:23:58.04	22.52 ± 0.02	21.50 ± 0.01	1.02 ± 0.03
583	483.66	380.20	14:04:29.91	54:23:47.79	24.52 ± 0.10	24.62 ± 0.13	-0.09 ± 0.16
584	503.83	402.27	14:04:29.93	54:23:44.82	23.67 ± 0.05	23.83 ± 0.06	-0.15 ± 0.07
585	417.39	295.88	14:04:29.93	54:23:58.46	24.70 ± 0.11	24.75 ± 0.16	-0.05 ± 0.19
586	518.51	417.46	14:04:29.95	54:23:42.72	24.32 ± 0.09	24.38 ± 0.10	-0.07 ± 0.14
587	489.93	381.12	14:04:29.96	54:23:47.32	24.23 ± 0.09	24.48 ± 0.15	-0.24 ± 0.17
588	478.73	366.94	14:04:29.96	54:23:49.12	24.45 ± 0.08	24.44 ± 0.11	0.01 ± 0.14
589	535.54	435.35	14:04:29.97	54:23:40.27	23.56 ± 0.04	23.62 ± 0.05	-0.06 ± 0.07
590	467.88	351.89	14:04:29.98	54:23:50.96	23.66 ± 0.05	23.47 ± 0.05	0.19 ± 0.07

continued on next page

· · · *continued from previous page*

ID	X pixel	Y pixel	R.A. (J2000)	Decl. (J2000)	m_{F547M} (mag)	$m_{F675W'}$ (mag)	m_{F547M} - $m_{F675W'}$ (mag)
591	453.85	326.60	14:04:30.03	54:23:53.80	22.70 ± 0.03	21.73 ± 0.03	0.97 ± 0.04
592	504.56	387.48	14:04:30.04	54:23:45.91	24.74 ± 0.10	24.54 ± 0.12	0.20 ± 0.16
593	516.35	397.87	14:04:30.07	54:23:44.37	23.91 ± 0.06	24.10 ± 0.12	-0.19 ± 0.13
594	483.80	358.35	14:04:30.07	54:23:49.46	25.09 ± 0.14	25.01 ± 0.21	0.07 ± 0.25
595	511.27	382.00	14:04:30.14	54:23:45.91	24.76 ± 0.10	24.72 ± 0.16	0.04 ± 0.19
596	517.41	386.97	14:04:30.16	54:23:45.14	22.86 ± 0.04	22.83 ± 0.06	0.03 ± 0.07
597	500.40	366.43	14:04:30.16	54:23:47.80	23.53 ± 0.09	22.87 ± 0.07	0.66 ± 0.11
598	484.82	346.45	14:04:30.17	54:23:50.32	23.94 ± 0.07	23.99 ± 0.06	-0.04 ± 0.09
599	536.06	406.69	14:04:30.19	54:23:42.45	25.08 ± 0.13	24.81 ± 0.20	0.28 ± 0.24
600	499.77	360.11	14:04:30.20	54:23:48.32	23.95 ± 0.06	22.95 ± 0.04	0.99 ± 0.07
601	468.66	319.60	14:04:30.22	54:23:53.40	25.10 ± 0.17	24.93 ± 0.20	0.17 ± 0.26
602	528.52	391.43	14:04:30.23	54:23:44.10	24.52 ± 0.09	24.47 ± 0.12	0.05 ± 0.15
603	449.73	293.76	14:04:30.23	54:23:56.59	23.81 ± 0.05	23.11 ± 0.04	0.71 ± 0.06
604	473.69	313.25	14:04:30.31	54:23:53.58	24.66 ± 0.09	24.47 ± 0.12	0.18 ± 0.16
605	544.23	396.28	14:04:30.33	54:23:42.74	23.23 ± 0.03	23.00 ± 0.03	0.23 ± 0.05
606	471.73	307.77	14:04:30.33	54:23:54.12	24.63 ± 0.09	24.93 ± 0.14	-0.30 ± 0.17
607	477.55	300.09	14:04:30.43	54:23:54.35	24.45 ± 0.08	24.16 ± 0.09	0.29 ± 0.12
608	523.52	355.82	14:04:30.44	54:23:47.16	22.17 ± 0.02	22.16 ± 0.02	0.01 ± 0.03
609	493.62	317.22	14:04:30.45	54:23:52.02	24.65 ± 0.09	24.80 ± 0.16	-0.15 ± 0.18
610	467.79	285.50	14:04:30.45	54:23:56.09	23.43 ± 0.05	23.36 ± 0.06	0.07 ± 0.08
611	495.20	309.95	14:04:30.52	54:23:52.48	25.14 ± 0.13	25.41 ± 0.21	-0.27 ± 0.25
612	493.36	306.19	14:04:30.53	54:23:52.89	25.47 ± 0.18	25.40 ± 0.20	0.07 ± 0.27
613	520.50	337.36	14:04:30.55	54:23:48.77	25.16 ± 0.19	24.52 ± 0.10	0.64 ± 0.21
614	513.53	325.28	14:04:30.57	54:23:50.14	24.57 ± 0.09	24.09 ± 0.07	0.48 ± 0.12

Table D.1: Stellar photometry results of NGC 5471.

References

Allende Prieto, C., Lambert, D. L., & Asplund, M. 2001, *ApJ* **556**, L63

Allington-Smith, J. & Content, R. 1998, *PASP* **110**, 1216

Alloin, D., Collin-Souffrin, S., Joly, M., & Vigroux, L. 1979, *A&A* **78**, 200

Aloisi, A., Tosi, M., & Greggio, L. 1999, *AJ* **118**, 302

Anderson, J. & King, I. R. 1999, *PASP* **111**, 1095

Aparicio, A. & Gallart, C. 1995, *AJ* **110**, 2105

Arribas, S., Mediavilla, E., García-Lorenzo, B., del Burgo, C., & Fuensalida, J. J. 1999, *A&AS* **136**, 189

Asplund, M., Grevesse, N., & Sauval, A. J. 2005, in T. G. Barnes, III and F. N. Bash (eds.), *Cosmic Abundances as Records of Stellar Evolution and Nucleosynthesis*, Vol. 336 of *Astronomical Society of the Pacific Conference Series*, p. 25

Baldwin, J. A., Phillips, M. M., & Terlevich, R. 1981, *PASP* **93**, 5

Ball, R., Sargent, A. I., Scoville, N. Z., Lo, K. Y., & Scott, S. L. 1985, *ApJ* **298**, L21

Barker, T. 1980, *ApJ* **240**, 99

Bastian, N. & Goodwin, S. P. 2006, *MNRAS* **369**, L9

Bellazzini, M., Ferraro, F. R., & Buonanno, R. 1999, *MNRAS* **307**, 619

Belley, J. & Roy, J.-R. 1992, *ApJS* **78**, 61

Bertelli, G., Bressan, A., Chiosi, C., Fagotto, F., & Nasi, E. 1994, *A&AS* **106**, 275

Bianchi, L., Thilker, D. A., Burgarella, D., Friedman, P. G., Hoopes, C. G., et al. 2005, *ApJ* **619**, L71

Bournaud, F. & Combes, F. 2003, *A&A* **401**, 817

Brandner, W. 2002, in E. K. Grebel and W. Brandner (eds.), *Modes of Star Formation and the Origin of Field Populations*, Vol. 285 of *Astronomical Society of the Pacific Conference Series*, p. 105

Braun, R. 1995, *A&AS* **114**, 409

Bruzual, G. & Charlot, S. 2003, *MNRAS* **344**, 1000

Burstein, D. & Heiles, C. 1984, *ApJS* **54**, 33

Cairós, L. M., Vílchez, J. M., González Pérez, J. N., Iglesias-Páramo, J., & Caon, N. 2001, *ApJS* **133**, 321

Cardelli, J. A., Clayton, G. C., & Mathis, J. S. 1989, *ApJ* **345**, 245

Carignan, C., Charbonneau, P., Boulanger, F., & Viallefond, F. 1990, *A&A* **234**, 43

Casoli, F., Clausset, F., Combes, F., Viallefond, F., & Boulanger, F. 1990, *A&A* **233**, 357

Castellanos, M., Díaz, A. I., & Terlevich, E. 2002, *MNRAS* **329**, 315

Chabrier, G. 2003, *PASP* **115**, 763

Chen, C.-H. R., Chu, Y.-H., Gruendl, R., Lai, S.-P., & Wang, Q. D. 2002, *AJ* **123**, 2462

Cid Fernandes, R., Gu, Q., Melnick, J., Terlevich, E., Terlevich, R., et al. 2004, *MNRAS* **355**, 273

Conti, P. S. 1991, *ApJ* **377**, 115

Cox, A. L., Sparke, L. S., Watson, A. M., & van Moorsel, G. 2001, *AJ* **121**, 692

Crowther, P. A. 2007, *ARA&A* **45**, 177

De Robertis, M. M., Dufour, R. J., & Hunt, R. W. 1987, *JRASC* **81**, 195

de Vaucouleurs, G., de Vaucouleurs, A., Corwin, Jr., H. G., Buta, R. J., Paturel, G., et al. 1991, *Third Reference Catalogue of Bright Galaxies*, New York: Springer

Degioia-Eastwood, K. 1985, *ApJ* **288**, 175

Degioia-Eastwood, K., Grasdalen, G. L., Strom, S. E., & Strom, K. M. 1984, *ApJ* **278**, 564

Denicoló, G., Terlevich, R., & Terlevich, E. 2002, *MNRAS* **330**, 69

Diaz, A. I. 1988, *MNRAS* **231**, 57

Díaz, Á. I. 1998, *Ap&SS* **263**, 143

Díaz, A. I., Castellanos, M., Terlevich, E., & Luisa García-Vargas, M. 2000, *MNRAS* **318**, 462

Diaz, A. I., Pagel, B. E. J., & Wilson, I. R. G. 1985, *MNRAS* **212**, 737

Díaz, A. I. & Pérez-Montero, E. 2000, *MNRAS* **312**, 130

Díaz, Á. I., Terlevich, E., Castellanos, M., & Hägele, G. F. 2007, *MNRAS* **382**, 251

Diaz, A. I., Terlevich, E., Pagel, B. E. J., Vilchez, J. M., & Edmunds, M. G. 1987, *MNRAS* **226**, 19

Diaz, A. I., Terlevich, E., Vilchez, J. M., Pagel, B. E. J., & Edmunds, M. G. 1991, *MNRAS* **253**, 245

Dolphin, A. E. 2000a, *PASP* **112**, 1397

Dolphin, A. E. 2000b, *PASP* **112**, 1383

Edmunds, M. G. & Pagel, B. E. J. 1984, *MNRAS* **211**, 507

Elmegreen, D. M., Chromey, F. R., & Santos, M. 1998, *AJ* **116**, 1221

Ercolano, B., Barlow, M. J., Storey, P. J., & Liu, X.-W. 2003, *MNRAS* **340**, 1136

Esteban, C., Peimbert, M., Torres-Peimbert, S., & Rodríguez, M. 2002, *ApJ* **581**, 241

Ferguson, A. M. N., Gallagher, J. S., & Wyse, R. F. G. 1998, *AJ* **116**, 673

Ferland, G. J., Korista, K. T., Verner, D. A., Ferguson, J. W., Kingdon, J. B., et al. 1998, *PASP* **110**, 761

Filippenko, A. V. 1982, *PASP* **94**, 715

French, H. B. 1980, *ApJ* **240**, 41

Garnett, D. R. 1992, *AJ* **103**, 1330

Garstang, R. H., Robb, W. D., & Rountree, S. P. 1978, *ApJ* **222**, 384

Giannakopoulou-Creighton, J., Fich, M., & Wilson, C. D. 1999, *ApJ* **522**, 238

Gil de Paz, A., Madore, B. F., & Pevunova, O. 2003, *ApJS* **147**, 29

Girardi, L. & Bertelli, G. 1998, *MNRAS* **300**, 533

Girardi, L., Bertelli, G., Bressan, A., Chiosi, C., Groenewegen, M. A. T., et al. 2002, *A&A* **391**, 195

Girardi, L., Bressan, A., Bertelli, G., & Chiosi, C. 2000, *A&AS* **141**, 371

González Delgado, R. M., Cerviño, M., Martins, L. P., Leitherer, C., & Hauschildt, P. H. 2005, *MNRAS* **357**, 945

Gonzalez-Delgado, R. M., Perez, E., Tenorio-Tagle, G., Vilchez, J. M., Terlevich, E., et al. 1994, *ApJ* **437**, 239

Grevesse, N. & Sauval, A. J. 1998, *Space Science Reviews* **85**, 161

Hägele, G. F., Díaz, Á. I., Terlevich, E., Terlevich, R., Pérez-Montero, E., et al. 2008, *MNRAS* **383**, 209

Hägele, G. F., Pérez-Montero, E., Díaz, Á. I., Terlevich, E., & Terlevich, R. 2006, *MNRAS* **372**, 293

Haro, G. 1956, *Boletin de los Observatorios Tonantzintla y Tacubaya* **2**, 8

Harris, J. & Zaritsky, D. 2001, *ApJS* **136**, 25

Harris, J. & Zaritsky, D. 2002, in T. Lejeune and J. Fernandes (eds.), *Observed HR Diagrams and Stellar Evolution*, Vol. 274 of *Astronomical Society of the Pacific Conference Series*, p. 600

Heckman, T. M. 1997, in S. S. Holt and L. G. Mundy (eds.), *American Institute of Physics Conference Series*, Vol. 393 of *American Institute of Physics Conference Series*, p. 271

Heyer, Biretta, e. a. 2004, *WFPC2 Instrument Handbook, Version 9.0 (Baltimore: STScI)*

Ho, L. C., Filippenko, A. V., & Sargent, W. L. W. 1997, *ApJS* **112**, 315

Hodge, P. W. 1969a, *ApJ* **156**, 847

Hodge, P. W. 1969b, *ApJ* **155**, 417

Hodge, P. W. & Kennicutt, Jr., R. C. 1983, *AJ* **88**, 296

Holtzman, J. A., Hester, J. J., Casertano, S., Trauger, J. T., Watson, A. M., et al. 1995, *PASP* **107**, 156

Holweger, H. 2001, in R. F. Wimmer-Schweingruber (ed.), *Joint SOHO/ACE workshop "Solar and Galactic Composition"*, Vol. 598 of *American Institute of Physics Conference Series*, p. 23

Hunter, D. A. & Thronson, Jr., H. A. 1995, *ApJ* **452**, 238

Indebetouw, R., de Messières, G. E., Madden, S., Engelbracht, C., Smith, J. D., et al. 2009, *ApJ* **694**, 84

Izotov, Y. I., Stasińska, G., Guseva, N. G., & Thuan, T. X. 2004, *A&A* **415**, 87

Izotov, Y. I., Stasińska, G., Meynet, G., Guseva, N. G., & Thuan, T. X. 2006, *A&A* **448**, 955

Izotov, Y. I., Thuan, T. X., & Lipovetsky, V. A. 1994, *ApJ* **435**, 647

Jenkins, L. P., Roberts, T. P., Warwick, R. S., Kilgard, R. E., & Ward, M. J. 2004, *MNRAS* **349**, 404

Karachentsev, I. D., Sharina, M. E., & Huchtmeier, W. K. 2000, *A&A* **362**, 544

Kauffmann, G., White, S. D. M., & Guiderdoni, B. 1993, *MNRAS* **264**, 201

Kehrig, C., Vílchez, J. M., Sánchez, S. F., Telles, E., Pérez-Montero, E., et al. 2008, *A&A* **477**, 813

Kelz, A., Verheijen, M. A. W., Roth, M. M., Bauer, S. M., Becker, T., et al. 2006, *PASP* **118**, 129

Kennicutt, Jr., R. C. 1984, *ApJ* **287**, 116

Kennicutt, Jr., R. C. 1998, *ARA&A* **36**, 189

Kennicutt, Jr., R. C., Bresolin, F., & Garnett, D. R. 2003, *ApJ* **591**, 801

Kennicutt, Jr., R. C. & Garnett, D. R. 1996, *ApJ* **456**, 504

Kewley, L. J., Dopita, M. A., Sutherland, R. S., Heisler, C. A., & Trevena, J. 2001, *ApJ* **556**, 121

Kewley, L. J. & Ellison, S. L. 2008, *ApJ* **681**, 1183

Kewley, L. J., Jansen, R. A., & Geller, M. J. 2005, *PASP* **117**, 227

Kingdon, J. & Ferland, G. J. 1995, *ApJ* **442**, 714

Kobulnicky, H. A., Kennicutt, Jr., R. C., & Pizagno, J. L. 1999, *ApJ* **514**, 544

Krist, J. 1995, in R. A. Shaw, H. E. Payne, and J. J. E. Hayes (eds.), *Astronomical Data Analysis Software and Systems IV*, Vol. 77 of *Astronomical Society of the Pacific Conference Series*, p. 349

Kroupa, P. 2002, *Science* **295**, 82

Kunth, D. & Sargent, W. L. W. 1983, *ApJ* **273**, 81

Lagos, P., Telles, E., Muñoz-Tuñón, C., Carrasco, E. R., Cuisinier, F., et al. 2009, *AJ* **137**, 5068

Larsen, S. S., Origlia, L., Brodie, J. P., & Gallagher, J. S. 2006, *MNRAS* **368**, L10

Le Borgne, J.-F., Bruzual, G., Pelló, R., Lançon, A., Rocca-Volmerange, B., et al. 2003, *A&A* **402**, 433

Leitherer, C., Robert, C., & Drissen, L. 1992, *ApJ* **401**, 596

Leitherer, C., Schaerer, D., Goldader, J. D., Delgado, R. M. G., Robert, C., et al. 1999, *ApJS* **123**, 3

Liu, X.-W., Storey, P. J., Barlow, M. J., Danziger, I. J., Cohen, M., et al. 2000, *MNRAS* **312**, 585

Luridiana, V., Esteban, C., Peimbert, M., & Peimbert, A. 2002, *Revista Mexicana de Astronomia y Astrofisica* **38**, 97

Luridiana, V., Pérez, E., & Cerviño, M. 2003, *AJ* **125**, 3196

Mackey, A. D., Broby Nielsen, P., Ferguson, A. M. N., & Richardson, J. C. 2008, *ApJ* **681**, L17

Madau, P., Ferguson, H. C., Dickinson, M. E., Giavalisco, M., Steidel, C. C., et al. 1996, *MNRAS* **283**, 1388

Maíz-Apellániz, J. 2001, *ApJ* **563**, 151

Maíz-Apellániz, J. 2004, *PASP* **116**, 859

Maíz-Apellániz, J. 2007, in C. Sterken (ed.), *The Future of Photometric, Spectrophotometric and Polarimetric Standardization*, Vol. 364 of *Astronomical Society of the Pacific Conference Series*, p. 227

Maiz-Apellaniz, J., Mas-Hesse, J. M., Munoz-Tunon, C., Vilchez, J. M., & Castaneda, H. O. 1998, *A&A* **329**, 409

Martin, D. C., Fanson, J., Schiminovich, D., Morrissey, P., Friedman, P. G., et al. 2005, *ApJ* **619**, L1

Mas-Hesse, J. M. & Kunth, D. 1999, *A&A* **349**, 765

Mateus, A., Sodré, L., Cid Fernandes, R., Stasińska, G., Schoenell, W., et al. 2006, *MNRAS* **370**, 721

Mayall, N. U. 1948, *PASP* **60**, 266

McCall, M. L., Rybski, P. M., & Shields, G. A. 1985, *ApJS* **57**, 1

McGaugh, S. S. 1991, *ApJ* **380**, 140

Melnick, J., Terlevich, R., & Eggleton, P. P. 1985, *MNRAS* **216**, 255

Meynet, G., Maeder, A., Schaller, G., Schaerer, D., & Charbonnel, C. 1994, *A&AS* **103**, 97

Mighell, K. J., Rich, R. M., Shara, M., & Fall, S. M. 1996, *AJ* **111**, 2314

Miller, J. S. & Mathews, W. G. 1972, *ApJ* **172**, 593

Morrissey, P., Schiminovich, D., Barlow, T. A., Martin, D. C., Blakkolb, B., et al. 2005, *ApJ* **619**, L7

Mould, J. R., Huchra, J. P., Freedman, W. L., Kennicutt, Jr., R. C., Ferrarese, L., et al. 2000, *ApJ* **529**, 786

Munoz-Tunon, C., Gavryusev, V., & Castoneda, H. O. 1995, *AJ* **110**, 1630

Olive, K. A. & Skillman, E. D. 2001, *New Astronomy* **6**, 119

Osterbrock, D. E. 1989, *Astrophysics of Gaseous Nebulae and Active Galactic Nuclei*, University Science Books

Osterbrock, D. E. & Martel, A. 1992, *PASP* **104**, 76

Östlin, G. 2000, *ApJ* **535**, L99

Pagel, B. E. J., Edmunds, M. G., Blackwell, D. E., Chun, M. S., & Smith, G. 1979, *MNRAS* **189**, 95

Pagel, B. E. J., Simonson, E. A., Terlevich, R. J., & Edmunds, M. G. 1992, *MNRAS* **255**, 325

Peimbert, M. & Costero, R. 1969, *Boletin de los Observatorios Tonantzintla y Tacubaya* **5**, 3

Pellerin, A. 2006, *AJ* **131**, 849

Pérez-Montero, E. & Díaz, A. I. 2003, *MNRAS* **346**, 105

Pérez-Montero, E. & Díaz, A. I. 2005, *MNRAS* **361**, 1063

Pérez-Montero, E. & Díaz, Á. I. 2007, *MNRAS* **377**, 1195

Pérez-Montero, E., Díaz, A. I., Vílchez, J. M., & Kehrig, C. 2006, *A&A* **449**, 193

Pérez-Montero, E., Hägele, G. F., Contini, T., & Díaz, Á. I. 2007, *MNRAS* **381**, 125

Pettini, M. & Pagel, B. E. J. 2004, *MNRAS* **348**, L59

Pradhan, A. K. 1976, *MNRAS* **177**, 31

Regan, M. W. & Vogel, S. N. 1995, *ApJ* **452**, L21+

Reshetnikov, V. P. & Combes, F. 1994, *A&A* **291**, 57

Rodríguez, M. & Rubin, R. H. 2004, in P.-A. Duc, J. Braine, and E. Brinks (eds.), *Recycling Intergalactic and Interstellar Matter*, Vol. 217 of *IAU Symposium*, p. 188

Rogstad, D. H., Shostak, G. S., & Rots, A. H. 1973, *A&A* **22**, 111

Rosa, M. 1981, *Ph.D. thesis*, PhD Thesis, Landessternwarte Heidelberg/Königstuhl (1981).

Rosa, M. & Mathis, J. S. 1987, *ApJ* **317**, 163

Rosa, M. R. & Benvenuti, P. 1994, *A&A* **291**, 1

Roth, M. M., Kelz, A., Fechner, T., Hahn, T., Bauer, S.-M., et al. 2005, *PASP* **117**, 620

Rubin, R. H., Bhatt, N. J., Dufour, R. J., Buckalew, B. A., Barlow, M. J., et al. 2002, *MNRAS* **334**, 777

Sánchez, S. F. 2004, *Astronomische Nachrichten* **325**, 167

Sánchez, S. F. 2006, *Astronomische Nachrichten* **327**, 850

Sánchez, S. F., Aceituno, J., Thiele, U., Pérez-Ramírez, D., & Alves, J. 2007a, *PASP* **119**, 1186

Sánchez, S. F., Cardiel, N., Verheijen, M. A. W., Pedraz, S., & Covone, G. 2007b, *MNRAS* **376**, 125

Sánchez, S. F., García-Lorenzo, B., & Pecontal-Rousset, A. 2006, in *Proceedings of the XIII IAC Winter School, ed. S. Arribas, E. Mediavilla, & M. Roth, in press*

Sargent, W. L. W. & Searle, L. 1970, *ApJ* **162**, L155

Schlegel, D. J., Finkbeiner, D. P., & Davis, M. 1998, *ApJ* **500**, 525

Schulte-Ladbeck, R. E., Crone, M. M., & Hopp, U. 1998, *ApJ* **493**, L23

Searle, L. & Sargent, W. L. W. 1972, *ApJ* **173**, 25

Searle, L., Sargent, W. L. W., & Bagnuolo, W. G. 1973, *ApJ* **179**, 427

Shaklan, S., Sharman, M. C., & Pravdo, S. H. 1995, *Appl. Opt.* **34**, 6672

Shaw, R. A. & Dufour, R. J. 1995, *PASP* **107**, 896

Shi, F., Kong, X., Li, C., & Cheng, F. Z. 2005, *A&A* **437**, 849

Shields, G. A. 1990, *ARA&A* **28**, 525

Skillman, E. D. 1985, *ApJ* **290**, 449

Smith, D. A., Allen, R. J., Bohlin, R. C., Nicholson, N., & Stecher, T. P. 2000, *ApJ* **538**, 608

Smith, L. F. 1991, in R. Haynes and D. Milne (eds.), *The Magellanic Clouds*, Vol. 148 of *IAU Symposium*, p. 267

Smith, L. J., Norris, R. P. F., & Crowther, P. A. 2002, *MNRAS* **337**, 1309

Smits, D. P. 1996, *MNRAS* **278**, 683

Stasińska, G. 1978, *A&A* **66**, 257

Stasińska, G. 1990, *A&AS* **83**, 501

Stasińska, G. 2006, *A&A* **454**, L127

Stasińska, G., Tenorio-Tagle, G., Rodríguez, M., & Henney, W. J. 2007, *A&A* **471**, 193

Stetson, P. B. & Harris, W. E. 1988, *AJ* **96**, 909

Stetson, P. B., Saha, A., Ferrarese, L., Rawson, D. M., Ford, H. C., et al. 1998, *ApJ* **508**, 491

Storchi-Bergmann, T., Calzetti, D., & Kinney, A. L. 1994, *ApJ* **429**, 572

Storey, P. J. & Hummer, D. G. 1995, *MNRAS* **272**, 41

Tacconi, L. J. & Young, J. S. 1986, *ApJ* **308**, 600

Telles, E. & Terlevich, R. 1995, *MNRAS* **275**, 1

Tenorio-Tagle, G. 1996, *AJ* **111**, 1641

Tenorio-Tagle, G., Muñoz-Tuñón, C., Pérez, E., Silich, S., & Telles, E. 2006, *ApJ* **643**, 186

Terlevich, R. 1997, in J. Franco, R. Terlevich, and A. Serrano (eds.), *Revista Mexicana de Astronomia y Astrofisica Conference Series*, Vol. 6 of *Revista Mexicana de Astronomia y Astrofisica Conference Series*, p. 1

Terlevich, R. & Melnick, J. 1981, *MNRAS* **195**, 839

Terlevich, R., Melnick, J., Masegosa, J., Moles, M., & Copetti, M. V. F. 1991, *A&AS* **91**, 285

Terlevich, R., Silich, S., Rosa-González, D., & Terlevich, E. 2004, *MNRAS* **348**, 1191

Thuan, T. X., Hibbard, J. E., & Lévrier, F. 2004, *AJ* **128**, 617

Torres-Peimbert, S., Peimbert, M., & Fierro, J. 1989, *ApJ* **345**, 186

Tully, R. B. 1988, *Nearby Galaxies Catalog*, Cambridge University Press

Úbeda, L., Maíz-Apellániz, J., & MacKenty, J. W. 2007, *AJ* **133**, 932

Vacca, W. D. & Conti, P. S. 1992, *ApJ* **401**, 543

van Dokkum, P. G. 2001, *PASP* **113**, 1420

Veilleux, S. & Osterbrock, D. E. 1987, *ApJS* **63**, 295

Viallefond, F., Allen, R. J., & Goss, W. M. 1981, *A&A* **104**, 127

Vilchez, J. M. & Esteban, C. 1996, *MNRAS* **280**, 720

Walborn, N. R. 2002, in P. Crowther (ed.), *Hot Star Workshop III: The Earliest Phases of Massive Star Birth*, Vol. 267 of *Astronomical Society of the Pacific Conference Series*, p. 111

Walborn, N. R., Barbá, R. H., Brandner, W., Rubio, M., Grebel, E. K., et al. 1999, *AJ* **117**, 225

Walborn, N. R. & Blades, J. C. 1997, *ApJS* **112**, 457

Walborn, N. R., Maíz-Apellániz, J., & Barbá, R. H. 2002, *AJ* **124**, 1601

Waller, W. H., Bohlin, R. C., Cornett, R. H., Fanelli, M. N., Freedman, W. L., et al. 1997, *ApJ* **481**, 169

Walsh, W., Beck, R., Thuma, G., Weiss, A., Wielebinski, R., et al. 2002, *A&A* **388**, 7

Wang, W., Liu, X.-W., Zhang, Y., & Barlow, M. J. 2004, *A&A* **427**, 873

Wesson, R. & Liu, X.-W. 2004, *MNRAS* **351**, 1026

Westera, P., Lejeune, T., Buser, R., Cuisinier, F., & Bruzual, G. 2002, *A&A* **381**, 524

Whitmore, B. C., Lucas, R. A., McElroy, D. B., Steiman-Cameron, T. Y., Sackett, P. D., et al. 1990, *AJ* **100**, 1489

Young, J. S., Xie, S., Tacconi, L., Knezek, P., Viscuso, P., et al. 1995, *ApJS* **98**, 219

Zeippen, C. J. 1982, *MNRAS* **198**, 111

Zwicky, F. 1966, *ApJ* **143**, 192